Universitat Autònoma de Barcelona

High precision measurements of magnetic fields and synchronization in optomechanical cavities

Martin F. Colombano Sosa

DOCTORAL THESIS

High precision measurements of magnetic fields and synchronization in optomechanical cavities

Author:
Martin F. Colombano Sosa

Under the supervision of:
Dr. Daniel Navarro Urrios
Dr. Marius Vasile Costache

A thesis submitted in fulfilment of the requirements for the degree of Doctor of Philosophy in the

Universitat Autònoma de Barcelona
Facultat de Ciències
Departament de Física

Photonic and Phononic Nanostructures
Group leader: Prof. Dr. Clivia Sotomayor-Torres
Physics and Engineering of Nanodevices
Group leader: Prof. Dr. Sergio O. Valenzuela

ICN2
Institut Català de Nanociència i Nanotecnologia
EXCELENCIA SEVERO OCHOA

2020

Declaration of Authorship

El doctorando / *The doctoral candidate* MARTÍN F. COLOMBANO SOSA, y los directores de la tesis / *and the thesis supervisors*, Dr. DANIEL NAVARRO URRIOS y Dr. MARIUS VASILE COSTACHE

Garantizamos, al firmar esta tesis doctoral, que el trabajo ha sido realizado por el doctorando bajo la dirección de los directores de la tesis y hasta donde nuestro conocimiento alcanza, en la realización del trabajo, se han respetado los derechos de otros autores a ser citados, cuando se han utilizado sus resultados o publicaciones.

Guarantee, by signing this doctoral thesis, that the work has been done by the doctoral candidate under the direction of the thesis supervisors and, as far as our knowledge reaches, in the performance of the work, the rights of other authors to be cited (when their results or publications have been used) have been respected.

Date: Barcelona, July 3, 2020

Abstract

Mechanical resonators are one of the most fundamental and omnipresent physical systems at all scales. They play a substantial role in all kinds of physical and technological systems, for example, computers, cell phones or televisions. In the last decade, efforts have been made different approaches to control, to couple and to read out their motion. At the micrometre- and nanometre-scale, the first approach that emerged was to couple mechanical structures to electrical circuits. More recently, researchers have investigated the use of electromagnetic radiation to control and probe mechanical elements. This field, called optomechanics, has been used to explore fundamental physics problems like testing quantum mechanics on heavy mass structures or for quantum information processing. Many of these experiments require the mechanical resonator to be at the ground state of motion. This only happens at low temperature and under very specific conditions.

The aim of my thesis is to unravel other important aspects of coupling light to mechanical objects that do not require to operate at the ground state. In particular, I will discuss two experiments performed at room temperature focused on applying optomechanics to technological approaches.

The first experiment is related to the ability of optomechanical systems to detect small forces applied to a mechanical resonator. We employ a microsphere optomechanical sensor to detect the force induced by an extremely small magnetic field. The force is produced by a resonant phenomena that involves magnons and phonons on a ferromagnetic material. The magnetic field sensor is characterized by a pico-Tesla peak sensitivity with a bandwidth of 100 kHz. In addition, the tunability of the frequency response increases the device frequency operation up to a dynamic range of 1.1 GHz. This device is a proof of concept that opens a window to develop ultra-high sensitive optomechanical magnetometers, which are crucial in many areas covering geology, medical imaging systems, or defence.

The second experiment reported in this thesis describes a fundamental challenge of nanoscale physics that is the synchronization of two optomechanical cavities connected by a weak coupling. We show that exploiting the interaction between the mechanical elements and the nonlinearity of the light field, we can strategically modify the dynamic state of the oscillators. We show that the nanobeams are oscillating individually in a coherent, high amplitude and sustained state. We also experimentally demonstrate that the system evolves to a regime where the two oscillators are fully synchronized in anti-phase. The results of this experiment could be setting a base for low-noise communications between optomechanical devices.

Acknowledgements

When I started my PhD in 2016 at ICN2, the optomechanical *branch* of Clivia's group was reactivated. At the beginning, the optomechanical laboratory was started by my supervisor Daniel Navarro Urrios and Jordi Gomis. It's amazing how important boundary conditions can be in life. Looking back, it is very easy to see that I was very lucky to coincide with Dani's return to the group as my thesis supervisor. I hope to pay the debt that I have with him, facing the future with the idea of treating and teaching others as he has done with me. Later, more people joined the group, we moved to a bigger lab, we improved the set up and we faced theoretical and experimental challenges. This thesis shows a small part of all this. I have practiced team sports throughout my life and something they have taught me is that good results are the product of teamwork. Scientific research is a collective affair, not an individual effort, and here I would like to be able to thank all the people who have made this thesis possible.

I am grateful to Clivia for choosing me and giving me her trust to join their group. Throughout these years I have enjoyed your advices. You gave me all the freedom to get involved in many activities and you always gave your hundred percent so nothing was missing for us to do our job in the best conditions. I hope I have learned enough of your leadership and vision.

I want to thank my thesis supervisors, Dani and Marius. Dani, I have shared many moments with you, both personally and professionally. I keep with your way to enjoy spending time in the lab and also with your hardwork in all the aspects of the research life. I greatly appreciate your advice, shared moments of trust and friendship. I also thank you Marius, you guided me in the most unknown part of my investigation, the magnetism. Thank you for all that you have taught me, I greatly admire your dedication and enthusiasm.

I would also like to thank Sergio Valenzuela for giving me all the support from the PEND group. You gave me good advices all the times we were able to discuss. You also substantially helped me to improve the magnetometer study.

I have to thank all the other members of the P2N group for the nice atmosphere, constructive feeback and interesting discussions. I really appreciated the group meetings, group outings, specially bbq's where we spend time together. Guille, you almost caught me defending your thesis before me, although you joined several months later. I am also lucky to have shared time with you. It was great to share our frustrations with experiment, coding, theory, and fabrication. You are a terrific phycisist. Marianna, thank you for teaching me fabrication at the beggining of my thesis. I thank Jeremie, for working with us during part of your time at ICN2. David thank you for your advices and discussions about all kind of topics during lunch. Emigdio, Alex, Jordi, Juliana, Omar and Francisco, thank you for the good moments,

also apart from the scientific work. Thank you Francesc for your good disposition at all times. I am thankful to the Project managers of the group, first Cristina and then Ariadna, for the help in many different issues during my stay in the group. External to my research group, I would also like thank Alessandro Pitanti and Simone Zanotto for allowing to spend three months in Pisa. They were very nice with me and I could learn a lot from them.

Me gustaría agradecer a mis amigos de física de Granada, Alfonso, Alba, Cuchi, Marta e Irene, porque seguimos unidos a pesar de la distancia y el tiempo. Desde Granada, tengo que agradecer a mis padres, Luis y Mónica, porque como dice Residente, ellos *se pusieron nuestras botas, y sus vidas fue de nuestros logros y nuestras derrotas*. Todo lo bueno que pueda conseguir en el futuro será gracias a ellos. A mis hermanos Renzo, Flavia y Mica, porque siempre han estado presentes para celebrar mis buenos momentos y apoyarme en los no tan buenos. Ustedes también son responsables de que yo haya podido realizar mi tesis. Finalmente a Maribel, porque ella es mi Constante.

Contents

Declaration of Authorship iii

Abstract v

Acknowledgements vii

1 Introduction 1
- 1.1 Motivation . . . 3
- 1.2 Thesis outline . . . 5
- 1.3 Chapter overview . . . 5

2 Fundamentals of Cavity Optomechanics 7
- 2.1 Introduction . . . 7
- 2.2 Mechanical effects of light . . . 9
- 2.3 Equations of motion . . . 10
  - 2.3.1 Mechanical modes solution . . . 11
    - Fluctuation dissipation theorem . . . 12
    - Quantum fluctuation dissipation theorem . . . 14
  - 2.3.2 Optical mode solution . . . 14
- 2.4 Mechanical mode detection . . . 18

3 Optomechanical resonators 21
- 3.1 Whispering gallery modes in silica microsphere . . . 21
  - 3.1.1 Introduction . . . 21
  - 3.1.2 Optical properties of WGM resonators . . . 23
  - 3.1.3 Fabrication of silica microspheres . . . 26
  - 3.1.4 Coupling scheme to WGM with a tapered fiber fabrication procedure . . . 27
- 3.2 Optomechanics in a corrugated nanobeam . . . 29
  - 3.2.1 Introduction to 1D optomechanical crystals . . . 29
  - 3.2.2 The corrugated nanobeam . . . 30
  - 3.2.3 Fabrication . . . 32
  - 3.2.4 Optomechanical properties of the nanobeam . . . 32
  - 3.2.5 Self Pulsing mechanism . . . 33
  - 3.2.6 Non linear dynamics activated by self pulsing . . . 37

4 Spin waves and phonons in ferromagnets 39
- 4.1 Introduction . . . 39

4.2 Spin waves in ferromagnetic materials . . . 40
4.3 Growth method of YIG films . . . 42
4.4 Magnetization dynamics . . . 42
4.4.1 Ferromagnetic resonance . . . 44
4.5 Ferromagnetic resonance characterization of YIG films . . . 45
4.5.1 Experimental set up . . . 46
4.5.2 FMR results . . . 47
4.6 Magnon interaction with phonons . . . 47
4.6.1 Spin waves equations in YIG. . . . 48
4.6.2 Elastic wave equations . . . 51
4.6.3 Magnetoelastic coupling . . . 52

5 Resonant magnon optomechanical magnetometer 57
5.1 Introduction . . . 57
5.2 Fabry Perot cavity . . . 59
5.3 Stress induced magnetostriction . . . 61
5.4 Magnetometer mechanical response . . . 61
5.5 Magnetometer sensitivity . . . 63
5.6 Optomehcanical characterization of BTS microspheres . . . 67
5.6.1 Optomechanical setup . . . 67
5.6.2 Optical characterization . . . 68
5.6.3 Mechanical characterization . . . 70
5.7 Magnetometer characterization . . . 71
5.7.1 Incoherent spectral response . . . 71
5.7.2 Coherent response . . . 73
5.7.3 Magnetometer sensitivity . . . 74
5.8 Vibrometer measurement . . . 78
5.9 Comparison with the State of the Art . . . 79
5.10 Perspective . . . 81
5.11 Conclusions . . . 82

6 Synchronization of two optomechanical crystals by mechanical interaction 85
6.1 Introduction . . . 85
6.2 Synchronization definition . . . 87
6.3 Previous experiments on synchronization . . . 88
6.4 Device description . . . 91
6.5 Synchronization experiments . . . 94
6.5.1 Optical differentiation of cavities . . . 94
6.5.2 Synchronization in the frequency domain . . . 95
6.5.3 Synchronization in the time domain . . . 98
6.6 Synchronization switching experiment . . . 100
6.7 Numerical model for synchronization . . . 102
6.8 Conclusion . . . 108

7 Conclusions and perspectives 111

A Finite element method simulations and OM coupling calculations 119

B Magnetic field calibration **123**

C Laser Doppler Vibrometer Characterization of YIG **127**

List of Figures

2.1 Fabry-Perot Cavity 8
2.2 Mechanical Susceptibility 12
2.3 Power spectral density 13
2.4 Single and Double-Sided coupling 15
2.5 Reflection spectrum 17
2.6 Phase Response of the reflected signal 18
2.7 Derivative of the reflection spectrum with detuningl 19

3.1 WGM microsphere resonator 22
3.2 Intensity distribution of a WGM 25
3.3 Tapered fiber fabrication set up 27
3.4 Transmission spectra of the tapered fiber fabrication process . 28
3.5 SEM image of the corrugated nanobeam 30
3.6 Photonic and phonic band diagram of the corrugated nanobeam 31
3.7 Optical spectrum of the corrugated nanobeam 33
3.8 Transmission spectra of the tapered fiber fabrication process . 34
3.9 Phase trajectories of $N, \Delta T$ for different wavelengths 36
3.10 2D color plot of RF spectra as a function of wavelength 38

4.1 Schematic representation of ferromagnet 41
4.2 Fabrication methods of single crystal YIG 43
4.3 Schematic view of vectors on the YIG sample 44
4.4 Experimental set up for the FMR characterization 46
4.5 Ferromagnetic resonance measurements 48
4.6 Magnon and phonon bands in a ferromagnet 51
4.7 Magnetoelastic bands 54

5.1 State of the art in optomechanical magnetometers 58
5.2 Fabry-Perot model 60
5.3 Mechanical modes of the microsphere 62
5.4 Magnetometer mechanical response 64
5.5 Magnetic field sensitivity as a function of frequency 67
5.6 Experimental set-up 68
5.7 Optical modes of the microsphere 69
5.8 Top view of contact position of the fiber 70
5.9 Radiofrequency spectrum of thermal modes in the microsphere 71
5.10 Magnetometer experimental set up 72
5.11 Magnetometer power dependence and magnetic field calibration 73

5.12 Magnetometer coherent response 74
5.13 Frequency dependent sensitivity 75
5.14 Magnetometer sensitivity 76
5.15 Peak sensitivity for a frequency range of 50 MHz to 1.2 GHz . 77
5.16 Laser Doppler Vibrometer measurements 78
5.17 State of the art magnetometers sensitivities 80
5.18 YIG disk magnetometer design 82

6.1 Example of synchronized systems 87
6.2 Previous works on synchronization 89
6.3 Huygens pendulum at the nanoscale 90
6.4 Mechanically coupled corrugated nanobeams 91
6.5 Simulated optical and mechanical modes of the OMCs 92
6.6 Optical differentiation experiment 94
6.7 Synchronization of optomechanical oscillators in the frequency domain 97
6.8 Synchronization in the temporal domain 98
6.9 Poincare map of the dynamical system 99
6.10 Switching synchronization experiment 101
6.11 Numerical simulations of the coupled OMCs 104
6.12 Numerical simulations of the coupled OM as a function of the coupling strength 105
6.13 Temporal dynamics of the transmitted optical signal 106
6.14 Temporal traces of the mechanical deformation 107
6.15 Simulated radio-frequency (RF) spectrum of the optical transmission 108
6.16 Network of synchronized OMCs 109

7.1 Design of a magneto-optomechanical cavity 113
7.2 Opto-electromechanical system 116

A.1 Top-view SEM micrograph of the coupled Optomechanical Crystal Cavities 120
A.2 Optomechanical coupling contributions 121

B.1 Transmission line schematic 123
B.2 Magnetic field calibration 124

C.1 Vibrometer measurement 128

List of Abbreviations

OM	**O**pto **M**echanics
OMCs	**O**pto **M**echanical **C**rystals
WGM	**W**hispering **G**allery **M**ode
YIG	**Y**ttrium **I**ron **G**arnet
GGG	**G**adolinium **G**allium **G**arnet
FMR	**F**erro **M**agnetic **R**esonance
GMR	**G**iant **M**agneto **R**esistance
NMR	**N**uclear **M**agnetic **R**esonance
LLG	**L**andau **L**ifshitz **G**ilbert
LPE	**L**iquid **P**hase **D**eposition
CVD	**C**hemical **V**apor **D**eposition
MBE	**M**olecular **B**eam **E**pitaxy
VNA	**V**ector **N**etwork **A**nalyser
SQUID	**S**uper **C**onducting **Q**uantum **I**nterference **D**evice
SERF	**S**pin **E**xchange **R**elaxation **F**ree
BTS	**B**arium **T**itanium **S**ilicate
SNR	**S**ignal **N**oise **R**atio
LVD	**L**aser **V**apor **D**eposition
NEMS	**N**ano **E**lectro **Me**canical **S**ystem
EOM	**E**lectro **O**ptical **M**odulator
SP	**S**elf **P**ulsing
RF	**R**adio **F**requency
FPC	**F**iber **P**olarization **C**ontroller
VOA	**V**ariable **O**ptical **A**ttenuator
LDV	**L**aser **D**oppler **V**ibrometer
SEM	**S**canning **E**lectron **M**icroscopy
EBL	**E**lectron **B**eam **L**ithography
TO	**T**ermo **O**ptic
PMMA	**P**oly**M**ethyl **M**eth**A**crylate
NIR	**N**ear **I**nfra**R**ed
FCD	**F**ree **C**arrier **D**ispersion
FCA	**F**ree **C**arrier **A**bsorption

Chapter 1

Introduction

The use of measures has been one of the fundamental pillars of societies to advance throughout history. Measurements are used daily to study nature. Today, people interact with measurement instruments directly, such as thermometers, clocks or scales, and indirectly, such as accelerometers or heart rate monitors in a smartphone. Scientific research demands more and more precise measurement devices in order to understand, for example, the most fundamental elements that make up matter, basic functions of living microorganisms or astronomical events in the universe. Measurements are at the basis of scientific and technological progress.

Among the multiple existing measurement methods, those based on optical forces play an important role in current measurement advances. Optical forces were noticed since the 17^{th} century, when Johannes Kepler observed that the tail of comets always pointed away from the sun [1]. Since then, the use of optical forces applied to measurement instruments has been significantly studied and broadly extended, for example, in optical trapping experiments, where a highly focused laser beam is employed to isolate, manipulate and measure microscopic particles, atoms or ions [2]. They are also used for high precision measurements in interferometer sensors, such as gravitational waves detectors [3–5].

Most sensors used today require the ability to measure mechanical motion with high sensitivity since many physical parameters can be inferred from a position shift of a certain component. Optical techniques offer high accuracy to measure displacement due to the interaction of light with mechanical elements. A natural way to increase this displacement sensitivity consists on trapping light in an optical cavity, increasing the interaction time between the light field with the mechanical object. As the cavity volume becomes smaller, the optical and mechanical interaction becomes stronger. Thus, to obtain high precision sensors it becomes crucial to combine optical microcavities and mechanical resonators. This thesis reports on two experiments, which in principle follow different objectives, but both have in common the idea of employing optomechanical cavities as the sensing element that allows

transducing the magnitude to be measured into a dynamical modulation of the light stored within it.

In the recent decades, mechanical resonators have undergone a huge development. The emergence of Nano-Electro-Mechanical Systems (NEMS), gave rise to the appearance of multiple sensors to detect physical quantities such as displacement [6], mass [7] or magnetic fields [8]. At the same time, optical microcavities accomplished a rapid progress. Their small sizes allowed the confinement of light at high powers. They also offered high quality factors, resulting in devices with low loss. The use of optical microcavities rapidly extended from studying fundamental physical problems [9, 10] to applied research, ranging from laser sources [11–13], filters [14], switches [15], delay lines[16] to biosensors [17–19]. This thesis is focused on optomechanical systems, which combines the properties of optical micro- and nanocavities with mechanical resonators embedded in it [20].

The coupling in optomechanical systems is enhanced by storing light during long times in a confined space. Multiple optomechanical systems can be found in the literature, covering a large range of sizes, extending from levitated nanoparticles in optical traps [21] to suspended mirrors with kilogram-scale mass [22]. There exist multiple different geometries for the optical and the mechanical cavities including microspheres [23], microdisks [24, 25], microtoroids [26], capacitive drum resonators coupled to resonant microwave cavities [27] and photonic crystals cavities [28–31].The canonical example of a sensor based in optomechanics is the modified version of a Fabry Perot cavity with one of its two mirrors attached to a spring. The operational principle of this device relies on measuring the variation in distance between the two mirrors using light. The electromagnetic field amplitude in the cavity increases as it bounces between the mirrors. The optical force exerted on the moving mirror makes it to displace, changing the total length of the cavity. This effect modifies the resonant frequency of the cavity and the light phase that decouples from it and finally collected by the detector. Similar effects are observed in whispering gallery mode cavities [9, 23], where light propagating within a circular dielectric cavity applies optical force on its boundary, exciting radial modes.

Recently, with an improved understanding of the optomechanical interactions and the fast progress in nanofabrication technologies of optical microcavities and mechanical resonators with high quality factors, the micro- and nanophotonic community has explored the possibility of integrating optomechanical devices within photonic circuits [20, 32, 33]. Contrary to standards photonic circuits, the response of which can be difficult to be reconfigured, the use of optical forces in optomechanical circuits reveals a new approach to develop integrated systems with a high tuning response. In addition, optomechanical devices also offer the possibility to explore and measure mechanical systems in the quantum regime [34, 35].

In optomechanical systems, the coupled light can offer unprecedented sensitivity to detect mechanical motion [36, 37]. Early studies of optomechanical

microspheres showed displacement sensitivity similar to traditional optical sensors [38]. Nowadays, one of the most remarkable experiments developed in the last decades are the gravitational wave detectors [3–5]. The best sensitivity was obtained by the LIGO detector, which is able to detect displacement of $10^{-19}\frac{m}{\sqrt{Hz}}$ [39]. At the nanoscale, optomechanical crystals are not yet capable of the same level of performance, but they can reach a displacement sensitivity of $10^{-16}\frac{m}{\sqrt{Hz}}$ [40]. With this sensitivity, optomechanical cavities were considered for integrated sensing applications. For example mass sensors and accelerometer, with reported sensitivities of $10^{-15}\frac{kg}{\sqrt{Hz}}$ [41] and 10 $\frac{\mu g}{\sqrt{Hz}}$ [42] , respectively.

In addition to sensitivity, another figure of merit required for a high performance sensor is related to noise. In any functional measurement, signals are mixed with noise arising from contributions of various sources. One of the main advantage of optomechanical sensors is that light can transport information with low noise. However, the operation of optomechanical systems at high power increases the noise level and can degrade the sensing performance. Moreover, intrinsic sources associated with mechanical resonators coupled to the thermal environment are unavoidable and need to be considered. Then, reducing the noise level becomes important for several sensing applications like time keeping and frequency stabilization. The motivation of this thesis, which is detailed in the next section, is to explore the use of optomechanics in sensing applications and the problem of reducing the phase noise level by weakly coupling two optomechanical systems.

1.1 Motivation

Among the physical quantities mentioned in the Introduction that can be measured with high sensitivity using optomechanical cavities, this thesis explores the possibility to detect small magnetic fields. Magnetic field detection is critical in multiple areas such as geology, medical imaging systems and space exploration [43]. Currently, the Superconducting Quantum Interference Device (SQUID) magnetometers are one of the leaders in ultra-sensitive magnetometry, achieving sensitivities of 10 $^{-15}$ T Hz$^{-1/2}$ [44, 45]. This sensitivity is even surpassed by the Spin Exchange Relaxation Rate magnetometer (SERF), reaching sub-femto Tesla sensitivities [46, 47]. Nevertheless, most of the mentioned systems present restrictions like working at cryogenic temperatures, like in the case of SQUID's magnetometers, or they are limited to work at small dynamical range, that is, they are restricted to work over a low magnetic fields. Also, the frequency sensitivity is constrained to operate at low frequencies ($\sim$ 100 Hz).

In the last decade, optomechanical magnetometers have emerged as a new tool for measuring magnetic fields with high sensitivity at room temperature

[48–50]. The operation of optomechanical magnetometers relies on the deformations that mechanical objects suffer under the influence of an applied magnetic field. The response of the material to magnetic fields alters the mechanical structure of the cavity and this provokes a shift of the optical resonance. This modulation can be read out giving a measurement of the applied field. Our approach consist of using glass microspheres with high quality factor optical and mechanical modes deposited on a Yttrium Iron Garnet (YIG) thin film. The transduction principle involves the conversion of an RF magnetic field that resonantly excites magnons, into mechanical vibrations in the YIG film via magnetostriction. The mechanical vibrations excite the mechanical modes of the sphere and the response is detected on the optical signal. The sensitivities obtained is comparable with state-of-the-art optomechanical magnetometers. The system described in this thesis presents a tunable frequency operation extending the magnetometer use to the GHz range, which exceeds by one order of magnitude other optomechanical magnetometers.

Optomechanics has opened a landscape for integrated optomechanical circuit, combining several functions in a single chip. Nevertheless, most of these functionalities are studied at a single level, ignoring the possibility of connecting two or more optomechanical cavities. From this situation, it emerges the question concerning the connection of several optomechanical crystals. This idea leads to the second motivation of this thesis, which consists of exploring the dynamics of coupled optomechanical cavities, in particular, the synchronization of two optomechanical crystals. The motivation for synchronizing optomechanical crystals relies on the possibility of reducing the phase noise of optomechanical systems when driven to a mechanical lasing regime. This is important in several sensing applications that require low noise. It is known that the noise could be reduced by N^{-1} when synchronizing N mechanical oscillators [51]. Thus, synchronization could be seen as an effective strategy to develop optomechanical sensors with low noise.

Experimentally, the phenomena has previously been explored by several routes, including disk resonator placed in proximity and coupled through a common optical mode [52, 53],cascaded microdisks connected by an optical waveguide [54], to optomechanical cavities placed in distant chips [55, 56]. However, these experiments are controversial since it is not clear if all the requirements imposed by the definiton of synchronisation are satisfied. In this thesis, we adopt a very rigorous set of criteria for synchronization to discuss some previous experiments and to demonstrate that our system really fulfils the requirements imposed by the adopted definition. In addition to the sensing aspects, the results reported within this thesis are important to develop precise metrology systems with low noise like frequency stabilization and time keeping applications.These results open the route towards scaling up the number to N coupled oscillators that could show different complex dynamic, paving the way to future optomechanical networks.

1.2 Thesis outline

In this thesis, I describe two different experiments concerning the coupling of light to mechanical objects. In the first experiment I present a new type of optomechanical sensor to measure magnetic fields. The sensitivity of the device is characterized by a state-of-the-art peak value for room temperature optomechanical magnetometers. The system consist of a hybrid device that involves magnons in a ferromagnetic substrate with phonons and photons in a high-Q optomechanical resonator. The chapters that are related to this experiment are Chapter 4 and Chapter 5.

The second experiment presented on this thesis that demonstrates the spontaneous synchronization of two optomechanical cavities mechanically linked. The system fulfils all the requirements of a synchronized system. We record the optical transmission temporal traces of each of the two cavities concluding that, in the synchronized state, they mechanically oscillate in anti-phase, which is in agreement with the predictions of our numerical model. The results of the experiments are found in Chapter 6.

1.3 Chapter overview

The results of the experiments shown in this thesis are part of the collaborative work carried out in a laboratory where many colleagues have participated. The contents of each individual chapter are given below.

- **Chapter 2** is an introduction to Cavity Optomechanics. The Fabry Perot model is discussed and the governing equations of motion for the mechanics and the optics are given. The fluctuation dissipation theorem is briefly discussed to illustrate the link between the spectral density with the displacement quantity. Finally, the mechanism used to transduce mechanical motion with light is given.
- **Chapter 3** is a general introduction to optomechanical resonators. Two types of optomechanical systems are used throughout this thesis: the whispering gallery modes microspheres and the one dimensional optomechanical crystals. The mechanical and optical properties of these systems are given here. In this chapter is also explained the experimental technique used to couple to optomechanical cavities, the fiber tapered method.
- **Chapter 4** investigates the main properties of magnetically ordered material and spin waves. The ferromagnetic resonance method is described and used to characterize Yttrium-Iron-Garnet thin films. Finally, a description about the coupling of magnons with mechanical degrees of freedom is given.
- **Chapter 5** describes the experiment of the optomechanical magnetometer. Mechanical and optical characterization of the device is given. The

transduction principle on which it is based is discussed and a sensitivity measurement is given.

- **Chapter 6** demonstrates the spontaneous synchronization of two optomechanical crystals by mechanical interaction. In order to illustrate the challenge a definition of synchronization is given and also the previous approach to the synchronization problem at the nanoscale is mentioned. Then a description of the devices used is given, followed by the optomechanical characterization of the system. Then, the description of the synchronization experiment is described. A switching experiment of the synchronized state by external actuation is discussed. Finally, a numerical model that supports the obtained results is given.
- **Chapter 7** discuss the main results of this thesis. A perspective view on future experiments is also given.
- In **Appendix A** is described the integrals used to calculate the optomechanical coupling value. The discussions of this appendix are used mainly in the context of Chapter 3 and Chapter 6.
- In **Appendix B** the magnetic field calibration is given. The transmission line equation of the system are derived and the circulating current is obtained. The results of this appendix are used in Chapter 5.
- In **Appendix C** the Laser Doppler Vibrometer interferometry technique is described. This set up is used to measure the vibrations generated in the ferromagnetic film induced by the ferromagnetic resonance. The results of these measurements are used in the context of Chapter 5.

Chapter 2

Fundamentals of Cavity Optomechanics

In this chapter, I will introduce some basic concepts founds Cavity Optomechanics (OM). Since this field and their significance in physics is vast, I will focus on the aspects that are related with the purpose of this thesis. The typical model of OM systems will be given and the governing equations will be derivated. I will describe the solution for the particular case when the mechanical frequency is much smaller than the optical decay rate. Finally, I will show how the mechanical motion can be detected from the optical signal.

2.1 Introduction

The paradigmatic figure of an optomechanical cavity is a Fabry Pérot cavity with a movabale mirror. It is shown in Fig. 2.1. The cavity has two mirrors, one with perfect reflectivity and mounted on a spring. The second mirror has a partial reflectivity and is fixed in position, allowing the interaction and coupling of a light field with the cavity. A laser illuminating the cavity that is in resonance with one of the mode of the undeformed caivity. Light inside of the cavity will satisfy the relation of a standing wave: $n\lambda_n = 2L_{eff}$, being L_{eff} the effective length of the cavity (the distance between the mirrors) and n an integer number. This means that the wavelengths of the optical modes in the Fabry Pérot are multiples of two times the cavity length. Therefore, the frequencies of the modes are: $\omega_n/2\pi = \dfrac{cn}{2L_{eff}}$, being c the speed of light in the medium. The fact of being mounted on a spring causes that the second mirror is displaced $x(t)$ by the effect of radiation pressure force. This makes the total length to vary in time and consequently leads to a dependency of the optical resonances with the mechanical motion that can be written as $\omega_n = \dfrac{cn\pi}{L_{eff} + x(t)}$. This modulation changes optical path of the cavity and modulates the light outcoupled from it. This is the key point of Cavity

Optomechanics: a mechanical displacement will induce a change in the optical properties of the system [20, 57]. This effect reveals a direct application of optomechanics that is detecting displacement with high sensitivity. From this example we can observe that in order to maximize the frequency shift, it is on our interest to use the smallest possible cavity length. This is the motivation behind using micro and nanoscale cavities, where light is confined in a very small volume for a long time, providing extremely high displacement sensitivity.

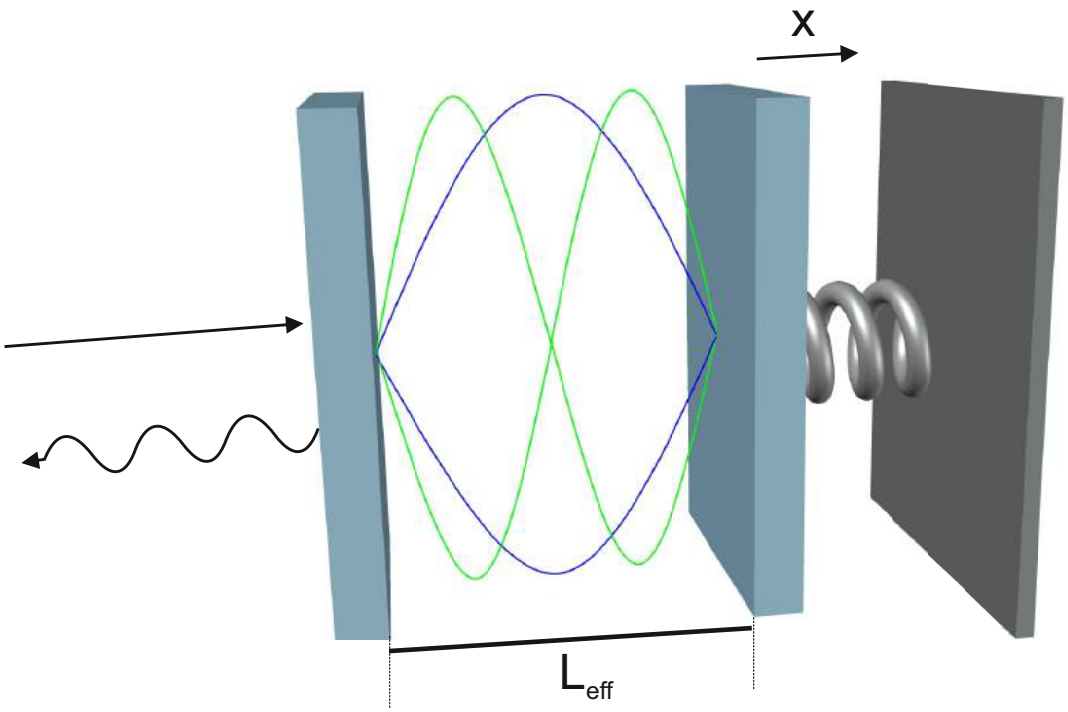

Figure 2.1: Incident laser light is trapped in a optical cavity formed by two mirrors. The left one is fixed and is partially reflective, allowing light to couple in and out of the optical cavity. The right mirror is perfectly reflective and is mounted on a spring. The motion of the right mirror by a length x modifies the effective length of the cavity L_{eff}, which modulates the amount of energy stored in the cavity, causing the modulation of the out coupled light.

The effect of light being modulated by the mechanical motion also occurs in the opposite direction. If the mirror is small enough, or the number of photons inside the cavity is high enough, the mirror spring constant can be modified by radiation pressure. This additional effect causes on the optomechanical system to change also the mirror's position, and modifying again the optical force applied to the mirror, moving again the mirror and so on... Then, the optomechanical interaction can dynamically make the spring constant softer or stiffen, and amplify or damp the mirror's motion.

At first glance, the optomechanical cavities used in this thesis do not present similarities with the Fabry Pérot model of Fig. 2.1. Nevertheless, in both cases all the relevant physics is contained in the simple model of mirrors and spring. On the following section, we will explain the origin of this coupling between light and mechanical motion.

2.2 Mechanical effects of light

It turns out from the equation of the Fabry Pérot cavity, that the optical frequency of the cavity depends on the motion $x(t)$. Considering only that the displacement $x(t)$ is small relative to the effective lenght, $|x| \ll L_{eff}$, we can make a Taylor expansion for the optical frequency ω_c at x =0 and get:

$$\omega_c = \omega_{c,0} + \frac{d\omega_{c,0}}{dx}x(t) + ... \simeq \omega_{c,0} + g_{OM}x(t) \tag{2.1}$$

where $\omega_{c,0}$ is the optical cavity resonance for n =0 at x =0.

We have truncated Eq 2.1 at the first term since all the experiments described in this thesis are in the linear regime. The nonlinear effect treated in Chapter 6 is also explained by a linear optomechanical coupling $\frac{\omega_c}{L_{eff}}$ and its nonlinear aspect comes from the optical material properties. The term that couples the mechanical motion with the optical resonance of the cavity is defined by $g_{OM} = \frac{d\omega_{c,0}}{dx} = \frac{\omega_c}{-L_{eff}}$. This constant represents how much the optical mode is shifted by unit of displacement and is frequently known as optomechanical coupling strength.

In the Fabry Perot example introduced in section 2.1, radiation pressure force arises from the momentum imparted by photons to the movable mirror. It is connected with the optomechanical coupling g_{OM} by:

$$F(t) = -\hbar n_c \frac{\omega_c}{L_{eff}} \tag{2.2}$$

where n_c is the number of photons stored in the optical cavity. The force is obtained from an interaction Hamiltonian by given $F = -\frac{dH_{int}}{dx}$, being $H_{int} = -\hbar n_c g_{OM} x$. From these relations, we observe that the mutual interaction has reciprocal effects. On the one hand, the optical mode is frequency shifted by an amount $g_{OM}x(t)$. On the other hand, a single photon in the cavity pushes the mechanical element with a force $\hbar g_{OM}$, and thus the spring constant of the mechanical motion is changed by $k = \frac{\hbar g_{OM}}{x(t)}$.

2.3 Equations of motion

To derive the equations of motion of the optomechanical system we consider first the classical limit where the mechanical motion $x(t)$ is a classical variable and the optical field is the complex amplitude of the electric field $a(t)$. At the quantum limit the mechanical motion will be obtained by substituting the classical variables by the operator $\hat{x} = x_{zpf}\left(\hat{b} + \hat{b}^{\dagger}\right)$, being x_{zpf} the zero point fluctuation $x_{zpf} = \sqrt{\langle 0|\hat{x}^2|0\rangle}$. The standard equation of motion for the mechanical position, x, and the optical field, a, are given by:

$$m\ddot{x}(t) + m\omega_m^2 x(t) + m\Gamma\dot{x}(t) = F_{th} + \hbar g_{OM} n_c(t) \tag{2.3}$$

$$\dot{a}(t) = i\left(\omega_c - x(t)g_{OM}\right)a(t) - \frac{\kappa}{2}a(t) + \sqrt{\kappa_{in}}a_{in}(t) \tag{2.4}$$

The Eq. 2.3 correspond to a forced harmonic oscillator. We have used Γ as the mechanical damping rate of the mechanical motion, m is the moving mass of the mode, and ω_m is the mechanical resonance frequency. We have also considered the thermal noise that accounts for the interaction of the mechanical degrees of freedom with the environment. This interaction is approximated as a heat bath, and its action on the system as a random force F_{th}. The last term of the Eq. 2.3, is the radiation pressure force of the photons on the mechanical oscillator defined on section 2.2.

For the optical mode we have used the optical total decay rate of the cavity κ. We have also separated the decay rate to the environment into detected (extrinsic), and undetected (intrinsic) channels, κ_e and κ_i, and the input laser drive a_{in}. Finally, we also note that the intracavity photon number, n_c is given by the normalized intensity of the optical field $|a(t)|^2$. Therefore, the dynamic of the system is governed by two coupled differential equation which are not linear in their interaction.

A useful procedure to solve the Eq. 2.4 is to consider that the driving term is usually done by a single laser at a frequency ω_l, so we can rewrite the driving amplitude $a_{in}(t) = a_{max}e^{-i\omega_l t}$, where the input rate of photons is $a_{max} = \sqrt{\frac{P_{in}}{\hbar\omega_l}}$, with P_{in} the input laser power. Thus, we can make in Eq. 2.4 a rotating frame substitution for the optical field $a(t) = \hat{a}(t)e^{-i\omega_l t}$ and rewrite the equation of motion:

$$\dot{\hat{a}}(t) = i\left(\Delta - x(t)g_{OM}\right)\hat{a}(t) - \frac{\kappa}{2}\hat{a}(t) + \sqrt{\kappa_{in}}\hat{a}_{in}(t) \tag{2.5}$$

where we have defined the detuning of the laser from the cavity as $\Delta = \omega_l - \omega_c$. The state of the system can be classified by the sign of Δ: for $\Delta < 0$ the state is named "red detuned", for $\Delta > 0$ is called "blue detuned" and $\Delta = 0$

correspond to a state in resonance with the laser field. For simplicity, we can rename $\hat{a} = a$, and use it from now on understanding that we are solving the equations in the rotating frame. Therefore, the equations of motion to solve are:

$$\dot{a}(t) = i\left(\Delta - x(t)g_{OM}\right)a(t) - \frac{\kappa}{2}a(t) + \sqrt{\kappa_{in}}a_{in}(t) \tag{2.6}$$

$$\ddot{x}(t) = -\omega_m^2 x(t) - \Gamma\dot{x}(t) + \frac{F_{th}}{m} + \frac{\hbar g_{OM}}{m}n_c(t) \tag{2.7}$$

A more complete description needs a coupled mode theory treatment and can be found on the following References [58, 59].

2.3.1 Mechanical modes solution

The coupled set of equations Eq. 2.6 and Eq. 2.7 are nonlinear and in most of the cases they do not present an analytical solution. However, it is a standard procedure to consider that the optomechanical interaction and the mechanical amplitudes are small enough to approximate numerically solutions. For convenience, we disregard the optomechanical coupling ($g_{OM} = 0$), and study the behavior of the mechanical mode driven by thermal forces. It is useful to rewrite the solutions of Eq. 2.7 in the Fourier space:

$$-\omega^2 m x(\omega) = -\omega_m^2 m x(\omega) - i\Gamma\omega m x(\omega) + F_{th}(\omega) \tag{2.8}$$

where we have used the Fourier transform of the mechanical motion, $x(\omega) = \mathscr{F}[x(t)]$, the property $\mathscr{F}[\dot{x}(t)] = i\omega x(\omega)$ and $\mathscr{F}[F_{th}(t)] = F_{th}(\omega)$. After reagruping, the solution for the displacement spectrum of x is:

$$x(\omega) = \frac{1}{m(\omega_m^2 - \omega^2) - i\Gamma m\omega}F_{th}(\omega) = \chi(\omega)F_{th} \tag{2.9}$$

where we have defined the oscillator's susceptibility as $\chi(\omega) = [m(\omega_m^2 - \omega^2) - i\Gamma m\omega)^{-1}]$. For a general non linear interacting force it will be hardly possible to calculate the susceptibility. We define the mechanical quality factor, $Q_m = \frac{\omega_m}{\Gamma}$, that is related with the time that takes to the resonator to release the energy stored in a particular mechanical mode into the thermal bath. For mechanical resonators with high Q_m we can approximate the susceptibility in Eq. 2.9 like a sharp Lorentzian. In Fig. 2.2 we show examples of the absolute value of susceptibility, $|\chi(\omega)|$. These plots serve to examine how is the response of the mechanical resonator to varying typical parameters. We note that the response of the system decreases like $1/\omega^2$ for $\omega \gg \omega_m$ and the DC value ($\omega = 0$) decreases like $1/\omega_m^2$. The response on resonance at $\omega = \omega_m$ gives the mechanical quality factor Q_m.

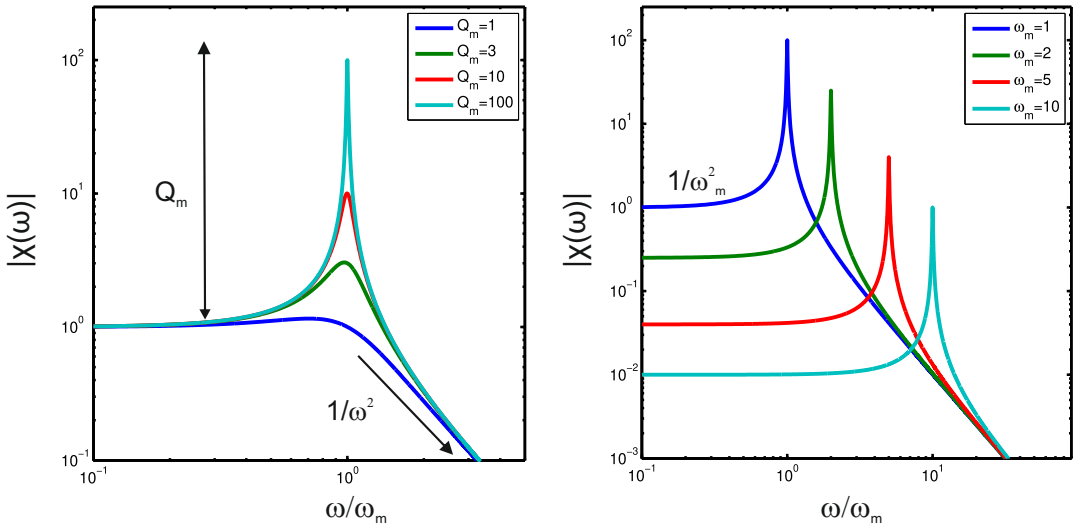

Figure 2.2: (a) A plot with several norm susceptibility $|\chi(\omega)|$, with multiples Q_m values. We observe that the system decreases like $1/\omega^2$ for $\omega \gg \omega_m$ (b) A plot of $|\chi(\omega)|$, with varying ω_m. We note that the response of the resonator decreases like $1/\omega_m^2$ for $\omega = 0$.

Fluctuation dissipation theorem

The detection of displacement x on the experiments described on this thesis is not direct but instead is made by measuring the spectral density. This quantity is related with the spectrum associated to a fluctuating quantity. We assume that $x(t)$ is a time homogeneous process so there is no special time t on the process, which allows to correlate the displacement of two different time t and t' like $x(t')x(t) = x(t-t')x(0)$. According to the Wiener-Khinchin theorem, the spectral density is equal to the Fourier transform of the autocorrelation function (see ref. [60]),

$$S_{xx}(\omega) = \int \langle x(t)x(0)\rangle e^{i\omega t} = \langle xx\rangle_\omega \tag{2.10}$$

The latter expression is very convenient because the autocorrelation function is associated with theoretical considerations while the spectral density is what we measure in the experiments. For a classical variable x, the spectral density is a symmetric function: $S_{xx}(\omega) = S_{xx}(-\omega)$. The units of the spectral density for the discplacement, $S_{xx}(\omega)$, are $\mathrm{m}^2\ \mathrm{Hz}^{-1}$. It is also common to find in literature the square root of the spectral density, $\sqrt{S_{xx}(\omega)}$, which has units of $\mathrm{m}\ \mathrm{Hz}^{-1/2}$. It can also be demostrated the property that the integral of spectral density give the variance of the displacement,

$$\int S_{xx}(\omega)\frac{d\omega}{2\pi} = \langle x^2\rangle \tag{2.11}$$

The classical version of Fluctuation Dissipation Theorem links the displacement spectral density with the dissipative term of susceptibility. The dissipation term of susceptibility is given by its imaginary part, $Im[\chi(\omega)] = \frac{\Gamma\omega}{\left(\omega_m^2-\omega^2\right)^2+(\omega\Gamma)^2}$, and the relation with spectral density is,

$$\langle xx \rangle_\omega = \frac{2k_BT}{\omega} Im[\chi(\omega)] \tag{2.12}$$

where k_B is the Boltzmann constant and T is the temperature of the bath. Thus, considering the case $\Gamma << \omega_m$ and $\omega_m \simeq \omega$, we can approximate the dissipative term of susceptibility like:

$$Im[\chi(\omega)] \simeq \frac{\omega}{4\omega_m^2} \frac{\Gamma}{(\omega-\omega_m)^2+(\frac{\Gamma}{2})^2} \tag{2.13}$$

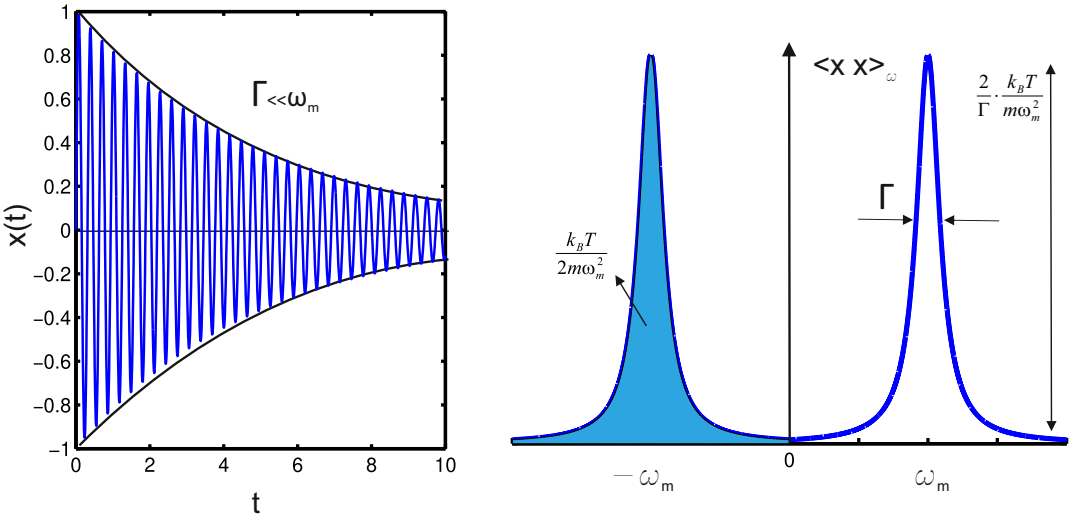

Figure 2.3: (a) Plot of the displacement as a function of time for a case with a mechanical damping rate, Γ is much smaller than the mechanical frequency. The mechanical motion oscillates many times before losing the energy. This case allows to approximate the dissipation term as a Lorentzian $Im[\chi(\omega)]]$ (b) Spectral density of the mechanical motion as a function of frequency.It correspond to a lorentzian function centered at ω_m with a FWHM= Γ and a peak height of $\frac{2}{\Gamma}\frac{k_BT}{m\omega_m^2}$. The area of $\langle xx \rangle_\omega$ is equal to the variance $\langle x^2 \rangle$ due to thermal motion.

which gives the following expression for the spectral density:

$$\langle xx \rangle_\omega = \frac{k_BT}{2m\omega_m^2} \frac{\Gamma}{(\omega-\omega_m)^2+(\frac{\Gamma}{2})^2} \tag{2.14}$$

The last equation obtained for the spectral density, corresponds to a lorentzian function with a linewith of Γ, and a peak height of $\frac{2}{\Gamma}\frac{k_BT}{m\omega_m^2}$. It is straightforward

to demonstrate that integrating for all frequencies this expression, we obtain the displacement variance due to thermal motion:

$$\int \langle xx \rangle_\omega \frac{d\omega}{2\pi} = \frac{k_B T}{m\omega_m^2} = \langle x^2 \rangle \tag{2.15}$$

Quantum fluctuation dissipation theorem

Although this thesis will not deal with experiments described by quantum formalism, the quantum version of fluctuation dissipation theorem is given in a similar way as the classical case considering that the phonons in thermal equilibrium are described by the Maxwell-Boltzmann distrubution. Therefore the spectral density is given by:

$$\langle xx \rangle_\omega = \frac{2\hbar}{1 - e^{\frac{\hbar\omega}{k_B T}}} Im[\chi(\omega)] \tag{2.16}$$

It is immediate to check that the classical theorem is obtained by making $k_B T \gg \hbar\omega$.

2.3.2 Optical mode solution

The mode amplitude $a(t)$ follows a time evolution according Eq. 2.5. In a similar spirit like in the mechanical equation of motion, we can neglect first the optomechanical coupling interaction ($g_{OM} = 0$) and consider the steady state solution of Eq. 2.6 for a constant drive and setting $\dot{a}(t) = 0$, we get the following expression for the intracavity amplitude field:

$$a = \frac{\sqrt{\kappa_{in}} a_{in}}{\frac{\kappa}{2} - i\Delta} \tag{2.17}$$

We find two different schemes in Optomechanics to couple light into the cavity that has an impact on how we can interrogate the system to extract its response. The two different types of schemes are shown in Fig. 2.4. They are named single and double-sided coupling cavities. They are classified considering the number of channels that light has to couple out from the optical cavity.

For both schemes, it is valid that $\kappa = \kappa_e + \kappa_i$. The difference resides in the rate at which light couples into/out of the optical resonator. In Fig. 2.4a, we show the single-sided case, where light leaving the cavity has only one channel to couple. Practically, this means that for an experiment with such a configuration scheme, it would be possible, in principle, to collect 100% of

the light decoupled from the cavity, which is something desirable for a maximum signal collection. In this case we have $\kappa_{in} = \kappa_e$. In the double-sided coupling cavity (see Fig. 2.4b), light has two ways to leave the optical cavity, either forward or backward. Thus, for this case $\kappa_{in} = \kappa_e/2$ and this means that an experiment with this scheme it only possible to detect 50% of light outcoupled from the optical cavity in the best case.

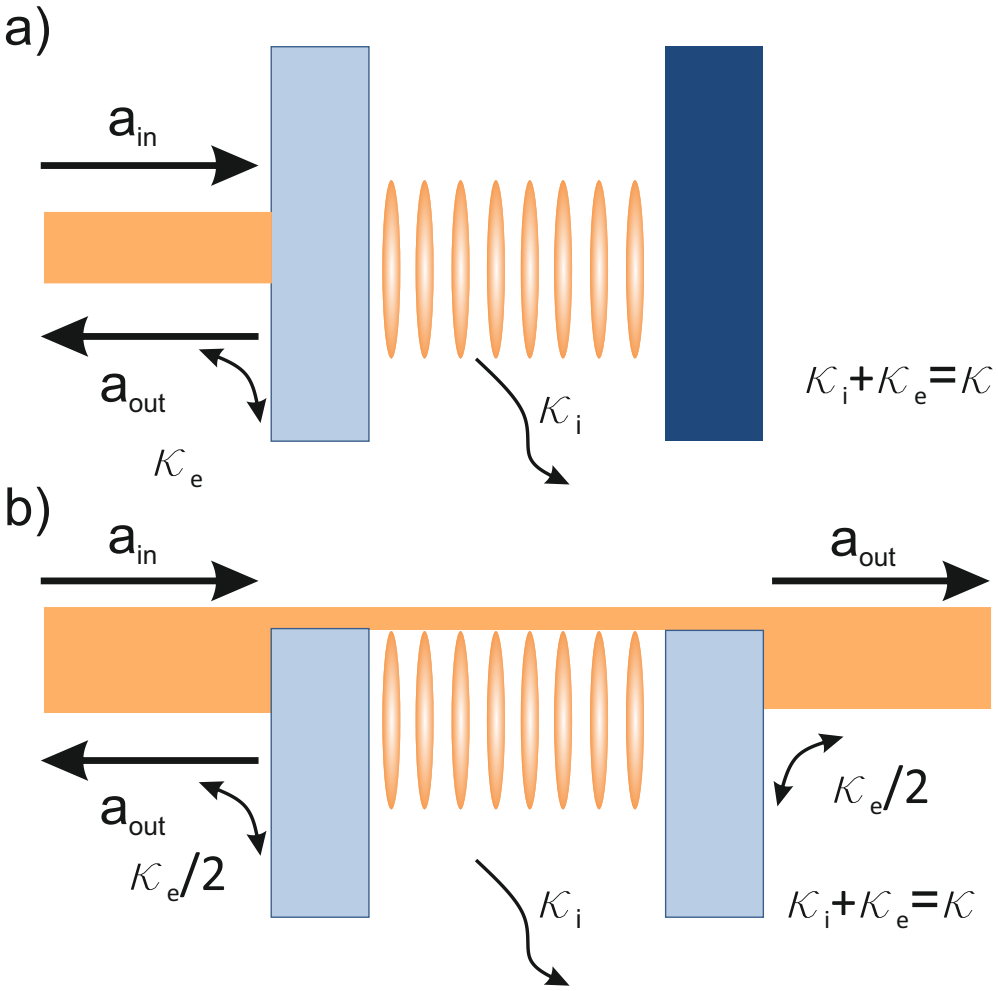

Figure 2.4: (a) A single sided coupling showing a waveguide (orange recatangle) and a cavity, schematized by two mirrors. The input optical field a_{in} is coupled from the waveguide with a coupling loss rate $\kappa_{in} = \kappa_e$. The cavity reflects a_{out} characterized by an intrinsic loss κ_i (b) The double-sided coupling correspond when the light of the waveguide is coupled backward and forward from the cavity with a extrinsic loss rate κ_e in each direction. For the single and double-sided coupling scheme the total decay rate is $\kappa = \kappa_e + \kappa_i$.

The work in this thesis has used both single and double-sided coupling schemes. For simplicity, the following derivations will be performed on the single

sided coupled cavity but keeping in mind that the derivations for the double-sided scheme is similar with basic modifications.

Since normally we can not obtain directly the optical field a, we need to interrogate the cavity response by using a light field and measuring the reflection or transmission signal a_{out}. This is accomplished by coupling a laser field in and out of the cavity to an optical waveguide or an optical fiber taper and place it in the near field of the optical mode. The relation between the a_{out}, a_{in}, and a is obtained by energy conservation requirements [59], and is given by:

$$a_{out} = \sqrt{\kappa_e} a - a_{in} \tag{2.18}$$

For convenience, we introduce the coupling efficiency parameter defined as $\eta = \kappa_e/\kappa$ to distinguish between different regimes [23] that will be described in the following derivations. The Eq. 2.18 allows to calculate the cavity parameter knowing the input and output fields by using Eq. 2.18 in Eq. 2.17:

$$a_{out} = a_{in}\left(\frac{\kappa\eta}{i\Delta + \frac{\kappa}{2}} - 1\right) \tag{2.19}$$

We can now compute the power reflected by the cavity and collected by a photodetector. The detected signal is given by $R = \left|\frac{a_{out}}{a_{in}}\right|^2$:

$$R = 1 - \frac{\kappa^2\eta\,(1-\eta)}{\Delta^2 + \frac{\kappa^2}{4}} \tag{2.20}$$

We observe from this equation that sweeping the frequency detuning between the laser and the cavity, the reflection spectrum presents a lorentzian shape. When the losses are dominated by intrinsic losses of the cavity, we have $\eta < 1/2$ ($\kappa_i > \kappa_e$). The signal collected back from the cavity into the waveguide channel is smaller than the field propagating in the waveguide. When the cavity loss rate equals the coupling rate, we have $\eta = 1/2$ ($\kappa_i > \kappa_e$). This regime is called critical coupling since the signal coupled back from the resonator and the field propagating in the waveguide interferes leading to zero reflection. Finally, when coupling rate exceeds the intrinsic loss rate, we obtained $\eta > 1/2$ ($\kappa_e > \kappa_i$), and the magnitude of the field collected from the resonator is larger than the propagating field on the waveguide channel. This is shown in Fig. 2.5 where we plot the reflection spectrum for different values of η. We note that the reflection spectrum can be written like $R = 1 - \frac{\kappa^2\eta(1-\eta)}{\kappa^2/4}$. The reflection dip on resonance increases from 1 to 0 as the coupling factor η increases from 0 to $1/2$. Then, when η increases from $1/2$ to 1, the resonance dip decreases and the reflection goes from 0 to 1.

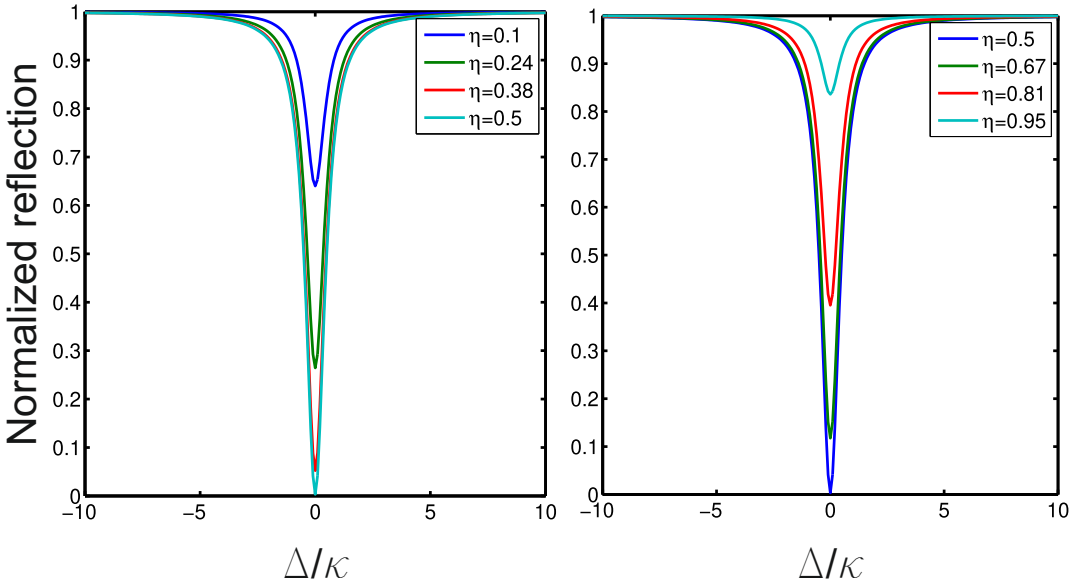

Figure 2.5: (a) Plot of the normalized reflection spectrum in under-coupled regime. The lorentzian dip on resonance goes to zero as $\eta = \kappa_e/\kappa$ approaches to $1/2$. This condition implies that $\kappa_e = \kappa_i$ and all the light coupled to the cavity is lost to the environment (b) Reflection spectrum in the over-coupled regime. Note that while η approaches to one, the extrinsic decay rate κ_e approaches to κ and no light is lost through κ_i

Looking at the imaginary part of Eq. 2.19 normalized by a_{in}, we can observe the phase response of the optical signal. The expression of the phase response ϕ is given by:

$$\phi = \frac{\kappa\eta\Delta}{\Delta^2 + \frac{\kappa^2}{4}} \tag{2.21}$$

This expression is important to monitor the mechanical motion when system is in resonance. The phase response of the reflected light is plotted in Fig. 2.6 a. Note that the phase change is maximized at $\Delta = 0$, where the reflection spectrum is 0.

Finally, we can obtain the steady-state number of photon in the cavity n_c. In Fig. 2.22, we plot the phase response as a function of the detuning Δ. The expression for the phase of the reflected signal is calculated by taking the norm-square of Eq. 2.17, and is given by:

$$n = \frac{\kappa\eta}{\Delta^2 + \frac{\kappa^2}{4}} |a_{in}|^2 \tag{2.22}$$

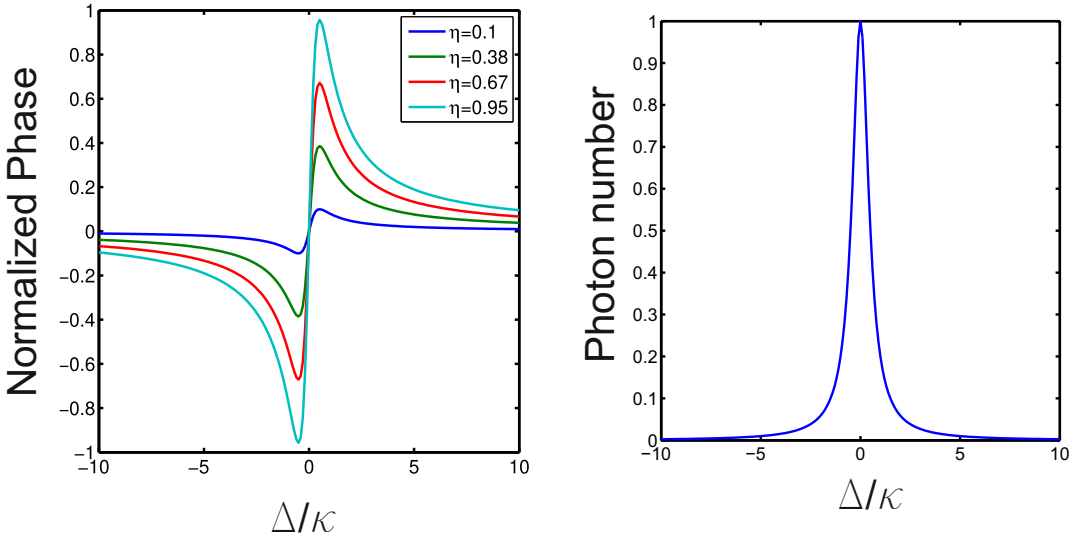

Figure 2.6: (a) Plot of the Phase response of the reflected signal as a function of the detuning for various values of η. The phase response increases with the value of η. The Phase change is maximized on resonance (b) Plot of the normalized intracavity photon number setting $a_{in} = \sqrt{\kappa_{in}}$

2.4 Mechanical mode detection

Once derived the reflection spectrum, we can illustrate an experimental way to measure the mechanical motion $x(t)$. As it was explained in section 2.2, the optomechanical coupling $g_{OM} = \frac{d\omega}{dx}$ links the mechanical motion with the optics of the resonator. This means that mechanical motion shifts the frequency resonance of the optical cavity. Therefore, setting the detuning at relative value to the optical resonance, the mechanical motion will cause a change in the reflected power. To first order, the reflected signal is:

$$R(t,\Delta) = R(\Delta) + \frac{dR}{d\Delta}\frac{d\Delta}{dx} = R(\Delta) + \frac{dR}{d\Delta}g_{OM}x(t) \tag{2.23}$$

We observe that to first order, the first term correspond to a DC value of the reflected signal and the second term of the equation reveals that the mechanical motion is proportional to the derivative of the reflected signal. Using Eq. 2.20, we get an expression for $\frac{dR}{dx}$ in terms of the extrinsic and intrinsic rate losses:

$$\frac{dR}{d\Delta} = \frac{2\kappa^2\eta(1-\eta)\Delta}{\left(\Delta^2 + \frac{\kappa^2}{4}\right)^2} \tag{2.24}$$

In Fig.2.7, we plot the derivative of the reflected signal as a function of detuning. Note that the maximum transduction of motion is obtained when

$\Delta = \kappa/2$. It is also relevant to note that the transduction is zero when $\delta = 0$. However, when the system is on resonance, a phase sensitive detection technique can be used, since the derivative of the phase $\frac{d\phi}{d\delta}$ is maximized, such as the homodyne detection. We can calculate now the modulated power due to mechanical motion is given by:

$$P(t) = P_{in}\frac{dR}{d\Delta}g_{OM}x(t) = 2g_{OM}\hbar\omega_l \left|a_{in}\right|^2 \frac{\kappa^2\eta(1-\eta)\Delta}{\left(\Delta^2 + \frac{\kappa^2}{4}\right)^2}x(t) \tag{2.25}$$

where we have used that input power $P_{in} = \hbar\omega_l \left|a_{in}\right|^2$. Normally, this power is measured on a spectrum analyzer, thus the power spectral density $S_{PP}(\omega)$ is related with the displacement spectral density $S_{xx}(\omega)$ as:

$$S_{PP} = \left(P_{in}\frac{dR}{d\Delta}g_{OM}\right)^2 S_{xx}(\omega) \tag{2.26}$$

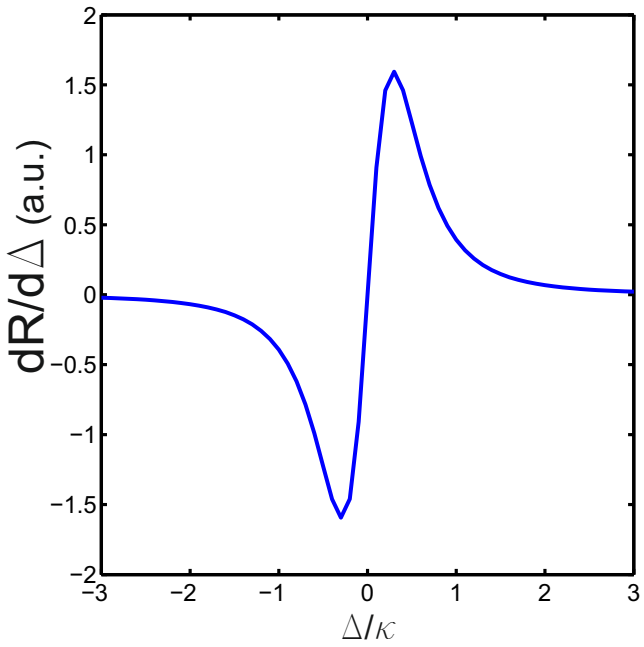

Figure 2.7: Derivative of the reflection signal with respect to detuning, as a function of detuning. We have used Eq. 2.23 with $\kappa_e/\kappa = 0.8$.

Chapter 3

Optomechanical resonators

In this chapter, I will discuss the two types of OM resonator used throughout this thesis. First, I will focus on the Whispering Gallery Modes (WGM) microspheres that are going to be used in Chapter 5. I will explain the confinement of optical modes in the microspheres and give approximated formulas to calculate the eigenmodes frequencies. Then, the WGM glass microsphere fabrication process will be specified. To couple light on the cavities, we use a tapered fiber, which fabrication and characterization will be given. Then I will discuss the one dimensional optomechanical crystals (1D OMC's), in particular, the corrugated nanobeam used in Chapter 6. In this second part I explain the engineering, fabrication, characterization and dynamics of the OM crystals triggered by non linear optical effects.

Either in the WGM and the 1D OMC cavitties, light is confined in the cavity with sufficiently high OM coupling g_{OM} such that allows the transduction of mechanical modes. However, the difference between both cavities, apart from the geometry, resides on the mechanism used to drive the mechanical modes. On the microsphere experiment explained in Chapter 5, we will drive this motion with an external mechanical force originated by an alternate magnetic field via magnetostriction. On the OMC's cavity experiment explained in Chapter 6, mechanical motion will be driven by an internal mechanism whose origin comes from the competition of optical nonlinear effects.

3.1 Whispering gallery modes in silica microsphere

3.1.1 Introduction

The light confinement on spherical dielectric particles was first studied by Mie in the 19th century [61]. He observed that the scattered light spectrum of these elements presented sharp resonances for specific wavelengths. These dips were attributed to the resonant circulation of light within the sphere, close to its surface. The optical modes are confined in the sphere by a repetitive process of total internal reflection at the dielectric-air interface. These

optical mode are commonly known as whispering gallery modes (WGM), by analogy with the acoustic phenomenom studied by Lord Rayleigh on his work titled "The problem of the whispering gallery" [62]. It described the situation that ocurred in the gallery of the dome of St. Paul's cathedral in London, where a word whispered against the wall could be heard at the opposite side of the gallery. The explanation comes by the fact that travelling waves propagated close to the 32 meter diameter wall.

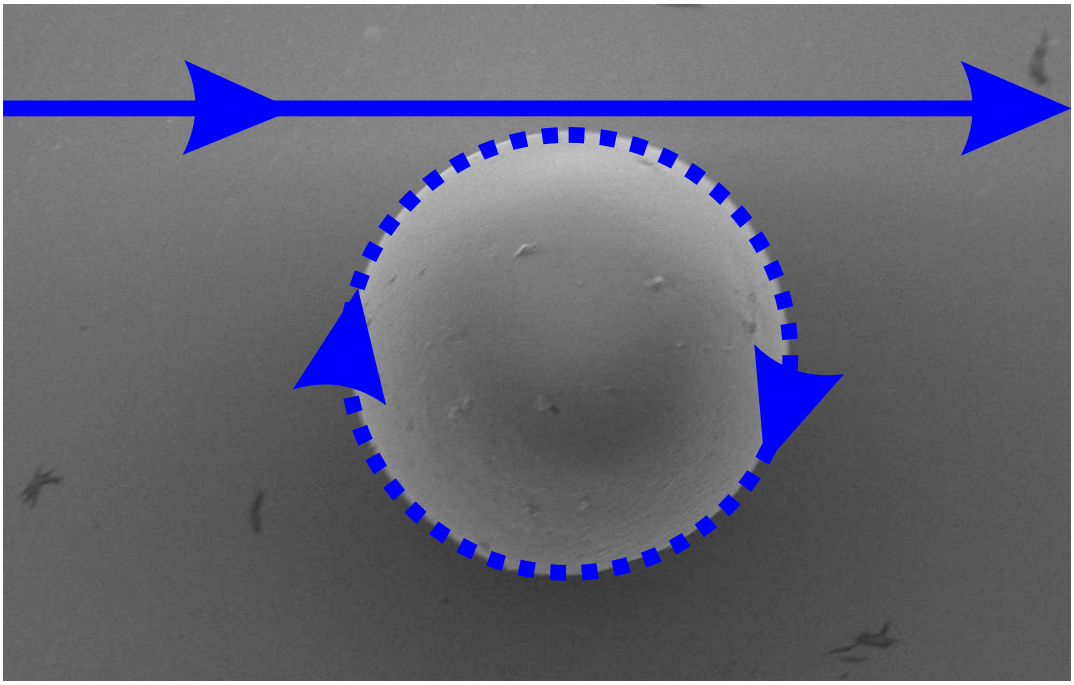

Figure 3.1: Top view of the whispering gallery mode resonators used on this work. Incident light is coupled to the microsphere using a tapered optical fiber, via frequency matching between the optical mode of the fiber and the WGM of the sphere.

Whispering gallery modes in silica microspheres have been extensively studied in the last decades. The light confinement in these optical microcavities is both temporally, since they can exhibit quality factors above 10^9, and spatially, since they are tipically characterized by optical mode volumes in the microscale range [63–65]. Originally, the WGM cavities consisted on dielectric droplets created by surface tension. Due to their high Q factor, they attracted the interest for multiple experiments, ranging from fundamental physics [66, 67] to low threshold laser [68]. Later, micro-droplets spheres were substituted by silica spheres created by different methods like polishing, chemical etching, and fast solidification of liquid droplets. Another successful technique to create permanents, single pure and undoped silica microspheres consisted on heating the tip of a fiber. The fabricated sphere could have typical sizes covering from 10 to 200 μm in diameter [69]. The fiber can be melted by an hydrogen torch [70], electric arc [71] or a focused beam of a CO_2 laser[23, 72]. The melted fiber adopts a spherical shape by the pulling effect of surface tension.

The adopted fabrication method for the spheres used in this thesis relies on the use of a vertical furnace were an inert gass melts a glass previously prepared [73–75]. This method allows to obtain spheres with diameters from 4 to 100 μm. The advantage with respect to other fabrication methods resides on the possibility of fabricating a large number of microspheres in one fabrication batch. Another advantage that this method presents is that the primal glass could be prepared with a doping material.

The main disadvantage that microsphere resonators present are related with the difficulties to integrate these devices with electrical and micromechanical functions. In the last decades, fabrication processes were developed with the objective of circumvent the incompatibilities of fiber based WGM resonator with microelectronic integration. The fabrication of disk and microtoroids employing standard lithography on silicon supposed a step forward on integration and a potential tool for experiments on Quantum Optics [35, 76, 77]. Nevertheless, microspheres are convenient devices to work due to their high simmetry. WGM resonator are used for studying biophysical applications [78–80], non linear optics [63, 81], and quantum electrodynamics [77, 82]. The natural circulation of light in WGM cavities makes them useful to create laser cavities by incorporating a gain medium. This is usually performed in silica microsphere via doping of the bulk glass with a rare earth ion before the melting process [83]. If the doping concentrations is high enough, the microsphere becomes an active cavity and a gain medium for lasing emission. The lasing action can enhance the sensitivity of the WGM cavity, achieving low detection due to their narrow linewidths [73, 84–86]

In the following sections, I will describe the electromagnetic field distribution of the WGM cavities. The resonant frequencies of WGM will be derived. It will serve as the theoretical introduction and terminology used throughout this thesis, especially the experiment described in Chapter 4.

3.1.2 Optical properties of WGM resonators

The optical modes of a spherical WGM resonator is obtained by solving the Helmholtz equation in spherical coordinates (this has can be found in detail in [87–89]). A simplified version is given by:

$$\frac{1}{r^2}\frac{\partial^2}{\partial r}(rE) + \frac{1}{sin\theta}\frac{\partial}{\partial r}\left(sin\theta\frac{\partial}{\partial\theta E}\right) + \frac{1}{r^2 sin^2\theta}\frac{\partial^2}{\partial\phi^2} - n^2k^2E = 0 \qquad (3.1)$$

The problem has been simplified assuming that the sphere is an homogeneous medium and the electric field polarization is constant along the optical trajectories. This allows to calculate the field components analytically by separation of variables [87]. Two classes of solutions are obtained from the scalar Helmholtz equations, TE-modes and TM-modes. TE-modes are characterized by having an electric field parallel to the surface of the sphere ($\vec{E}||\vec{\theta}$) while TM modes are characterized by having the magnetic field parallel to

the surface of the sphere ($\vec{B}||\vec{\theta}$), giving an electric field predominantly radial for the TM case. The solutions for the field are given obtaining the radial, azimuthal and polar components from the scalar Helmholtz equation, and they are associated to a specific mode number which are q for the radial component, l for the polar component and m for the azimuthal. The field solutions for both TE and TM modes are given by:

$$\begin{aligned} E^{TE}_{l,m}(r,\theta,\phi) &= E_0 \frac{f_l(r)}{k_0 r} \vec{Y}^m_l(\theta,\phi) \\ B^{TE}_{l,m}(r,\theta,\phi) &= -\frac{i}{ck_0} \nabla \times E^{TE}_{l,m}(r,\theta,\phi) \end{aligned} \tag{3.2}$$

and

$$\begin{aligned} E^{TM}_{l,m}(r,\theta,\phi) &= -\frac{i}{ck_0 n^2} \nabla \times B^{TM}_{l,m}(r,\theta,\phi) \\ B^{TM}_{l,m}(r,\theta,\phi) &= -\frac{iE_0}{c} \frac{f_l(r)}{k_0 r} \vec{Y}^m_l(\theta,\phi) \end{aligned} \tag{3.3}$$

where n is the refractive index of the sphere, $k_0 = \omega/c$ is the wavevector and $f_l(r)$ is a function associated to the radial dependence that can be expressed as the Bessel function $j_l(r)$ and the Hankel function $h_l(r)$. $\vec{Y}^m_l(\theta,\phi)$ are the vector spherical harmonic, which are obtained from the scalar spherical harmonic in the following way:

$$\vec{Y}^m_l(\theta,\phi) = \frac{1}{\sqrt{l(l+1)}} \nabla Y^m_l(\theta,\phi) \times \vec{r} \tag{3.4}$$

with

$$Y^m_l(\theta,\phi) = \sqrt{\frac{2l+1}{4\pi} \frac{(l-m)!}{(l+m)!}} P^m_l(cos(\theta)) e^{im\phi} \tag{3.5}$$

being P^m_l the Legendre functions. The optical modes are finally determined by matching the solutions at the sphere-air boundary, given by

$$\frac{j'_l(nk_0a)}{j_l(nk_0a)} = \frac{h'_l(k_0a)}{h_l(k_0a)} \tag{3.6}$$

where the prime denotes the dericative of the function with respect to the argument and a is the radius of the sphere $r = a$.

The equation Eq. 3.6 depends only on the polar number l, supporting infinite number of solution given the oscillatory nature of the Bessel and Hankel functions. These solutions are labeled by the radial number q, which gives the number of zeros of the electric field inside the sphere. For this reason, the

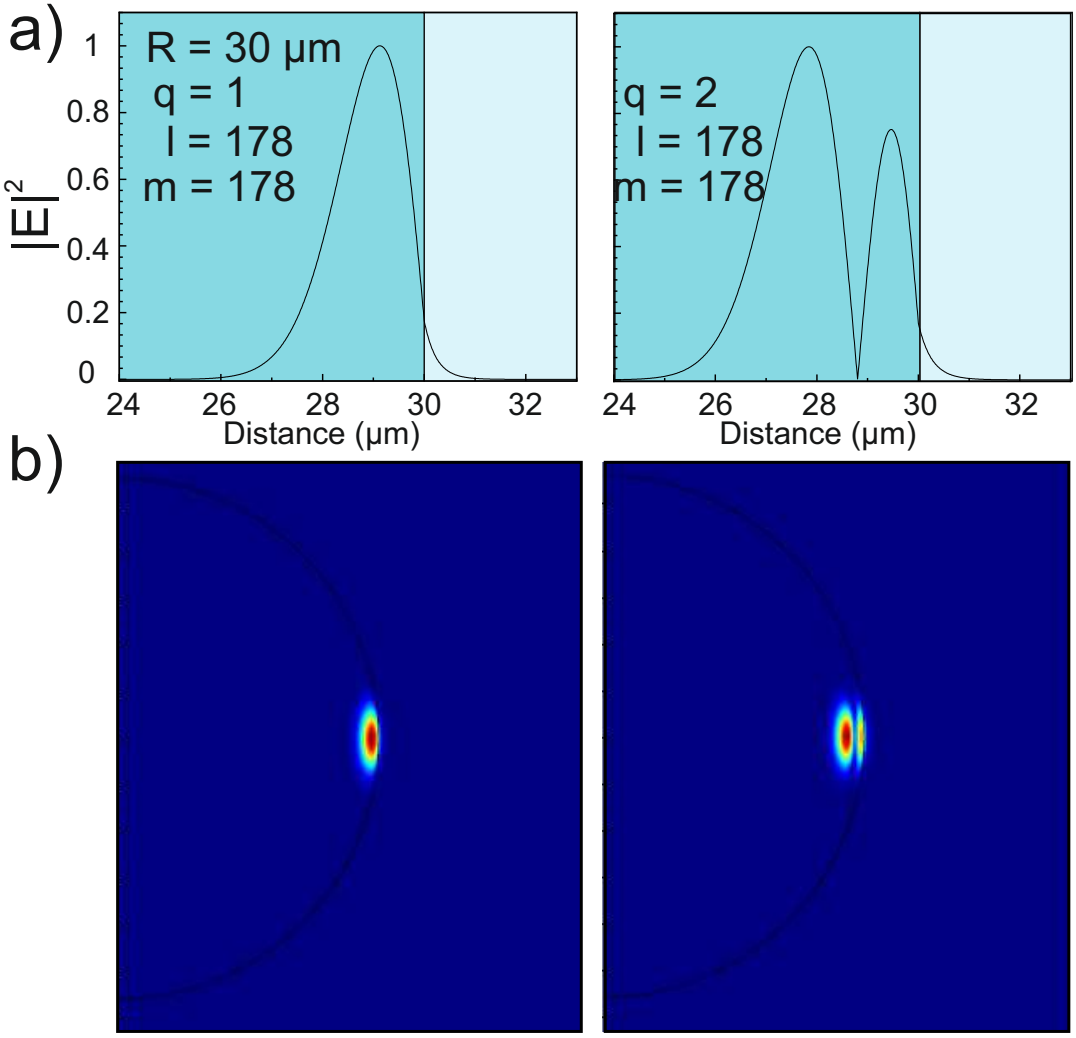

Figure 3.2: (a) Calculated Intensity $|E|^2$ in the radial direction for a microsphere with a radio of 30 μm for a radial number q=1 and q=2. The cyan color is associated to the dielectric and the light blue to the air medium. Part of the WGM leaks the energy outside to the air and decays exponentially. (b) Intensity profile of the electromagnetic field obtained with COMSOL for the radial numbers plotted in (a).

solutions associated to WGM are the one with low q value, since the mode is localized at the sphere surface. Since for WGM's it is needed a low q value, it can be demonstrated that $|m| \sim l$. The azimuthal mode number presents a degeneracy of 2l+1 and can be field intensity distribution on the polar plane (θ =cte). Fig. 3.2a shows the solution to the radial equation for the first two radial number for a 30 μm microsphere. The Intensity distribution is obtained by using a *WGM Toolbox* for Matlab explained in Ref. [90].The field intensity is plotted at the dielectric-air interface, with magenta/light bue colors associated, respectively. The electromagnetic field node are given by the radial number q. Outside the sphere the field decays exponentially. The total electromagnetic field is plot in Fig. 3.2b in the (r,θ) plane.

Approximated formulas to obtained the eigenmodes for spheres in the relevant condition of high l for WGM can be found in Refs. [87]. The solutions are given in function of the zero of the Airy functions ζ_q^0, with $Ai(\zeta_q^0) = 0$ and the radial number q ($\zeta_1^0 \approx 2.338$). The first three terms of the eigenfrequencies are given by:

$$\omega_{q,l} = \frac{c}{2\pi R}\left(l + 1/2 + \zeta_q^0\left(\frac{l+1/2}{2}\right)^{1/3} + \mathcal{O}\left(\frac{l+1/2}{2}\right)^{1/3} + ...\right) \quad (3.7)$$

3.1.3 Fabrication of silica microspheres

The microspheres used on this thesis are fabricated from a barium titanium silicate (BTS) glass. The fabrication was performed at Universidad de la Laguna [73, 83, 84, 91] , where the glass microsphere elaboration was developed based on the technique explained by Elliot et al [75]. This method is based on the spherical shape that a melted particle gets by surface tension pulling when it rapidly passes to a cooler region. Due to the fact that one of the original purposes for the microspheres was the study of lasing emission, they were doped with 1.5% Nd_2O_3 (in the molar ratio).

The first part of the process is to obtain the BTS bulk substrate. Commercial powders with certified purity larger than 99.9% of $BaCO_3$, TiO_2, SiO_2 and Nd_2O_3 were combined and melted in a platinum-rhodium crucible at 1500 °C for one hour in an electric furnace. The bulk glass is crushed with a pestle and mortar to the convenient size before the microsphere fabrication. Then the particles are classified by size. This classification helps to use only the particles with the similar size to the one desired for the sphere. The large particles can be separated easily but the small are normally attracted to the recipient surface and form conglomerates. This is normally solved by using isopropanol. Once the particle size is obtained, the mixture is dropped through a vertical tube furnace at the BTS fusion temperature, which is around 900 °C. While the particle are falling, most of the splinters melt and surface tensions pulls them into a spherical shape. When the spheres fall from the hot part to the room temperature zone, they cool down and quickly solidify.

The obtained material after the quenching process is a mixture of microspheres and undesired particles. A classification process is again needed. This can be done by an iterative decantation process. The smaller spheres will be placed at the bottom of the container. Using this method it is possible to obtain spheres with diameters ranging from 4 to 100 μm (see Fig. 3.1).

3.1.4 Coupling scheme to WGM with a tapered fiber fabrication procedure

In this section, I will describe the coupling of light to the WGM. This method will be also used to couple light within the 1D OMC's. Here it will also be possible to find the fabrication procedure characterization of tapered fibers.

The coupling of light into and out of the WGM microsphere is achieved by using a tapered optical fiber. This are essentially fiber on which the central part is pulled to a diameter on the order of the wavelength of the coupled light. A fiber with this diameter only allows the propagation of a single mode. The electromagnetic field propagates through the fiber but part of the mode leaks to the surrounding air, where it decays exponentially, in a similar way as the intensity drop in transverse direction of the WGM's shown in Fig. 3.2. Light is coupled into the structures thanks to the long tail of the evanescent field of the optical mode of the fiber. The coupling is enabled when the propagation constant of the taper equals with the propagation constant of the WGM [88].

For the fiber fabrication,a homemade setup is used, in which a telecom optical fiber (SMF-28) is stretched in a controlled way using two motorized stages. The setup is shown in Fig. 3.3. The central part of the fiber is locally heated to a temperature of 1180 °C with a microheater.

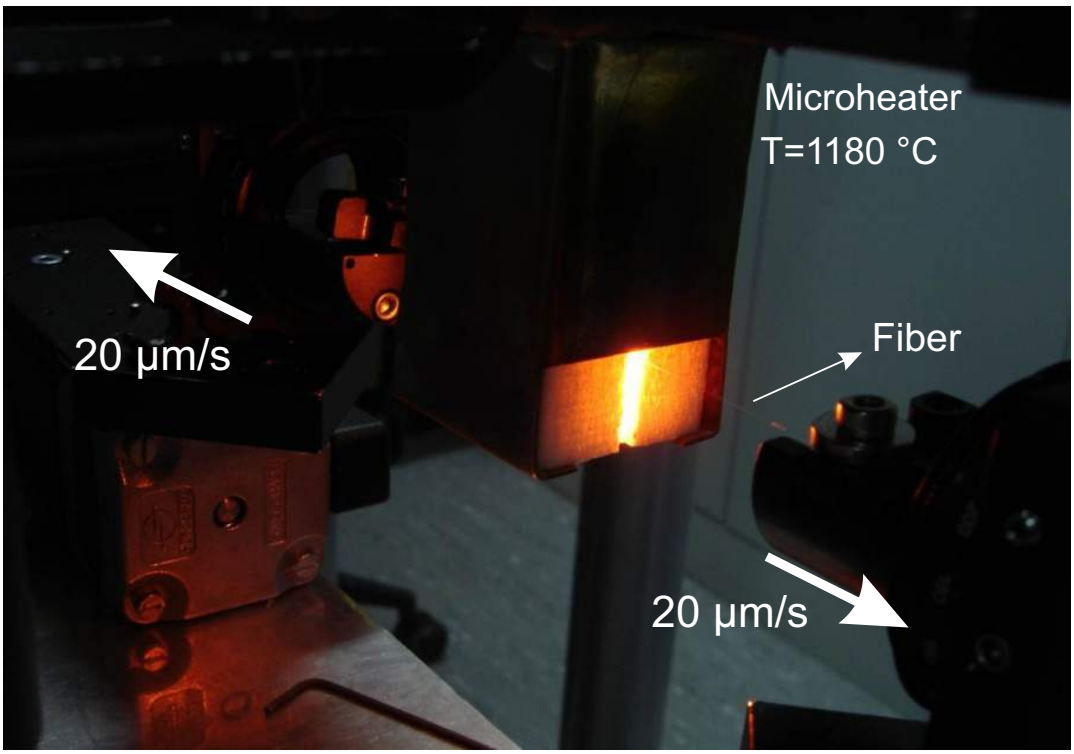

Figure 3.3: Lateral view of the tapered fiber fabrication setup. Two motorized stages on which the fiber is clampled, pulled at a 20 μm/s. The central part of the fiber is heated with a microheater to a temperature of 1180 °C

The fiber transmission at the wavelength of 1.5 μm is monitored during the pulling process (see Fig. 3.4b). The signal is applied to a short time Fast Fourier Transform(FFT) algorithm to check the frequency components of propagating mode. Before starting the pulling process, the fiber is monomode and when is heated and pulled it becomes multimode, so that the signals starts to show intereferences between different supported modes. This is shown in the left part of Fig. 3.4b where the transmission signal is oscillating. The multimode character is confirmed by Fig. 3.4c, showing the FFT signal with a peak function. When these frequency components disappear, the monomodal condition is achieved (see Fig. 3.4d and the right part of Fig. 3.4b). The experiments are carried out with optical fibers having diameters in the thinnest section of ~ 1.8 μm Fig. 3.4a, which is commensurate with the wavelength needed and ensures an evanescent field tail of several hundreds of nanometers.

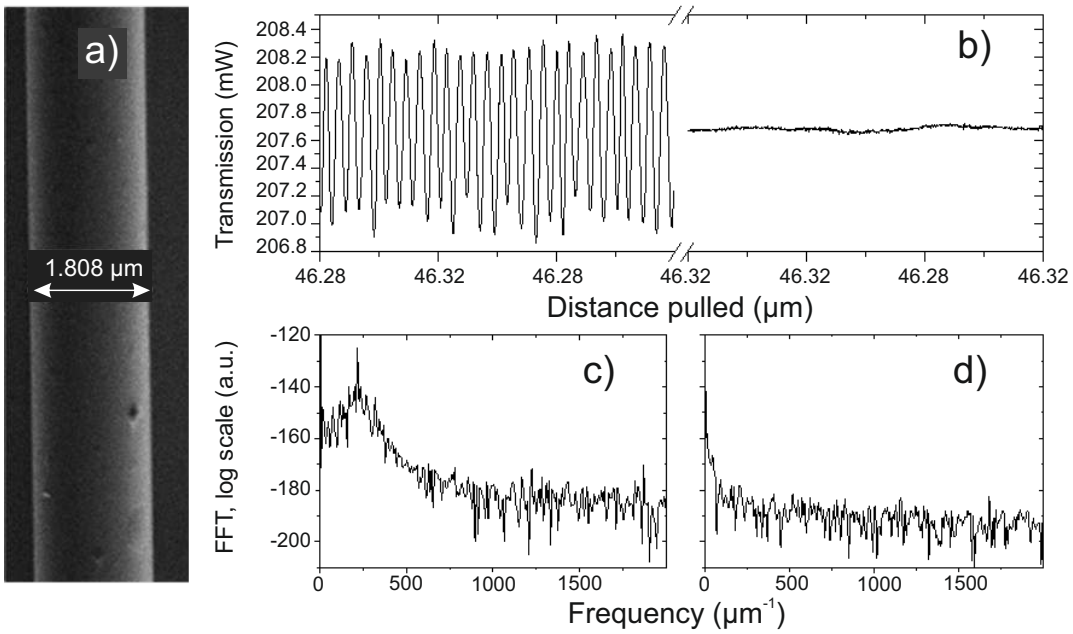

Figure 3.4: (a) SEM image of the thinnest part of a tapered fiber.(b) Transition from multimode to monomode while pulling the two extremes of the fiber as seen in temporal scale. (c) FFT of the transmitted signal before the transition to single mode. (d) FFT of the transmitted signal after the transition to single mode.

The WGM resonator is placed below the tapered fiber and its position is controlled with nanometer-scale precision. The thickness of the tapered fiber is $\sim 1\mu$m. The fiber is shaped into a microloop form with a radio of R$\sim 10\mu$m, allowing the local excitation of microsphere (and nanobeams) with a nanometer-scale precision on a region of $5\mu m^2$. The microloop is created once the pulling process is stopped by first rotating the fiber clamps around itself. This will twist the fiber. Then, the two fiber ends are gently approach several hundreds of micrometers so that the loop is formed with a large diameter. Finally the two ends are pulled again apart reducing the loop size. In that process, the

two parts of the fiber at the loop thinnest point slide in opposite senses. The microspheres resonator have been measured approaching the fiber in contact with the sample.

3.2 Optomechanics in a corrugated nanobeam

3.2.1 Introduction to 1D optomechanical crystals

Alternative structures to WGM that confine light and couple to mechanical vibrations is achieved by optomechanical crystals. OMC's are simultaneously photonic and phononic crystals, so that the electromagnetic field and the mechanical displacement is co-localized spatially in a particular zone of the structure leading to an enhanced interaction [29, 30, 92–95]. OMC's are fabricated by a periodic modulation at the nanoscale of the refractive index and material density. This allows to include a structural defect in the otherwise regular dielectric lattice forming a cavity. Analogously, due to the density modulation it is possible to confine mechanical modes to the same structural defect. In practice, this is performed by doing periodic holes in a membrane (2D OMC) or a nanobeam (1D OMC). Such periodicity modifies the phonon and photon dispersion relation, giving rise to photonic and phononic band gaps, i.e., forbidden wave propagation for a given frequency range.

These structures have applications in both classical and quantum phenomena. One of the most practical advantage of the OMC's with respect, for example, with microspheres is that they can be integrated in chip platforms, enabling the design of multiple elements as optomechanical circuits. The optical transduction of phonons in OMC's has leveraged sensing systems of different magnitudes, like small displacements, mass, and force [6, 41, 96, 97]. Moreover, several experiments have exploited interaction between phonons and photons at a fundamental level, like optomechanical induce transparency [98], the ground state cooling of a mechanical resonator [99] or squeezed light [100]. All this experiments among other suggest that OMC's can be considered possible building blocks for phonon circuits.

The P2N group has a strong experimental background using the efficient optomechanical coupling obtained in nanobeams structures in a Silicon platform to create phonon sources [30, 101–105] and to study complex dynamics by exploiting material nonlinearities [95]. In order to understand the synchronization experiment described in Chapter 6 with two linked nanobeams, an introduction to the single OMC used and the its main properties must be given in the following section.

3.2.2 The corrugated nanobeam

The 1D OMC device that will be investigated in this thesis is crystal built in a Silicon nanobeam with circular holes and a corrugation shape made with rectangular stubs. A SEM image of the nanobeam is shown in Fig. 3.5. The design of the lattice is based on the repetition of the unit cell shown in Fig. 3.5. It consists on a square with a circular holes and two symmetric stubs on the sides. The geometrical parameters that characterize the unit cell are the pitch distance (a), the radius of the hole (r), and the stubs length (d) with the following nominal values a= 500 nm, r= 150 nm, and d= 250 nm. The full structure is formed by a total number of 32 cells with a cavity length of 15μm. The thickness of the nanobeam is given by the SOI wafer of 220 nm.

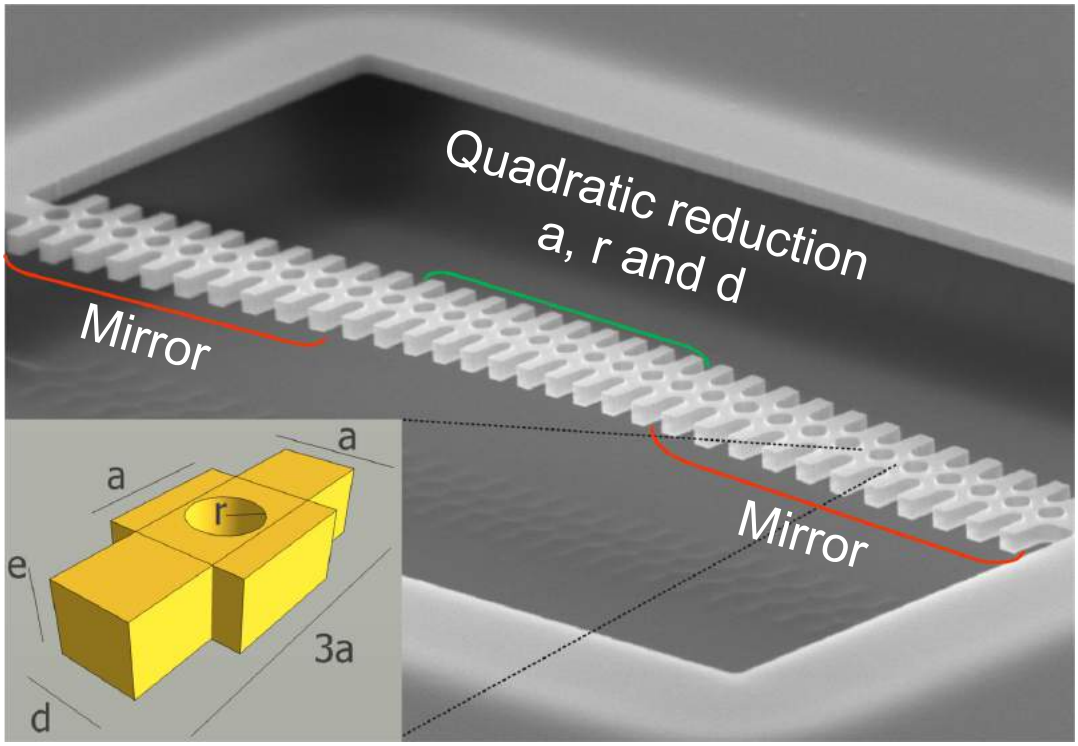

Figure 3.5: SEM image of the corrugated OMC. The structure consists on the repetition of the unit cell (yellow inset) with the following geometrical parameters: a= 500 nm, r= 150 nm and d= 250 nm. The mirror cells have nominal values and the defect is created decreasing quadratically towards the center the values of a, r and d.

The ten initial cells at both sides are mirror cells defined by the nominal geometrical parameters. The 12 central cells are the structural defect that forms the cavity. The cavity is created by varying quadratically towards the center of the structure the geometrical parameters of pitch, hole radius and the stub simultaneously. The maximum reduction of the parameters is denoted by Γ, which is the quotient between pitch of the central cell and the nominal cell of the mirror.

One of the key features in the choice of the geometry described above for the corrugated OMC structure is because it presents a photonic band diagram with a TE pseudogap and phononic band diagram with full gap [30]. This aspect is the main difference with respect to other OMC used in the literature, which presented pseudo gaps in their phononic band diagrams [28, 92, 106]. The advantage is that a full gap guarantees the absence of propagation of phonons from any band in frequency range while a pseudogap is defined by the absence of bands in a particular symmetry.

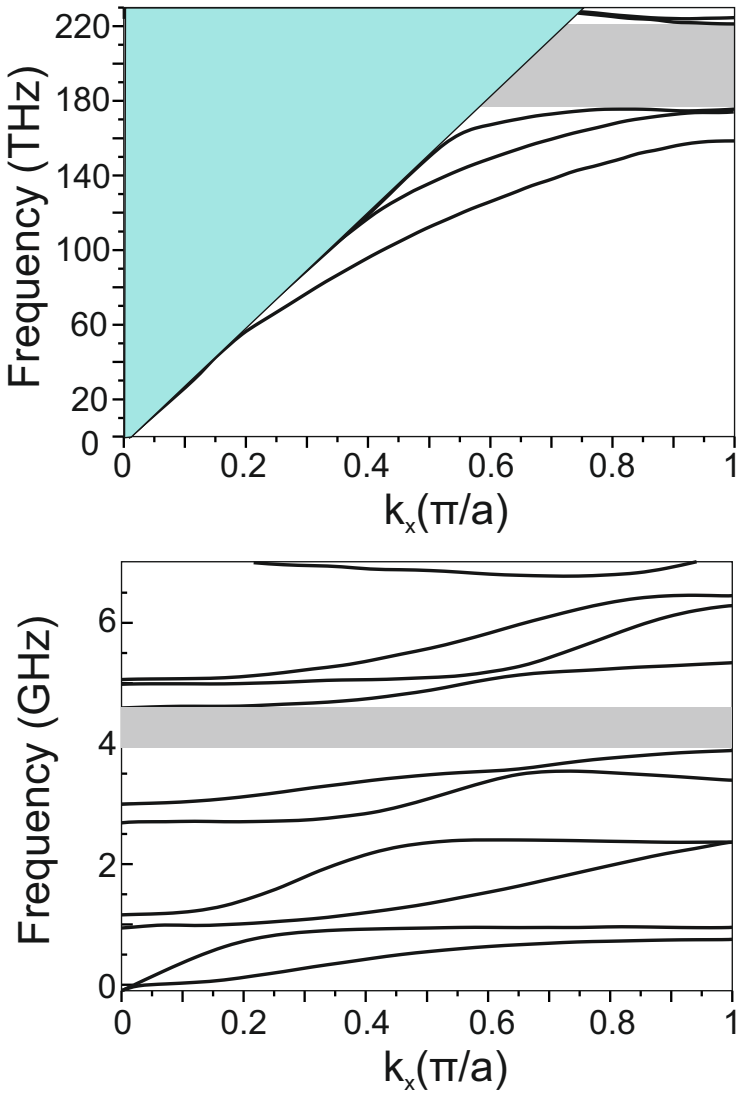

Figure 3.6: (a) Photonic band diagram of the mirror cell. It shows a bandgap for TE modes (grey area). (b) Phononic band diagramd of the mirror cell with symmetry in the z=0 plane (half of the cell). The diagram presents a full gap between 3 to 4.5 GHz (grey area).

The photonic band diagram of the corrugated OMC is shown in Fig. 3.6a. It is obtained by simulating the mirror cell using COMSOL. The diagram presents a full gap for bands with TE polarization (TM polarization is not shown). The variation on the geometrical parameters towards the center of

the cavity creates an effective potential that confines the optical modes. In particular the modes of the second and third TE band are pulled towards gap region from the X point (k=π/a).

The phononic band diagram is represented in Fig. 3.6b. The spectrum is calculated for the perfect structure. It reveals a phononic bandgap which expands from about 3.5 GHz to 4 GHz. The investigation of high frequency modes can be found in Refs. [30, 104]

3.2.3 Fabrication

The structures were fabricated at the Politechnic University of Valencia. We use a standard silicon-on-insulator (SOI) SOITEC wafers with a top silicon layer thickness of 220 nm (resistivity ρ $\sim 1^{-10}$ Ω cm^{-1}, p-doping of $\sim 10^{15}$ cm^{-3}) and a buried oxide layer thickness of 2 μm. The OMC's fabrication process is based on electrom beam lithography (EBL) on a 170 nm resist layer of polymethyl methacrylate (PMMA) baked at 950 K.

The optimized structures were obtained with an EBL exposure characterized by the following parameters: acceleration voltage of 10 KeV and an aperture size of 30 μm with a Raith150 equipment. Since the PMMA is a positive resist, the exposed pattern are negatives, then, the developer removes the areas that have been exposed, leaving the remaining resist as a mask. After developing the samples with MIBK/IPA, the patterns were transfer to the silicon layer with an inductively coupled plasma-reactive ion etching. The gases used were SF6/C4F8. The two gases are injected simultaneously under typical recipes for silicon etching (pressure: 20 mT, low-bias voltage, and a SF_6/ C_4F_8 flow ratio: 1.5), which produce anisotropic etching with smooth lateral walls. Finally, once the silicon is etched, the nanobeams are released from the silicon oxide substrate by a buffered HF wet etching process.

3.2.4 Optomechanical properties of the nanobeam

In this section I will address the optical and mechanical properties of the nanobeams. By placing the tapered fiber close to the OM structures, it is possible to couple light in and out of the cavities. Detecting the transmission of an infrared laser at a low power (<10 μm), the optical spectrum like the one shown in Fig. 3.7a is obtained. Several resonances are measured corresponding to the localized optical modes of the OMC.

The tapering introduced by design allows to confine optical modes with high Q factor. For example, the optical mode shown in Fig. 3.7b, that correspond to the mode highlighted in blue in Fig. 3.7a. From a Lorentz fit of the optical resonance the optical mode is characterized by an optical quality factor Q= 2.3$\cdot$ 10^4, with an extrinsic decay rate κ_e= 1.88 $\cdot$ 10^{10} s^{-1} and intrinsic decay rate κ_i= 3.58 $\cdot$ 10^{10} s^{-1}.

In order to identify how is the electric field distribution of the localized optical mode measured, an imported SEM image of the real device was simulated in COMSOL. Fig. 3.7b shows the obtained electric field distribution E_y of the optical mode measured at $\sim$ 196.8 THz. The observed mode correspond to an hybridization of the mode families associated to the second and third band. The optical modes presents an asymmetry distribution of E_y along the x-y plane. This is goind to play an important role on the optomechanical coupling calculation. (See Appendix **??** for details on the obtention of g_{OM})

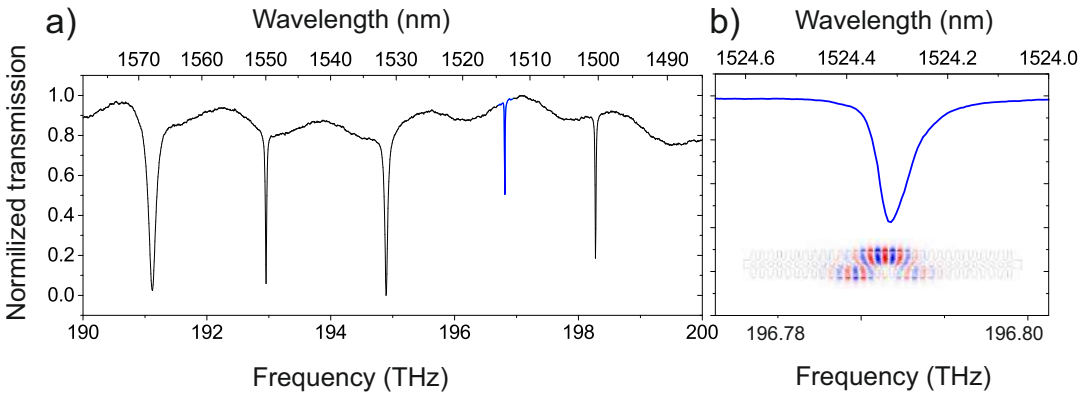

Figure 3.7: (a) Normalized transmission spectrum of the corrugated nanobeam. The spuctrum is taken for low laser power (<10 μW). (b) Optical resonance under study is highlighted in blue. The electric field componen E_y associated to the optical mode

The RF spectrum associated to the optical transduction of thermally activated mechanical modes is shown in Fig. 3.8. Several peaks are obtained that correspond to in-plane and out-of-plane string-like mode of the nanobeam. For symmetry consideration, this mechanical modes should not present a high g_{OM} value, however, since the optical mode is asymmetric in the yx plane by geometrical inhomogeneities in the vertical direction (see Fig. 3.7), the different integral involved in the g_{OM} extraction, contributes in an unbalanced way giving high optomechanical coupling values. In particular, the displacement profile of the eigenmode at 54 MHz is shown in Fig. 3.8. This mechanical mode corresponds to a third order in-plane mode, since it displays two antinodes in the center of the beam. The mentioned eigenmode is particularly relevant since is the one that will be exploited to explore the non linear dynamics activated by self pulsing in the next section and also Chapter 6.

3.2.5 Self Pulsing mechanism

In this section I will discuss the self pulsing (SP) mechanism in an optical cavity. SP is a process that emerges in optical cavities that is driven by an optical power large enough to activate the nonlinear effects on the resonator, involving free-carriers and temperature rises [101, 105, 107–109]. When these

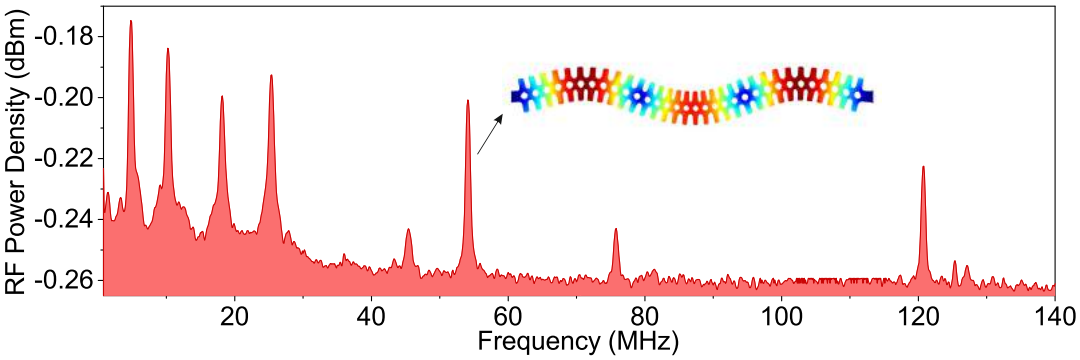

Figure 3.8: RF spectrum obtained by exciting the cavity with the first-order optical mode. Displacement profile of the third order in-plane mechanical mode.

nonlinearities are activated they start to compete, and are described by a coupled system of equation. For specific conditions, the solutions result in a periodic modulation of the refractive index of the optical mode, and then, the intracavity radiation pressure force. SP then experimentally described as an "optical frequency comb" with multiple peaks spectrally located at integers of main SP frequency (ν_{SP}). The dynamic behavior of the intracavity photon number is equivalent to what could be reached by an external modulation of the input laser, although in this case the optical modes are pumped with a continuous wave source.

In Silicon-based optical resonators in the near infrared, two photon absorption (TPA) is the main process in generating free carriers. The free carriers generated can decay through several processes with a particular decay time. This effect is described by a rate equation for the free carrier density (N) and is named free-carrier-dispersion, since the free carrier population induces a dispersion effect on the in the optical resonance λ_r, resulting in a blueshift of its cold position (λ_0) [108]. A second effect that needs to be considered is related with the temperature rise (ΔT) of the cavity due to the fact that the free carriers generated by photon absorption is given to the lattice, converting this energy into heat, and obeys its own rate equation. This second effect is named thermo-optic (TO), and results in a redshift of the optical resonance with increasing temperature [109]. The rate equation for N and ΔT are given by [107]:

$$\begin{aligned} \dot{N} &= -\frac{1}{\tau_{FC}} N + \beta \left(\frac{hc^3}{n^2 \lambda_0 V_0^2} \right) n_0^2 \\ \Delta\dot{T} &= -\frac{1}{\tau_T} \Delta T + \alpha_{FC} N n_0 \end{aligned} \tag{3.8}$$

where V_o is the optical mode volume, λ_0 is the cavity resonance wavelength at room temperature and α_{FC} is defined as the rate of temperature increase per photon and unit free-carrier density. The first term of the free carrier concentration equation rate, is a surface recombination term governed by a

characteristic lifetime τ_{FC}. The second term is a generation of free carriers by TPA, being β the tabulated TPA coefficient. The TO effect equation reflects the balance between the fraction of photons that are absorbed and transformed into heat due to FCA and the heat dissipated to the surroundings of the cavity volume, which is governed by a characteristic lifetime τ_T. Both generation terms of Eq. 3.8 are coupled by the intracavity photon number n, which can be written as

$$n = n_0 \frac{\Delta\lambda_0^2}{4\left(\lambda_l - \lambda_r\right)^2 + \Delta\lambda_0^2} \tag{3.9}$$

where $n = n_0 = 2P_l\kappa_e\lambda_0/\kappa^2 hc$ is the number of photons in perfect resonance. P_l and λ_l are the laser power and the wavelength, respectively. Both P_l and λ_l are the only tunable parameters in the experiment, being controlled by the infrared laser source. Also in Eq. 3.9, κ_e and κ and are the extrinsic and overall optical damping rates, respectively.

The dispersion effects on the cavity resonant wavelength can be approximated to first order, giving:

$$\lambda_r \approx \lambda_0 - \frac{\partial\lambda_r}{\partial N}N + \frac{\partial\lambda_r}{\partial T}\Delta T \tag{3.10}$$

We can also asume that the number of photons is given by the steady state solution in the linear case, due to the different timescales between the dynamics of N and ΔT and the decay of the cavity ($\kappa^{-1} << \tau_{FC}, \tau_T$), which can be considered to respond adiabatically to any perturbation in time.

Other processes can be considered, but these are the leading one in silicon in the NIR and suffice to explain the dynamics that will be described later on, so we concentrate on solving these group of equations. As it was mentioned before, experimentally, we have access to both laser parameters (P_l and λ_r), which are included in the dynamic equations implicitly in n, thus impacting the generation rates.

The dynamic of the system can be illustrated from the phase trajectories of $\{N, \Delta T\}$ for different wavelengths, obtained from the simulated solutions of Eq. 3.8. Fig. 3.9 plots the simulated phase portraits $\{N, \Delta T\}$ for specific values of λ_l, keeping P_l fixed. The trajectories (red curves) are calculated by imposing initial conditions in such a way that the cavity is red-detuned with respect to the laser by an amount equal to λ_0.

The nullclides have been included in Fig. 3.9, defined as the curves where either $\dot{N} = 0$ (green curves) or $\dot{\Delta T} = 0$ (blue curves). Generally, the solutions of Eq. 3.8 are given by a stable fixed point, where either for $\dot{N}$= 0 and $\dot{\Delta T}$= 0. This is illustrated in Fig. 3.8a. In this case, if the system is driven away from the fixed point, its dynamic decays exponentially to equillibrium.

By continuing increasing λ_l to specific value, the stable fixed point undergoes a supercritical Hopf bifurcation. The fixed point becomes a weak stable

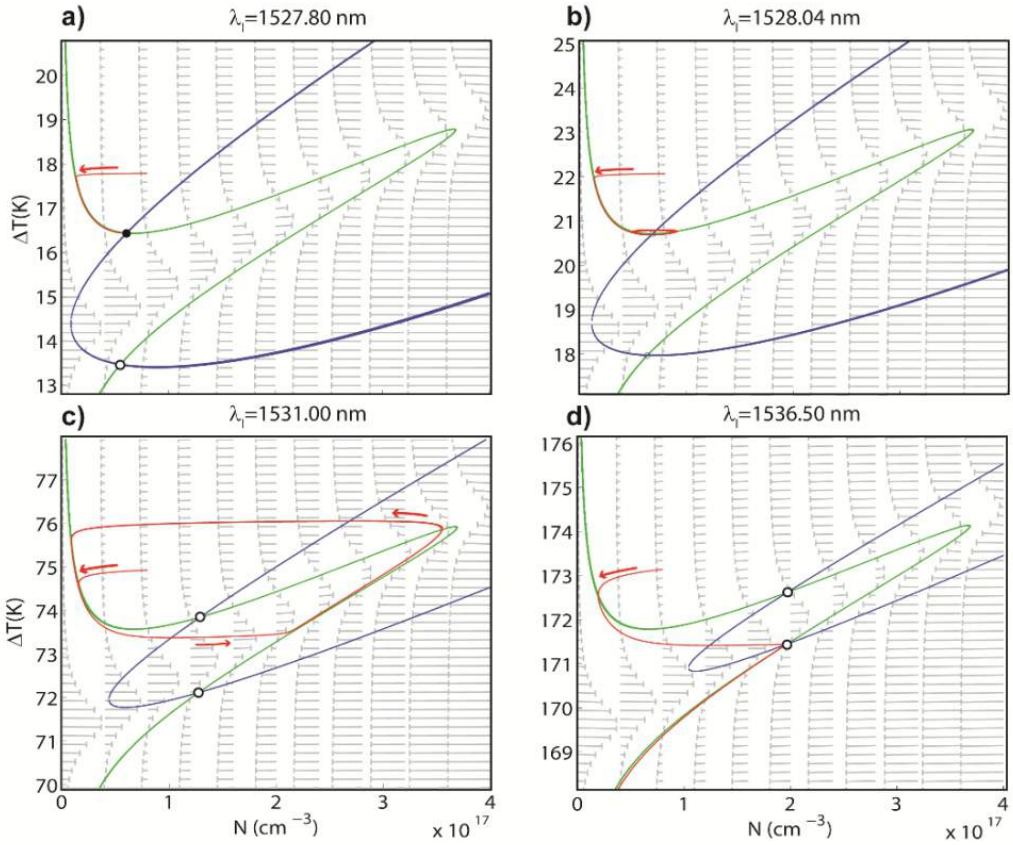

Figure 3.9: Phase trajectories of $N, \Delta T$ for different wavelengths λ_r. Different cases are shown (a) below the supercritical Hopf bifurcation, (b) above the bifurcation (c) SP limit cycle and (d) interception with a second unstable fixed point and end of SP. The green and blue lines correspond to values of $\dot{N} = 0$ and $\Delta\dot{T} = 0$, respectively. The red lines correspond to the trajectories evolution. This figure has been obtained from [95]

fixed point (see Fig. 3.9). For λ_l above the Hopf bifucartion, the fixed point becomes unstable and the systems enters into the SP regime. The trajectories starts to oscillates periodically at a frequency ν_{SP}. This dynamic is called a limit cycle in nonlinear physics. Although the trajectories are periodic, they oscillate in highly anharmonic way.

The SP dynamic is robust for a wide frequency range, being only deactivated when a second unstable fixed point is close enough to deflect the trajectory again to equilibrium (see Fig. 3.9).

In this thesis, the operational frequencies of SP ν_{SP} are found in the from tens of MHz to a few hundred MHz (1 to 0.01 μs) [101]. Several works reporting SP regimes at room temperature can be found in literature. For example, in Ref. [110], it is reported a slow SP with periodicity from hundreds of miliseconds to hundreds of seconds in Si Nitride microdisk. In fused silica microsphere, SP dynamics governed only by TO effect has been observed in Ref. [111]. Similar works to the SP dynamics explained in this sections can be found in Refs. [107, 112–114].

3.2.6 Non linear dynamics activated by self pulsing

The main consequence that the SP mechanism has on the OM cavity is the fact that its intracavity photon number will be modulated, following the dynamic of N and ΔT. Then, the radiation pressure force, that is related with n by $F_0 = \hbar g_{OM} n$, will be also modulated at the frequency of the SP, ν_{SP}. For convenience neglecting the Langevin force, the mechanical modes of the nanobeam can be described as damped linear harmonic oscillators driven by the anhamonic force:

$$m\ddot{x} + m\frac{\omega_m}{Q_m}\dot{x} + k_{eff}x = F_0 \tag{3.11}$$

where x is the generalized coordinate for the displacement of the mechanical mode and m, k_{eff} and ω_m are its effective mass, spring constant and eigenfrequency, respectively.

The dispersive effect that these nonlinear processes produce on the resonance position, including the mechanical motion is given by $\lambda_r \approx \lambda_0 - \frac{\partial \lambda_r}{\partial N}N + \frac{\partial \lambda_r}{\partial T}\Delta T + \frac{\lambda_0^2 g_{OM}}{2\pi c}x$. It worth noting that response of n to mechanical deformation is adiabatic since κ is few orders of magnitude smaller than ω_m.

The dynamics of the system is now described by the four variables $N, \Delta T, x, \dot{x}$. Eq. 3.11 with to the pair of equations in Eq. 3.10, form a four dimensional nonlinear system, being all linked through the intracavity photon number. The phase trajectories portraits becomes more complex. A detailed description of the phase trajectories can be found in Ref.[95].

The most significant feature that needs to be highlighted occurs when the frequency of the SP ν_{SP} equals one integer multiple of the the mechanical motion frequency, M$\nu_{SP} = \omega_m$. When this condition is satisfied, a self sustained mechanical motion state is achieved. The main properties of this state are that is of high amplitude and coherent, which together with the self sustained property, fulfills the requirements to be identified as a phonon lasing state [101].

In Fig. 3.10a, the RF spectra is presented in a 2D color plot as a function of the laser wavelength λ_l. The plot shows the system evolution from a simple transduction, that is shown in the graph for λ_l <1527 nm, to a chaotic regime (λ_l >1536 nm) passing through different lasing states and pure SP regimes. For the purpose of this thesis, we are particularly interested in the lasing state that correspond to the wavelength in yellow for λ_l= 1533.5 nm, where the system is found at a lasing state at $\nu_{SP} = \omega_m$ for ω_m= 54 MHz. This mode correspond to the third order flexural mode described in Fig. 3.8. From Fig. 3.10 it is observed that the lasing state is very robust, since once the system start to lase, it is frequency and phase locked for a large range in wavelength. The single wavelength RF spectra is shown in Fig. 3.10b. From this plot, the lasing state becomes evident since the linewidth of the main RF peak is a few kHz. Finally, for specific values of λ_l, the dynamics of the system becomes

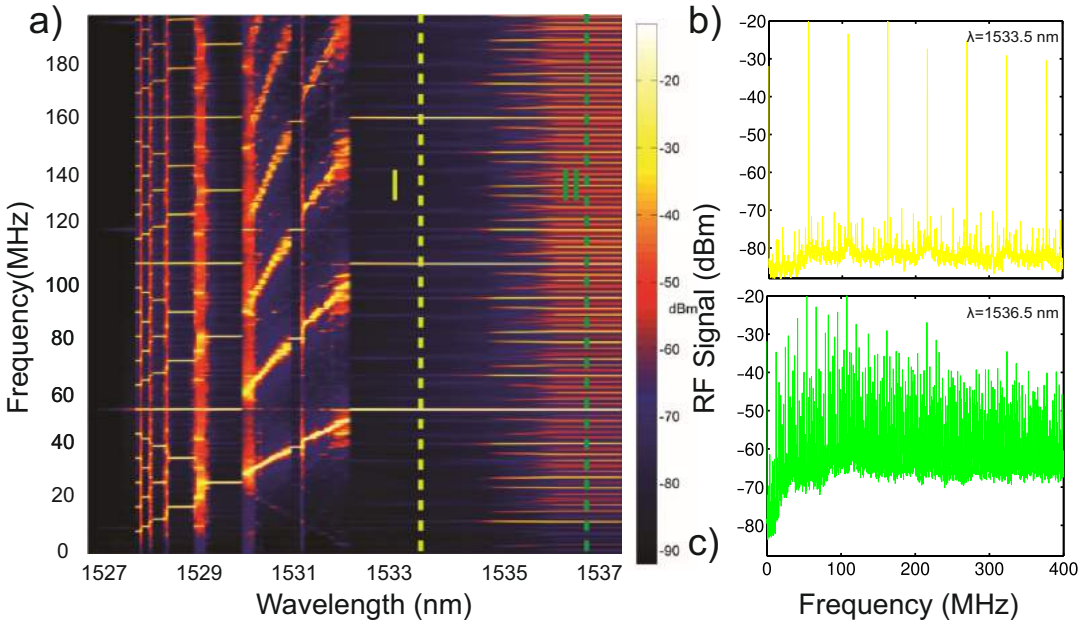

Figure 3.10: (a) Color contour plot of the RF spectra as a function of wavelength. The system evolves from pure transduction to chaos (green light) passing through mechanical lasing (yellow line). (b) RF spectra obtained for λ_l = 1534 nm. It correspond to a mechanical lasing state ($\nu_{SP} = \omega_m$). (c) RF spectra below at λ_l = 1537 nm. The systems evolves to a chaotic regime.

more complex, giving rise to a period doubling and finally a chaotic regime (see Fig. 3.10c). A detailed description on the complete dynamical evolution of the system is given in Ref. [101]

To conclude, the phonon lasing regime in an 1D OMC is the first challenge that needs to be tackle for the synchronization experiment treated in Chapter 6. In order to synchronized two mechanical resonator, the first requisite is that the system needs to be in a self sustained oscillation. This condition is satisfied by the phonon lasing state triggered by the SP.

Chapter 4

Spin waves and phonons in ferromagnets

In this chapter I will discuss about the main properties of magnetic ordered material and the resonant excitations that can be excited and measured on them. I will describe a particular technique for exciting and detecting magnons with microwave photons, the ferromagnetic resonance technique. Then, I will characterize the uniform magnetization precession of a YIG film that is used throughout this thesis. Finally, I will explain the interactions between the magnetic degrees of freedom with elastic deformations, showing the dispersion relations and the hybrid bands that emerge as a consequence of the mutual coupling.

4.1 Introduction

The history of magnetism goes back a long time. In 1800, Alessandro Volta discovered the electric battery as a voltage source [115], which was the beginning of a new era of acive investigations of galvanic processes. In 1820, Oesterd experimentally demostrated that the orientation of a needle was affected when a wire with circulating current was placed in proximity [116]. In 1865, James Clerck Maxwell presented a theory that unified electricity and magnetism in four basic equations [117]. From that moment, the understanding and control of electric and magnetic phenomena has supposed a technological revolution in the past 20th century. In 1947, John Bardeen, Walter Brattain and William Shockley invented the transistor, establishing the foundation of modern computer technology [118]. Ever since, the information processing technology has been accelerated and became crucial in the modern age. However, the size of transistor is approaching a physical limit. This has increased the fundamental problem of dissipation of charge currents due to Joule effect. Thus, new routes and concepts for information technology are vigorously investigated nowadays.

In parallel, at the beginning of 20^{th} century, since the Stern-Gerlach experiment, the spin property of electrons and nuclei started the investigation of spin related phenoma [119]. This field of physics had a huge impact in fundamental physics. It also brought relevant technological applications. For example, the nuclear magnetic resonance [120], which is an important imaging resource for medical diagnosis nowadays. The giant magnetoresistance (GMR) [121] effect is nowaday exploited by hard disk to read out data efficiently.

A novel approach to process data consists on exploiting the spin nature of materials rather than its charge. The control of pure spin currents, i.e., a directional wave of angular momentum, are predicted to be dissipationless [122]. The sources based on these principles could set the beginning of low power consumption technology, enabling the transition from electronics to spintronics [123], which is about coupling spin waves in condensed matter structures and devices. In recent years, new fields based on spin waves have emerged, namely, spin caloritronics [124, 125] and spin mechanics [126], which deal with the coupling and control of spin waves/magnons via temperature gradients and coherent vibrations in solids. Understanding the coupling of magnons to other fundamental quasi particles reveals to be crucial to develop new technological applications.

In the section below, I will present a brief introduction to the magnetic properties of materials.

4.2 Spin waves in ferromagnetic materials

Magnons are collective excitations of spin waves found in magnetically ordered materials. Ignoring some exceptions, all materials can be classified in two classes according to their magnetic properties: those that are formed by atoms having permanent magnetic moments and those that do not. Among the ones that contain permanent magnetic moments, we can differentiate between those that do not present large volumes where the magnetic dipoles are aligned parallel to each other and those that do present long range order. In this thesis we are dealing with the last group mentioned, which are called ferromagnetic materials.

Ferromagnets are materials in which, below a critical temperature, all their magnetic moments are spontaneously aligned parallel to each other. The permanent moments in ferromagnetic media are generally formed by local domains in absence of external magnetic field. The collective ordering of the electron spins creates a macroscopic magnetic moment, i.e., magnetization. In a given domain, the moments are aligned but the direction between different domains is considered to change significantly at the boundaries, as shown in Fig. 4.1a. Thus, it is possible to consider each individual domain as a single magnet of smaller volume. In equilibrium, the individual domains are oriented in a way that they try to minimize the magnetostatic energy,

so the net magnetization is minimal. When a magnetic field is applied, the domains begin to align with the external magnetic field giving a nonzero magnetization.

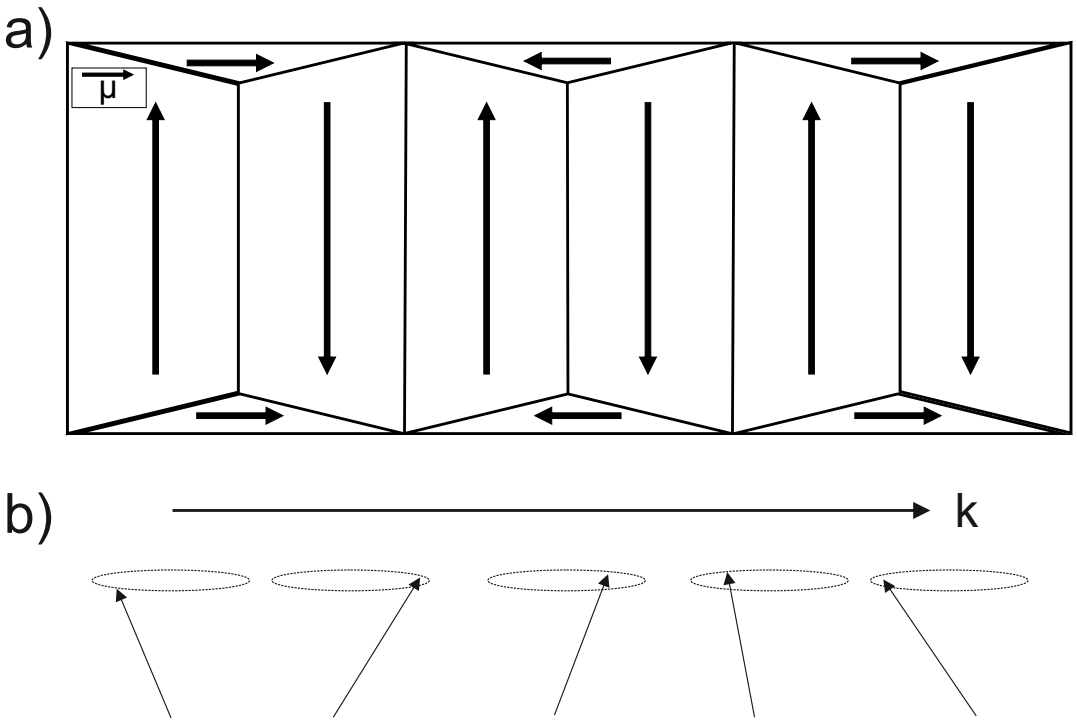

Figure 4.1: (a) Schematic representation of a ferromagnetic material. Each domain can be considered an individual magnet with large number of magnetic moments.(b) Spin wave schematic. The precession angle varies on individual domain in the direction of $\vec{k}$

Any disturbance in the local magnetic order propagates in the ferromagnet in form of a wave (see Fig. 4.1b), which are called magnons. They were first predicted by Bloch in 1930 [127]. Magnons present dispersion relation and can be treated in a similar way as lattices vibration, i.e., phonons [128]. Thermal fluctuations try to prevent the alignment of magnetic materials at nonzero temperature. Increasing temperature, the thermal fluctuations increase and the magnetic order becomes smaller and smaller until it vanishes. The temperature at which ferromagnetism dissapears is called Curie temperature. Above this temperature, the ferromagnetic material becomes paramagnetic.

An important aspect of magnonics is the magnetization control and manipulation for diverse spin waves applications. Therefore, it is important to control the magnetic degrees of freedom by coupling magnons with diverse quantized particles. Possible candidates to couple magnons are phonons via magnetoelastic effect. In this thesis we investigate this coupling following an inverse approach, using magnons to induce vibrations using the magnetoelasticity of materials, or magnetostriction [129]. This strategy of inducing vibrations in a ferromagnetic material has been used to resonantly couple

to the mechanical modes of an optomechanical cavity and detect magnetic fields.

4.3 Growth method of YIG films

Magnons exist over a broad frequency range, covering from hundreds of megahertz to terahertz frequencies. Their wavelength can be reduced to the micro and nanoscale, making them good candidates for information processing technologies [130]. Among the most important materials for microwave applications we found the magnetic garnets and ferrites. In particular, in this thesis, we have used films of single crystal yttrium iron garnet (YIG), $Y_3Fe_5O_{12}$. YIG has been extensively used for microwave devices, like delay lines, filters or high Q microwave oscillators. The only magnetic component of YIG comes from the Fe^{3+} ions. The lattice arrangement of these ions gives a net moment due one iron ion per formula unit. YIG presents very low magnetic damping, which allows the propagation of magnons over centimeters distances [131].

YIG also presents good properties for magneto-optical applications. It is transparent in the infrared, and it has a large Verdet constant, which characterizes the strength of Faraday effect. The main optical devices that employ YIG are Faraday rotators, isolators, and sensors [132, 133]. In recent years, there has emerged new hybrid systems that are both high Q magnon and photon cavities. Those systems offer the possibility of coupling magnons to photons with high efficiency [134, 135].

The sample used in this thesis consists on a commercial YIG film. The sample is a 1 μ m thick layer of single crystal YIG (see the Fig 4.2 a). The sample is grown by liquid phase epitaxy (LPE) on gadolinium gallium garnet substrate (GGG), $Gd_3Ga_5O_{12}$. LPE is a growth technique that produces high quality YIG films with the thickness ranging from a few microns to several microns. This technique is preferred with respect to other like molecular beam epitaxy (MBE), chemical vapor deposition (CVD) or pulsed laser deposition (PLD) because LPE growth rate is a factor of 10 to 100 times faster. However, PLD or MBE techniques are required to obtain layers with nanometer thickness, like the sample shown in Fig. 4.2c. A typical LPE growth equipement is shown in Fig. 4.2b, which is detailed in [136]. It consists on a vertical heat chamber, with several heaters, a motor to dip and rotate the substrate (GGG) on a crucible that contains the oxides. A detailed description of the chemical process can be found in reference [137].

4.4 Magnetization dynamics

I will employ a classical approach to describe the behavior of spins in ferromagnets. A common procedure is to replace the spins by the classical vector

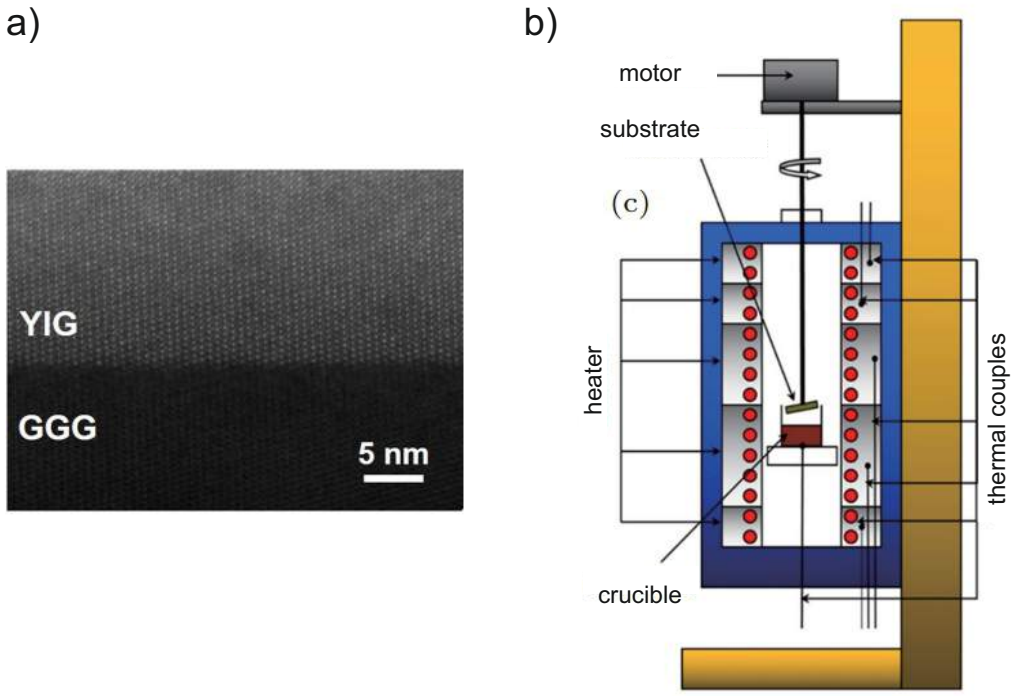

Figure 4.2: (a)Schematic of the YIG sample used in this thesis. Single crystal YIG is grown by LPE on a GGG substrate. (b) Representation of the LPE equipment for growing YIG. [136] (c) TEM image of a YIG film of 30 nm thick grown on a GGG substrate grown by PLD. [133]

of Magnetization, $\vec{M}$, that takes into account the collective spins of the individual magnetic domains. The time evolution of the magnetization by an effective magnetic field $\vec{H}$ is given by the torque applied on $\vec{M}$.

$$\frac{d\vec{M}}{dt} = -\gamma \vec{M} \times \vec{H} \tag{4.1}$$

where $\gamma = \frac{g\mu_B}{\hbar}$ is the gyromagnetic ratio, $\mu_B = \frac{e\hbar}{2m_e}$ is the Bohr magneton and g is the Landé factor. Note that the effective magnetic field $\vec{H}$ is the contribution of all fields that produce a torque on $\vec{M}$. The equation 4.1 describes a precession of magnetization that does not contemplate damping. Thus the magnetization vector would be precessing foreverer at a given frequency. Considering that in real experiments the magnetization precession decays in a finite time, we usually add phenomenologically a damping term, which modifies the magnetization dynamic as

$$\frac{d\vec{M}}{dt} = -\gamma \vec{M} \times \left(\vec{H} - \frac{\alpha}{\gamma M_s} \frac{d\vec{M}}{dt} \right) = -\gamma \vec{M} \times \vec{H} + \frac{\alpha}{M_s} \vec{M} \times \frac{d\vec{M}}{dt} \tag{4.2}$$

where we have introduced the term α. This term is a dimensionless damping constant. The term M_s is the saturation magnetization. This form of equation receives the name of Landau-Lifshiftz-Gilbert equation (LLG). The equation was first obtained by Gilbert [138], but it can be derived from a previous version suggested by Lifshiftz and Landau[139]. This damping term results from the transfer of energy from the magnon to the lattice vibrations. The coupling can be visualized in this way, the spin wave interaction depends on the distance between the spin location. Then, lattice vibration can modulate the interaction giving rise to the spin-lattice coupling [140].

4.4.1 Ferromagnetic resonance

A common technique to induce a coherent magnetization rotation is the ferromagnetic resonance (FMR). The magnetization precession at a frequency ω is excited by microwave photons via a transverse radiofrequency field $\vec{B}_{rf}$ in resonance with that frequency. The ferromagnetic sample measured in this thesis is a single cristal YIG layer with a saturation magnetization, $\vec{M}_S$, oriented along the $\hat{z}$ direction, as shown in Fig. 4.3. A static field B_{DC} is applied in the $\hat{z}$ direction and perpendicular to $\vec{B}_{rf}$, as shown in the left diagram in Fig. 4.3 ($\vec{B} = \mu\vec{H}$).

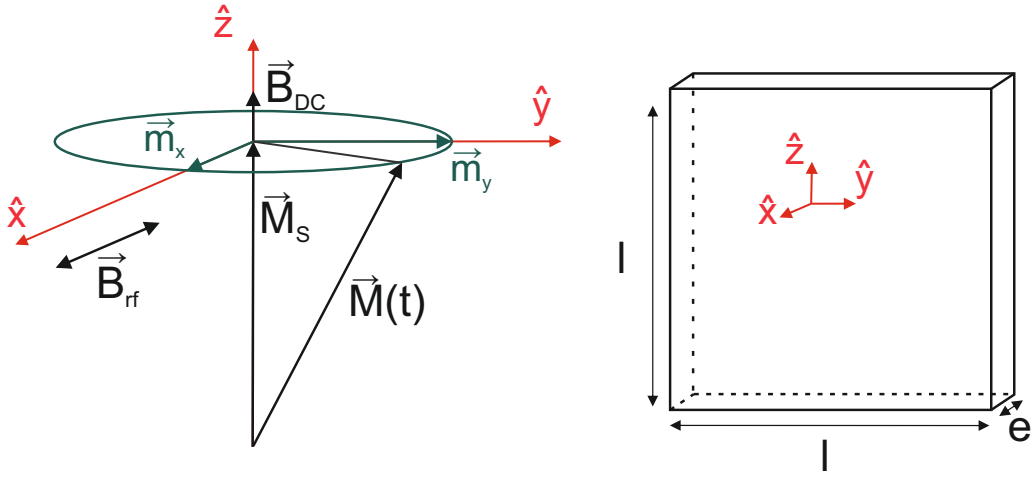

Figure 4.3: Left. Precession of $\vec{M}$ around the static magnetic field $\vec{B}_{DC}$. An external magnetic field $\vec{B}_{rf}$, pushes the magnetization and makes it to precess around $\vec{B}_{DC}$. Right. Geometry of the YIG film with dimensions $l = 5$ mm and thickness $e = 1$ μm

We define the effective field inside the YIG layer as the one that takes into account the static field, the demagnetization field and the rf field. The demagnetization is the field associated to the shape of the sample and is defined by the demagnetization factors N_x, N_y and N_z. Therefore, the effective field is defined by the following components: $\vec{B}$= (-N_x μ_0 m_x, -N_y μ_0 m_y , B_{DC}- N_z μ_0

m_z), with μ_0 defined as the vacuum magnetic permeability. For a configuration with the external field parallel to the plane of the film (see Fig. 4.3), we can consider $N_y = N_z = 0$ and $N_x = 4\pi\mu_0$ [141]. We simplify the problem by setting the time derivative of $\vec{M}(t)$ in the direction of $\vec{B}_{DC}$ equal to zero, such that $\vec{M}_z = M_s\hat{z}$. Thus, the magnetization rotation as a function of time is given by $\vec{M}(t) = \left(m_x(t), m_y(t), M_s\right)$. We consider also that the radio frequency field B_{rf} is an harmonic function, which allows to express the time evolution with a factor $e^{i\omega t}$, and assume the same for the magnetization components. Inserting the fields expression in Eq. 4.2, taking only linear terms in α and writing the equations in the frequency domain we get:

$$\begin{aligned} i\omega m_x &= \gamma B_{DC} m_y - i\omega\alpha m_y \\ i\omega m_y &= -\gamma\left[B_{DC} + 4\pi M_s\right] m_x - i\omega\alpha m_x \end{aligned} \tag{4.3}$$

The solution of Eq. 4.1 exists only if the determinant of the system of linear equations is zero, which gives the known Kittel equation:

$$\omega^2 = \gamma^2\left(B_{DC}\left(B_{DC} + 4\pi\mu_0 M_s\right)\right) \tag{4.4}$$

This equation gives the precessional frequency of the uniform magnon mode of the ferromagnet. FMR can be excited using an frequency dependent field B_{rf} . This happens when the sample is placed in a microwave field that is swept. When the resonance condition is achieved, $\omega_0 = \omega$, energy is absorbed and a dip appears in the reflected spectrum.

It can be demostrated that the linewidth of the resonance is proportional to the magnetic damping α (see for example page 101 of Ref. [140]). I will use FMR to characterized the YIG sample. Then, in Chapter 5, I will use this resonance phenomena to monitor the frequency of the uniform FMR mode.

4.5 Ferromagnetic resonance characterization of YIG films

In this section, I present the FMR characterization of a YIG film. The measurement is based on the coherent detection of the reflected power using a microwave coplanar waveguide. First, I will describe the measurement technique and, then, I will present the measurements results, showing the frequency dependence of the resonance position in the absorption spectrum. I will also show that the measurements agree well with the Kittel formula given by Eq. 4.4.

4.5.1 Experimental set up

We present here the set up used to measure FMR on YIG films. It is schematically shown in Fig. 4.4a. We measure the power reflected on a microwave coplanar strip waveguide (CSW). The waveguide is used to generate an alternate magnetic field B_{rf}. The YIG film that is charactized is placed on the waveguide. A parallel static magnetic field is applied by a dipole electromagnet (GMW 5403).

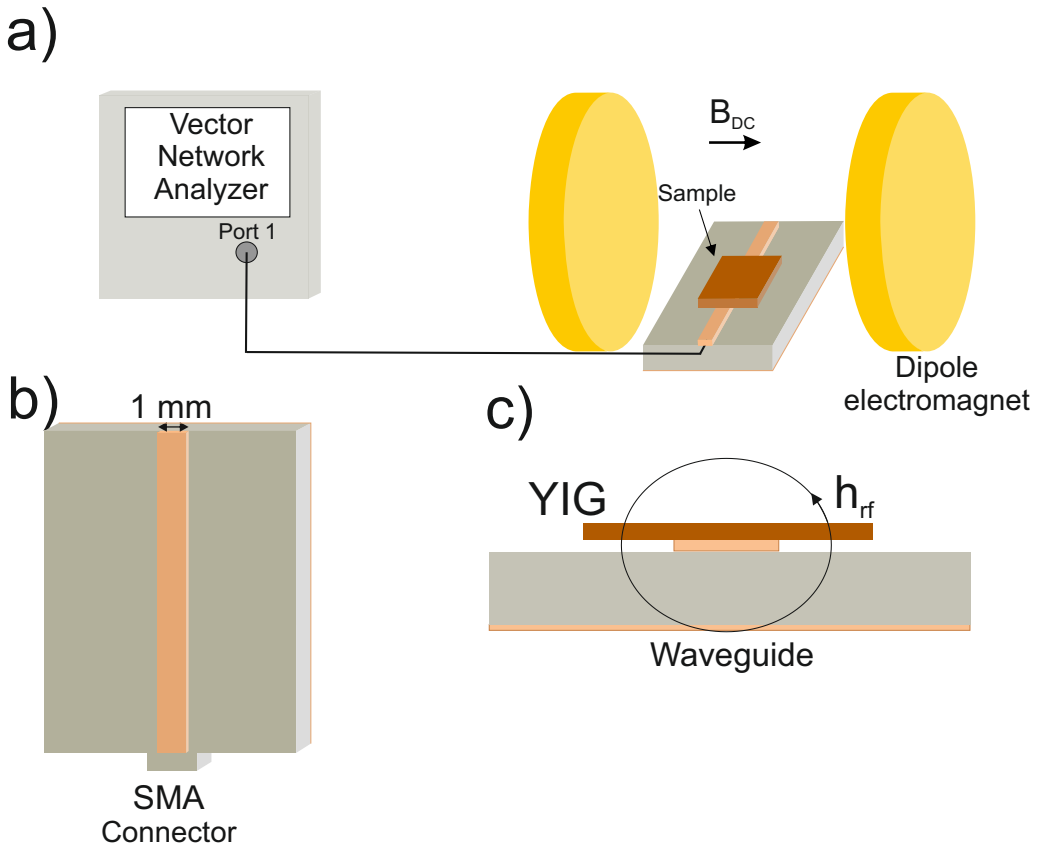

Figure 4.4: (a) Schematic of the FMR measurements. We use a VNA to drive a coplanar strip waveguide, that generates an rf field, B_{rf}. A dipole electromagnet is used to sweep the static magnetic field. (b) Top draw of the coplanar strip waveguide fabricated on copper. (c) Cross section of the YIG film deposited of the coplanar strip waveguide.

The microwave signals are generated by a Vetor Network Analyzer (VNA, *R&S* ZVA50) working in a frequency range from 10 MHz to 60 GHz. The reflected power from the waveguide is detected by measuring S_{11} on the VNA. The transmission line that sends the rf signal from the VNA to the waveguides is formed by the high frequency cables (*R&S* $\sim$ 50 GHz), the coplanar strip waveguide fabricated on a PCB board and a SMA connector (see FIg. 4.4b).

The coplanar strip waveguide consist on a copper stripline of 1 *mm* width and 3 *cm* large. It is shorted at its end in order to maximize the reflected

power. As it is shown in Fig. 4.4c, an oscillating magnetic field B_{rf} is generated by sending an alternating current through the waveguide. The magnitude of the magnetic field is given by the Biot-Savart law, $B_{rf}(\omega) = \frac{\mu_0 I(\omega)}{2\pi d}$, being μ_0 the magnetic susceptibility in vacuum and d the distance from the center of the wire. The field lines are circles around the stripline. To create a magnetic field of 3 μT at a distance of 1 μm of the stripline, one would need to apply a current of 0.015 mA. The high frequency currents applied through the transmission line will carry losses due to energy dissipation. In order to extract the magnetic field generated by the waveguide, we needed to calibrate the losses on the line (See Appendix A).

4.5.2 FMR results

In this subsection I present the FMR detection on YIG films. We use the technique described in the previous subsection, to generate the rf magnetic field created by the waveguide to excite the uniform magnetization precession on YIG, i.e, uniform magnon mode or FMR mode. All measurements described here were done at room temperature, and using a fixed microwave power 0 dBm.

Fig.4.5b and c shows the reflected power S_{11} as a function of frequency. The VNA sweeps the frequency excitation driving the microwave waveguide and collects back the power reflected. On Fig. 4.5b, a static field of 81 mT drives the uniform magnon mode at 4.06 GHz, the YIG absorbs energy from the microwave field and a dip is measured in the power reflected. In Fig. 4.5c we plot the absortion spectrum for different static fields. The resonance frequencies are found in the range of hundreds of MHz, and correspond to B_{DC} from 0 to 2.5 mT. We observe that the resonance linewidths at high frequencies are narrower than the one obtained for low magnetic fields.

In Fig. 4.5a, we show the position of the resonance for different applied statics field. The blue dots correspond to the experimental data and the solid black line is the curve fitted to the Kittel formula for the FMR mode, $\omega = \gamma\sqrt{B_{DC}\left(B_{DC} + 4\pi\mu_0 M_S\right)}$, that was derived in Section 4.4.1. The fit agrees well with the data and demonstrates that we are exciting the uniform magnon mode. From the fit, it is possible to obtain the saturation magnetization $\mu_0 M_S$= 0.17 $\pm$0.01 mT and the gyromagnetic ratio γ= 28 GHz/T for YIG. The values are consistent with the ones reported in literature (see Appendix A from Ref. [140]).

4.6 Magnon interaction with phonons

In this section we deal with the propagation of spin waves and phonons in ferromagnetic materials. In particular, we will describe the uniform magnon

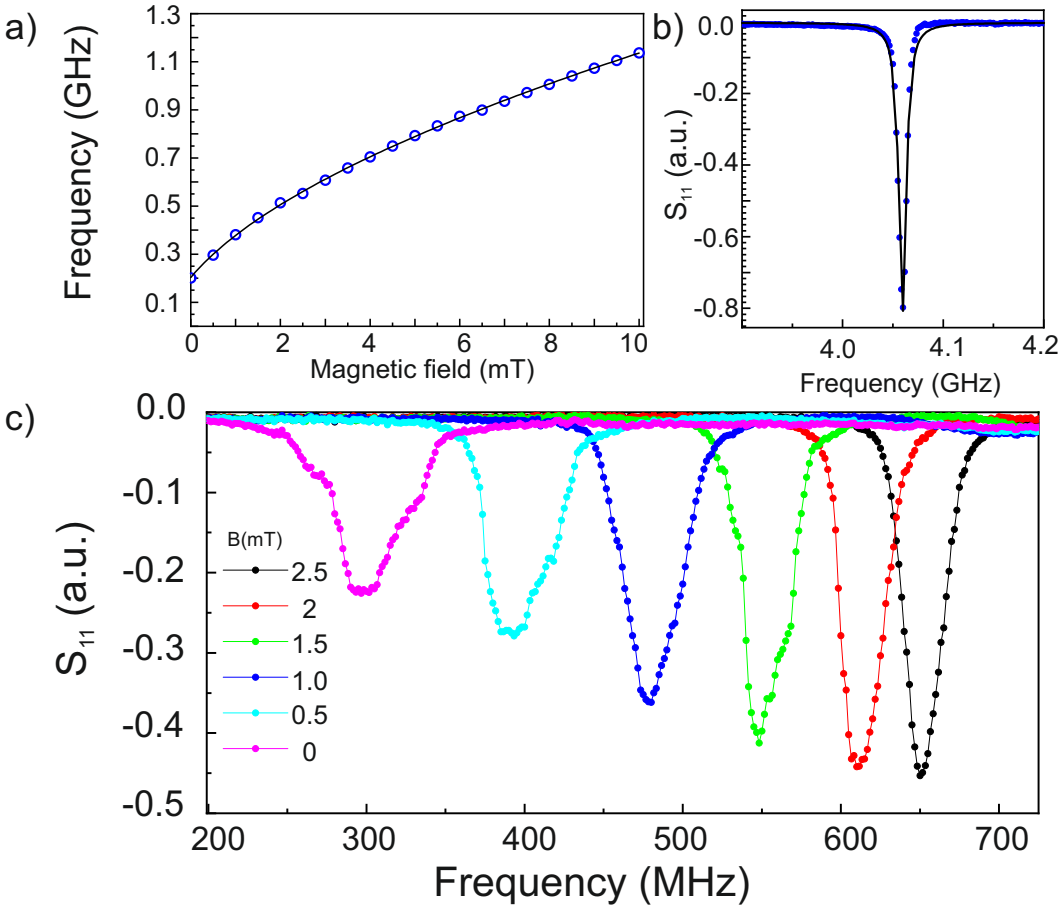

Figure 4.5: (a) The static magnetic field B_{DC} (in-plane) dependence of the FMR mode frequency. The frequency of the mode increases with B_{DC} following the Kittel law. The blue dots correspond with the data and the solid line correspond to the fitting curve to Eq. 4.4. (b) Measured S_{11} for a static magnetic field of 81 mT. The FMR mode is measured at 4 GHz. (c) For low magnetic fields, the FMR is measured in the MHz range.

modes found for YIG. First, I will derive the wave equations and the band diagrams. I will also show how the magnon bands are flat in the large k-limit. Then, we will describe the phonon bands in YIG films and how they cross with the magnon bands.

4.6.1 Spin waves equations in YIG.

In this subsection, I describe the propagation of magnons in YIG considering the time and space dependence of fields like $e^{i\vec{k}\cdot\vec{r}-i\omega t}$, with $\vec{k}$ being the vector in the propagation direction. This allows us to rewrite the Maxwell equations replacing the time derivatives with the factor $-i\omega$. The action of ∇ operator on $i\vec{k}$ can be written in the following way,

$$\nabla e^{i\vec{k}\cdot\vec{r}} = \left[\vec{x}ik_x + \vec{y}ik_y + \vec{z}ik_z\right] e^{i\vec{k}\cdot\vec{r}} = i\vec{k}e^{i\vec{k}\cdot\vec{r}} \tag{4.5}$$

Then the Maxwell equations can be written as follow:

$$\begin{aligned} \vec{k}\times\vec{H} &= -\omega\epsilon\vec{E} \\ \vec{k}\times\vec{E} &= \omega\mu_0\left(\vec{H}+\vec{M}\right) \end{aligned} \tag{4.6}$$

Taking the cross product at both sides on the first equation and substituting $\vec{k}\times\vec{E}$ gives

$$\vec{k}\vec{k}\cdot\vec{H} - k^2\vec{H} = -\omega^2\mu_0\epsilon\left(\vec{H}+\vec{M}\right) \tag{4.7}$$

where we have used the identity $\vec{k}\times\vec{H} = \bar{k}\cdot\vec{H}$, being $\bar{k}$ the antisymmetric matrix given by $\bar{k} \equiv k\times\bar{I}$, and being $\bar{I}$ the identity matrix. The term $\vec{k}\vec{k}$ is defined as the dyadic product that satisfy the identity, $\vec{k}\vec{k} = \bar{k}\cdot\bar{k} + k^2\bar{I}$. We have also used $\vec{k}\cdot\vec{B} = \mu_0\vec{k}\cdot\left(\vec{H}+\vec{M}\right) = 0$, that allows to get $\vec{k}\cdot\vec{H} = -\vec{k}\cdot\vec{M}$. Then, it is possible to solve $\vec{H}$, giving

$$\vec{H} = \frac{k_0^2\vec{M} - \vec{k}\vec{k}\cdot\vec{M}}{k^2 - k_0^2} \tag{4.8}$$

being $k_0^2 = \omega^2\mu_0\epsilon$. A similar procedure can be followed to obtain $\vec{E}$ in terms of $\vec{M}$, that is given by

$$\vec{E} = \frac{\omega\mu_0\vec{k}\times\vec{m}}{k^2 - k_0^2} \tag{4.9}$$

Finally, using the maxwell equation $\nabla\times\vec{H} = -\omega\epsilon\vec{E}$ we get

$$\nabla\times\vec{H} = -\frac{k_0^2\vec{k}\times\vec{m}}{k^2 - k_0^2} \tag{4.10}$$

Note that in the limit for large k, Eq. 4.9 and Eq. 4.10 vanish as k^{-1} while Eq. 4.8 is finite since both the numerator and denominator depend on k^2. Thus, it is possible to approximate in first terms the following

$$\begin{aligned} \nabla\times\vec{H} &= 0 \\ \nabla\cdot\vec{B} &= 0 \end{aligned} \tag{4.11}$$

These equations are known as magneto-quasiestatic approximation and describe waves in the large k limit [140]. The fields can be determined considering the constitutive relations for a magnetized ferrite, $\vec{B} = \bar{\mu} \cdot \vec{H}$, with $\bar{\mu} = \mu_0 (\bar{I} + \bar{\chi})$, the permeability tensor which for a isotropic material, in absence of exchange and considering the static field is applied in the $\hat{z}$ direction $\vec{H} = H_{DC}\hat{z}$, can be written as

$$\bar{\mu} = \mu_0 \begin{bmatrix} 1+\chi & -i\kappa & 0 \\ -i\kappa & 1+\chi & 0 \\ 0 & i\kappa & 1 \end{bmatrix} \tag{4.12}$$

where $\chi = \frac{\omega_0 \omega_M}{\omega_0^2 - \omega^2}$, $\kappa = \frac{\omega \omega_M}{\omega_0^2 - \omega^2}$, with $\omega_M = -\gamma \mu_0 M_S$ and $\omega_0 = \gamma \mu_0 H_{DC}$. We can write $\vec{H} = -\nabla \phi$ using $\nabla \times (\nabla \phi)$, being ϕ a scalar function. Introducing this expression in Eq. 4.11, we get

$$\nabla \cdot (\bar{\mu} \cdot \nabla \phi) = 0 \tag{4.13}$$

The solutions of Eq. 4.13 can be obtained assuming a plane wave approximation for $\phi \sim e^{i\vec{k}\cdot\vec{r}}$. Using Eq. 4.5, the plane wave propagation becomes $(1+\chi)\left(k_x^2 + k_y^2\right) + k_z^2 = 0$. Considering an arbitrary direction parametrized by the angle β with respect to the $\hat{z}$ direction, we get $k_x^2 + k_y^2 = k^2 sin^2\beta$ and $k_z^2 = k^2 cos^2\beta$. Substituting these equations in Eq. 4.13, we get

$$\chi sin^2\beta = -1 \tag{4.14}$$

which in terms of frequency gives

$$\omega_k = \left[\omega_0 \left(\omega_0 + \omega_M sin^2\beta\right)\right]^{1/2} \tag{4.15}$$

This equation is the Kittel equation obtained in Eq. 4.4. We note that the dispersion relation is independent of k. The band for this mode is flat for all values of k, in the large k limit. For $\beta = 0$, the dispersion relation correspond to the propagation parallel to the B_{DC} and for $\beta = \pi/2$, correspond to propagation perpendicular to the static field. In Fig. 4.6, we present the two bands of uniform magnetization precession in a YIG film for the two configurations. The value of static magnetic field used was B_{DC} = 0.1 mT. We note that the magnetostatic approximation is not valid when the exchange effects or finite sample effects are considered. The exchange term becomes relevant when $\lambda_{ex} k^2 \sim 1$, being λ_{ex} the exchange constant and with a value of $\lambda_{ex} = 3 \times 10^{-16} m^2$ for YIG [141]. When $k^2 \lambda_{ex} \ll 1$, the excitations are called dipole waves or magnetostatic waves.

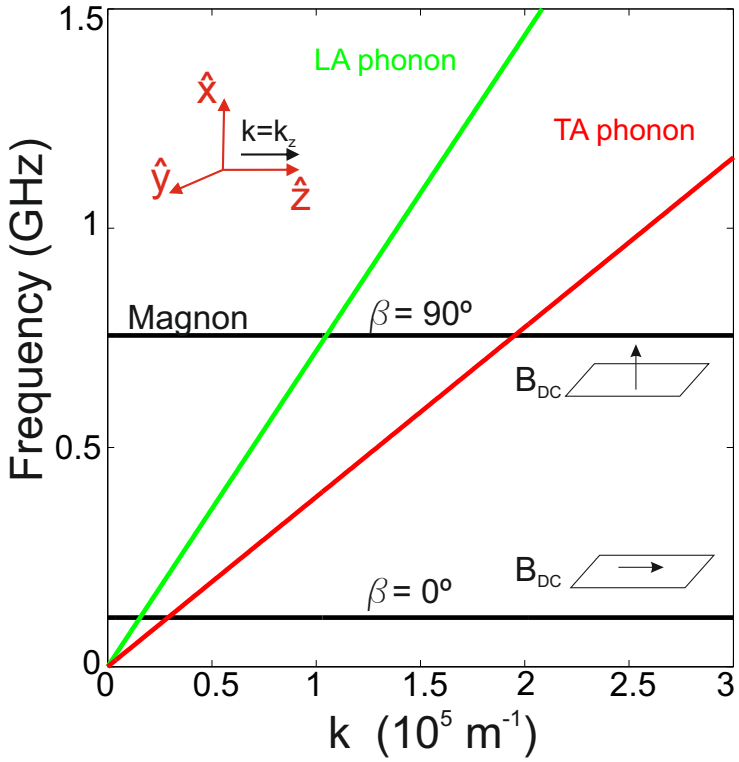

Figure 4.6: Dispersion relation for magnons (black lines) in YIG calculated using Eq. 4.15. The band for β =0 correspond to the propagation parallel to B_{DC} and for $\beta = \pi/2$, for propagation perpendicular to B_{DC}= 0.1 mT. Acoustic phonon bands for YIG. The green curve correspond to longitudinal phonon calculated using Eq. 4.17. The red line correspond to transverse phonon calculated using Eq. 4.18.

4.6.2 Elastic wave equations

The quanta of lattice vibrations are described in a continuum approximation by the displacement function u(x,y,z,t). In the long wavelength limit, the equation of motion for the elastic displacement is given by [141]

$$\rho\ddot{u} = (\lambda + 2\mu)\,\nabla\,(\nabla \cdot u) - \mu\nabla \times \nabla \times u \tag{4.16}$$

where ρ is the density, μ and λ are the Lamé coefficient that are characteristic of the material. The equation of motion solution considering a plane wave approximation for the displacement field, is defined by two dispersion relations. For displacement parallel to the propagation direction we get the longitudinal band

$$\omega = \sqrt{\frac{2\mu + \lambda}{\rho}}k = v_L k \tag{4.17}$$

being v_L the longitudinal propagation velocity, which has the value of $v_L = 7.2 \cdot 10^3 m/s$ for YIG [142]. For transverse waves

$$\omega = \sqrt{\frac{\mu}{\rho}} k = v_T k \tag{4.18}$$

being v_T the transverse velocity with a corresponding value of $v_T = 3.84 \cdot 10^3 m/s$ for YIG. Both dispersion relations are linear with ω. In Fig. 4.6 we show the two bands for phonons in YIG propagating in the [100] direction.

4.6.3 Magnetoelastic coupling

The coupling between spin waves and acoustic waves in ferromagnets is described in this subsection. Magnetic interaction depends on the distance between the interacting particles. This fact suggests the possibility of resonantly couple magnons with the lattice vibration when the frequencies of both are similar [143]. The effect that causes a ferromagnetic material to change its shape upon a magnetization is the magnetostriction. Mechanical deformations are introduced in the equations of magnetization dynamics and vice versa, the elastic degrees of freedom are affected by a modification in the magnetic properties of the system. A mechanistic approach of magnetostriction arises from the strain dependence on the magnetocristalline free energy density F [144]. It is described by the contribution of several components: magnetocrystalline anisotropy F_k, elastic F_e, Zeeman F_Z and exchange energy F_{ex}

$$F = F_k + F_e + F_Z + F_{ex} \tag{4.19}$$

The magnetoelastic energy, F_{me}, is obtained by a Taylor expansion of the magnetocrystalline anisotropy energy, giving

$$F_K\left(m, \epsilon_{ij}\right) = F_a + F_{me}\left(m, \epsilon_{ij}\right) \tag{4.20}$$

where F_a is the anisotropy energy and represents the energy required to flip magnetization between different crystalline axes. For a cubic symmetry it can be expressed as

$$F_a = K_1\left(m_x^2 m_y^2 + m_y^2 m_z^2 + m_z^2 m_x^2\right) \tag{4.21}$$

where K_1 is the anisotropy constant, m is a unit vector along the direction of the magnetization M. For YIG, the anisotropy constant is K_1= -610 J/m^3 [140]. The magnetoelastic interaction is given by

$$F_{me}\left(m, \epsilon_{ij}\right) = \sum_{ij} \sum_{\nu\mu} \left(b_{ij}\right)_{\mu\nu} m_\mu m_\nu \epsilon_{ij} \tag{4.22}$$

where $(b_{ij})_{\mu\nu}$ is the tensor of magnetoelastic interaction constants and ϵ_{ij} is the elastic strain tensor. For a cubic crystal, which is the case of YIG, we have $B_1 = b_{1111} = B_2 = b_{2323}$. The reported value B_2 for YIG is $7.3\ 10 \cdot 10^{-5} J/m^3$ [142]
The low order term of the elastic interaction energy has the form of

$$F_e = \frac{1}{2}\sum_{ijkl}\sum_{\nu\mu} c_{ijkl}\epsilon_{ij}\epsilon_{kl} \tag{4.23}$$

The Zeeman energy is given by

$$F_Z = -M_s\left(\vec{m}\cdot\vec{H}\right) \tag{4.24}$$

The final coupled equations of motion for the magnetization and the elastic displacement are given by

$$\begin{aligned} \dot{m}_i &= \frac{\gamma}{M_s}\left(\vec{m}\times\vec{m}\nabla_m F\right) \\ \rho\ddot{u}_i &= \frac{\partial}{\partial x_k}\frac{\partial F}{\partial \epsilon_{ik}} \end{aligned} \tag{4.25}$$

where $\epsilon_{ij} = \frac{\partial}{\partial x_i}u_j + \frac{\partial}{\partial x_j}u_i$ and $\epsilon_{ii} = \frac{\partial}{\partial x_i}u_i$. In these equations it is straightfoward to check that in the solution for longitudinal elastic waves there is no coupling to magnetization (there are no crossing terms multiplied). From now on we consider only transverse phonon in the coupling to magnetization.

We consider elastic waves linearly polarized propagating perpendicular to the static field $\vec{B}_{DC} = B_{DC}\hat{z}$. For simplicity, we neglect exchange term and assume that $\vec{B}_{rf} = B\hat{y}$ with an $e^{i\omega t}$ dependence. Then, the nonvanishing terms of Eq. 4.25, for propagation in the $\hat{x}$ direction, are given by the following equations

$$\begin{aligned} i\omega\dot{m}_x &= -\gamma\left(B_{dc}m_y - M_s B_{rf}\right) \\ i\omega\dot{m}_y &= -\gamma\left(B_{dc}m_x + B_2\frac{\partial}{\partial x}u_z\right) \\ -\rho\omega^2 u_z &= \mu\frac{\partial^2}{\partial x^2}u_z + \frac{B_2}{M_s}\frac{\partial}{\partial x}m_x \end{aligned} \tag{4.26}$$

The time dependent magnetization, $m_x(t)$, can be decomposed into a spatially dependent $m_x(x)$ part and a uniform part, m_{0x}. Combing the first two equations from Eq. 4.26, regrouping and solving for m_x we obtain

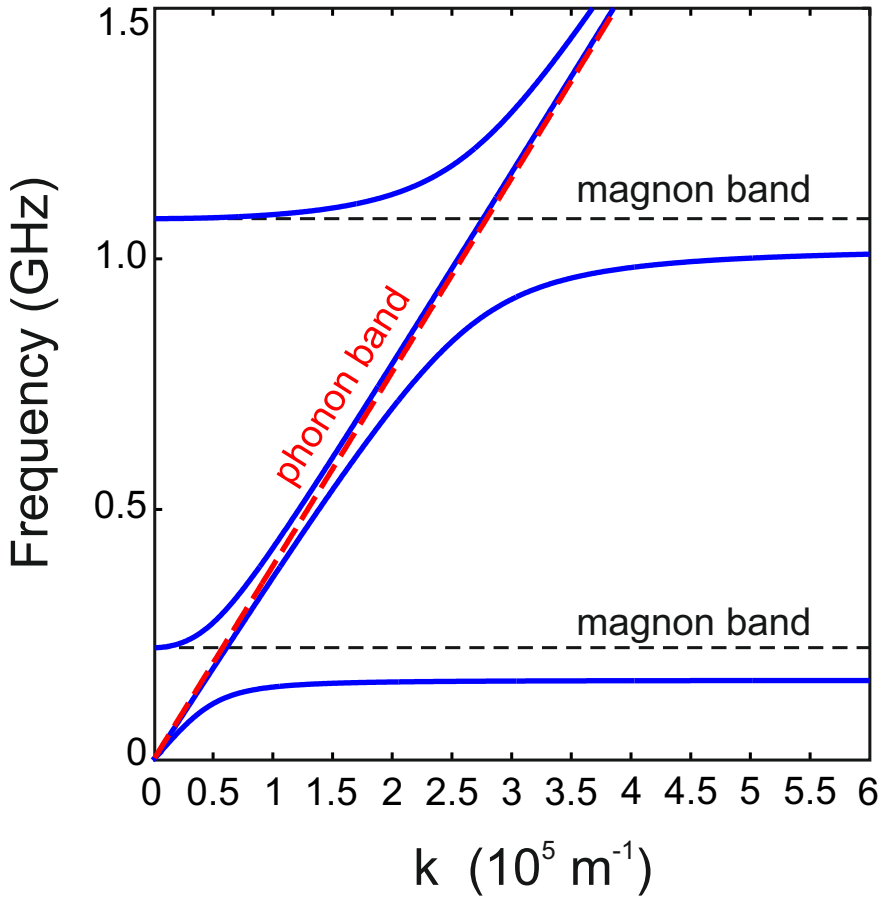

Figure 4.7: Magnetoelastic bands(blue curves) resulting from the coupling of uniform magnon modes (black curve) and a transverse elastic wave (straight line covered by the blue curves). The antricrossing region plotted was obtained for a $B_{DC} = 8$ mT

$$m_x = m_{0x} + m_x(x) = -\frac{i\omega_M \omega B_{rf}}{4\pi\left(\omega^2 - \omega_H^2\right)} + \frac{\omega_k \gamma B_2}{\left(\omega^2 - \omega_k^2\right)} \frac{\partial}{\partial x} u_z \tag{4.27}$$

where ω_k is the magnon frequency obtained in Eq. 4.15. Once obtained the the spatially dependent magnetization term, we can get the partial derivative of magnetization $\frac{\partial}{\partial x} m_x$ in the last equation of Eq. 4.26, getting

$$-\rho\omega^2 u_z = \left(\mu + \frac{\gamma B_2^2 \omega_k}{M_s\left(\omega^2 - \omega_k^2\right)}\right) \frac{d^2 u_z}{dx^2} \tag{4.28}$$

taking the plane wave approximation, $u_z \sim e^{-ikx}$ we get the dispersion relation, which is given by

$$\left(\omega^2 - \omega_k^2\right)\left(v^2 k^2 - \omega^2\right) + \frac{\gamma B_2^2}{\rho} \omega_k k^2 = 0 \tag{4.29}$$

The dispersion band with the corresponding uncoupled band is shown in Fig. 4.7. We observe that the coupling at the crossing point for the band at $\beta = \pi/2$ is smaller than the coupling with the magnon band at $\beta = 0$.

Chapter 5

Resonant magnon optomechanical magnetometer

5.1 Introduction

The ability to measure low amplitude and broadband frequency range magnetic fields has revealed to be crucial for nanoscale magnetic applications and plays an important role in many areas such as geology, space exploration, biology and medical imaging [43, 145]. Ultra senstive magnetic field sensors, i.e. magnetometers, are based on multiple different physical phenomena, including quantum intereference in superconductors [46], the Hall effect [146], the electron spin resonance [147], magnetostriction [148], optical pump [47], among others [149, 150]. Currently, the superconducting quantum interference device (SQUID) magnetometers, are used for the most demanding applications [44, 151, 152], since they reach femto tesla sensitivities. For example, SQUID magnetometry is used for measuring the residual magnetization of ancient rocks, which brings useful geological information like establishing the distributions of continents, providing critical proofs to the theory of plate tectonics [153]. Although they achieve excellent sensitivities, SQUID based magnetometers present the disadvantage of being restricted to operate at cryogenic temperature. The recent development of atomic magnetometers has offered the possibility of reaching subfemto tesla sensitivities in noncryiogenic environments, opening new possibilities for ultra low field magnetometry. For example, the magnetometer using the spin exchange relaxation free (SERF) technique has reported a sensitivity of 160 aT Hz $^{-1/2}$ at 40 Hz [47], operating at room temperature.

In terms of dimensions, combined with high sensitivity, a small sensor is important for many applications. For example, magnetic resonance force microscopy can detect the single magnetic dipole moments. Then, it is crucial to reduce the distance between the sample and the sensor [154]. In medical applications, imaging of the magnetic fields generated by small organs, demand sensors with small sizes and high sensitivity. For instance, neurons in

the brain generate fields in the order of tens of fT [43] and magneto cardiography relies on the detection of pT fields [155]. Therefore, an array of multiple small and highly sensitive magnetometers could be the ideal platform to map magnetic fields of organs.

In the last decade, optomechanical magnetometers have emerged as a new platform for measuring magnetic fields with high sensitivity at room temperature [48–50, 156]. Their key point is to exploit the highly developed fabrication techniques of cavities with high optical and mechanical quality factors. Optomechanical cavities support low–volume resonant optical modes that are coupled to the mechanical degrees of freedom of the device through the optomechanical interaction. This enables ultra sensitive optical transduction of mechanical motion, allowing, for instance, the possibility to resolve the position of a mechanical resonator close to the Heisenberg uncertainty limit [35]. The operation principle of optomechanical magnetometers are founded on the deformations that mechanical objects suffers under the influence of an applied magnetic field. The response of the material to magnetic fields modifies the mechanical structure of the cavity and this causes a shift of the optical resonance. This modulation can be read out giving a measurement of the applied field. Previous works based on this principle consisted on using Terfenol-D as the magnetostrictive material deposited on a microtoroidal optomechanical cavity (see Fig. 5.1).

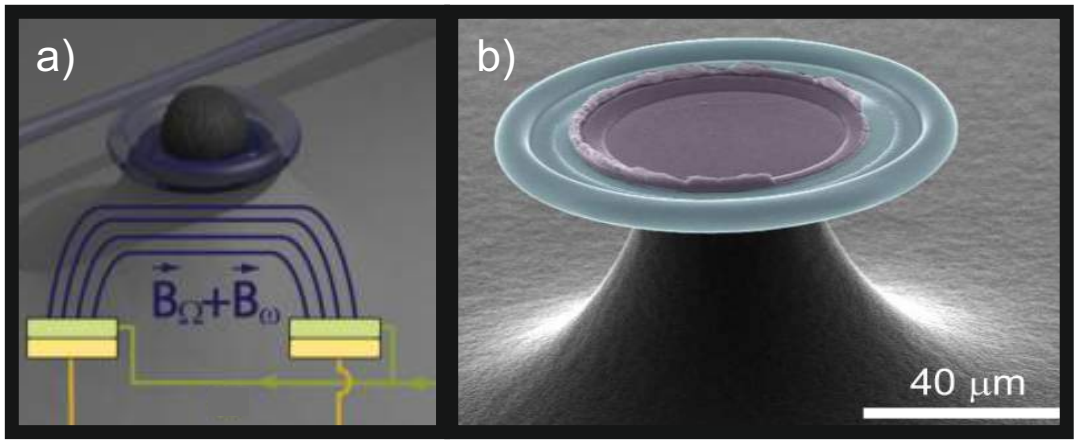

Figure 5.1: Optomechanical magnetometer. (a) Silica microtoroidal optomechanical cavity with major and minor diameters of 60 μm and 4 μm, respectively on which it is deposited a Terfenol-D grain. The graph is obtained from [48]. (b) An improved fabricated magnetometer where the Terfenol-D has been sputtered. The image is obtained from [156].

Optomechanical magnetometers offer state of the art magnetic field sensitivity, room temperature operation and excellent micro and nano integration. They require low optical power consumption and present a bandwidth of hundreds of kilohertz. This chapter presents our approach to exploit optomechanics for magnetometry. It combines the use of glass microspheres with high quality factor optical and mechanical modes with thin films of YIG

with narrow FMR. The basic transduction principle involves the conversion of an RF magnetic field, that resonantly excites magnons, into mechanical vibrations in the YIG film via magnetostriction. As it is treated in Chapter 4, at microwave frequencies, magnons excited on YIG are coupled to transverse mechanical modes on the film. The mechanical vibration of the film resonantly excites the mechanical breathing modes of the sphere and a response above the thermal noise is obtained in the spectrum. By using an external DC magnetic field, we tune the frequency of the magnon and extend the response range of the magnetometer by driving mechanical modes at different frequencies.

The chapter structure is organized in this way: first, it is presented the magnetometer concept in correspondence to the Fabry Perot scheme presented in Chapter 2. Then, it is described the measurement noise treatment to calculate the magnetometer sensitivity. The following this section shows an optomechanical characterization of the microspheres. In order to confirm the vibrations induced on the YIG film we use a Laser Doppler Vibrometer to measure the YIG vibrations, which is described afterwards. Finally the magnetometer principle is shown and the sensitivity is calculated.

5.2 Fabry Perot cavity

The success of cavity optomechanics relies on the development of optical microcavities with high quality factors and the advances of mechanical microresonators. The performance of an optomechanical system is described by the efficiency to couple light to mechanical degrees of freedom. The fundamentals of cavity optomechanics have been briefly discussed in Chapter 2. Here we use a particular type of optomechanical system, the whispering gallery mode resonator. Like in most of optomechanical cavities, light is coupled to the cavity by frequency match between the fundamental mode of a tapered fiber and optical mode of the resonator. When the fiber is placed in the near field of the optical resonator, light is coupled from one to the other. A scheme of the light coupling mechanism is shown by Fig 5.2. Once light is coupled to the cavity, it remains confined in terms of total internal reflections and is characterized by a quality factor. Inside the cavity, light interacts with mechanical modes and is collected back by the fiber following the same mechanism. A more detailed descriptions of the whispering gallery modes cavities can be found in Chapter 3.

A schematic picture of the optomechanical magnetometer principle is shown in Fig. 5.2.a The sensor can be modeled as a Fabry Perot optical interferometer in which one of the mirrors is attached to a spring and responds mechanically to an applied magnetic field. Typically, in a realistic system this response is due to magnetostriction that originates in the ferromagnetic material, i.e, the generation of an oscillating stress when an alternate magnetic field is applied. This stress acts as a source force for mechanical motion of the mirror, greatly amplified when the initial drive is resonant with

a mechanical eigenfrequency. The two main forces actuating the mechanical modes are thus the thermal Langevin force F_{th} and the one associated with the RF magnetic field, F_{mag}. It is worth noting that the optical forces are neglected and are only exploited to transduced the mechanical oscillations. These forces cause a variation of the cavity length, shifting the optical resonance by $\delta\omega_{optical} = g_{OM}x$, where g_{OM} is the optomechanical coupling rate, defined as the optical frequency shift by a unit mechanical displacement.

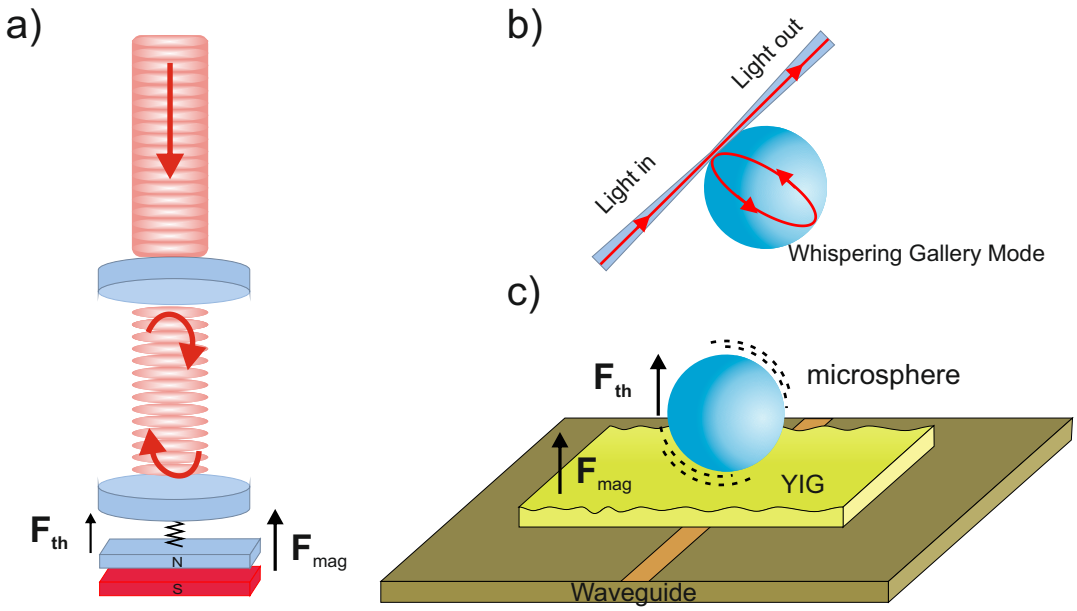

Figure 5.2: (a) Conceptual schematic of the cavity optomechanical magnetometer. The optomechanical magnetometer is presented as a Fabry Perot cavity with one of the mirror attached to a spring. The motion of the spring by the fact of having a temperature will exert a thermal forced on the spring F_{th}. The novelty of the model is that we incorporate an extra force that is coming associated to the magnetic field, F_{mag}. (b) Coupling light scheme between the tapered fiber and the BTS microsphere. (c) Schematic figure of the real system. The microsphere is placed on YIG films, which is at the same time on a coplanar waveguide.

An illustration of the main part of the real hybrid system is shown in Fig. 5.2c. It consists of a 0.5 $\times$ 0.5 mm^2 and 1 μm thick film of YIG grown over a Gadolinium Garnet substrate. The YIG film is the one that was characterized in Chapter 4. Glass microspheres of BTS with a diameter between 40 μm and 70 μm were deposited on the YIG thin film. These microspheres are used as high quality OM cavities supporting both optical WGM and mechanical breathing modes with large g_{OM} values[77, 157].

5.3 Stress induced magnetostriction

Optomechanical magnetometers are based on the use of magnetostrictive materials, i.e., the stress that is induced in a material when a magnetic field is applied. The magnetostrictive material selected in the experiment is a single crystal YIG thin film. Generally, the stress is described by the magnetostrictive tensor, $\hat{T}(\vec{r})$, which is defined as the force per unit of area [158]. For simplicity, in this thesis we consider only an homogeneous and unidirectional stress along the x direction. These simplifications gives only a single nonzero component of stress and allows to relate the magnetic field with the stress in the following way

$$T_{xx} = \lambda_M B \tag{5.1}$$

being λ_M the magnetostrictive coeficcient that is characteristic of each magnetostrictive material. The first experiments on optomechanical magnetometers exploited the fact of using the highest magnetostrictive material available commercially. The material selected was Terfenol D since it is an alloy of iron, dysprosium and terbium and was characterized by the largest magnetostrictive coefficient known with a value of $\lambda_M = 5 \cdot 10^8 \frac{N}{Tm^{-2}}$ [159]. Despite YIG is less magnetostrictive than Terfenol D, with a value of $\lambda_M = 3.8 \cdot 10^7 \frac{N}{Tm^2}$ [160], it presents a very low damping parameter (see Chapter 4). This allows the excitation of magnons that can propagate long distances on the sample. It also grant to measure ferromagnetic resonance at room temperature. This will help to excite different mechanical modes by magnetostriction.

For what concerns to the experiment of this Chapter, we can consider that on the surface of the YIG layer, an effective force will drive the mechanical modes of the optomechanical resonator placed on top. The origin of this force is the mentioned magnetostriction of the YIG layer.

5.4 Magnetometer mechanical response

The performance of the optomechanical magnetometer described in this thesis relies on how efficient is the magnetic signal to drive the mechanical modes of the mechanical resonator. In this experiment the optomechanical oscillator used were glass microspheres of Barium-Titanium-Silicate (BTS) deposited on the YIG layer.

According to the equipartition theorem, each mechanical degree of freedom of the microsphere is defined by a mean energy of $k_B T/2$ (with k_B is the Boltzmann constant and T the temperature). As it was treated in Chapter 2, this energy excites incoherent motion of the resonator close to the mechanical modes. The mechanical modes detected on optical signal will be the one with sufficiently high optomechanical coupling g_{OM}, this is, the mechanical modes that are able to couple with the optical WGM of the microsphere. The

mechanical eigenmodes can be obtained from a model microsphere with a Finite-Element-Method (FEM) simulation.

We use the solid mechanics package of the software COMSOL Multiphysics to obtain the eigenmodes of a microsphere with BTS elastic constants and a dimension similar to the one used in the real experiment. Several modes are found ranging from hundreds of MHz to the GHz. The fundamental mechanical breathing mode for a sphere of R =30 μm radius is shown in Fig. 5.3.

The magnetic field detection efficiency also depends on the competition between the signal response to magnetic field, with the particular noise associated to the experiment. The first source of noise is intrinsic of the material, and is related with the fact that the mechanical resonator is at a finite temperature, and therefore is thermally excited. The second source of noise are the one that are given by the measurement, like the shot noise from the laser.

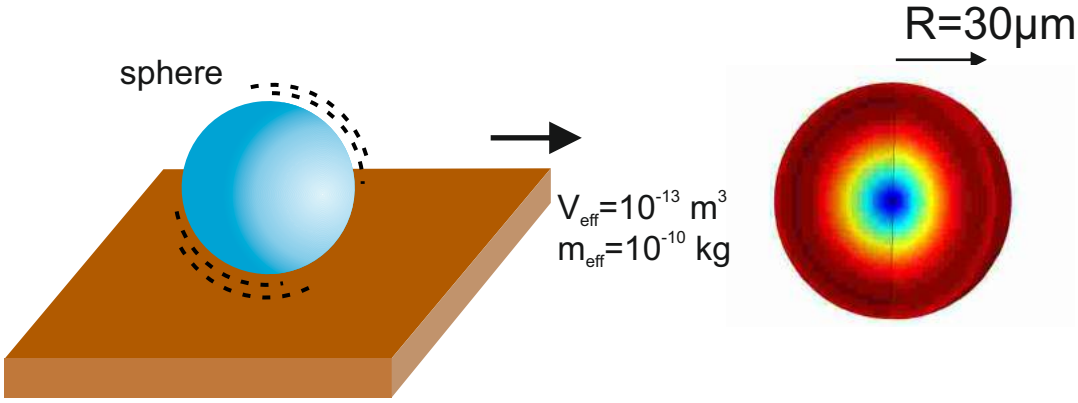

Figure 5.3: Conceptual schematic of the YIG film and the BTS sphere. At the right we show the mechanical eigenmodes of a sphere with similar size to the one used in the experiment is shown (R = 30 μm). FEM simulations shows that the effective mass for the radial breathing is $m_{eff} = 1 \cdot 10^{-10}$ kg.

Fluctuation dissipation theorem (see Chapter 1) states that the thermal force noise F_{th} corresponding to one degree of freedom ω_m, is associated to a thermal force power spectral density S_{th}, given by

$$S_{th} = \int \langle F_{th}(\tau) F_{th}(0) \rangle d\tau = \frac{2 m_{eff} \omega_m k_B T}{Q_m} \tag{5.2}$$

where m_{eff} is the effective mass of the mechanical mode. Then the thermal force can be express as:

$$F_{th} = \sqrt{\frac{2 m_{eff} \omega_m k_B T}{Q_m}} \tag{5.3}$$

A good magnetometer must present characteristics that allows it to have a low thermal noise. From Eq. 5.2 we can extract that a low effective mass is

important for reducing the thermal noise. The effective mass m_{eff} for one mechanical modes resonance ω_m is calculated from the maximum displacement $max(\vec{u})$ as:

$$m_{eff} = \frac{\rho}{max(\vec{u})} \int |\vec{u}|^2 dV \tag{5.4}$$

The effective mass obtained for a microsphere of R = 30 μm is $m_{eff} \sim 10^{-10}$kg. It is also important a high mechanical Q_m factor, since it would take longer to the resonator to dissipate its energy.

In the previous section we mentioned that the magnetic field response is encoded in a mechanical forced exerted on the microsphere. We assume that the relation between the magnetic response, F_{mag}, and the magnetic field is in the following way:

$$F_{mag} = c_{mag} B \tag{5.5}$$

being c_{mag}, a magnetic parameter. In principle, before experimental confirmation, this parameter can present a complex expression. Nevertheless, we will assume that the relation between F_{mag} and the magnetic field B is linear, giving a constant value for c_{mag}. This will be supported by the experimental results in the following sections.

We can model the mechanical response due to the magnetic field applied by using a an effective foces applied (F_{mag}) on the base of the mechanical oscillator. In Fig. 5.4a we show the modeled system, the BTS microsphere are deposited on a PMMA substrate layer and a YIG layer. In order to simulate a more realistic situation that is that the microsphere can presents imperfections, we have cropped the base of the microspheres by a distance of 0.5 μm. This flattes the base of the sphere increasing the contact region between the mechanical modes of the resonator and the vibrating layer.

If the mechanical driving exists, the energy density stored in the cavity would vary in frequency with a coherent forced in a frequency domain study. In Fig. 5.4b we illustrate the simulated configuration. The displacement energy stored as a function of frequency for sinusoidal force a force applied is shown in Fig. 5.4c. The resonances shown correspond to radial mechanical modes of the microsphere that are excited by the applied force. We have assumed a linear elastic model for all materials of the simulation. In order to open the system and also allow energy to dissipate through the substrate we have used perfect matching layers on the bottom part of the system.

5.5 Magnetometer sensitivity

The sensitivity of a magnetometer sensor is defined as the minimum magnetic field that can be measured by the device. As we have seen in Section 5.4,

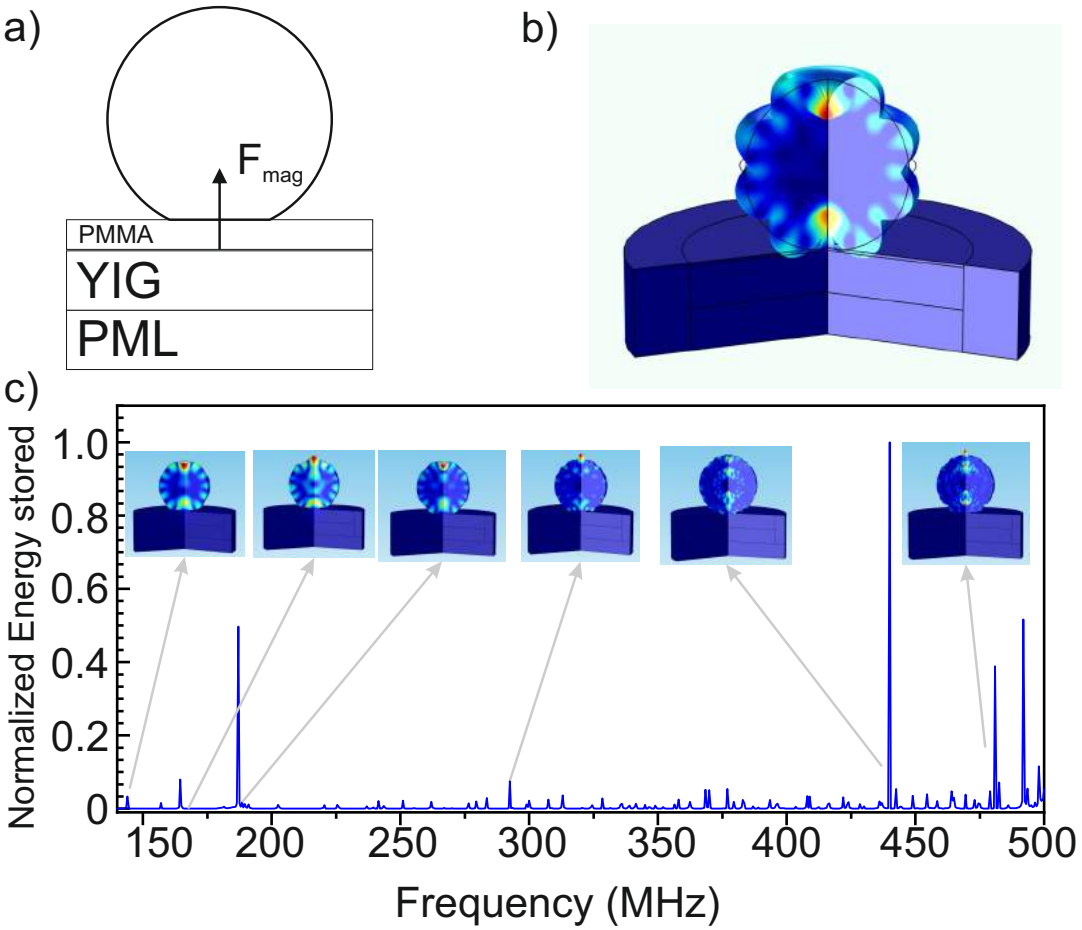

Figure 5.4: (a) Conceptual schematic of the model used to simulate the mechanical excitation of the microspheres resonances. (b) 3D visualization of the model used. A thin layer of PMMA (100 nm) is used on top of the YIG layer (1 μm). A BTS microspheres (R = 30 μm) is placed on top of the film. (c) Normalized energy stored in the microsphere with an applied magnetic force F_{mag}. The displacement profile of the eigenfrequency excited is shown in the graph.

the mechanical resonator presents multiple mechanical modes, with different displacement profiles, mechanical frequency, dissipation rates, and effective masses. As it was discussed in Chapter 2, considering a single mechanical mode, the equation of motion that describes the mechanical resonator is given by a forced harmonic oscillator. Also each mode is excited differently by the forced associated to the magnetic field. Nevertheless, the physics of the system is well described with a single mode and it can be extended immediately to include multiple resonances.

With similar arguments than in Chapter 2 for Eq. 2.9, and also in Ref. [145], the mechanical motion is given by,

$$\ddot{x} + \Gamma\dot{x} + \omega_m^2 x = \frac{F_{th}}{m} + \frac{F_{mag}}{m} + \frac{F_{OM}}{m} \tag{5.6}$$

where F_{mag} is the force applied by the magnetic field, F_{OM} is the radiation pressure force from the presence of the optical field coupled to mechanical motion, Γ is the dissipation rate of the mechanical mode ω_m, and m is the mass of the mechanical oscillator, or the effective mass of a more complex vibration mode of the structure. In this case, is the effective mass of the mechanical mode in the sphere and is calculated by Eq. 5.4.

Eq. 5.6 can be expressed in the frequency domain as

$$x(\omega) = \chi(\omega)\left(F_{th}(\omega) + F_{mag}(\omega) + F_{OM}(\omega)\right) \tag{5.7}$$

being $\chi(\omega)$ the mechanical susceptibility of the sistem given by

$$\chi(\omega) = \frac{1}{m\left(\omega^2 - \omega_m^2 + i\Gamma\omega\right)} \tag{5.8}$$

From fluctuation dissipation theorem, the force is $F_{th} = \sqrt{2m_{eff}\omega_m k_B T Q_m^{-1}}$. As treated in Chapter 2, the radiation pressure force term is given by $F_{OM} = \hbar g_{OM} n$, being $g_{OM} = \frac{d\omega_c}{dx}$, the optomechanical coupling rate and n the intracavity photon number.

The mechanical displacement shift the optical resonance via the optomechanical coupling, as $\delta\omega_c = g_{OM}x$. In real experiments, mechanical motion is measured via the frequency shift in the optical resonance. This is given by

$$\delta\omega_c = g_{OM}\chi(\omega)\left(\sqrt{2m_{eff}\omega_m k_B T Q_m^{-1}} + \hbar g_{OM} n + F_{mag}\right) \tag{5.9}$$

Due to the small number of photon fluctuations on the experiment, we can neglect the radiation pressure force term from now on.

The spectrum analyzer measures the power spectral density. It is composed by the spectral density from the magnetic field to detect, $S_{mag}(\omega)$, and the noise in the signal detected, $S_{noise}(\omega)$. These terms are given by [161]

$$\begin{aligned} S_{mag} &= |\langle\delta\omega_c(\omega)\rangle|^2 \\ S_{noise} &= \langle|\delta\omega_c(\omega)|^2\rangle - |\langle\delta\omega_c(\omega)\rangle|^2 + S_{meas}(\omega) \end{aligned} \tag{5.10}$$

where $S_{meas}(\omega)$ is the noise power spectral density, and represents the noise introduced by the measurement apparatus due to electronic noise, and laser noise[162]. In the experiment that I am discussing here, the main source of noise is the laser shot noise. The measurement noise is independent of the mechanical motion $x(t)$. We take $F_{mag}(\omega)$ at a single frequency ω_{mag}, $F_{mag}(\omega) = F_{mag}\delta(\omega - \omega_{mag})$, which in terms of spectral noise gives $S_{mag}(\omega) = g_{OM}^2|\chi(\omega)|^2 F_{mag}^2\delta(\omega - \omega_{mag})$. Then, the spectral noise term is given by

$$S_{noise} = g_{OM}^2 |\chi(\omega)|^2 \left[2m_{eff}\omega_m k_B T Q_m^{-1}\right] + S_{meas}(\omega) \tag{5.11}$$

The minimum forced that can be detected is obtained by integrating the magnetic and noise spectral densities contribution over the bandwidth $\Delta\omega_{RBW}$ and making the signal to noise ratio (SNR) equal to one, i.e. setting the magnetic and noise power spectral densities equal:

$$\frac{F_{mag}^{min}}{\Delta\omega_{RBW}} = \sqrt{2m_{eff}\omega_m k_B T Q_m^{-1} + \frac{S_{meas}}{g_{OM}^2 |\chi(\omega)|^2}} \tag{5.12}$$

Finally, according to Eq. 5.5, the minimum detectable magnetic field is given by

$$\frac{B^{min}}{\Delta\omega_{RBW}} = \frac{1}{c_{mag}} \left[S_{th} + \frac{S_{meas}}{g_{OM}^2 |\chi(\omega)|^2}\right]^{1/2} \tag{5.13}$$

From this equation we observe that the measurement noise, S_{meas}, and the magnetic estimated field, B^{min}, are minimized at the mechanical frequency, since the mechanical susceptibility diverges at ω_m. In contrast, we know from Eq. 5.3 that the thermal noise is flat. A high mechanical quality factor Q_m is always advantageous for reducing the thermal noise S_{th} and also, in resonance, reducing the S_{meas} due to the contribution on the susceptibility.

In Fig. 5.5a, we plot the sensitivity as a function of frequency, ω, for different normalized measurement spectral noise, considering that S_{meas} is flat. This assumption is acceptable since assuming that S_{meas} is only limited by the shot noise of the laser, it depends mainly on the optical linewidth κ [161]. We have defined the term B_{th} as $B_{th} = \left(2m_{eff}\omega_m k_B T Q_m^{-1}\right)/c_{mag}$ and B_{meas} as $B_{meas} = S_{meas}^{1/2}/c_{mag} g_{OM}^2 |\chi(\omega)|$. When B_{th} dominates, the sensitivity is flat on the range of frequency from $\omega = 0$ until it reaches the value $\omega = \omega_m$.

In Fig. 5.5b, we plot the on resonance ($\omega = \omega_m$) minimum detectable magnetic field as a function of the measurements noise inaccuracies (B_{meas}/B_{th}). When the thermal term B_{th}, dominates over the measurement term, B_{meas}, the sensitivity (B_{min}) is flat. Once the measurements noise equals the thermal noise, the sensitivity B_{min} increases.

The optical quality factor Q_{opt}, does not have an influence on the sensitivity. However, high Q_{opt} cavities are useful for reducing the S_{meas}. The measurement method consist on measuring currents I on the detector, which is proportional to the resonance frequency $\delta\omega_{opt}$, and consequently to mechancial motion x(t). Therefore, the current is increased by the optical quality factor

$$I \sim \delta\omega \cdot Q_{opt} \sim x \cdot Q_{opt} \tag{5.14}$$

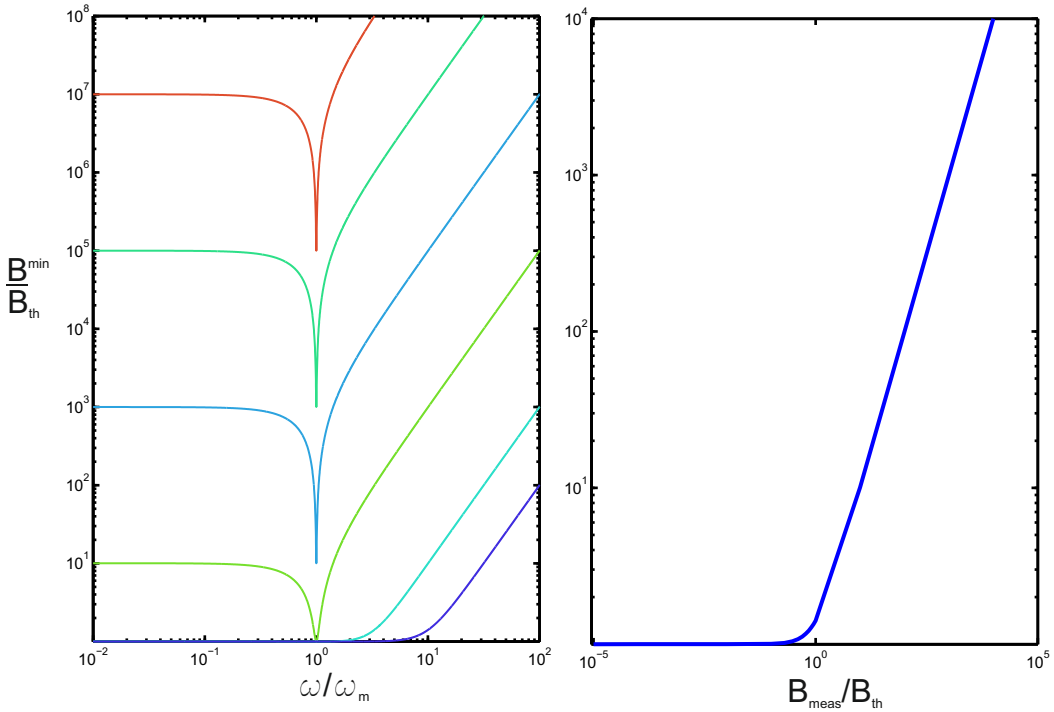

Figure 5.5: (a) Magnetic field as a function of frequency. The detectable magnetic field strength B^{min} is normalized by B_{th}, which is defined as $B_{th} = \left(2m_{eff}\omega_m k_B T Q_m^{-1}\right)/c_{mag}$. The noise spectral density due to noise is written like $B^{meas} = S_{meas}^{1/2}/c_{mag}g_{OM}^2|\chi(\omega)|$. The different color lines correspond to values of $B_{meas}/B_{th} = \left(10^5, 10^3, 10, 10^{-1}, 10^{-3}, 10^{-5}\right)$. (b) On resonance ($\omega = \omega_m$) magnetic field sensitivity normalized by B_{th} as a function of the measurement spectral noise normalized B^{meas}/B_{th}. The mechanical quality factor used was Q_m = 100 and the bandwidth $\Delta\omega$ = 1 Hz.

5.6 Optomehcanical characterization of BTS microspheres

5.6.1 Optomechanical setup

The experimental set up used to characterize the microsphere is the standard one employed in multiple experiments in optomechanics [95, 101, 134]. The set up is schematized in Fig. 5.6. A infrared tunable laser, that covers the spectral range between 1440 nm to 1640 nm, is used as a light source. Light is coupled to a tapered fiber. A fiber polarization controller is used to set the polarization state of light that will be coupled to the microsphere. The thinnest part of the tapered fiber is placed in contact with the microsphere. In order to make the characterization in similar conditions to those used during the magnetometer operation, the microsphere is characterized on the YIG film, which is placed on the micro strip waveguide (see the picture on Fig. 5.6). The presence of a radio frequency modulation of the transmitted signal, was

detected by an InGaAs fast photodetector with a bandwidth of 12 GHz. The radio-frequency voltage output is connected to the 50 Ω input impedance of a signal analyser with an operational bandwidth of 13.5 GHz. All measurements of the optomechanical characterization and the magnetometer operation were performed in an antivibration cage at atmospheric conditions of air and temperature.

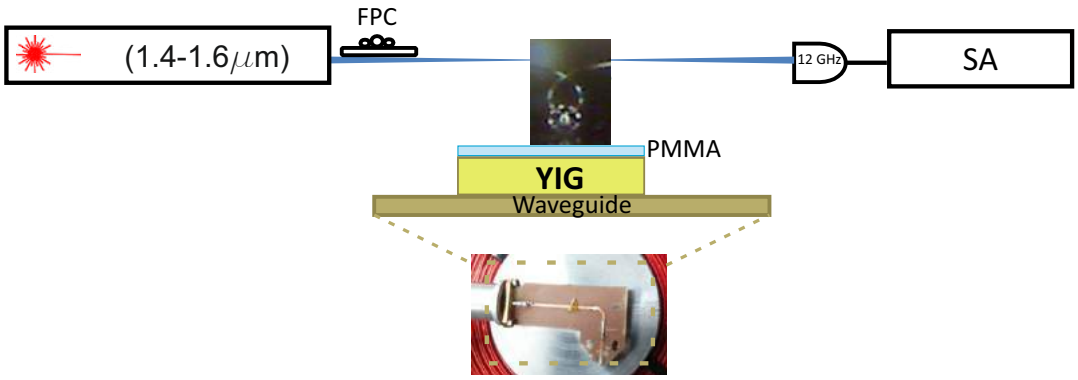

Figure 5.6: Schematic of the optomechanical set up. We measure the optical whispering gallery modes of the microspheres with an infrared tunable laser source connected to tapered fiber. The tapered fiber has a loop shape and couples light evanescently to the microsphere. The outcoupled light is collected by the fiber and analysed with a spectrum analyser.

5.6.2 Optical characterization

We selected microsphere resonators since they are versatile cavities to store light with high quality factors. They can be made of multiple materials, from polymers to glassy compounds [9, 84, 157]. In such geometry, quality factors Q_{opt} up to 10^9 have been reported, on which the main mechanism of loss is established by the material absorption [9]. The normalized spectrum of optical modes of the microsphere is shown in Fig. 5.7. The characterization is performed using the set up described in the previous section and schematized in Fig. 5.6, but instead of using a fast photodetector connected to the spectrum analyser, we used a Ge biased detector (Thorlabs, DET550B) connected to a voltmeter.

In Fig. 5.7 we show the typical optical transmission spectrum from a microsphere of about 40 μm in diameter with multiple WGMs. The optical power used for this characterization was about 60 μW. The multiple dips are obtained every time the laser wavelength is resonant with the a WGM. We note that the resonances are compound by multiple modes, whose linewidths are found to be smaller than $\delta\lambda < 1$ pm, exceeding then the laser resolution ($\delta\lambda = 1$ pm). This sets a lower bound for the quality factors of $Q_{opt} > 10^6$. Independent measurements with an oscilloscope confirmed quality factors around $Q_{opt} \sim 10^8$. The measurement consisted on scanning the optical mode with the photodetector connected to the oscilloscope which offers a

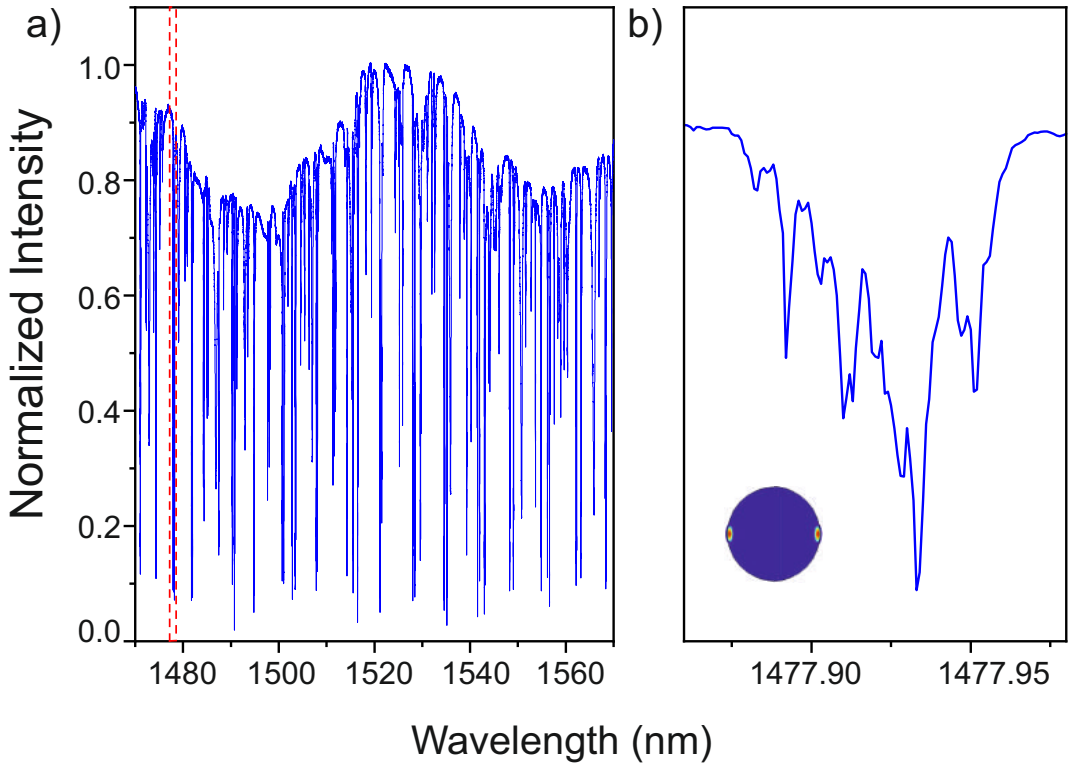

Figure 5.7: (a) Optical whispering gallery modes spectrum measured on a microsphere of R = 38 μm radius. (b) Zoom region highlithed in red on (a). The optical modes linewidth is smaller than the laser resolution $\delta\lambda < \sim 1$ pm. The inset shows a simulation of the optical WGMs.

better time resolution. By knowing the speed scan, we were able extract the linewidths of the mode and then obtain the quality factor.

An important comment that is needed to be made is that due to the difference of the refractive index between the YIG film (n = 2.19) and the BTS microsphere sphere (n = 1.4), we use an intermediate layer of 100 nm of PMMA that preserves the high Q-factors of the optical modes (see Fig. 5.6). With this configuration, the light confined on the microsphere did not leaked to the substrate. The use of PMMA does not change the experimental result since PMMA is non magnetic.

The contact position of the fiber on the microsphere is also an important aspect to take into account in order to avoid light to be lost to the YIG substrate. The electromagnetic energy of the WGM is assumed to be confined in the equatorial plane of the contact position between the microsphere and the fiber. Then, a vertical contact position of the fiber loop on the sphere is translated on an optical path which finds YIG the substrate (either YIG or PMMA), resulting on an extra channel for losses. In Fig. 5.8, two optical images showing a top view of the fiber-microsphere contact. We preferred a lateral position in order to avoid losing light to the YIG substrate.

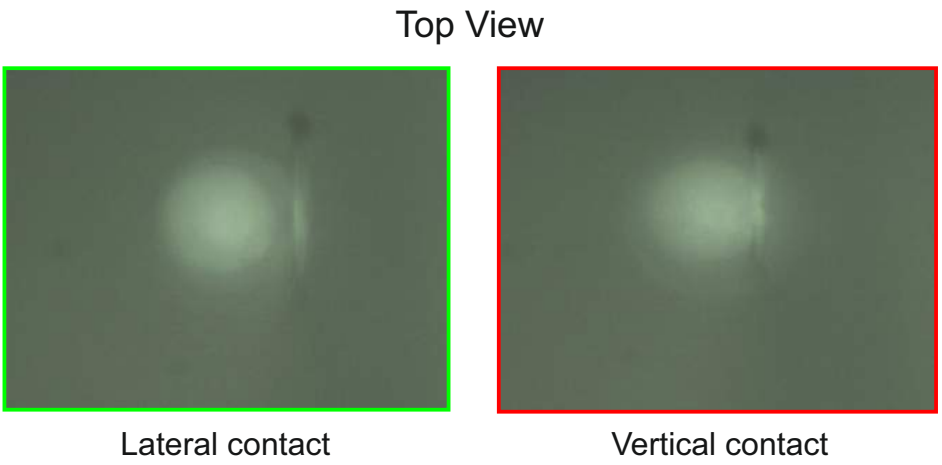

Figure 5.8: Optical images showing a top view of the fiber-microsphere contact. The vertical contact was excluded in order to avoid losing light to the YIG substrate.

We also note that, the laser power used during the whole experiment was maintained in such a way that the optical nonlinear effects were not activated. Optical powers above $\sim$ 100 μW leaded to homogeneous heating effects inducing thermo-optic non linearity. This results in a redshift of the optical resonance on the transmission spectrum. The resonance shift in wavelength can reach several nanometers.

5.6.3 Mechanical characterization

The long tail of the evanescent field of the fiber excites the resonant optical mode of the sphere. Once in resonance, the mechanical motion of thermal populated mode activated by thermal Langevin force causes that the transmitted intensity to be modulated around a static value (see Fig. 5.7). The strength of this modulation is given by the optomechanical coupling rate (see Chapter 1). In Fig. 5.9 we show the radiofrequency spectrum obtained on the spectrum analyzer. Mechanical modes with a non-negligible optomechanical coupling rate appear as narrow peaks in the spectrum.

The spectrum shown in Fig. 5.9 correspond to a sphere of 40 μm radius. We observe that by measuring microspheres with different sizes, the frequency of the fundamental mechanical mode decreases with increasing the microsphere size. Nevertheless, the mechanical quality factor Q_m factor measured was found between 10^2 and 10^3 for all sizes. This is because the main source of loss of displacement energy is given by the visco-elastic damping with air.

Interestingly, not all WGMs from Fig. 5.7 show enough optomechanical coupling rate to transduce mechanical eigenmodes above the noise level of the RF spectrum. For the sphere used in this experiment there was only one optical mode at 1509 nm with a coupling strength enough to transduce mechanical modes. On the spectrum shown in Fig. 5.9 we observe five mechanical modes at 109, 206, 292, 338 and 465 MHz. According to FEM simulations

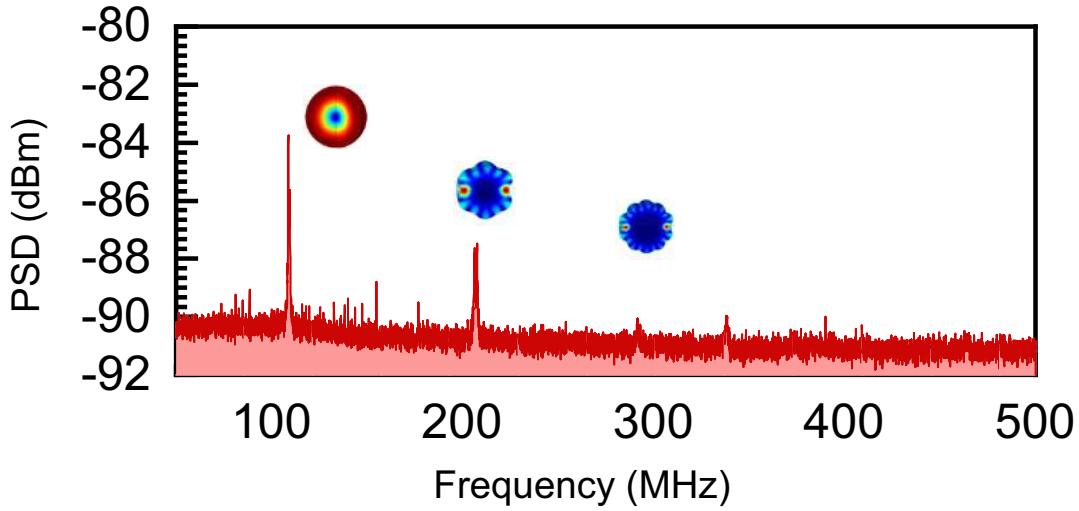

Figure 5.9: Transduced mechanical modes of the characterized microsphere. A radiofrequency modulation is detected on the Spectrum Analyzer.

from COMSOL, we can identify the displacement profile of the mechanical modes, they correspond to radial modes and they are also shown in Fig. 5.9.

5.7 Magnetometer characterization

In this section, I describe the different characterization of the magnetometer perfomance. First, I will show the signal observed in the Spectrum Analyzer and magnetic field calibration for a single peak. Then, I will describe the coherent response of the magnetometer using a Vector Network Analyzer, showing the operational bandwidth of the magnetometer. After the dynamic response is shown, I will show that by tuning the ferromagnetic resonance of YIG we can move the dynamic range of the magnetometer for different frequency ranges up to 1.1 GHz. Finally, I will show the design of a future magnetometer fabricated YIG.

5.7.1 Incoherent spectral response

The experiment that sets the first proof of principle of the optomechanical magnetometer with a resonant ferromagnetic resonance is shown in the top part of Fig. 5.10. We use the same optomechanical set up shown in Fig. 5.6 for the optical excitation and read out of mechanical motion on the BTS microsphere. The novelty here is that an alternate magnetic field will be applied on the system YIG film-microsphere. The microsphere is placed on top of the YIG film and in turn the film is placed on a microstrip coplanar waveguide that creates the AC field that is going to be detected. The microstrip is driven by the Vector Network Analyzer. The FMR mode is tuned by two copper

coils on which by being circulated by a current, they create a static magnetic field B_{DC}. For the first part of the experiment, we will use a low B_{DC} in order to find the FMR mode at low frequencies.

In the bottom part of Fig. 5.10, we show the transduction spectrum of the same sphere characterized in Fig. 5.9. We apply an alternate field oscillating at a frequency of $\omega_{cal} = 206$ MHz. This frequency will be used for calibration. The RF power applied on this measurement was -10 dBm. On Fig. 5.10, above the thermal motion corresponding to the mechanical modes close to that frequency, the spectrum shows a peak at the frequency of the applied magnetic field. The force induced by vibrations on the YIG modifies the mechanical spectrum of the microsphere with a corresponding signal response characterized by a Signal-to-Noise-Ratio (SNR) of 8 dB, as illustrated on the zoom spectrum in Fig. 5.11. Such a peak disappears when the sphere is lifted from the YIG and the mechanical contact is lost, which demonstrates the mechanical origin of the signal.

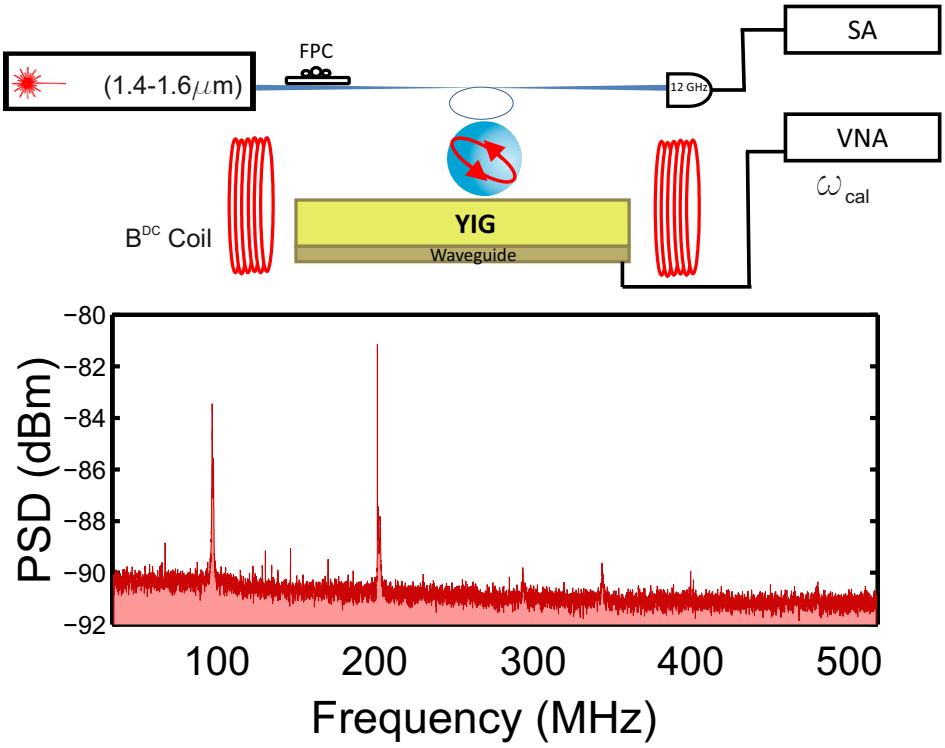

Figure 5.10: A simplified schematic of the full experimental setup. A fiber taper is used to probe the optomechanical modes of the microsphere. Two electromagnetic coils are used to generate static magnetic field. This static field tunes ferromagnetic (magnon) resonance mode on the YIG film. The microwave magnetic field is provided by the waveguide. The FMR of the YIG film are monitored by the measurement of S_{11} on the Vector Network Analyzer. In the bottom image we show the Brownian noise spectrum with magnetic excitation at 206 MHz.

We measure the SNR for different applied magnetic fields at ω_{cal}. As shown in Fig. 5.11b, we observe a linear dependence of square root of SNR at frequency on the applied RF magnetic field (B). The amplitude of the field B acting on the YIG and the sphere is obtained estimating the RF current that passes through the CSW, by measuring the characteristic impedance of the circuit and considering the applied RF power (see Appendix A for detail).

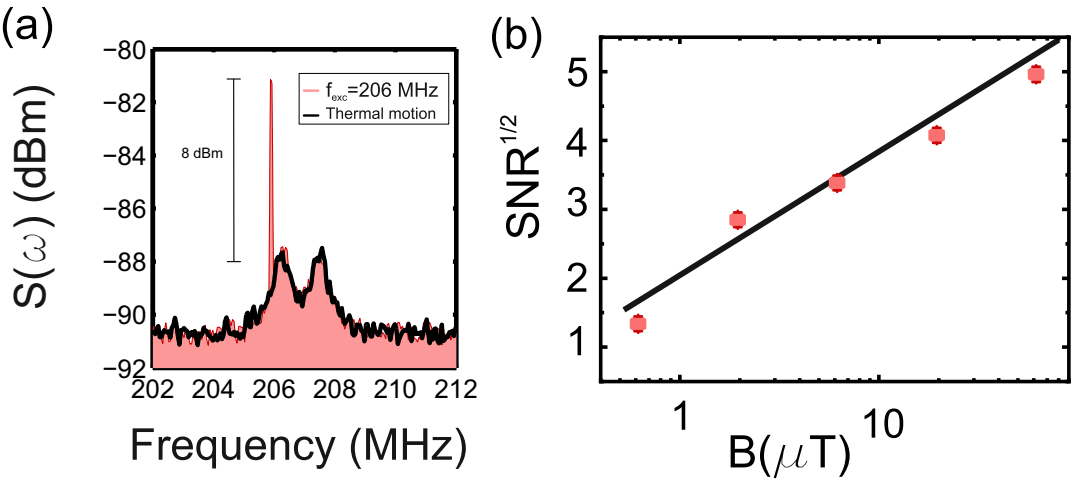

Figure 5.11: (a) Mechanical spectrum of the silica microsphere excited by applying an RF magnetic field of 2.3 μT at 206 MHz, in red. The black curve corresponds to the mechanical mode without excitation. (b) Signal to noise ratio (SNR) of the system as a function of RF magnetic field applied

We use the magnetic field dependence in Fig 5.11b to calculate the sensitivity at a single frequency, which is given by the field strength at which the spectral peak height is equal to the noise (SNR=1), for a 1 Hz measurement resolution bandwidth. The correspondent magnetic field obtained at ω_{cal} is $B = 0.51$ mT with a resolution bandwidth of $\Delta\omega_{RBW} = 30$ kHz. Then the sensitivity is given by

$$\delta B_{min} = \frac{B_{min}}{\sqrt{\Delta\omega_{RBW}}} = 2.94\frac{nT}{\sqrt{Hz}} \tag{5.15}$$

5.7.2 Coherent response

The dynamic response of the sensor over a wide frequency range is demonstrated by using the set up schematized in Fig. 5.12. We measure the S_{21} trace on the VNA, on which we have connected the waveguide excitation from port 1, and port 2 is connected directly with the detector. We use the VNA to sweep the frequency of the AC field from 50 MHz to 1.2 GHz. This allows to detect coherently the optical modulation, N(ω), coming only at the frequency of the AC field.

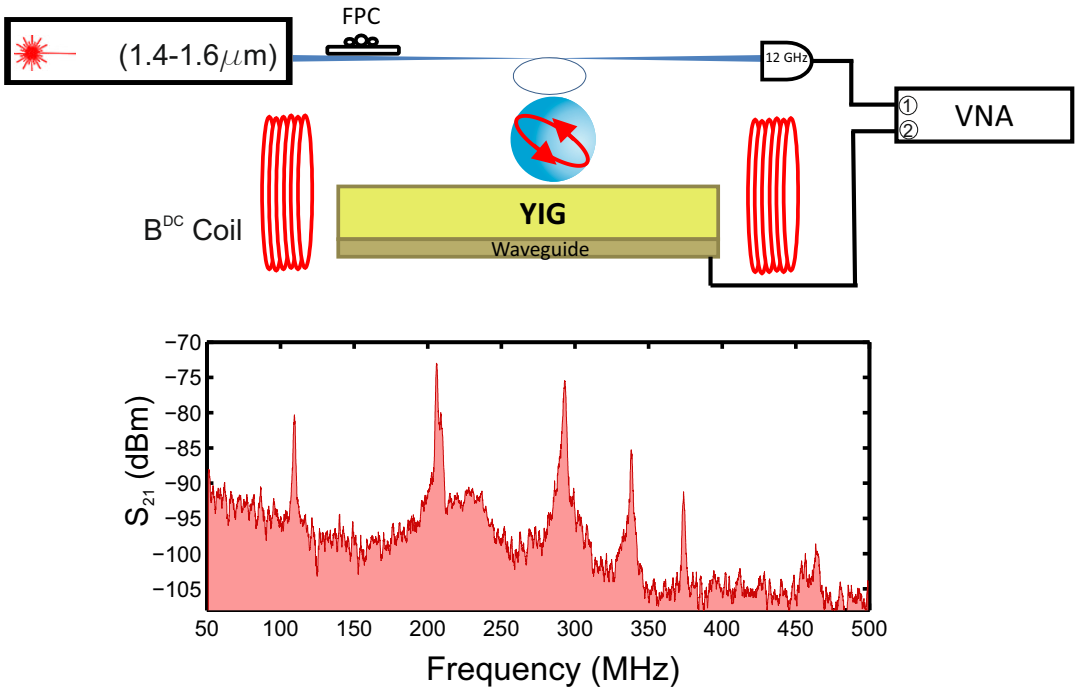

Figure 5.12: (Top) Schematic illustration of the set up used for the magnetometer coherent response characterization. In this configuration, we measured the S_{21} trace on the VNA on which we have connected the waveguide excitation on port 1, and the signal from the photodetector on port 2. (Bottom) System response N(ω) measured using the VNA to sweep the frequency of the rf field.

In bottom part of Fig. 5.12, we observe a dip in the VNA signal N(ω) wherever ω is resonant with a mechanical mode with sufficiently high value of g_{OM} (see Fig. 5.9). Besides the mechanical modes that were transduced on the Spectrum Analyzer on Fig. 5.9, we can detect modes at 374 MHz and 456 MHz that in the thermally activated spectrum obtained in Fig. 5.9 were below the noise level. The reason of this resides on the enhanced noise rejection of the VNA.

5.7.3 Magnetometer sensitivity

A frequency dependent sensitivity is obtained by combining the spectral calibration at a single frequency, performed in the previous subsection, the noise power spectrum in absence of a magnetic field S(ω), and the network response N(ω). We follow a similar procedure as in Refs. [162] and [163]. The operational bandwidth of the magnetometer is defined wherever ω is resonant with a mechanical mode. Then, it will determined by the mechanical modes linewidths. This is shown in Fig. 5.13a, where the spectrum is separated by different windows (labeled from I to V). The frequency dependent sensitivity on every window is given by

$$\delta B_{min}(\omega) = \sqrt{\frac{S(\omega)\cdot N(\omega_{cal})}{S(\omega_{cal})\cdot N(\omega)}}\delta B_{min} \tag{5.16}$$

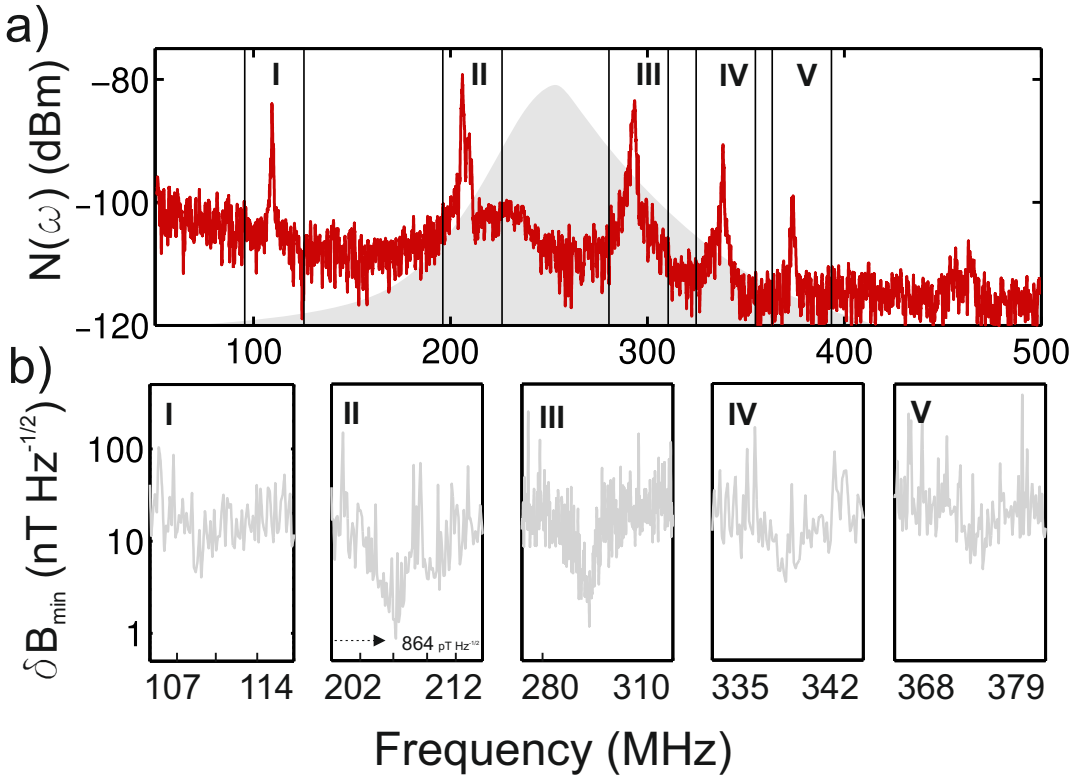

Figure 5.13: (a) System response N(ω) measured using a VNA as a function of the frequency of the RF field. The FMR is shown (inverted) on the back of the graph to illustrate the mechanical modes affected by the resonant effect. (b) Magnetic field sensitivity $\delta B_{min}(\omega)$ of the optomechanical magnetometer as a function of the frequency defined where there is overlap with mechanical modes. The five mechanical modes (labelled from I to V) excited allow to calculate sensitivity in a frequency window of $\sim$ 10 MHz around the frequencies of the mechanical resonances. A peak sensitivity of $\delta B_{min}(\omega)$ = 864 pT Hz $^{-1/2}$ is achieved close to the mechanical mode at 206 MHz.

In Fig. 5.13b it is shown the sensitivity within the frequency range associated to the first five mechanical modes of the microsphere observed in Fig. 5.13. The FMR is shown on the back of the graph of Fig. 5.13a in grey color. This correspond to a value of static magnetic field B_{DC} of 0.17 mT.

The lowest sensitivity value obtained is 864 pT Hz$^{-1/2}$ close to the mechanical mode at 206 MHz. This mode presents a large overlap with the optical whispering gallery mode, since its displacement field profile is concentrated along the edge of the sphere (see Fig. 5.9 and Fig. 5.7). It is also worth noting that the frequency of the mode is still several tens of MHz away from the

center of the FMR resonance (see Fig. 5.13a) so that the reported value of minimum sensitivity may still be substantially improved by fine tuning the FMR position. The sensitivity remains around 1 nT $Hz^{-1/2}$ within the linewidth of the mechanical resonances (10 MHz), for five mechanical modes.

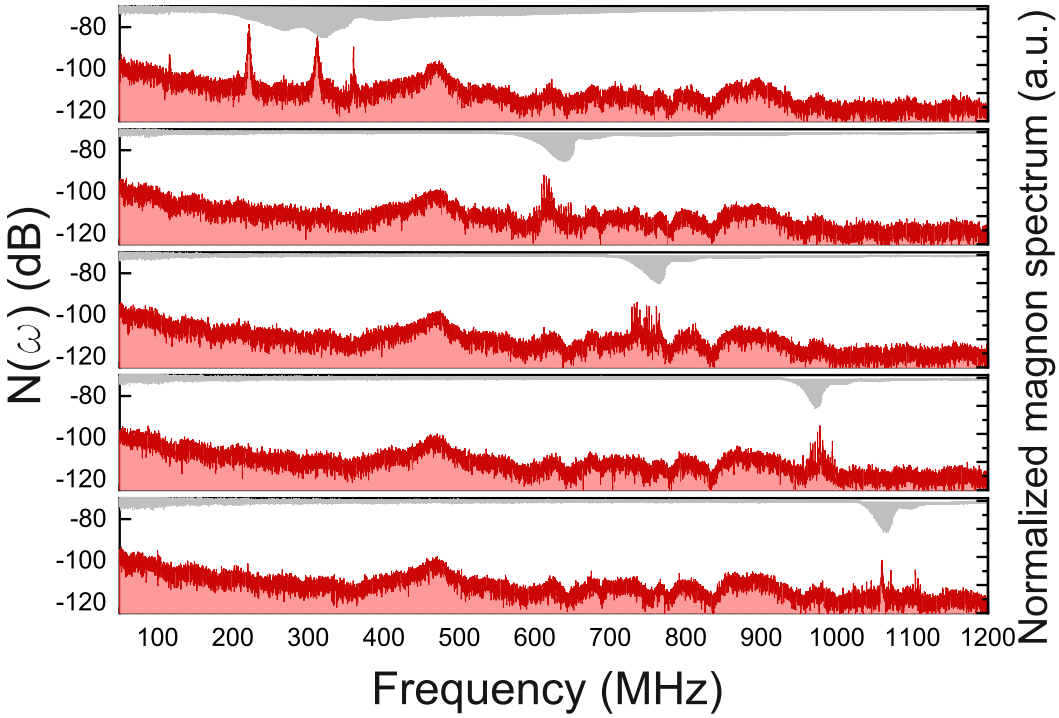

Figure 5.14: System response as a function of frequency for different FMR modes excited on the YIG film. Gray curves show FMR resonances for different values (0.17, 2.2, 3.6, 6.1 and 7.4 mT) of the applied static magnetic field.

The control of the FMR resonant frequency with B_{DC} provides our system with precise tunability in the operational frequency range. In Fig. 5.14, we show the system response $N(\omega)$ as a function of frequency for different values of B_{DC}.

It is worth noting that for this measurement a second sphere with a similar radius, mechanical spectrum and optical quality factors was measured. The grey curves of Fig. 5.14, show VNA-FMR spectra as a function of frequency. As mentioned earlier the FMR frequency increases with increasing the B_{DC}, accompanied by a spectral narrowing of the dip. This behavior confirms that the signal appears only when the linewidth of the FMR resonance overlaps with the mechanical resonances of the microsphere. In addition, it evidences the presence of mechanical modes that are hidden below the noise level of the SA. This confirms the necessity of the magnon to enhance the magnetostriction effect and the magnetometer performance.

In Fig. 5.15a we obtain the peak sensitivity for the different measured positions of the FMR mode. We note that the magnetometer detects magnetic fields even above 1 GHz because of the presence of mechanical modes on

the GHz range. This is shown in Fig. 5.15b, where a signal peak is imposed on top of the mechanical modes at 936 MHz. An SNR=11dB is obtained for a power of -10dBm applied on the waveguide. On Fig. 5.15c, we show the corresponding FMR position for the previous measurement. The linewidth of the FMR and the mechanical mode cover the same frequency region, enhancing the resonant effect and the sensitivity of the magnetometer. The measured sensitivities shown in Fig. 5.15a, are comparable with the one reported in Fig. 5.13 (~ 1 nT $\mathrm{Hz}^{-1/2}$). This value is a lower bound of the operational frequency limited by experimental constraints on the B_{DC}. In a typical FMR setup, frequencies of 10 GHz are achievable.

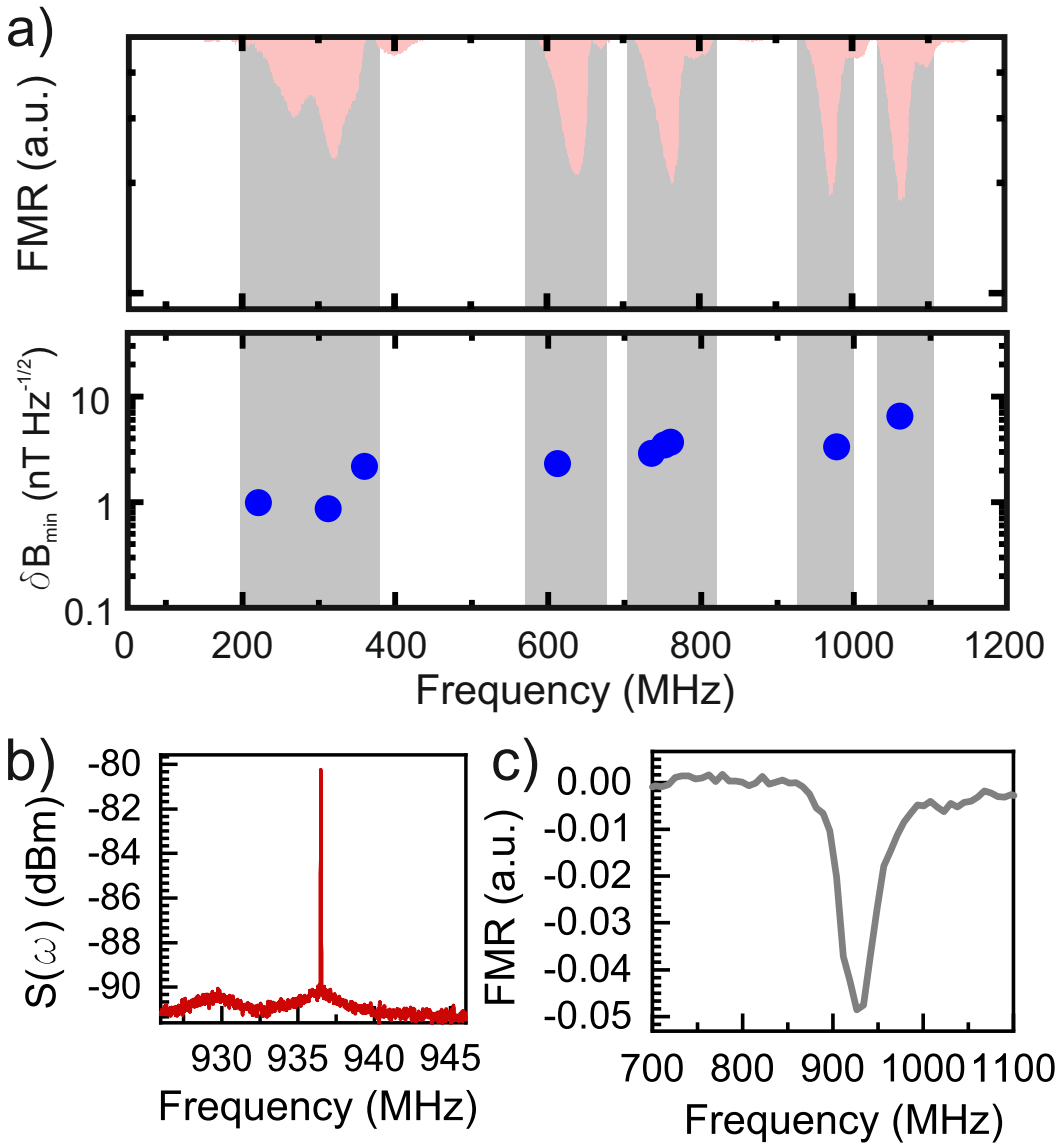

Figure 5.15: (a) Peak magnetic field sensitivity obtained by moving the magnon mode on a wide range of frequency.(b) Zoom in of the spectrum showing in detail the mechanical mode of the microsphere and the signal peak with a corresponding SNR=11dB (c) FMR measured on the waveguide for a static magnetic field applied of 7 mT.

As noted above, the FMR resonance obtained are rather broad given that the electromagnets were placed several centimeters away from the sample, resulting in a not fully uniform B_{DC}. The linewidths of the FMR resonances shown in Fig. 5.14 are a factor of two larger than the one shown in Fig. 4.5c, which were obtained measuring YIG in a set up with a highly homogeneous B_{DC}. On the positive hand, under these conditions, the operational frequency range is increased several mechanical modes can be covered without changing the B_{DC}. On the other hand, a much improved sensitivity could be attained with a narrower and deeper FMR.

5.8 Vibrometer measurement

We have performed additional experiments to support the interpretation that the results that we report here are due to vibrations on the YIG film. The alternative technique was based on Laser Doppler Vibrometry.

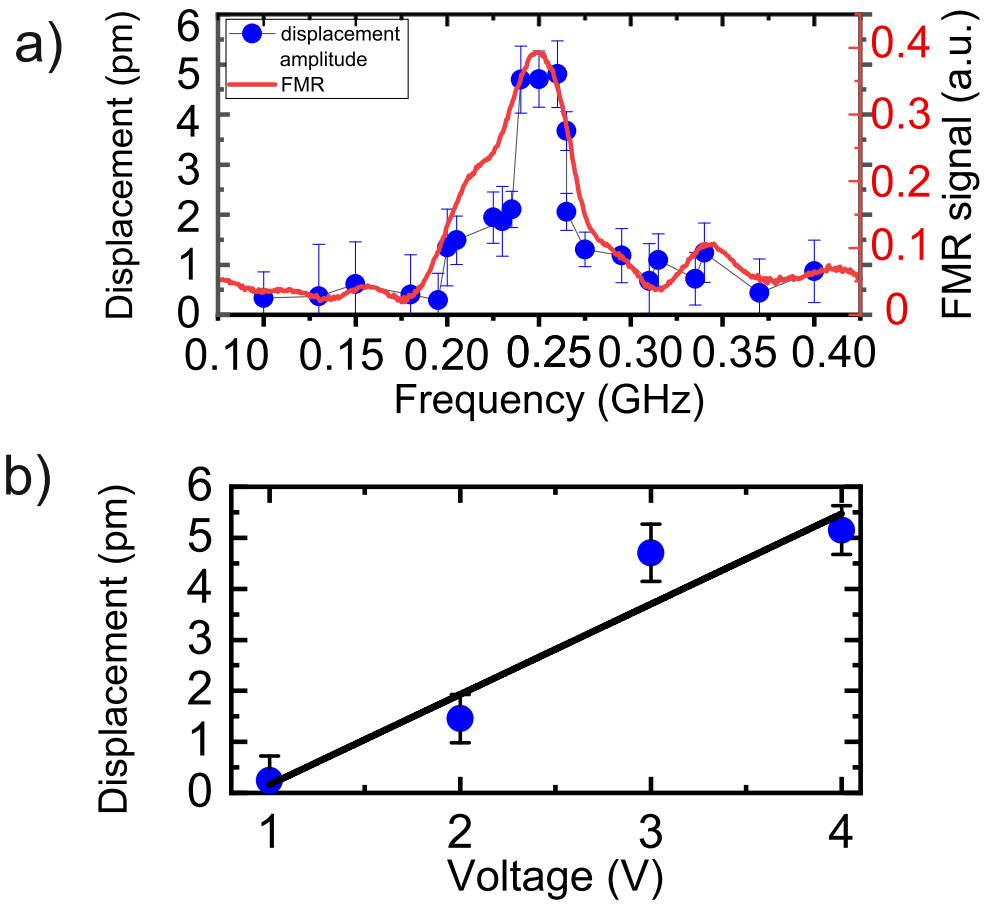

Figure 5.16: (a) Magnon resonance resolved with LVD on the YIG film. A peak amplitude of 4.7 pm is obtained at the center of the resonance (RBW = 2.5 kHz). (b) Amplitude dependence with voltage of the LDV. The measurement was taken at 250 MHz at the resonance peak.

A high frequency laser Doppler vibrometer (LDV) was used to measure vibration at the surface of YIG in the absence of the microsphere. This laser interferometric technique measures displacement in absolute units with picometer sensitivity. The basic principle relies on the Doppler shift that light suffers when is reflected from a moving object. From this spectral shift the motion velocity can be extracted, from which finally displacement can be obtained (See Apendix C for more details). The advantage of using this technique is its non-contact nature, allowing the possibility of measuring vibrations in YIG without the optomechanical cavity.

We applied an RF magnetic field to the waveguide and tune the FMR mode resonance with a permanent magnet like it is described in Fig. 5.12. Using a VNA as RF source and measuring S_{11} allows a standard measurent of FMR as it is described in Chapter 4. The measurement of FMR is shown at the right axis of Fig. 5.16a in solid line, where the resonance is centered at 250 MHz. This measurement is used as reference to compare with the one that will be obtained with the LDV.

The left axis of Fig. 5.16a shows the LDV measurement of displacement as a function of frequencies. The measured amplitudes were obtained for frequencies between 100 MHz to 400 MHz at 3 V applied from the vibrometer source. The dots correspond to the measurement values. Comparing the two measurements, we observe that LDV values coincide with the FMR, having similar linewidths. This means that the vibrometer registers vibrations in the same spectral range than FMR, confirming the YIG layer generates mechanical vibrations on its surface on the FMR frequency range via magnetostriction.

We report the linear dependence between amplitude and voltage in Fig. 5.16b. From the linear fit we can estimate the amplitude that corresponds to the equivalent voltage applied to the waveguide for the minimum peak sensitivity on the microsphere experiment. The details of the experiment and the measurement results are described in Appendix C.

5.9 Comparison with the State of the Art

As it was mentioned on Section 5.1, magnetometers have multiple applications, depending on the sensitivity, work requirements and the physical operating nature. The size and sensitivity are considered two crucial and competing parameters, that indicate how small will be the sensor and what is the smallest magnetic field that may be detected.

In Fig. 5.17, I have plotted the main parameters that characterizes several recent magnetometers found in literature. The most extended used magnetometers with high sensitivity are the SQUID, which can reach sensitivities of 1 fT $Hz^{-1/2}$ [151, 152]. However, the main limitation they present is that they need to operate at cryogenic temperature conditions. As it was mentioned

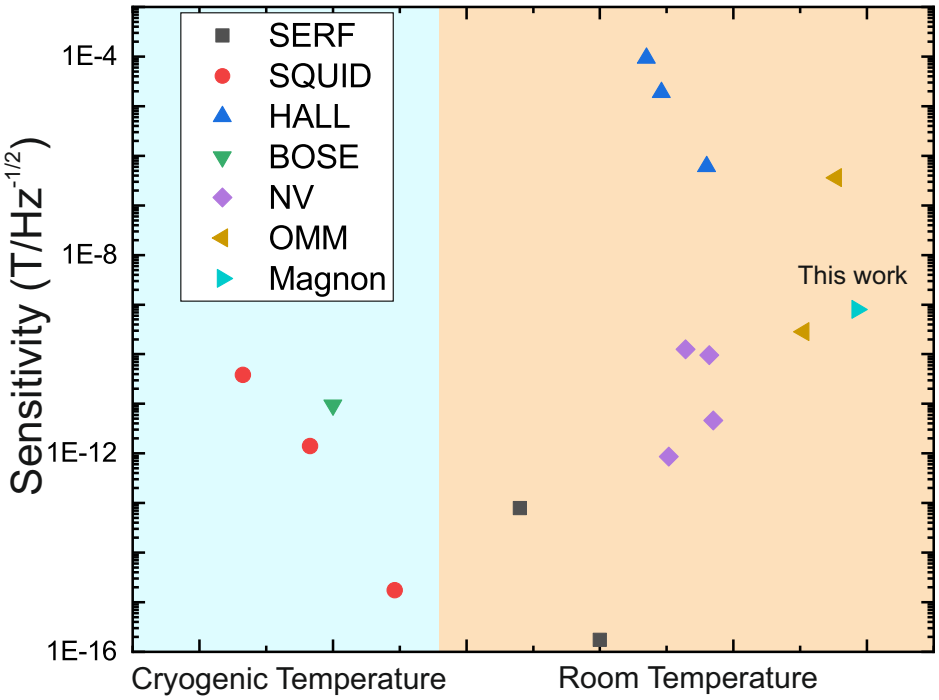

Figure 5.17: The sensitivity values plotted correspond to SQUID magnetometers [151, 152, 164], spin exchange relaxation free magnetometers [46, 47, 165], Hall magnetometers [166], Bose Einstein condensate magnetometers [149], NV center [167–170], cavity optomechanical magnetometers [49, 162] and magnon assited optomechanical magnetometer

in the introduction of the chapter, the cryogenic operation was surpassed by the spin exchange relaxation free magnetometer, reaching sensitivities of 160 aT $Hz^{-1/2}$ at 40 Hz. Nevertheless, these magnetometers are restricted to small bandwidth and dynamic range [46]. NV diamond magnetometers can achieve sensitivities from 1 nT $Hz^{-1/2}$ to 1 pT $Hz^{-1/2}$. Their bandwidth are on the hundred Hz range. The main advantage this type of magnetometer presents is the possibility of using ensembles with micrometer spatial resolution.

Recently, cavity optomechanical magnetometers present nano and pico tesla sensitivities [49, 50, 156, 162]. They operate at room temperature and have bandwidths of hundreds of kilohertz. The FMR assisted optomechanical magnetometer presented in this chapter can reach comparable sensitivities and bandwidths. Instead of using the highest magnetostrictive material, it exploits the resonant effect induced by magnons on material with high quality ferromagnetic resoance. This allows to detect magnetic field on the GHz range that compared with the other conventional optomechanical magnetometers was restricted to 40 MHz in the best case. Despite that single crystal YIG was found to be less magnetostrictive than Terfenol-D [171], the high performance of the OMM reported here is due to the use of YIG to display a high quality FMR and the use of a high Q optical resonator.

Compared with room temperature operation devices like diamond NV centers magnetometers, the device reported here shows a similar peak sensitivity as the decive reported in Ref [147], with the advantage of having a fiber based optical detection. The sensitivity values reported here outperform electrically Lorentz Force magnetometers [172] of comparable size by three orders of magnitude. Furthermore, our sensitivity is five orders of magnitude larger than magnetometers based on superconducting quantum interference devices.

5.10 Perspective

On this subsection, we will present a possible future magnetometer that would be one step forward following the idea proposed in this Chapter. It consists on joining the optical and mechanical cavity on the ferromagnetic material. The fact of having the optomechanical cavity on YIG would allow to excite a high quality and intense FMR on the device, bringing the magnon-mechanical-photon interaction to the same scenario and increasing the coupling efficiency.

On Fig. 5.15a, we show an schematic illustration of the coulpling mechanism. The fiber taper would couple to the optical whispering gallery modes via the evanescent field. In Fig. 5.15b, we show the optical mode confinement calculated by FEM simulations. The contrast of refractive index between the GGG substrate (n= 1.93) and YIG (n= 2.19) is sufficiently high to allow the localization of optical modes on the THz range. Several disk thicknesses and diameters have been calculated in order to know the minimum dimension that can localize optical resonances. The minimum disk dimensions found was 1 μm thick and a 20 μm radius. With these dimensions, radial breathing modes are found well in the GHz range.

The fabrication of nanostructured ferromagnetic thin films is a challenging process that is being intensively investigated [173, 174]. In order to preserve the ferromagnetic properties of the material, it is important to control the shape anysotropies. Then it is crucial to develop a high resolution geometric patterning of the ferromagnet. The fine etching of single crystal YIG thin film has long been a demanding process for studying magnon applications at submicrometer dimensions. The main etching processes for YIG consist on wet etching process based on using phosphoric acid after ion milling or photoresist patterning [175, 176]. The main complications of these processes are that they are restricted fabricate devices with large dimensions, high roughness and not vertical walls. Novel processes have recently emerged, offering the fabrication of nanometers devices by lithographical lift-off of YIG on a GGG substrate followed by an annealing at high temperature [174]. This last process would be ideal to fabricate YIG disk to create the optomechanical-magnonic device proposed in this section and shown in Fig. 5.18.

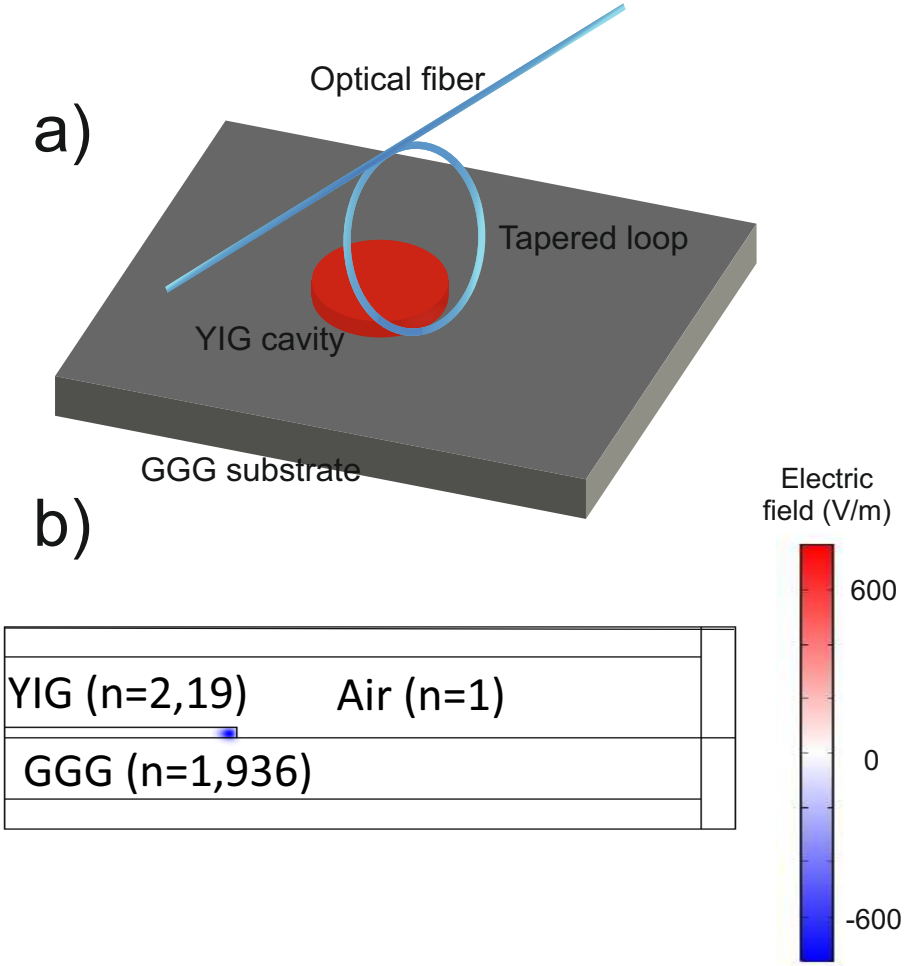

Figure 5.18: (a) YIG disk magnetometer design. The disk is a whispering gallery optical and mechanical resonator. (b) The contrast of refractive index between GGG and YIG allows the optical confinement of modes in the THz's.

5.11 Conclusions

To conclude, we have demonstrated a hybrid system composed by a magnetic resonator coupled by mechanical interaction to a whispering gallery mode optomechanical cavity to detect weak oscillating magnetic fields. A peak magnetic field sensitivity of 864 pT $Hz^{-1/2}$ is achieved associated to a mechanical mode at 206 MHz. In addition to the above excellent characteristics, the tunability of the frequency response up to 1 GHz by changing a static magnetic field, room temperature operation and simplicity in fabrication offer the opportunity of designing a high-performance magnetometer. Larger bandwidths are necessary for real-time applications such as high-speed detection, mechanical signal processing and for high resolution imaging methods [145]. The conversion efficiency can be improved by using the disk cavities made of ferromagnetic YIG. Efforts are in process towards scaling down and also improving the surface quality of the YIG sphere to increasing the WGM quality factors [134]. In addition to the possibilities of designing a

new magnetometer our hybrid device also opens a path towards studying phenomena related to phonon-magnon coupling. Currently, magnons are gathering increasing attention in spintronics experiments (e.g. magnonics [128] and spincaloritronics areas [124, 177]) as a means of processing spin information and managing heat in nanoscale structures. Its superior properties make YIG nearly ideal choice for spintronic applications. However, little is known about the underlying physical mechanisms involved, mainly related to phonon-magnon interactions. Our experiment can be seen as a novel method to improve the understanding about these interactions, in particular investigating phonon contributions via the magnetostrictive coupling.

Chapter 6

Synchronization of two optomechanical crystals by mechanical interaction

6.1 Introduction

Back in the 17^{th} century, Lord Huygens was the first scientist that observed and described a physical phenomena that later on was identified as synchronization [178]. He discovered that two separated pendulum clocks suspended from the same wooden support, that were oscillating at first one independently from the other, ended up oscillating in phase opposition. Huygens accurately described his observations and suggested that synchronization was established because of the oscillation of the wooden beam on which the pendulum were hanging from. The original objective of Huygens's experiment with clocks was to determine the longitude during a sea trial [179].

Synchronization is a physical phenomena that manifest in all branches of nature and science. It happens when two or more oscillatory and independent systems, which are not isolated from their environment, spontaneously lock to a common frequency. After Huygens's experiment, in the nineteenth century, Lord Rayleigh discovered synchronization in acoustic systems [180]. He observed that two distinct organ-pipes started to sound in unison if they were similar enough. He also discovered the suppression of oscillation when the coupling became too strong, phenomena that is known as quenching.

Synchronization studies reached a new level with the development of radio and electrical engineering. Eccles and Vincent demonstrated that two coupled triode generators oscillate with the same frequency even when their natural frequencies were different before the coupling force was turned on [181]. Shortly after that, Appleton and van der Pol extended the experiments of Eccles and Vincent and developed the first theoretical analysis of

synchronization on triode generators [182, 183]. This research was of particular importance since triode generators were the main elements of radio communication devices.

The mechanism of synchronization appears at all observational lengths extending from the subatomic to the cosmic scales [184–189]. Traditionally, the center of gravity of research in synchronization phenomena was established in biological systems, where it was possible to find synchronization in multiple cases: from fireflies blinking in synchronicity [186], group formation of schools of fish and flocks of birds [187] to synchronous phenomena in bacteria [188] and cells [189].

In the last decade, with the advents of modern technology, there has been interest in the observation of synchronization on different devices. For example, a laser emits coherent light from synchronized atoms emitting in phase [190]. Josephson Junctions are systems formed by two superconductors separated by a thin insulating layer. The synchronization of two Josephson Junction is the basic principle of a SQUID device, which is used to measure extremely low magnetic fields (see Chapter 5) [191, 192].

Technological interest on synchronized nano mechanical oscillator systems (NEMS) is also high, because of their wide practical applications that goes from their scalable architecture, accurate control of operating frequencies to their quality factors by design [193–195]. Synchronized NEMS will provide the basis for a new class of self-driven NEMS networks for on-chip robust time keeping [196] and for mass [197], gas [198, 199], or force sensors [154] with extremely low phase noise [179]. Another possible use of synchronized NEMS would by the implementation of neural networks[200], which would be supported on the vast theoretical literature dedicated to the synchronization of oscillator networks [201–203].

The impressive progress in the field of optomechanics (OM) during the last decade [99, 100, 204, 205] has led to the conclusion that micro and nano-optomechanical systems are also ideal platforms for the observation, control and exploitation of synchronization phenomena [198]. However, the field of OM oscillator networks is in its infancy, being restricted to purely theoretical work and experimental proposals [206, 207].

In this chapter it is demonstrated unambiguously the synchronization of the coherent mechanical motion of a pair of one-dimensional silicon OM photonic crystals (OMCs) integrated in the same chip. The OMCs interact weakly by means of an engineered mechanical link, thus avoiding the need for external feedback loop schemes. The Chapter is organized as follows: first I give a precise definition for synchronization; then, I explain different synchronization approaches in optomechanics and NEMS systems; after that I will describe the device used in this experiments; finally, I will detail the experiments that demonstrate synchronization of the OMCs.

6.2 Synchronization definition

Synchronization is a deep tendency towards order in nature. Despite that synchronization phenomena is pervasive, it is possible to assign some basic fingerprints to synchronized systems. They obey some fundamental laws even though the differences in the coupling nature and dynamics of the particular examples. Therefore, in order to discard ambiguity, a precise definition for synchronization must be given. This will address synchronization to specific conditions that different experiments need to achieve so we can distinguish what is and what is not synchronization. A clear-cut definition for synchronization, and the one used throughout this Chapter, can be found in Ref [179] (see, for example page 8) and can be summarized in the following way:

- First and foremost, the individual system needs to be in a particular state of self sustained oscillation. The rhythm must be maintained by a source that is characterized only by internal properties of the system. However, since real systems present dissipation channels because of multiple processes, the overall system needs to pump energy from a DC source and convert it into and oscillatory motion. In this sense, the system can not be a resonantly driven mechanical oscillator.

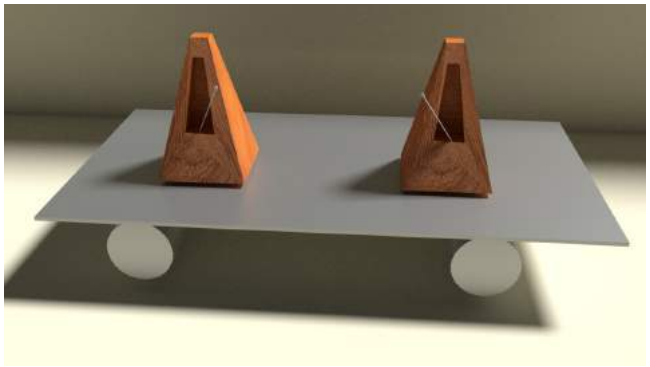

Figure 6.1: A classical example of synchronization of two metronomes sitting on a board which lies on two wheels. The metronomes start at different frequencies and after a while they end up oscillating sharing the same phase.

- The second condition is that the systems adjust their frequency due to a weak coupling. This means that the oscillators need to be almost independent from each other. If we look at any of them at a particular instant we can find them oscillating with different amplitudes and different frequencies. This is summarized by saying that the energy scale of the mechanism that induces the interaction is much smaller than their particular energy scale. The weak coupling in Huygens experiment was the bar on which the pendulums were supported. This beam could bend, or it may vibrate slightly but this motion was not affecting much to the pendulums. The significant role of the supporting

structure was only that the motion of each pendulum was transmitted through it. In Fig. 6.1, it is shown a classical synchronization experiment with metronomes supported by a common platform on two wheels. The metronomes oscillate independently at different frequencies at the beginning and finally end up oscillating in phase due to the fact of sharing the same movable floor.

- The third condition is that such synchrony only happens when the natural oscillation frequencies of the set of objects are close enough to each other. The adjustment of rhythm occurs from a certain range of systems mismatch. Therefore, the detuning of the oscillating system should be small.

6.3 Previous experiments on synchronization

Several routes have been explored to demonstrate synchronization of two or more systems at the nanoscale in the last decade. However, regarding optomechanical oscillators, there is some controversy if these experiments satisfy all the requirements imposed by the definition given in the previous section for a synchronized system.

As examples that illustrate how challenging is to achieve synchronization, we name two works from Zhang et al. [52, 208] and Bagheri et al. [53]. The first reference deals with the synchronization of two double disk resonator separated by a distance of 400 nm, as shown on Fig. 6.2a. As a consequence of the near field coupling, the optical modes of the disks formed one symmetric and an anti-symmetric supermode. This makes that light coupled to one of these optical resonances travels through both cavities. Then, by optomechanical interaction, the mechanical oscillation of one cavity was coherently driven and this tuned the mechanical oscillation of the second cavity. Due to the mutual optical interaction, the modulation of the second cavity was reciprocal on the first cavity, recieving also an incoming modulation from the second system. The two cavities then evolved to an oscillating frequency common to both cavities. On the second experiment referenced from Zhang, the number of cavities was extended up to an array of six double disk resonator [208]. The work from Bagheri investigates the synchronization of two mechanical resonators separated by 80 μm distance [53] (see Fig. 6.2b). The two resonator consisted in a beam that could be buckled up or down and both were part of a single optical racetrack. Light coupled from a laser circulated by the two beams.

In both experiments explained in both articles by Zhang and Bagheri, two mechanical oscillators were coupled to one single optical cavity driven at high power. Then, both experiments compromise the weak interaction condition to observe spontaneous synchronization. This becomes more evident if the interaction of both modes with the optical field is strong because of the emergence of mechanical hybridized modes that naturally induces the

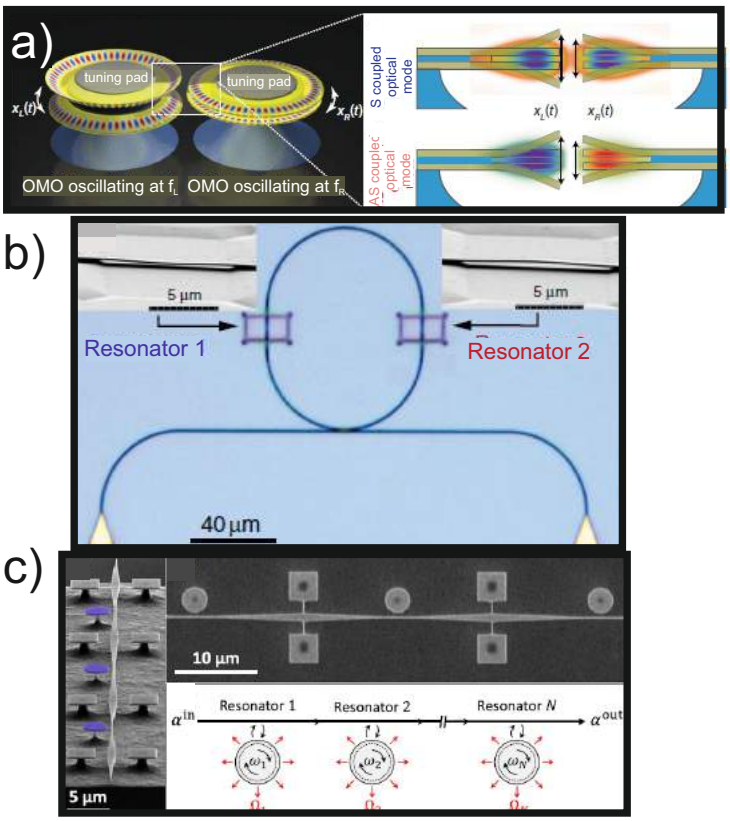

Figure 6.2: (a) Synchronization of two double disk separated by a distance of 400 nm. [52, 208] (b) Mechanical resonators linked in an optical racetrack [53] (c) Optomechanical GaAs disk resonators coupled to a suspended tapered waveguide [54].

simultaneous oscillation of the resonators at intermediate frequencies. We cite another experiment, reported by Gil-Santos et al. [54], in which they report the frequency locking in optically coupled cascaded resonators (see Fig. 6.2c). They used a single laser to shift the wavelength of one cavity via the termo-optic effect, reducing the spectral difference between the resonances of the different cavities and driving both of them to mechanical lasing state and finally frequency locking. They used this mechanism to synchronize several OM disk resonators. However, the coupling mechanism involved a biderectional optical coupling, as in the previous works referred.

Concerning NEMS with purely mechanical coupling, Shim et al. [193] reported a resonant excitation of coupled resonators using an external source. This conflicts with the condition that the oscillators must be self-sustained. It is particularly relevant the work from Matheny et al. [195], where they set a playground for the study of synchronization since both the coupling strength and the natural frequencies of the oscillators could be controlled, however the high impact of the external feedback loops required for both self-sustained motion and weak interaction make this type of system a complicated candidate for strictly on-chip operation.

A couple of works have reported long-range synchronization between OM cavities placed in different chips [55, 56, 209]. The coupling mechanism in the first case relies on modulating the optical excitation of one of the cavities with an electro-optical modulator (EOM) that reproduces the dynamics of the other cavity. On the second case the two cavities are connected to an electrically driven frequency comb. The conflict with the definition of spontaneous synchronization in both cases would be on the external actuation (in this case the EOM or the comb) are affecting the dynamical state of both systems.

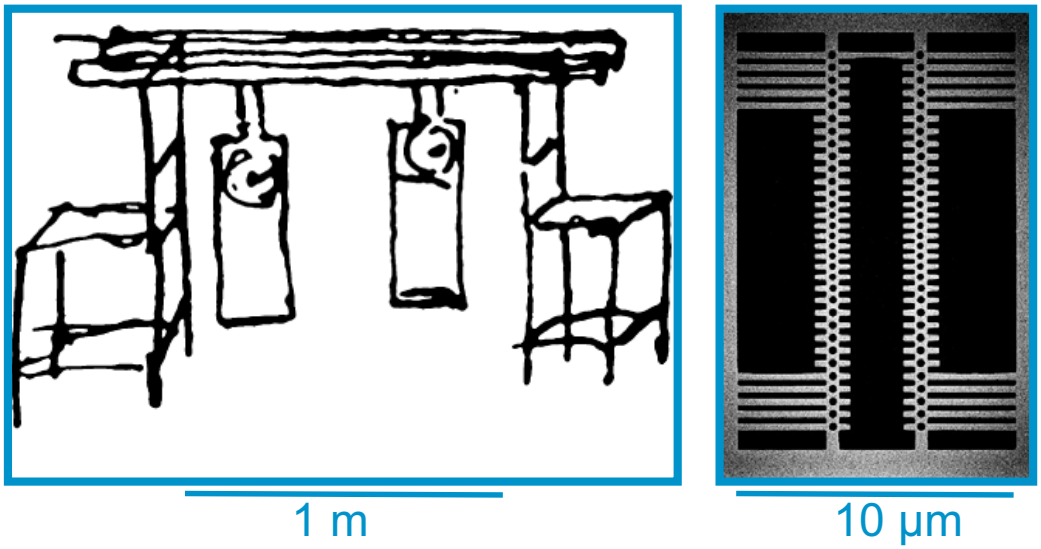

Figure 6.3: (Left) Original draw illustrated by Christiaan Huygens. The two pendulum clocks connected by a common support. (Right) Nanosized 'Pendulum' formed by two optomechanical crystals connected by a silicon beam. This experiment is equivalent to a shrunken version of Huygens's pendulum.

To summarize, the objectives of the experiments could be described in two:

- Unambiguously demonstrate synchronization of the motion of two mechanical oscillators based in optomechanical crystals, following the definition given in Section 6.2
- Ease on-chip integration. This would be guaranteed by the use of silicon based technology. In this experiments, the coupling of light is performed with tapered fiber with the possibility of waveguide integration in the same chip.

For such purpose we decided to take the primal experiment by Huygens with macroscopic pendula and to rescale it to the nanoscale. In the subsequent section we will describe the device use throughout this chapter and how it tackles the requisites imposed to achieve synchronization.

6.4 Device description

The device investigated in this Chapter is a pair of nominally equivalent one dimensional OMCs integrated on the same chip. The nanobeams are fabricated using standard Si nanofabrication processes in a silicon on insulator wafer. The relevant parts of the device are shown in Fig. 6.4.

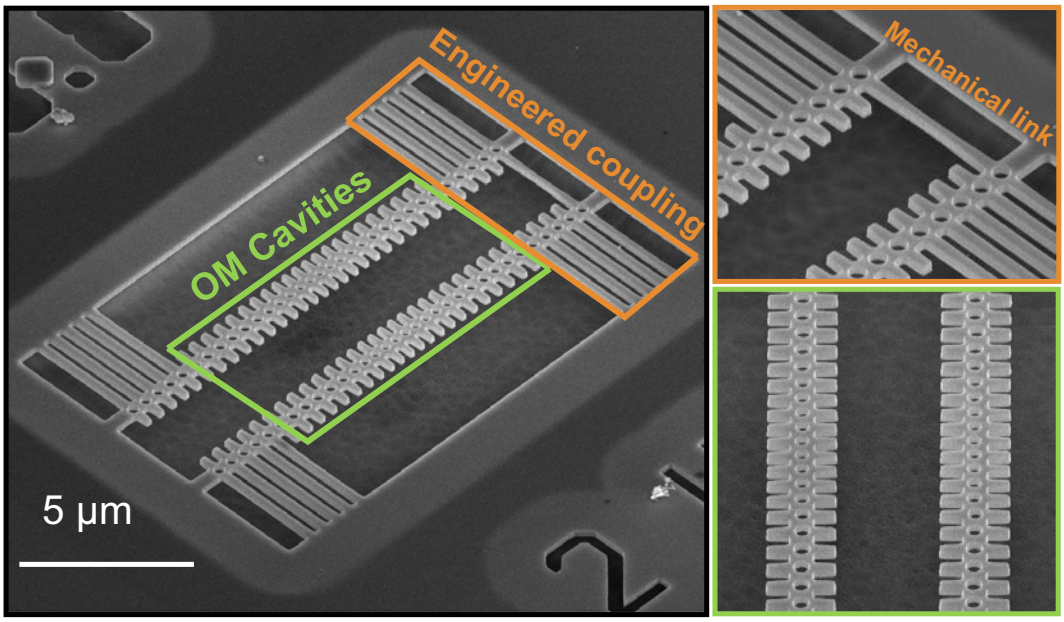

Figure 6.4: (a) SEM image of the pair of OMCs under study. The two cavities are corrugated nanobeams that are anchored to the frame. The two cavities are separated by a distance of 2 μm. Both system are mechanically couple by a mechanical link and also the common frame.

As it is shown in Fig. 6.4, the device is formed by two corrugated nanobeam separareted by a distance of 2 μm. The nanobeams are clamped to the partially underetched Silicon frame. This allows to decouple the mechanical modes from the frame and confine them to the central region of the OMCs. Each cavity is designed to support high Q optical cavity modes at around 1.5 μm.

The defect region of the OMCs, shown in the central part of the green square in Fig. 6.4, consists of 12 central cells in which the lattice distance (a), the radius of the hole (r) and the stubs length (d) are decreased in a quadratic way towards the centre. The maximum reduction of the parameters is denoted by the parameter Γ. At both sides of the defect region a 5 period mirror followed by 5 cells clamped to the frame are included. The nominal geometrical values of the cells of the mirror are a = 500 nm, r = 150 nm, and d = 250 nm. The total number of cells is 32 and the whole device length is about 15 μm. All the results presented in this work correspond to the structure with Γ = 85%.

The OMCs are mechanically interconnected on one side by a tether that links the inner stubs of the last cells. The physical separation between the two

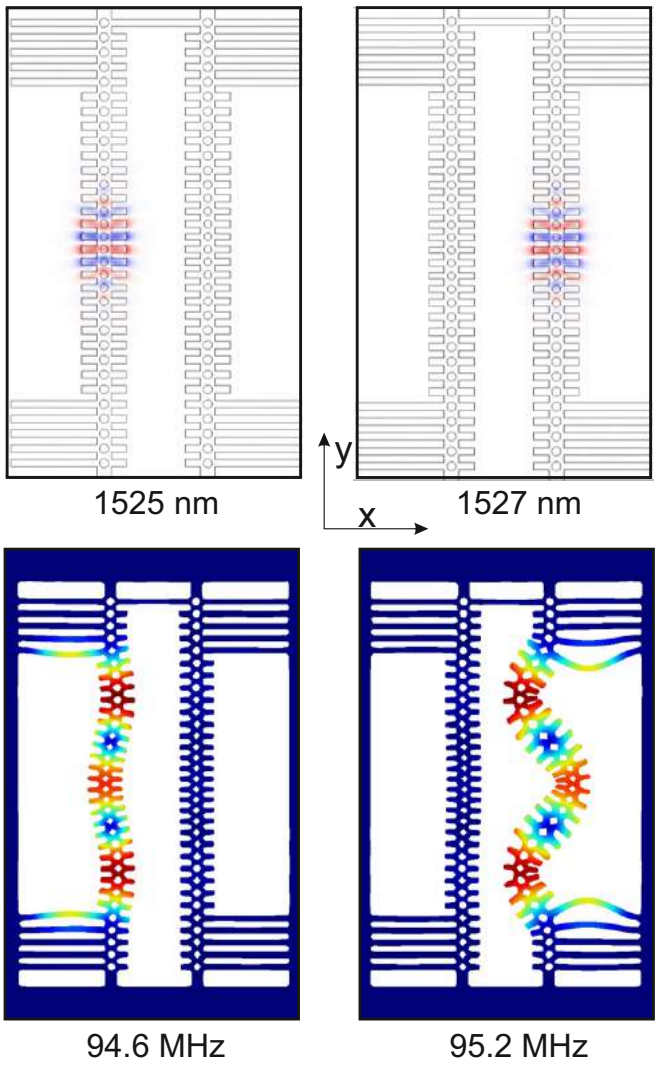

Figure 6.5: Optical and mechanical modes of the nanobeam. In the The cavity at the left (Slave) is charactirezed by an optical mode with wavelength λ_S = 1525 nm and a mechanical mode of 94.6 MHz. The cavity at the right (Master) presents an optical and mechanical mode of λ_M = 1527 nm and 95.2 MHz

nanobeams is large enough to prevent optical crosstalk while allowing for their simultaneous optical excitation using a single tapered fiber that is placed in between. We investigate the fundamental mode optical cavity mode of each OMC, which is shown in the top part of Fig. 6.5. These modes display high values of single-particle OM coupling rate (g_{OM}) for in-plane (xy plane) flexural modes. In particular, the ones having three antinodes along the x direction (shown in the bottom part of Fig. 6.5), which display a frequency of Ω_M= 95.2 and Ω_S= 94.6 MHz in each OMC and a calculated value of $g_{OM;M}/2\pi$ = 514 and $g_{OM;S}/2\pi$ 330 kHz. Hereinafter, we adopt the notation M and S to denote master and slave, where the OMC displaying higher frequency and longer optical resonance wavelengths is the master and the other the slave.

It is worth remarking that the adopted master and slave notation must not be associated with any sort of injection locking scheme since the oscillator used in this experiment can freely adapt their oscillation phase. The notation reflects the fact that, in the self sustained oscillation (mechanical lasing in this experiment), the master oscillation amplitude is significantly larger, so that its dynamics is much less sensible to the slave oscillations than the other way around. This notation is commonly found in literature for oscillators with unidirectional coupling.

To guarantee a weak mechanical interaction, it is important that the two cavities have different wavelengths in order to prevent direct optical interaction. In order to solve this, we use the intrinsic fabrication disorder, that for the fabricated geometry leads to a difference of 2 nm in the wavelength of the cavities. This is shown in Fig. 6.5, where the optical modes of the investigated device are obtained from imported SEM images. It can be seen that the spatial distribution of the electromagnetic field is localized on the center of each nanobeam. One cavity presents the fundametal mode at λ_S = 1525 nm and the second at λ_M = 1527 nm.

The last requirement for spontaneous synchronization about the slight mismatch in mechanical frequency is also granted by the dispersive effect of fabrication imperfections. The simulated mechanical modes are shown in Fig. 6.5. For our fabricated structure we see that the third order string-like mode (the one that eventually is driven to the self sustained state in the experiment) of the two beams exhibit a frequency mismatch of around 0.7 MHz.

In contrast to the previous works in literature [52–54, 208], the OMCs are optically isolated from each other, independently measured, and individually driven to a state of high-amplitude, coherent, and self-sustained mechanical motion using the anharmonic modulation of the radiation pressure force due to the activation of a self-pulsing (SP) regime described in Chapter 3 and detaily reported in literature [95, 107, 210]. Essentially, the SP limit cycle is the solution of the system of coupled differential equations governing the free-carrier concentration and the effective temperature of the cavity region within a wide range of excitation laser wavelengths and powers. That dynamical interplay between free-carrier-dispersion (FCD) and the thermo-optic (TO) effect implies an oscillation of the cavity resonance around the laser line at a frequency (ν_{SP}) that depends on the laser parameters. If a mechanical mode is partially resonant with one of the harmonics of νSP, it can be driven into mechanical lasing. Moreover, by means of the OM coupling, the mechanical motion frequency entrains the SP such that ν_{SP} is forced to be a simple fraction of the mechanical eigenfrequency. An important feature of this regime is that its frequency can be thermally tuned by modifying the laser wavelength, given that the average temperature of the OMC increases with the laser wavelength around which the mechanical lasing limit cycle takes place due to a larger average intracavity photon number (n_o).

6.5 Synchronization experiments

6.5.1 Optical differentiation of cavities

The first experiment that we performed on the studied device is an optical characterization of the OMCs. We observed a set of pairs of modes in the full span measured with the objective of identifying the optical resonances of both cavities. We show in the top panel of Fig. 6.6a the first two modes. In principle, before confirmation these two modes are supposedly the fundamental optical cavity modes of the two beams.

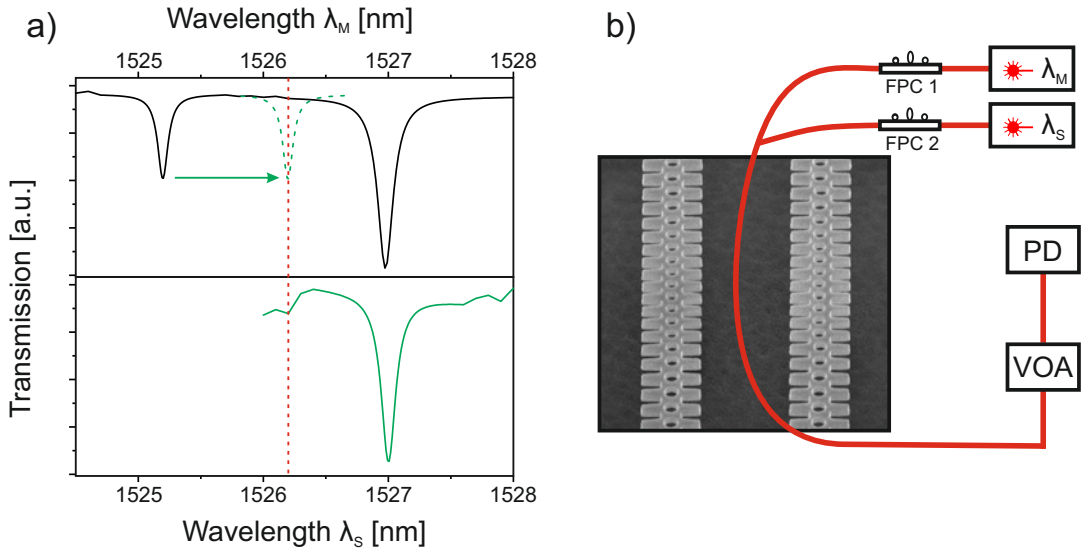

Figure 6.6: (a) The two cavities optically differentiated by using the spectral redshift of the TO effect. The top panel shows two optical modes from the transmission spectra and the position where the first optical mode is shifted at high power. The bottom panels is the optical spectra obtained with the second laser. It shows that the second resonances is not shifted confirming that it belongs to the second cavity. (b) Experimental set up. Two infrared laser are used to send light to the device. The two beams are TE polarized with a Fiber Polarization Controller (FPC) are combined before exciting the cavities. We use a tapered fiber placed in between the nanobeams. The light is attenuated with a Variable Optical Attenuator (VOA) and is sent to a photodetector.

In order to check whether the observed optical resonances are hosted by different OMCs, we excite the first resonance and redshift it using the TO effect around 1 nm from λ = 1525 nm to λ = 1526.2 nm. In the top panel of Fig. 6.6a, we show the position of the optical resonance with a green dash line. The power used in the laser was P$\sim$ 10 mW (the set up used is shown in Fig. 6.6b). In this configuration, we perform a low-power measurement with a second laser from λ = 1526.5 nm to λ = 1529 nm. If the spectral position of the second resonance is not changed it means that the region of space where

it is localized is not affected by the temperature rise, proving that the mode is localized in the other nanobeam.

In the bottom panel of Fig. 6.6a we show the measured spectra with the secondary laser around the spectral position of the second mode. It reveals that optical resonance remains unchanged, demonstrating that the optical cavity modes correspond to the other nanobeam. This procedure is used to identify the correspondence between optical modes a cavities on these devices.

6.5.2 Synchronization in the frequency domain

The experiment that demonstrates synchronization of the dynamics of the two OMCs is illustrated in Fig. 6.7, where the left (slave) and right (master) panels report the radio frequency (rf) spectra of the optical transmission associated to the laser exciting the slave and master, respectively. The protocol to observe synchronization needs to be carefully designed in order to maintain the two optical cavities spectrally apart despite the presence of themo-optic shifts.

We start using one laser to scan in between the two optical resonances and use it to push the resonance of the master at high power from λ_M = 1527 nm to λ_M = 1531 nm using the TO effect. The second laser is then used to excite the resonance of the slave at λ_S 1529 nm, also at high power. At this point the two cavities are 2 nm away from each other, ensuring no optical crosstalk.

The observed transmission spectra through the fiber with a Spectrum Analyzer setting the filter resonant with the second laser, shows the mechanical state of the left nanobeam. This is shown in Fig. 6.7a, where we observe a sharp and intense radio frequency tone when $\lambda-\text{filter}_1$ is tuned at λ_S 1529 nm. The incident power values were $P_{in,M}$ = 8 mW and $P_{in,S}$ = 3 mW, respectively. The master is mechanically excited by the coherent motion of the slave leaking its motion to the other cavity. This phonon detection from the master cavity is due to the nonzero mechanical intercoupling of both OMCs. Indeed, when detecting at λ_M = 1531 nm this excitation appears as a sharp rf tone at 94.6 MHz, as shown in Fig. 6.7b. A broad peak centered at 95.3 MHz is also present under this configuration, which is associated to the transduction of the thermally activated motion of the mechanical mode localized in the master.

From now on, we fix the laser driving and continue sweeping the first laser to drive the master cavity. By further redshifting λ_M up to λ_M = 1540.2 nm, a mechanical lasing regime is also established in the master. A strong tone appear in the spectra shown in Fig. 6.7c and 6.7d. At this point, the two oscillators are in a self sustained state but oscillating at different frequencies. We also observe that Ω_M decreases due to material heating. This latter effect appears to be also experienced by Ω_S to a weaker extent; i.e., part of the heat generated in the master could end up increasing the effective temperature of the slave. However, it is also plausible that the master is frequency pulling

the slave towards lower frequencies [184]. Due to the fact that both OMCs are in a mechanical lasing regime, the spectral oscillation amplitude of the optical resonance is much larger than its linewidth and the transduction becomes extremely nonlinear [211]. Therefore, an additional rf peak appears at the beating frequency ($\Omega_M - \Omega_S$) together with symmetric sidebands at both sides of the lasing tones of the OMCs, which still lase at their own rhythm (shown in Fig. 6.7c and 6.7d).

The comparison of the rf spectra of both OMCs show that the mechanical amplitude of the master is much larger than that of the slave as expected from the larger $g_{o,M}/2\pi$ and $P_{in,M}$ values. The dynamical state of the two OMCs remain qualitatively the same until λ_M reaches λ_M = 1542.3 nm, where the coupled system enters into a transition region. There, the slave displays a complex rf spectrum of multiple peaks in which the main one is at Ω_M (see 6.7e and 6.7f, where λ_M = 1542.9 nm). This state is not yet synchronization, even though the slave is strongly affected by the dynamics of the master, the resulting state being of a quite complex nature. The peak initially adscribed to its particular motion being already smaller in amplitude than the one coming from the other nanobeam, whose motion is barely affected by the oscillation state of the slave cavity.

Above λ_M = 1543 nm, both OMCs coherently oscillate at $\omega_{sync} \approx \Omega_M$. This is shown in Fig. 6.7g and 6.7h, where λ_M = 1543.6 nm. At this point, synchronization is achieved. Both rf spectra look very similar with the remarkable difference of the presence of broad sidebands on the signal corresponding to the slave, which are absent from the rf spectra of the master. Those sidebands are clear signatures of master-slave synchronization and have been reported and analyzed in previous works addressing synchronization of photonic cavities [53]. Their origin lies in the effect of the thermal force noise on the dynamics of the system. These forces push the slave phase trajectory out from the limit cycle of the synchronized state, returning back in an oscillatory fashion at a frequency of ($\Omega_M - \Omega_S$). On the contrary, no sidebands appear on the master spectrum, as it overdampedly returns to the limit cycle when driven away from it (see Supplemental Material of Ref. [212]).

The color 2D plots of Figs. 6.7i and 6.7j show the full travel in wavelength, showing the transition from independent lasing of the two oscillators to the synchronized state. It is clear that while the mechanical frequency of the master nanobeam is reduced due to increased heating, the frequency of the slave increases. This frequency pulling is a fingerprint present on the path toward synchronization. Even though the mechanical link is essentially bidirectional, the highest oscillation amplitude of the master cavity both due to a higher photon number and to a higher optomechanical coupling as seen via the simulated structure, they bias the bidirectionality of the interaction.

Despite having established that we are in a master- slave configuration, we can observe from Fig. 6.7i and 6.7j that this definition of the coupled system is fact an oversimplification since Ω_M is also slightly pulled towards Ω_S. This is evidenced in the abrupt frequency jumps of Ω_M both when entering the

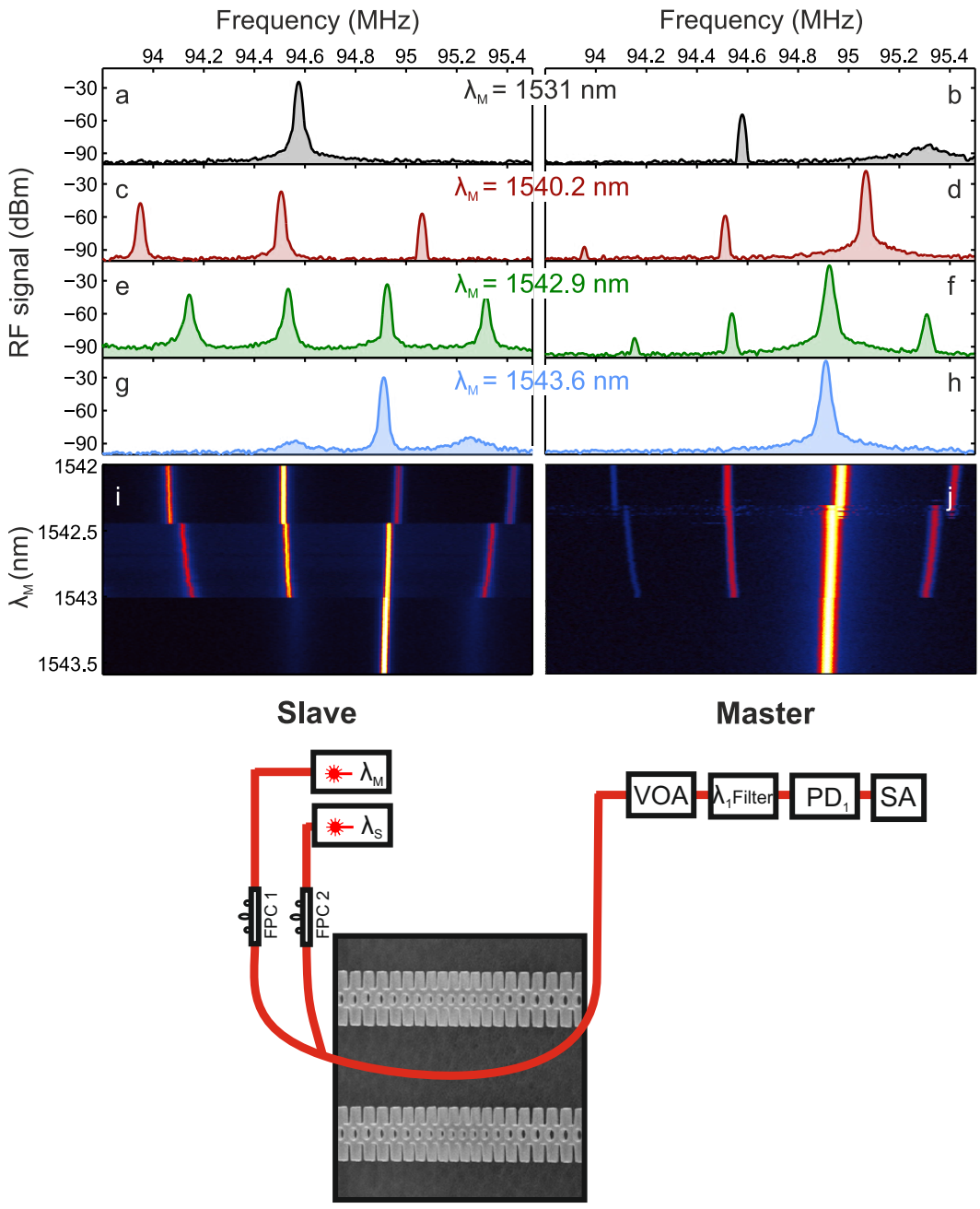

Figure 6.7: Top panel.(a)–(h) Radio-frequency spectra of the optical transmission associated to the slave (left panels) and the master (right panels) for different values of the wavelength of the laser driving the master (λ_M). The wavelength of the laser driving the slave is fixed at λ_S = 1529 nm. (i)–(j) Color contour plots of the rf spectra as a function of λ_M of the slave and master [(i) and (j),respectively]. Bottom panel. Schematic of the experimental setup. The optical transmission of a single cavity can be isolated from the other by means of λ-filters. Variable optical attenuator (VOA); fiber polarizer controller (FPC); spectrum analyzer (SA); oscilloscope (OSC); photodetector (PD)

transition region above λ_M = 1542.3 nm and the synchronized states above λ_M = 1543 nm.

6.5.3 Synchronization in the time domain

Besides the frequency domain analysis of the synchronization experiment, we have also measured and analyzed the temporal traces of the two oscillators. As shown by Fig. 6.8c, the set up configuration for this experiment used two λ-filters and two detectors connected to the oscilloscope.

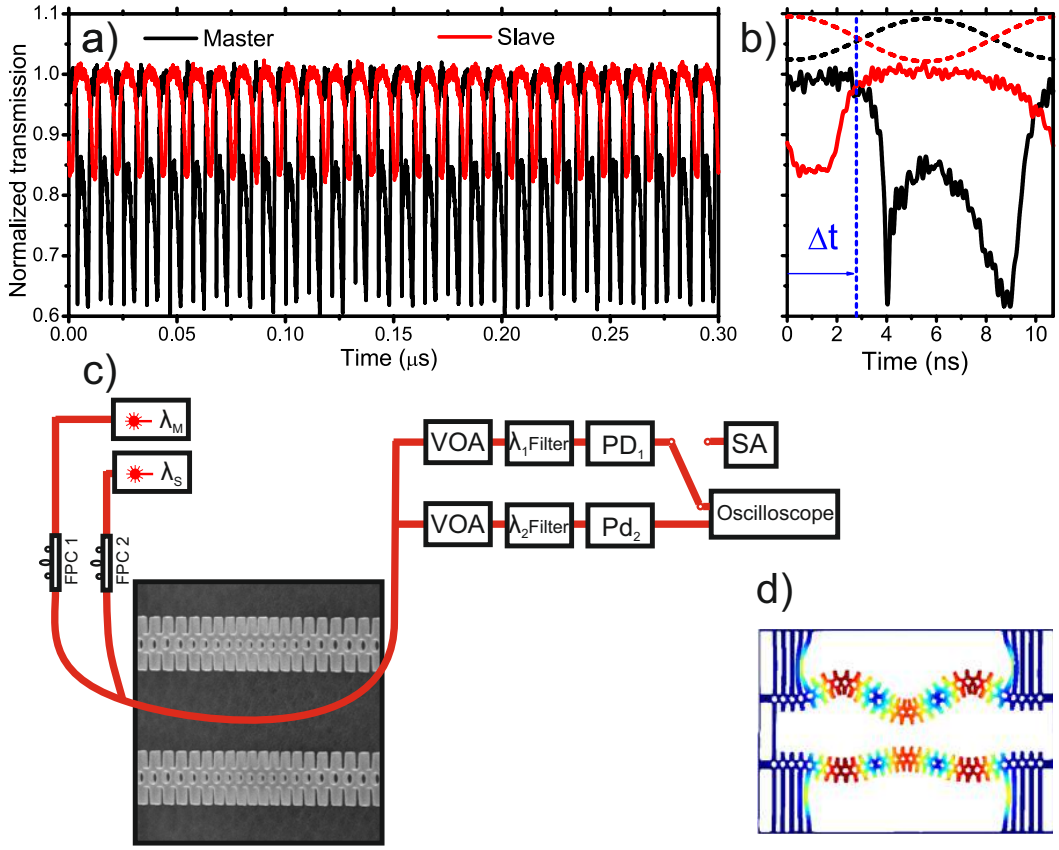

Figure 6.8: (a) Temporal traces of the optical transmission of the master and slave cavities (black and red curves, respectively) as recorded simultaneously in the two channels of the oscilloscope. (b) Enlargement of a single period of the two signals. The simulated normalized generalized mechanical deformation corresponding to the experimental transmission traces are also reported (dashed lines). (c) Schematic of the experimental setup. In this experiment the outcoupled light is splitted and we use two filter and two photodetectors.(d) Finite element simulation of the two nanobeams oscillating in antiphase.

The temporal traces of the transmitted optical signal associated with each OMC are simultaneously recorded over a time span of 4 μs. In Fig. 6.8a we report the first 300 ns and an enlargement of a single period appears in Fig.

6.8b. We note here that there is no phase retardation between the two signals, i.e., they have the same frequency. An important point to consider here is that the maximum mechanical deformation of the master is achieved in between the two minima of the optical transmission of the slave, as is shown in Fig. 6.8b. We can thus conclude that the temporal delay between the mechanical signals of each oscillator is about half of the period, i.e., there is a π phase shift between the mechanical oscillations. This type of configuration is depicted in Fig. 6.8d.

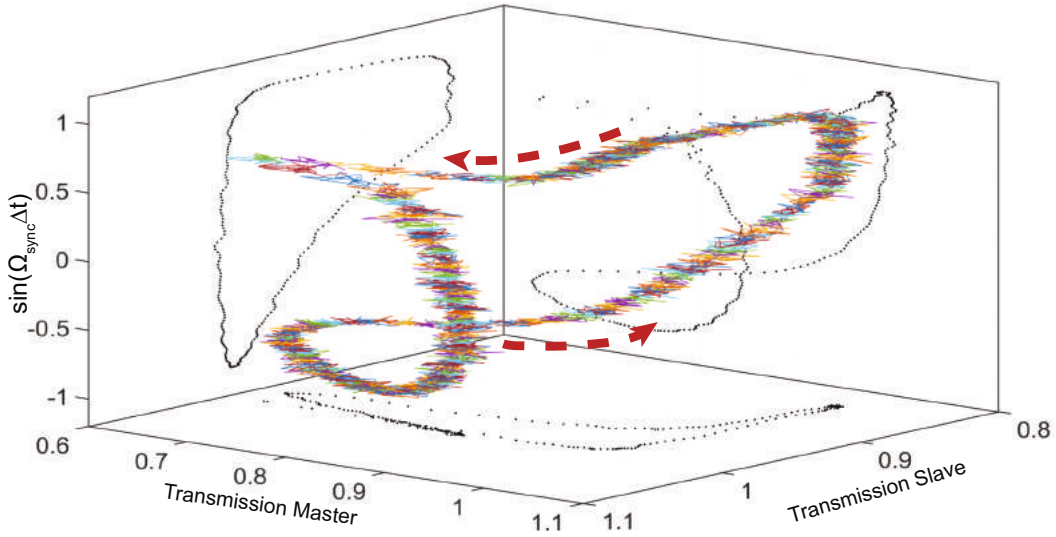

Figure 6.9: Poincare map of the full temporal traces using the stroboscopic technique with a sampling frequency of Ω_{Sync}. Each colored curve corresponds to a different value of the initial delay (Δt). The magnitude of the vertical axis has been chosen to be sin(Ω_{Sync}) to illustrate that the trajectory in the phase space is a closed cycle.

In order to analyze the quality of the synchronization signal, we show in Fig. 6.9 the Poincare map associated with both temporal traces. This map is obtained using a stroboscopic technique; i.e., we collect the pair of values transmission master, transmission slave at a specific sampling frequency. If the oscillators are synchronized and the temporal traces are sampled at ω_{sync}, a point on the Poincare map is always found in the same position. In that case the phases of the two oscillators are the same for every sampled point of the traces, which is consistent with the experimental observations. Each of the colored curves in Fig. 6.9 corresponds to a stroboscopic sampling at ω_{sync} for a specific value of the initial delay [Δt; see Fig. 6.8b]. The Poincare map of the system is then formed by changing the initial Δt from 0 to $2\pi = \Omega_{sync}$ in the following way,

$$t_i = \Delta t + \frac{2\pi N}{\Omega_{sync}}$$

it is possible to rebuild the limit cycle of the synchronized state in the optical transmission phase space. The points remain in a confined volume of the phase space that is dominated by the experimental noise.

6.6 Synchronization switching experiment

Finally, in order to add functionality to our system, we explore the effect of illuminating the master cavity region with a top heating laser. Based on previous work on a single OMC showed that its dynamical state is modified when the laser is switched on because of photothermal effects [213]. Now, before switching on the top pumping, we set the parameters of the laser driving the slave in a way that its dynamical state is a mechanical lasing regime at Ω_{Sync} activated by the 3rd harmonic of the optical force [210]. The master is then driven to a mechanical lasing regime using the 1st harmonic of the force, where both cavities synchronize their mechanical oscillations at Ω_{Sync}, as it is shown in Figs. 6.10a and 6.10c.

It is important to note that, under this configuration, the first harmonic of the optical transmission of the slave is at $\Omega_{Sync} = 3$ and that there are no signs of the 1st and 2nd harmonic of that signal when measuring the master. The latter observation is a conclusive evidence of a pure mechanical coupling between the OMCs, the leaked mechanical energy being enough to be transduced despite the rather low cross coupling go (see Supplementary Information of Ref. [212]).

When the heating laser is switched on the system is perturbed and the synchronized state is deactivated and a dynamical state similar to the one reported in Fig. 6.7c and Fig.6.7d is achieved in the slave. This is shown in Fig. 6.10b. The master still shows a coherent tone at Ω_{Sync} [Fig. 6.10d] but narrow symmetric sidebands appear associated with frequency beating with the coherent mechanical oscillation of the slave. Although the elastic constants of the master are slightly relaxed due to heating, Ω_M shifts to a higher frequency value. This counter intuitive effect is a result of the attenuation of the frequency pulling effect induced by the coupling to the slave mechanical dynamics; i.e., when the synchronized state is spoiled the coupling is reduced and Ω_M goes towards the eigenfrequency of the master at that temperature. The same phenomenon occurs to Ω_{Sync} in the opposite direction and in a much larger scale [red arrow of Fig. 6.10b].

By using the set up configuration shown in Fig. 6.10h, we can imposing a the modulation of the top pumping laser following the temporal profile of Fig. 6.10e. This allows to dynamically switch between the two states described above. We take the temporal traces of the master and the slave triggering the oscilloscope with the modulation signal. Both traces are shown in Fig. 6.10f and Fig. 6.10g, respectively. When the pump is switched off the OMCs take

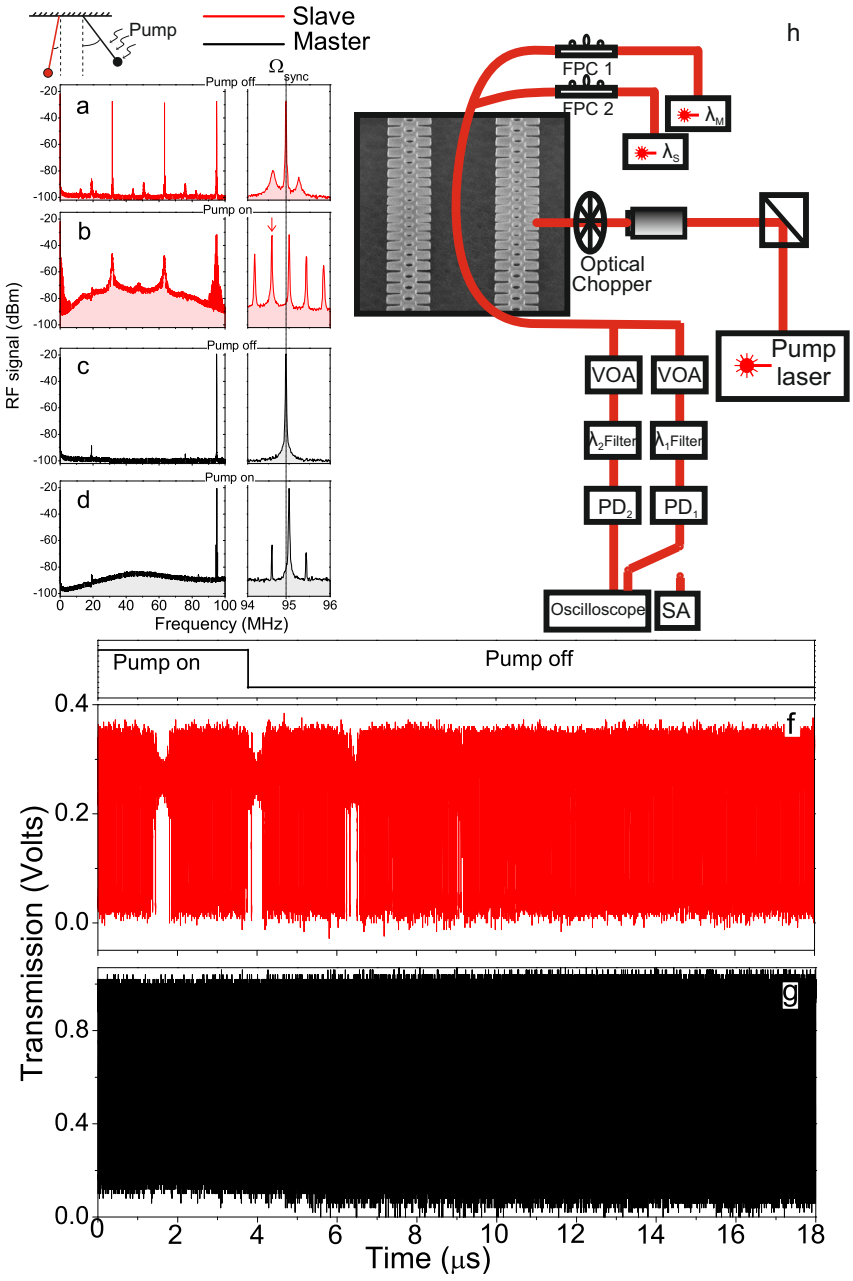

Figure 6.10: Switching on and off the synchronized state. (a)–(d) Radio-frequency spectra of the transmitted signal of the slave [(a) and (b)] and master [(c) and (d)] when the pump is off [(a) and (c)] and on [(b) and (d)]. The right panels correspond to an enlargement in the spectral region around the mechanical modes frequencies. The synchronized state frequency (Ω_{Sync}) is highlighted with a vertical line on the right panels. A vertical red arrow indicates Ω_{Sync} in the right panel (b). (e) Temporal trace of the top pumping laser when the modulation is active. (f)–(g) Temporal traces of the optical transmission of the master and slave cavities [(f) and (g), respectively] when the master is illuminated with a modulated top pumping laser. (h) Schematic of the set up configuration.

about ∼10 microseconds to adjust their oscillation rhythms and stabilize the mechanical synchronized state, which is a direct consequence of their weak interaction.

6.7 Numerical model for synchronization

In this section, a numerical model to study the dynamics of the coupled OMCs is presented. The model consists on a set of eight first order non linear equations, four for each of nanobeam. The full dynamic of each system is described by the nonlinear effects that trigger the self pulsing mechanism (already explained in Chapter 3), the mechanical displacement and its derivative (u_i and $\dot{u}$, respectively).Apart from the displacement variables we consider the free carrier population (N_i), the average cavity temperature increase (ΔT_i). The subindex i is associated to one of the two cavities i=M,S. For simplicity, we have considered that the OMCs are equivalent in all their characteristic parameters but the mechanical eigenfrequencies (Ω_i), which have been taken from the experiment.

Then, the dynamic of the system is described by the following equations:

$$\dot{N}_i = -\frac{1}{\tau_{FC}} N_i + \beta \left(\frac{hc^3}{n^2 \lambda_o V_o^2} \right) n_{o,i}^2 \tag{6.1a}$$

$$\Delta \dot{T}_i = -\frac{1}{\tau_T} \Delta T_i + \alpha_{FC} N n_{o,i}^2 \tag{6.1b}$$

$$\ddot{u}_i + \frac{\Omega_{m,i}}{Q_{m,i}} \dot{u}_i + \Omega_{m,i}^2 u_i + \delta_{i,S} D(u_M - u_S) = \frac{F_{o,i}}{m_{eff}} \tag{6.1c}$$

The four equations Eqs.6.1a and Eq.6.1b have been explained in Chapter 3 in the context of the self pulsing mechanism. Eqs. 6.1a describe the Two-Photon Absorption (TPA) generation term, where β is the tabulated TPA coefficient and a surface recombination term governed by a characteristic lifetime τ_{FC}. V_o is the optical mode volume and λ_o is the cavity resonance wavelength at room temperature. Eqs. 6.1b reflect the balance between the fraction of photons that are absorbed and transformed into heat due to free-carrier-absorption and the heat dissipated to the surroundings of the cavity volume, which is governed by a characteristic lifetimeτ_T. α_{FC} is defined as the rate of temperature increase per photon and unit free-carrier density.

Finally, the equations Eqs. 6.1c are the one that correspond to harmonic oscillators driven by optical forces $F_{o,i}$. The mechanical coupling is introduced as a reactive (non dissipative) contribution of the form D (u_M-u_S), being D the coupling strength coefficient. This coupling term can be understood as an elastic restoring force caused by the deviation of the length of the linking tether from its value at rest. The reactive contribution term introduces anharmonicity in the system and increases with the dephasing between oscillators,

being maximum when they are in complete antiphase. In order to implement the Master-Slave configuration we have considered that the coupling is unidirectional towards the Slave, i.e., the reactive term is only present in the Slave harmonic oscillator equation. This situation is equivalent to considering bidirectional coupling with the Master oscillating with a much larger mechanical amplitude. The optical pumping parameters of the model are chosen so that a mechanical lasing regime is achieved in each OMCs in the absence of coupling (D=0).

The two OMCs are coupled mechanically in a unidirectional way while, in the case of a single OMC, the SP and the mechanics are coupled bidirectionally. The driving terms of Eqs.6.1 depend on the number of intracavity photons (n), which can be written as $n = n_o \frac{\Delta\lambda_o^2}{4(\lambda_l-\lambda_r)^2+\Delta\lambda_o^2}$, where $n = n_o = \frac{2P_l\kappa_e\lambda_o}{\kappa^2 hc}$ in perfect resonance. P_l and λ_l are the laser power and wavelength, respectively. The terms κ_e and κ and are the extrinsic and overall optical damping rates, respectively, the latter determining the cavity resonant linewidth ($\Delta\lambda_o = \frac{\lambda^2\kappa}{2\pi}$). The position of the resonance incorporates the FCD and the TO contributions and the effect of the OM coupling with the mechanical mode localized in the same OMC and with that mostly localized in the other OMC.

Taking all the previous considerations into account, the optical resonance is determined by the following terms: $\lambda_{r,i} \approx \lambda_{o,i} - \frac{\partial\lambda_{r,i}}{\partial N_i}N_i + \frac{\partial\lambda_{r,i}}{\partial\Delta T_i}\Delta T_i - \frac{\lambda_{r,i}^2 g_{o,i}}{2\pi c}u_i - \frac{\lambda_{r,i}^2 g_{o,ij}}{2\pi c}u_j$. Importantly, the response of n to the various contributions is adiabatic since κ is much larger than $1/\tau_{FC}$, $1/\tau_T$ and $\Omega_{m,i}$.

The parameters used in Eqs. 6.1a and 6.1b are the one that reproduce the SP dynamics, identical to the ones used in Chapter 3. The corresponding values are τ_T= 0.5 μs, τ_{FC}= 0.5 ns and α_{FC}= 4 $\cdot 10^{-13}$K$\cdot$cm$^3 \cdot s^{-1}$. The initial conditions verify that $\frac{\partial\lambda_{r,i}}{\partial\Delta T_i}\Delta T_i(t=0) = \lambda_{l,i} - \lambda_{0,i}$ and $N_i(t=0) = u_i(t=0) = \dot{u}_i(t=0) = 0$. TO and FCD coefficients were independently calculated by assuming that the observed wavelength shift is only associated to an average change in the Si refractive index within the region overlapping with the electromagnetic fields and using tabulated values for its dependence with T and N. This procedure leads to the following values: $\frac{\partial\lambda_{r,i}}{\partial N_i}$ = 7$\cdot 10^{-19}$ nm$\cdot$ cm^3 and $\frac{\partial\lambda_{r,i}}{\partial\Delta T_i}$ = 6 $\cdot 10^{-2}$ nm$\cdot$K^{-1}. The simulations cover a temporal span of 1$\cdot 10^{-4}$ s discretized in time steps of 2$\cdot 10^{-11}$s, which ensure both enough sampling rate to account for the fastest dynamics of the system and reaching a stationary dynamical regime.

The stationary dynamics of the decoupled system is shown in Fig. 6.11. We have used a coupling coefficient that ensures synchronization (D = 1 $\cdot 10^{15}$ s^{-2}) for decreasing values of Ω_M, reproducing then the heating effect when increasing λ_M, as observed in the experiment. We define a relative change of Ω_M as $\Delta_M = \frac{(\Omega_M-\Omega_{M,o})}{\Omega_{M,o}}$, where $\Omega_M = \Omega_{M,o}$, o at room temperature. The Fast Fourier Transform (FFT) of the simulated optical transmission associated to

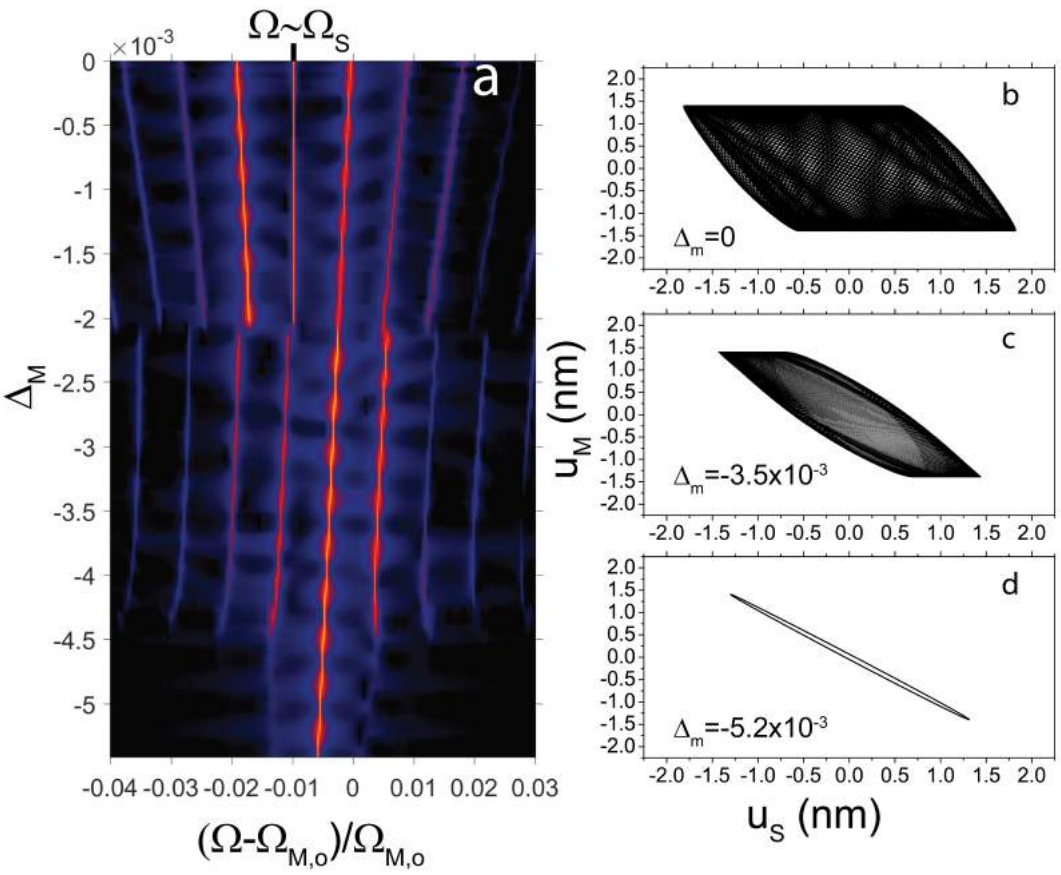

Figure 6.11: Numerical simulations of the coupled OMCs. (a), Colour contour plot of the simulated radio-frequency (RF) spectrum of the optical transmission of the Slave as a function of the normalized frequency shift of the Master $\Delta_M = \frac{(\Omega_M - \Omega_{M,o})}{\Omega_{M,o}}$ The frequency of the RF spectrum (f) is referred and normalized to the frequency of the Master at room temperature ($\Omega_{M,o}$). The dashed white line indicates the $f = \Omega_M$ curve (b)-(d), Phase portraits of the deformation of the Master (u_M) and the Slave (u_S) for different values of Δ_M

the Slave cavity as a function of Δ_M (Fig. 6.11a) shows several of the features appearing in the experimental results in Fig.6.7.

For Δ_M = 0 the main peak of the simulated RF spectrum of the Slave appears at a frequency $f \approx \Omega_S$ together with sidebands due to frequency beating. In this case, the phase diagram u_M, u_S almost fills the phase space in which the deformations are confined (Fig. 6.11b). By decreasing Δ_M, the sidebands become closer to the main peak, which remains fixed. An abrupt transition occurs at $\Delta_M \approx$ -2.1 $\cdot 10^{-3}$, where the main Fourier peak switches to $f \approx \Omega_M$, entering a transition region that we associate to that observed in the experiment reported in Fig. 6.7e and Fig. 6.7f. Interestingly, by further decreasing Δ_M the relative dephasing between u_M and u_S becomes more and more confined (Fig. 6.11c). Mechanical synchronization occurs for $\Delta_M <$ -4.5 $\cdot 10^{-3}$,

where a single peak appears at $f = \Omega_{sync} \approx \Omega_M$ with two symmetric sidebands that appear by introducing mechanical kicks in the u_M and/or u_S dynamical equations. Under those conditions, the FFT spectrum of the optical transmission associated to the Master cavity does not display sidebands (see below). Moreover, as shown in Fig 6.11d, u_M and u_S appear to be $\pi-$shifted with respect to each other, which is consistent with the experimental observations in the synchronized state reported in Fig. 6.8.

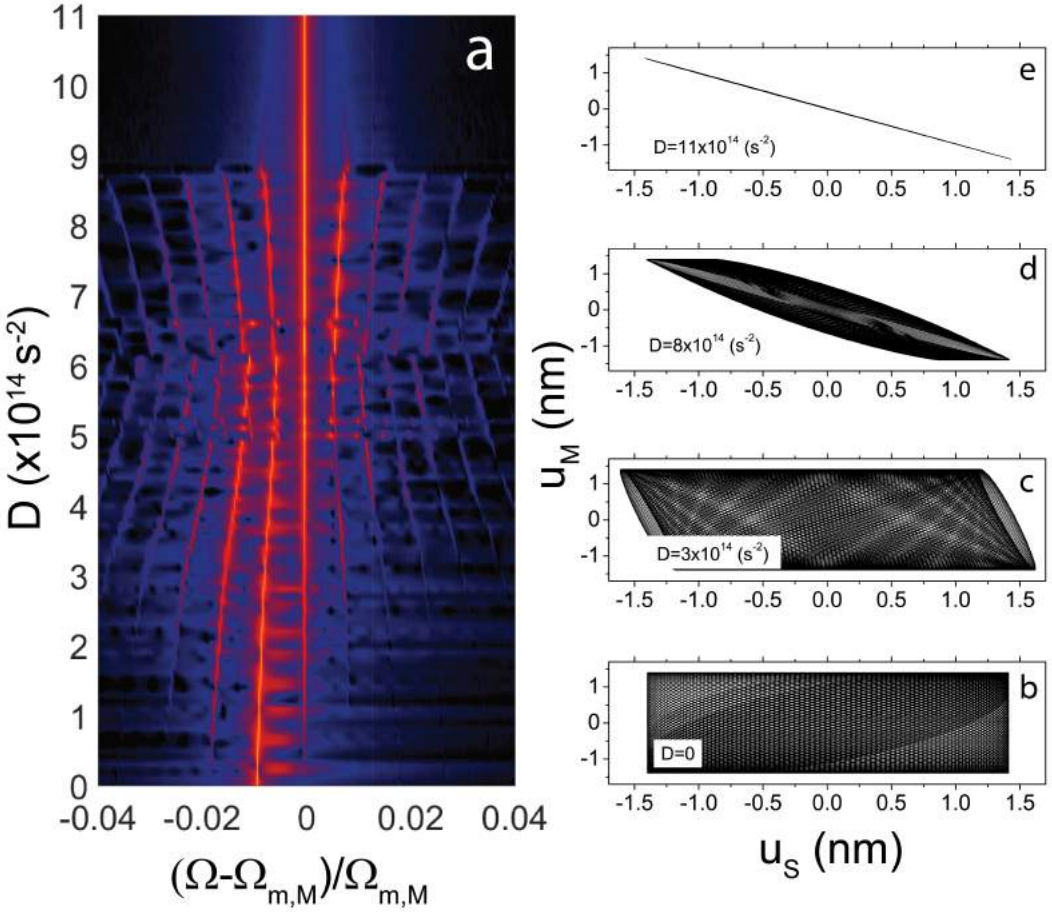

Figure 6.12: Numerical simulations of the coupled OM cavities. (a), colour contour plot of the simulated radio-frequency spectrum of the optical transmission as a function of the coupling constant (D). (b)-d, Phase portraits of the deformation of the Master cavity (u_M) and the Slave cavity (u_S) for different values of D.

Fig. 6.12 reports results of the stationary dynamics of the coupled system for different values of D. When analysing the Fast Fourier Transform (FFT) of the simulated optical transmission associated to the Slave cavity (Fig. 6.11a). In Fig. 6.11 we also analyse the relative dephasing of the mechanical deformations of each OMC by plotting u_M with respect to u_S (right panels of Fig. 6.12). As mentioned before, for $D = 0$ both OMCs are in the phonon laser regime with no interaction, so the spectrum of Fig. 6.12a consists of a single

peak at Ω_S and the phase diagram of Fig. 6.11b completely fills the phase space in which the deformations are confined. By increasing D, sidebands appear in the spectra of Fig. 6.12a, the relative dephasing becomes more and more confined (Figs. 6.12d and 6.12e). Eventually the main Fourier peak switches to Ω_M, which is the situation reported in Fig. 6.12e (D=$8\times10^{14}s^{-2}$). The dynamics of the two cavities become synchronized for D values greater than D$\sim 9\times^{14}s^{-2}$, where a single peak appears at $\Omega_{sync} \sim \Omega_M$ with two symmetric sidebands at a frequency of $\Omega_{sync} \pm (\Omega_M - \Omega_S)$.

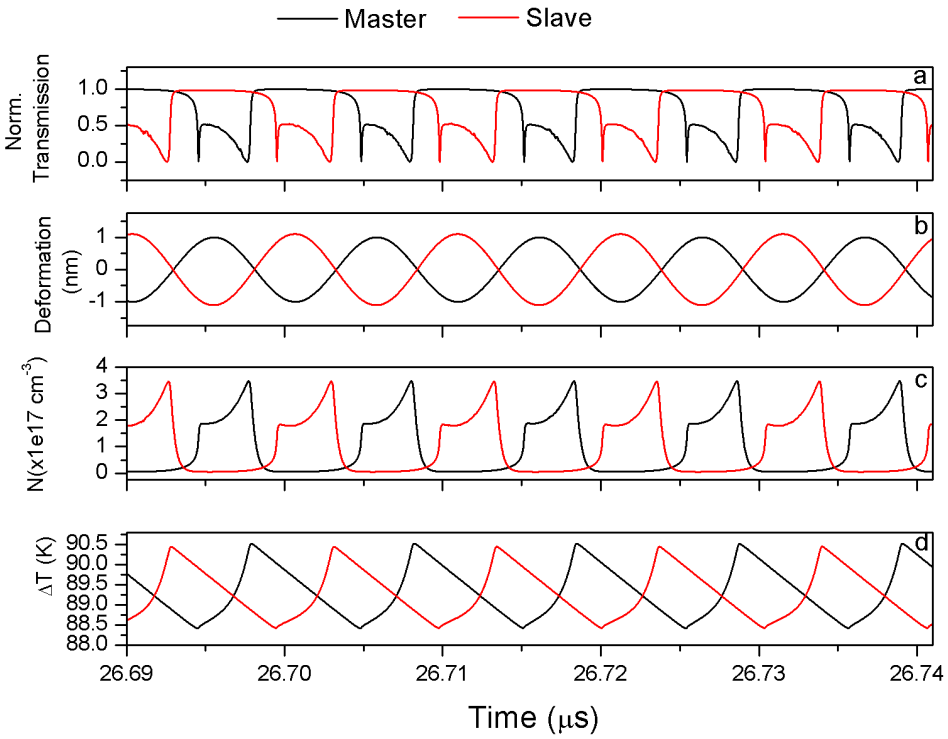

Figure 6.13: Temporal dynamics of the transmitted optical signal (a), deformation (b), free-carrier-population (c) and the average cavity temperature increase (d) associated to the Master (black) and the Slave (red) when the coupled system is in a synchronized state as in Fig. 6.11d.

In Fig. 6.13 we represent the stationary dynamics achieved in each OMC in a synchronized state obtained at D= $9\times^{14} s^{-2}$ (these are the conditions used also for the results showed in Fig. 6.11) and the associated optical transmission temporal traces. It is worthwhile emphasizing that the deformation maximum is found in between the two minima of the transmission trace, i.e., where the limit cycle trajectory verifies $\lambda_l > \lambda_r$. Thus, the direct OM coupling contribution not only locks the main frequency of the SP to a simple fraction of the mechanical eigenfrequency (in the case of Fig. 6.13 they are locked at the mechanical frequency of the Master) but also impacts the duty cycle by modifying the time distance between both transmission minima. The two trajectories belonging to Master and Slave appear to be $\pi-$shifted

with respect to each other, which is consistent with the experimental observations in the synchronized state reported in Fig. 6.8. The simulated mechanical amplitudes are similar as we have assumed the two OMCs to be roughly equivalent. Thus, it is reasonable that both simulated temporal traces shapes look alike, in contrast to what observed experimentally. Indeed the experimental temporal trace of the optical transmission associated to the Slave (Fig. 6.8a and Fig.6.8b) shows a smaller duty cycle than the Master counterpart because the mechanical amplitude is sensibly smaller in the former case.

We have also noted that the cross-linked OM coupling has negligible effects in what concerns the overall dynamics of the system, obtaining equivalent results when $g_{OM,MS} = 0$. From this latter result it is possible to conclude that the meaningful coupling between the two OMCs is purely mechanical, i.e., the important term is the reactive coupling one described above.

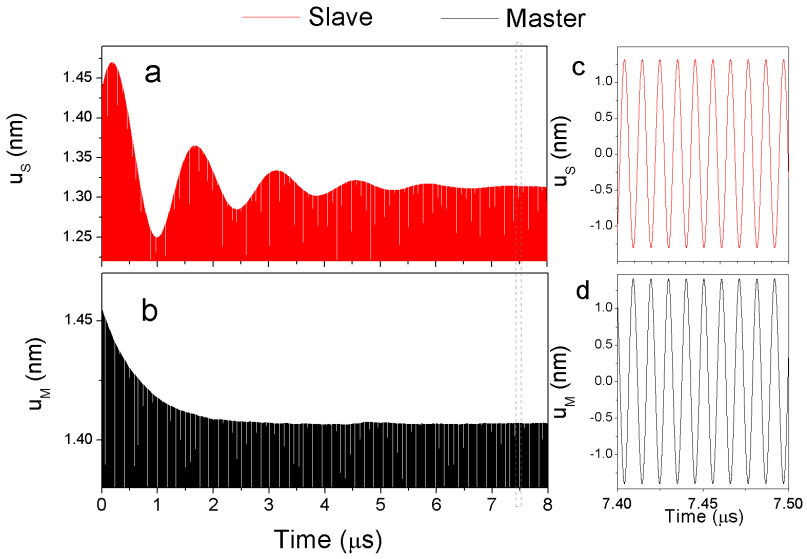

Figure 6.14: Temporal traces of the mechanical deformation associated to the Slave (panels a and c) and Master (panels b and d) after a kick has been applied to the system. A zoom of a region where the stationary regime has been achieved again is reported on the right panels.

Once the system has acquired a stationary dynamics we have perturbed both the Master and the Slave with a kick that would take the role of thermal forces or other sources of instability impacting the system. We have implemented the kick as a sudden change of the deformation of each of the OMCs of up to 10% with respect to the value taken in the previous time step. When the coupled system is initially found in a synchronized state, the phase trajectory described by the Slave after the kick is an oscillatory one around the synchronized state limit cycle solution performed at a frequency of $(\Omega_M - \Omega_S)$. The amplitude of this hypermodulation is exponentially decaying with time so that after a few cycles the synchronized state stationary solution is recovered. This effect is better illustrated by plotting the temporal trace associated

to u_S after the kick (Fig. 6.14a) but a consistent effect is also experienced by N_S and ΔT_S since they are coupled to u_s.

On the contrary, the Master overdampedly returns to the limit cycle when driven away from it. When comparing Fig. 6.14a and Fig. 6.14b it is clear that it takes more time for the Slave to converge again to its stationary limit cycle. After several μs the system has fully recovered the stationary synchronized dynamics, recovering the π phase-shift between the phase trajectories.

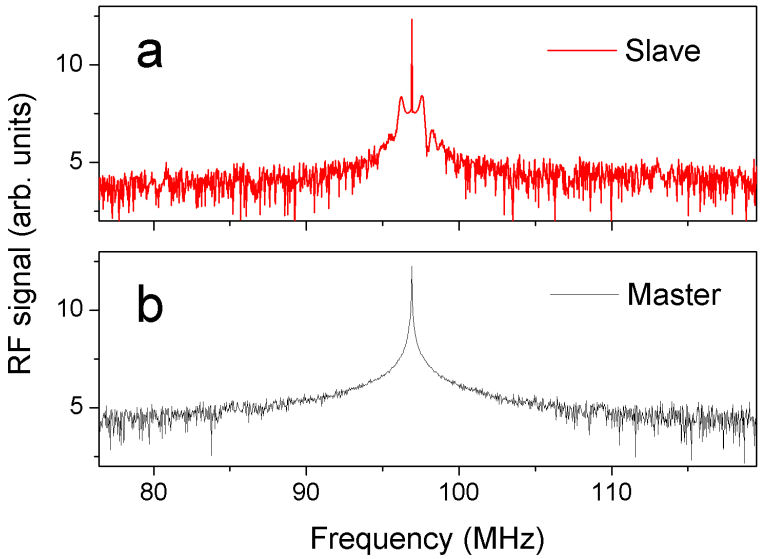

Figure 6.15: Simulated radio-frequency (RF) spectrum of the optical transmission of the Slave (a) and the Master (b) when a kick has been applied to the system.

Fig. 6.15 shows the Fourier transform of the simulated optical transmission (RF signal) corresponding to the data showed in Fig. 6.14, i.e., of temporal traces registered after the kick. Both RF spectra display a main peak at $\Omega_{sync} \equiv \Omega_M$, the clear difference between them being that the Slave spectra display sidebands associated to the modulation showed in Fig. **??**a. On the contrary, no sidebands appear on the Master RF spectrum. This is consistent with what observed experimentally, for example in Figs. 6.7g and 6.7h.

6.8 Conclusion

In conclusion, in this Chapter, we have unequivocally demonstrated spontaneous synchronization of the mechanical oscillations of a pair of optomechanical crystal cavities by introducing a weak mechanical coupling. Provided that our numerical model indicates that the observed features are compatible with a reactive type of coupling (see Supplemental Material of Ref. [212]).

Further experimental studies will unveil whether the transition to synchronization is through phase locking or suppression of the natural dynamics, which are the two mechanisms of synchronization in reactively coupled oscillators [184]. Finally, we have demonstrated that the synchronization dynamics can be dynamically switched off and on by introducing an external heating source on the master cavity.

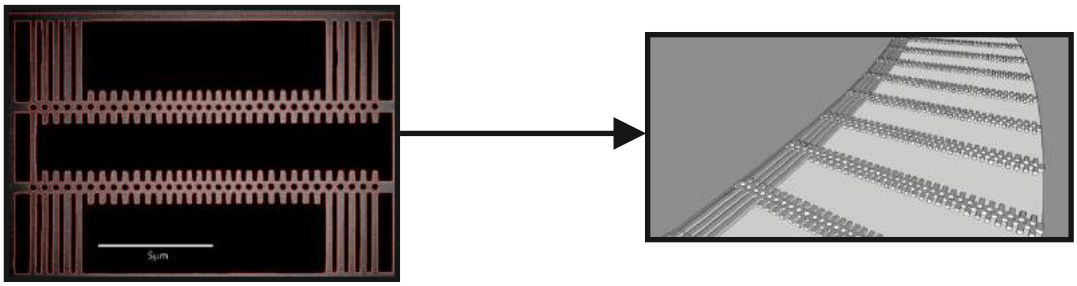

Figure 6.16: Toward network of synchronized optomechanical oscillators.

The system presented here could be upscaled to realize complex networks comprising many more nodes without substantially increasing the technological requirements. For instance, one could easily think of a silicon chip integrating an array of optomechanical cavities accessed optically via integrated waveguides [214, 215] and interconnected via mechanical links, similar to the illustration shown in Fig. 6.16.

Our results are the first step towards building networks of coupled optomechanical crystal cavities able to display collective dynamics prone to be modified by addressing single structures with external perturbations. These rather unique features are to be exploited in neuromorphic photonic computing applications [216], for instance, for pattern recognition tasks or more complex cognitive processing. Eventually it will be possible to experimentally investigate the limits, in terms of network complexity, of coherent collective behaviors and the intriguing transition towards incoherence, where the so called Chimera states [217, 218] of synchronous and incoherent behavior are expected to emerge.

Chapter 7

Conclusions and perspectives

In this chapter I summarise the main results presented in this thesis. After listing the main conclusions, I discuss the relevance of the results obtained here for optomechanics field. I suggest possible ideas to improve the performance of both systems. Finally I will propose a possible way to combine the magnetostriction properties of YIG and optomechanical crystals in a single experiment, which would open a window with multiple possibilities in the field.

First, a new type of optomechanical magnetometer is presented. It consists of a hybrid system that combines the synergies between magnons and phonons in ferromagnetic thin films of YIG and photons localized in whispering gallery mode glass microspheres. The resonant enhancement of mechanical and optical interaction in optomechanical cavities enables their use as an extremely sensitive magnetic field sensor. The main results of the optomechanical magnetometer presented in this work are:

- The magnon excitation in YIG has been observed and characterized using a standard tool for probing magnons and spin dynamics of ferromagnetic materials namely, ferromagnetic resonance.
- The optomechanical properties of the glass microspheres have been measured. A fiber taper system has been used to couple light in and out from the sphere in the near field. Optical and mechanical quality factors of $Q_o \sim 10^8$ and $Q_m \sim 10^2$ are found for the microspheres, respectively.
- The performance of the magnetometer relies on how efficient the magnetic signal is to drive the mechanical modes above the thermal noise. The magnetic response is modeled as an extra force that acts on the harmonic oscillator that describes the mechanical modes of the microsphere. From COMSOL simulations it is found that the magnetostrictive force drives the radial mechanical modes of the microsphere.
- The magnetic response that drives the mechanical modes with power was found to be linear. This means that the square root of the response is linear with the magnetic field, which is a typical requirement

for a magnetometer. This is checked by two measurements of the mechanical signal as a function of the magnetic field. The first measurement was registered in a spectrum analyzer, where the recorded signal showed the thermal spectrum and the magnetic driving of the mechanical modes. The second experiment used a vector analyzer, where only coherent signal coming from the magnetic driving was recorded.

- The magnetic response is found to have its origin on the surface of the YIG film where the spheres are deposited. A high frequency laser doppler vibrometer was used to measure vibration at the surface of YIG in the absence of the microsphere. This laser interferometric technique measures displacement in absolute units with picometer sensitivity. The vibrometer registered vibrations in the same spectral range than FMR, confirming that the YIG layer generates mechanical vibrations on its surface in the FMR frequency range via magnetostriction.
- The magnetometer sensitivity was characterized as a function of frequency in different spectral windows where the mechanical modes of the sphere were present was determined. A magnetic field peak sensitivity of $\sim$ 850 pT $Hz^{-1/2}$ at 206 MHz. The sensitivity remains around 1 nT $Hz^{-1/2}$ within the linewidth of the mechanical resonances, which for most of the mechanical modes are in the spectral range of $\sim$ 10 MHz.
- The magnetometer operates at room conditions of pressure and temperature.
- The frequency response of the magnetometer depends on the spectral overlap between the FMR and the mechanical modes of the sphere. Since this resonance can be tuned with a static magnetic field B_{DC} it is demonstrated that the spectral response of the magnetometer can be extended to frequencies into the GHz range with a sensitivity around a few nT $Hz^{-1/2}$.

The results enumerated before make the optomechanical magnetometer an excellent sensor of magnetic fields. The room temperature operation makes it a possible choice for a wide range of applications including magneto-encephalography, geology, and nuclear magnetic resonance spectroscopy to identify chemical composition, among others. Currently the most extended used magnetometer is the SQUID, which can reach sensitivities of $\sim$ 1 fT $Hz^{-1/2}$. However, the operation at cryogenic temperatures is a major disadvantage.

The full capabilities of the optomechanical magnetometer are yet to be explored. For example, the value of the operational frequency given is a lower bound limited by the maximum B_{DC} reachable in our experimental setup. A possible future experiment would be to test the magnetometer response well above 1 GHz using an improved static field and a FMR set up, that could reach 10 GHz operation.

The magnetometer sensitivity can be improved by using microspheres with higher mechanical quality factors. The sensitivity scales with quality factor as $\delta B_{min} \sim Q_m^{-1/2}$. For instance, by measuring in vacuum, a factor three in

sensitivity would be gained using microspheres with mechanical quality factors of $Q_m \sim 10^3$ instead of 10^2, used in this work. An order of magnitude could be gained using $Q_m \sim 10^4$, but this would increase the requirements for microsphere fabrication.

Apart from the previously mentioned applications purely related to magnetometry, numerous opportunities may arise based on the optomechanical magnetometer experiment. For example, it can be combined with the use of doped microspheres on the YIG film. If the bulk glass material from which the spheres are fabricated is doped with a rare earth ion, like Neodymium or Erbium, the passive cavity becomes active and a gain medium for lasing emission. Then, the modulation effect caused by the magnetic driving of the YIG layer will be imposed on the lasing wavelength. This would result in an alternative way to modulate light at megahertz rates.

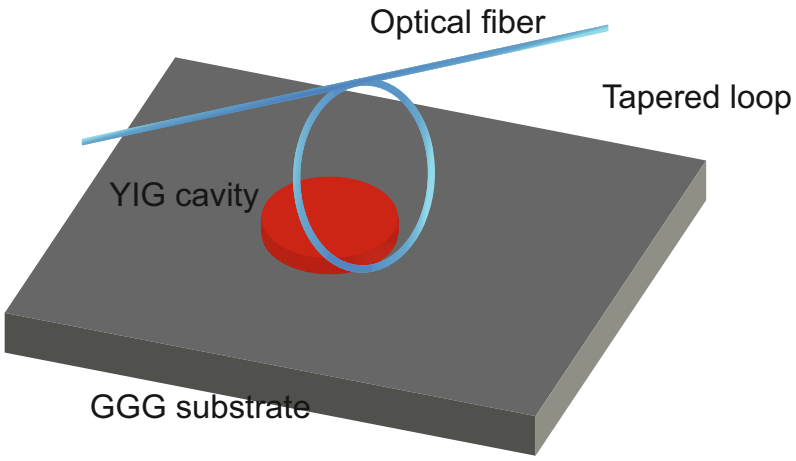

Figure 7.1: YIG disk magnetometer design. The disk is a whispering gallery optical and mechanical resonator. Since the disk is ferromagnetic, it would be possible to excite FMR, combining magnons, photons and phonons in a single platform.

Recently, magnons are gathering increasing attention in spintronics experiments (e.g. magnonics and spin caloritronics areas) as a means of processing spin information and managing heat in nanoscale structures. YIG is an ideal choice in spintronics applications due to its excellent magnetic properties. However, the underlying physical mechanism is still being under study, mainly related to phonon-magnon interactions. Most of the current experiments related to study the spin-phonon and magnon-phonon interactions are conceived to investigate the coupling through the spin or magnon manipulation. This is because the magnetic or spin aspect of devices are easier to access and actuate via voltages and currents at a chip level with the current fabrication technologies. In this sense, the phonon information is obtained indirectly from the magnetic measurement. Our hybrid-system can be also exploited to understand further the physics of phonon-magnon coupling in YIG, or other ferromagnetic and magnetostrictive materials, in a complementary way. With our device, the magnon-phonon information is obtained from

the phonons of the optomechanical cavities, which are driven by the phonons of the magnetic material.

In order to go advance on the investigation of magnon and phonons at a fundamental level, a strong magneto-elastic interaction is needed. A possible way to increase the magnon-phonon coupling and improve the optical readout efficiency of the device would be to fabricate the optomechanical cavity in YIG, either by testing a sphere geometry or a much more integrated one such as a disk or ring resonator (see Fig. 7.1). This type of devices would allow to control the operational frequency by design and increase the frequency of the mechanical modes. Nevertheless, with the current fabrication methods, this cavities are still very demanding to fabricate due to the difficulty in obtaining vertical etching of YIG with small roughness. Future efforts will be undertaken in this direction to fabricate YIG disk to create an optomechanical-magnonic device.

The second experiment studied in this thesis is related to the demonstration of synchronization of two optomechanical crystals. The two cavities, which at first start oscillating at a different frequency, end up oscillating in a common one. The optomechanical crystals are connected via a tiny mechanical link. This allows to create the analogy with Christiaan Huygens's primal synchronization experiment. The main conclusions of the synchronization experiment that can be found in thesis are summarized as follow:

- The optical and mechanical properties of the two corrugated optomechanical crystals are individually characterized using the taper fiber system. The optical modes of both cavities are found in the near infrared range with wavelengths of $\lambda \sim 1500$ nm. The mechanical modes used in the synchronization experiment correspond to in-plane flexural modes, in particular, the one of third order characterized by three antinodes of displacement along the beam and frequencies of ~ 90 MHz.
- It is shown that the oscillatory nature of the two optomechanical cavities works individually. In this sense, they can be considered independent optomechanical entities.
- An experimental method of heating the optical modes via the thermo-optic effect to differentiate each cavity.
- The optomechanical crystals are individually driven to a self sustained oscillation by employing the self pulsing mechanics, which is activated by the nonlinear effects present in optical cavities. However, since the real system presents dissipation, an optical DC source to pump energy to the overall system is used.
- A spectral analysis of the synchronization process is presented. This measurement confirms the dynamical process toward the synchronized state by a starting point with the two cavities lasing at different frequencies. The synchronization is achieved in a Master-Slave configuration since the oscillation amplitude of one of the two cavities is stronger than the other and this makes that the master pulls the frequency of the

slave towards frequencies closer to its own frequency. Nevertheless, both cavities are mutually affected. The spectral analysis also reveals 'transition zones' where the dynamics of the two cavities is not yet synchronized but both are affected as a consequence of the coupling.

- From the temporal analysis of the optical signals coming from each of the cavities it is demonstrated that they oscillate in anti-phase.
- A stroboscopic method is presented to confirm the synchronization state. By sampling at the synchronization frequency Ω_{sync} the temporal signals at a fixed time delay Δt, it is demonstrated that corresponds to a fixed point in the Poincare map formed by the amplitude of both oscillator and the sampling amplitude given by $\sin(\Omega_{sync}\Delta$ t) . It is also shown that by sweeping the temporal delay the for all times from 0 to $2\pi = \Omega_{sync}$, the point becomes a close trajectory in the Poincare map, which is what correspond to a synchronized state.
- It is presented a numerical model to study the dynamic of the coupled optomechanical crystals. The model is described by the eight nonlinear equations, four for each cavity. The mechanical link is modelled as a reactive coupling, introduced in a unidirectional way toward the slave cavity. The model describes well the dynamics of the system towards synchronization and are in agreement with the spectral and temporal measurements obtained. They also show consistency with the anti phase oscillation obtained in the measurement.
- A switching experiment is presented. The optomechanical crystals are initiated in a synchronized state. A top heating laser is used to modify the dynamics deactivate synchronization. By imposing a modulation on the heating laser, it is observed that the synchronization takes around 10 ms to be recovered. This is a consequence of the weak coupling.

The results related with the synchronization experiment suppose a significant contribution to optomechanical community. It is the first work that demonstrate synchronization of two optomechanical crystal by a mechanical coupling. All the optomechanical experiments found in literature proving synchronization are systems where the coupling is given through the optics [53, 56, 208, 209]. A laser is coupled to a single optical field common to all the mechanical oscillators, providing the driving power to achieve the self sustained oscillations and also the coupling mechanism. Then, the coupling on these works is internalized in the radiation pressure force F_o, which depends on the amplitude of the optical field $a(u_i)$ as $F_o \propto |a(u_i, u_j)|^2$, and this in turn depends on the displacement u_i of each oscillator. In the work shown in thesis the coupling is explained by an elastic restoring force with the form $D(u_i - u_j)$, which depends only on the displacement of each oscillator. This type of coupling results in a more simple and compact type of interaction. It allows to isolate the process to reach the self sustained state to the one to reach synchronization. From a fundamental point of view, the platform presented in this thesis is ideal to study in detail the onset of synchronization of

mechanical oscillators, not only in optomechanical systems but as a general process.

Future experiments on the optomechanical cavities will be directed to further study the transition zones prior to synchronization. Also, we will quantify the frequency size on which synchronization is achieved as a function of the coupling strength, which in the terminology of the field is known as the Arnold tongue. Reconstructing the Arnold tongue will give a more complete description of the system. Using the configuration presented in this work, synchronization has been observed with the slave cavity lasing at the second harmonic tone and the master at the first harmonic. Knowing the width of the Arnold tongue will also reveal if it is possible to observe synchronization at higher harmonics than the first and second order tones.

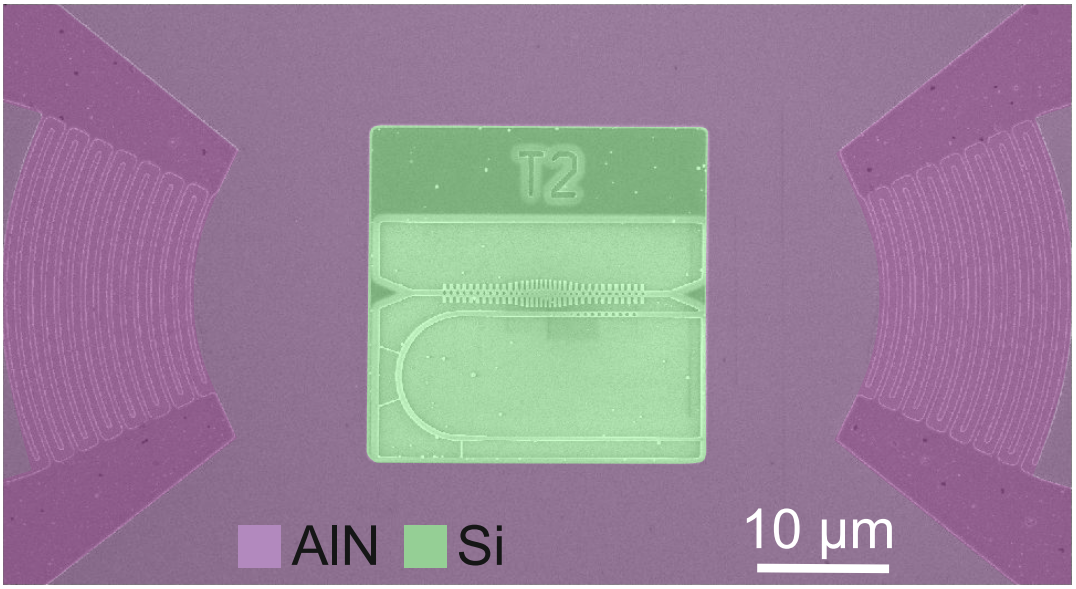

Figure 7.2: Opto-electromechanical device from the PHENOMEN project. The device consists on a silicon layer with a top layer of aluminum nitride (AlN) layer. The corrugated cavity is fabricated in silicon with a waveguide to couple light to the cavities. IDT's are fabricated in Aluminum to create coherent phonons by surface acoustic waves.

The synchronization results are part of an international collaboration included in the FET Open project PHENOMEN. The objectives of the project are the combined use of phonons, photons and RF electronic signals to achieve phonon circuits functionalities in a silicon chip operating at room temperature. The final device of the project is similar to the one depicted in Fig. 7.2. It consists on an electro-optomechanical circuit fabricated in a silicon platform with a top layer of Aluminum Nitride (AlN). The device fabricated on the silicon part (green rectangle), are the corrugated nanobeams shown in this thesis and the AlN is used as the medium to transport surface acoustic waves generated by interdigital transducers (IDT) fabricated in Al. PHENOMEN proposes to build the first practical optically-driven phonon sources and detectors including the engineering of phonon lasers to deliver coherent phonons

to the rest of the chip pumped by continuous wave optical sources. Different functionalities have been investigated on this project: phonon switching, memories, filters, polarization manipulation and mechanical phase synchronization. Future experiments will investigate the synchronization strength by the actuation of surface acoustic waves launched from the IDT's.

One of the main applications of synchronizing mechanical oscillators is related with the potential to improve measurements that require low noise. The theory predicts that the phase noise is reduced by N^{-1} when coupling N mechanical oscillators [51]. This can be important for systems where the noise is imposed by the fact that the mechanical oscillators are coupled to the thermal bath of the environment, which is the case of the two experiments studied in this thesis. The reduction of the thermal noise is important for several applications like time-keeping, frequency stabilization and sensing. In this way, it emerges a connection with the magnetometer experiment presented in this work. The sensitivity of the magnetometer was determined by the minimum force detectable above the noise floor. If the thermal noise is reduced by a factor N^{-1}, the sensitivity would improve by $N^{-1/2}$. Synchronization provides a way to reduce the thermal noise and then increase the sensitivity. Future experiments needs to be directed to develop self sustained oscillation of optomechanical coupled cavities in magnetostrictive material.

A possible idea to be explore in the future that combines optomechanics and magnetic properties in integrated systems would be the fabrication of optomechanical crystals on a silicon layer grown on a YIG substrate. This type of platform would result in a new way to actuate on the optomechanical systems, not by electric fields inducing SAW on the surface like it is shown in Fig. 7.2, but on magnetic fields inducing vibrations on the surface of the chip. The technological problem of fabricating optomechanical crystals in different platform than SOI wafers would be solved by using nanocristalline silicon (ncSi), which is obtained by annealing amorphous silicon deposited on a grown layer of silicon oxide [219]. This process allows to think on a design where multiple substrates can be used. In particular, an interesting choice would be to use a YIG layer under the silicon oxide. The YIG is known to grow with good crystal quality from a GGG substrate. Then the prototype chip would be composed by layers of GGG-YIG-SiO_2-ncSi.

A long-term goal that can be extracted from the results presented in this work is to explore the synchronization applied not in two optomechanical systems but in a collective arrangement of optomechanical cavities. The simple design presented here can be up-scaled to increase the number of optomechanical crystals coupled by mechanical links. This process can be seen as an improvement that would not add many extra technological difficulties. The challenge of building arrays of optomechanical oscillators is the dispersion in operational mechanical frequency of each oscillator presents due to unavoidable statistical variations in the fabrication [194, 195, 198]. This effect adversely affects operations that require a coherent performance of the system.

Several applications can be derived from exploiting the coherent operation of optomechanical arrays. For example, they can be used to create neuromorphic networks. These systems are artificial architectures that imitates its biological homologous to perform different tasks related with the manipulation of big amount of data, such as image recognition, natural language processing or communications. While neural networks have been introduced already in the 50's [220], they have really taken relevance in last decade. An hypothetical optomechanical neural network would be formed by matrices modules consisting on multiple optomechanical crystals connected a single or multiple mechanical links. One of the modules can be programmed to realize different tasks, leaving two module to input/output information on the network. The information could be transmitted in the amplitude of light pulses coupled into the network by external lasers. Light propagates through the different modules, which process the information by linear operations [221]. The operation on different modules needs to be activated by a nonlinear function [222]. Synchronization, which is intrinsicaly non linear, could be the nonlinear activation process on each neuron.

Finally, another interesting direction that can be taken from the results shown in this thesis are related with synchronization and the chaotic regime that can be achieved in optomechanical cavities. The chaotic dynamic can be exploited in the environment of secure communications. A secret message can be masked in the chaotic signal of one nanobeam, that would act as an emitter. A second nanobeam in a chaotic state would receive the secret emission and recover the information by subtracting the chaotic signal. If part of the signal of one crystal is injected in the other and vice versa both system will end up synchronizing obtaining a bidirectional communication system. The communication through a synchronized chaotic cavities presents the advantage of providing a way to detect any kind of external interception attempt, since the dynamical state of both cavities would immediately be affected, losing the synchronization state and interrupting the communication channel.

Appendix A

Finite element method simulations and OM coupling calculations

The effective masses and optomechanical coupling rates g_{OM} are obtained by using COMSOL finite-element-method (FEM) simulations of a complete structures. In order to obtained accurate values, the real fabricated devices are imported instead on the nominal designs from a SEM image. The contour of the SEM image shown in Fig. A.1 has been extracted graphically and then imported in the FEM solver. Since the thickness value can not be extracted from the SEM image, it is assumed that of the top Si layer of the SOI wafer (250 nm). This procedure ensures a good agreement between the measured optical and mechanical modes and those extracted from simulations.

The mechanical modes considered either in Chapter 3 and Chapter 6 are the in-plane flexural modes with three antinodes illustrated in Fig. 3.8 and Fig. 6.4. For the case of the coupled nanobeams illustrated in Fig. A.1 the calculated effective masses are m_{eff} = 5 pg for both mechanical modes. The optical modes used for both structures is the fundamental. From now on we will restrict to the coupled nanobeams.

The OM coupling rates are estimated by taking into account both the photoelastic (PE) and the moving interfaces (MI) effects [102, 106, 107]. The PE effect is a result of the acoustic strain within bulk silicon while the MI mechanism comes from the dielectric permittivity variation at the boundaries associated with the deformation. The calculation of the MI coupling coefficient g_{MI} is performed using the integral given by Johnson et al. [107];

$$g_{MI} = -\frac{\pi\lambda_r}{c}\frac{\oint(\mathbf{Q}\cdot\hat{\mathbf{n}})(\Delta\epsilon\mathbf{E}_{||}^2 - \Delta\epsilon^{-1}\mathbf{D}_{\perp}^2)}{\int \mathbf{E}\cdot\mathbf{D}dV}\sqrt{\frac{\hbar}{2m_{eff}\Omega_m}} \tag{A.1}$$

where $\mathbf{Q}$ is the normalized displacement (max$\{|\mathbf{Q}|\}$=1), $\hat{\mathbf{n}}$ is the normal at the boundary (pointing outward), $\mathbf{E}$ is the electric field and $\mathbf{D}$ the electric displacement field.ϵ is the dielectric permittivity, $\Delta\epsilon^{-1} = \epsilon_{silicon}^{-1} - \epsilon_{air}^{-1}$. λ_r is the optical resonance wavelength, c is the speed of light in vacuum, $\hbar$ is the

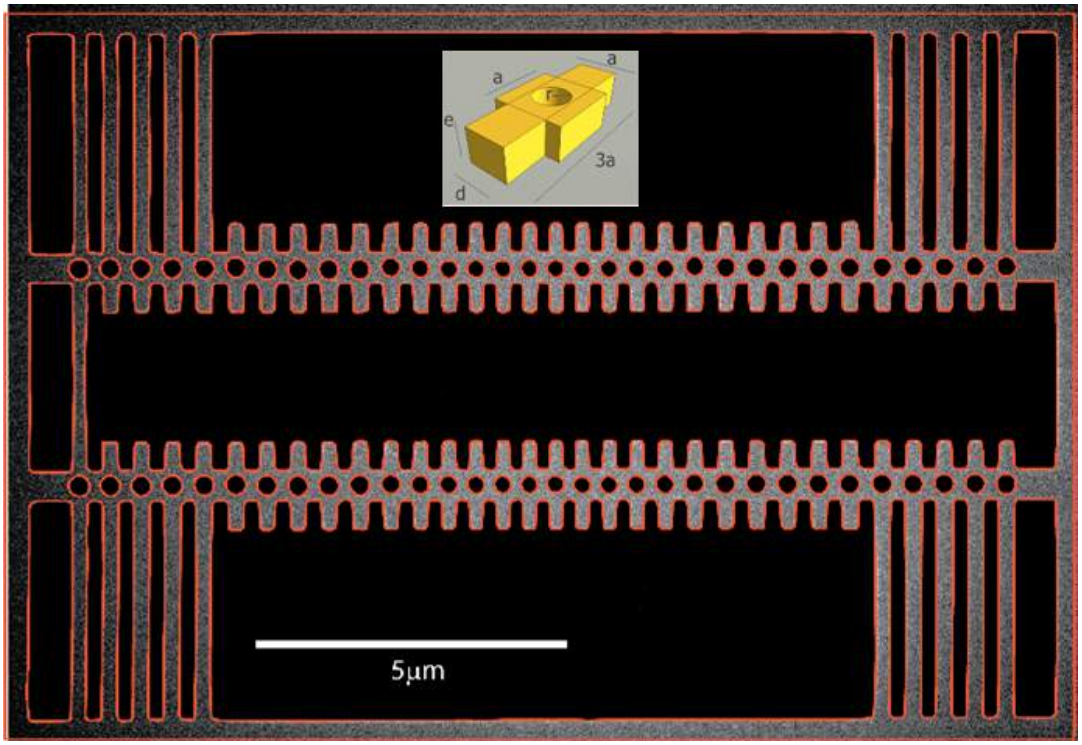

Figure A.1: Top-view SEM micrograph of the coupled Optomechanical Crystal Cavities. The extracted geometrical contour imported by the FEM solver is depicted in red. A sketch of the unit-cell is shown in the inset.

reduced Planck constant and Ω_m is the mechanical mode eigenfrequency, so that $\sqrt{\frac{\hbar}{2m_{eff}\Omega_m}}$ is the zero-point motion of the resonator.

A similar result can be derived for the PE contribution [102, 107]:

$$g_{PE} = -\frac{\pi\lambda_r}{c}\frac{\langle E|\delta\epsilon|E\rangle}{\int \mathbf{E}\cdot\mathbf{D}dV}\sqrt{\frac{\hbar}{2m_{eff}\Omega_m}} \tag{A.2}$$

where $\delta\epsilon_{ij} = \epsilon_{air}n^4 p_{ijkl}S_{kl}$, being p_{ijkl} the PE tensor components, n the refractive index of silicon, and S_{kl} the strain tensor components. The addition of both contributions results in the overall OM coupling rate:

$$g_{OM} = g_{MI} + g_{PE} \tag{A.3}$$

The PE contributions to the optomechanical coupling rate obtained in Eq. A.2 are on the order of Hz, that compared with the MI counterpart can be neglected. In Fig. A.2 we illustrate the MI surface density (the integrand of Eq. A.1) associated to the Slave optical mode when evaluating the contribution of the Slave and the Master flexural modes (panels a and b respectively). Similar results are obtained when performing the same study for the Master optical mode. The slight asymmetry of the field distribution with respect to

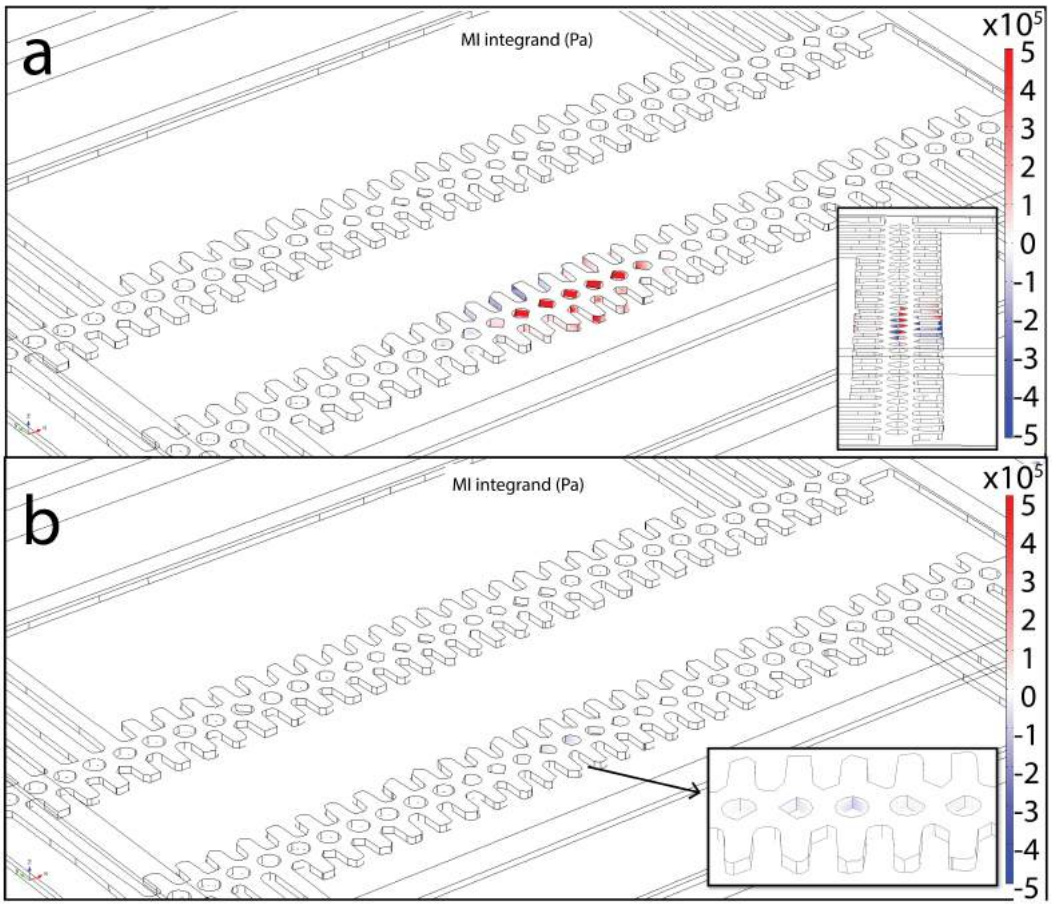

Figure A.2: Optomechanical coupling contributions. Normalized surface density of the integrand in Eq. A.1 for the Slave optical mode, showing the contributions to g_{MI} of the mechanical mode associated to the Slave (a) and the Master (b).

the centre of the OMCs along the xz plane unbalances the MI surface density towards the region of the OMC cavity that is closer to the centre of the frame, thus giving rise to overall calculated values of $g_{OM,M}/2\pi$=514 kHz and $g_{OM,S}/2\pi$=330 kHz for in-plane (xy plane) flexural modes belonging to the Master and Slave respectively.

Although the energy of the mechanical modes under consideration is mostly confined to the region between the clamping tethers of a single OMC, the presence of a mechanical link extends their spatial distribution to the central part of the other OMC. Cross contributions values of $g_{OM,MS}/2\pi$=6 kHz and $g_{OM,MS}/2\pi$=8 kHz were calculated as well, where the first subindex denotes the OMC associated to the optical mode. In this context, Fig. A.2b shows, for the case of the flexural mode of the Master and the optical mode of the Slave, that the source of cross MI contribution is the small partial overlap of the mechanical deformation with the Slave Cavity region, while there is a negligible contribution due to the overlap of the Slave optical mode with the Master OMC. The two order of magnitude in difference between the couplings and cross coupling allow us to consider that the two OMCs can be considered to

be optically isolated from each other by design.

Appendix B

Magnetic field calibration

The magnetic field in the waveguide is obtained by measuring the frequency dependent current circulating in the circuit. We calibrate the system using the equations of a lossy transmission line. The circuit diagram is shown in Fig. B.1. Standing waves losses due to the finite length of the RF cable ($l_c = 1.06$ m) and waveguide ($l_w = 0.04$ m) are described by the propagation constants $\gamma_c = \alpha_c + i\beta_c$ and $\gamma_w = \alpha_w + i\beta_w$. Alpha and beta are respectively the attenuation and phase constants. The voltage and current equations along the transmission line are:

$$V(x \geq l_w) = V_1 e^{\gamma_c (x - l_w)} + V_2 e^{-\gamma_c (x - l_w)} \tag{B.1a}$$

$$Z_0 I(x \geq l_w) = V_1 e^{\gamma_c (x - l_w)} - V_2 e^{-\gamma_c (x - l_w)} \tag{B.1b}$$

$$V(x \leq l_w) = V_3 e^{\gamma_w x} - V_4 e^{-\gamma_w x} \tag{B.1c}$$

$$Z_0 I(\leq l_w) = V_3 e^{\gamma_w x} + V_4 e^{-\gamma_w x} \tag{B.1d}$$

At the boundaries for $x = 0$, $x = l_w$ and $x = l_w + l_c$, we can extract from equations 2: $V(0) = 0 \rightarrow V_4 = -V_3$, $Z_w(x) = Z_0 \tanh(\gamma_w x)$, $V_2 = V_1 e^{-\gamma_w l_\omega}$, $V_3 =$

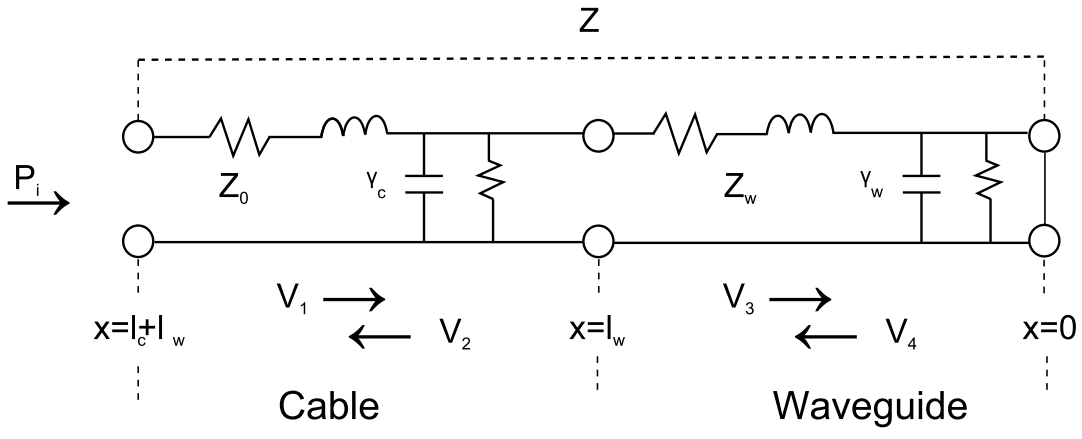

Figure B.1: (**a**) Conceptual schematic of the transmission line.

$-V_1 e^{-2\gamma_w l_\omega}$ and $V(l_\omega + l_c) = V_1(e^{\gamma_c l_c} + e^{-2\omega_w l_w} e^{-\gamma_c l_c}) = V_i + V_r$,where $V_{i,r}$ and $I_{i,r}$ are the incident (reflective) voltage and current on the transmission line. The power supplied to the waveguide $P_i(l_w)$ in function of the incident power from the VNA can be obtained as $P_i(l_c + l_w) = \frac{1}{2} Re[V_i(l_c + l_w) I_i^*(l_c + l_w)] = \frac{|V_1|^2}{2Z_0} e^{2\alpha_c l_c} = P_i(l_w) e^{2\alpha_c l_c}$. This allows to know V_3 and V_4 as a function of the source power $P_i(l_w + l_c)$. Finally, the current in the waveguide is:

$$i(x) = Re[I(x)] = \sqrt{\frac{2P_i}{Z_0}} e^{-\alpha_c l_c} [e^{-\alpha_w (x - l_c)} cos(\beta_w (x - l_w)) + e^{-\alpha_w (x + l_c)} cos(\beta_w (x + l_w))] \tag{B.2}$$

The magnetic field in the waveguide is

$$B(x) = \frac{\mu_0}{2d} i(x) \tag{B.3a}$$

being d=1 mm the width of the signal line.

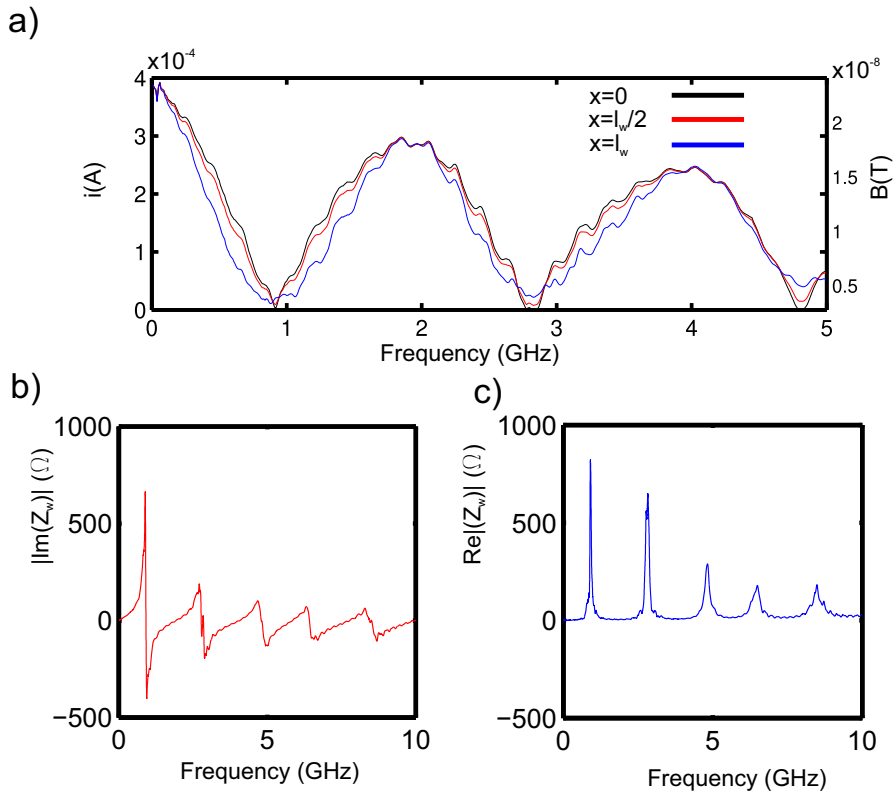

Figure B.2: (**a**)(Left) Frequency dependent current in A on the waveguide with P=-10dBm. (Right) Magnetic field B intensity in Tesla.(**b**)(**c**)Imaginary and Real part of the calculated impedance Z_w on the waveguide.

We can obtain $\gamma_c l_c$ and $\gamma_w l_w$ doing network analysis. From a transmission measurement connecting only the cables before the waveguide we get $S_{21} =$

$e^{-\gamma_c l_c}$, then $\gamma_c l_c = -ln(S_{21})$. The total impedance of the circuit can be obtained by measuring the parameter $S_{11} = \frac{Z-Z_0}{Z+Z_0}$, then solving for Z we have $Z = Z_0 \frac{1+S_{11}}{1-S_{11}}$. The impedance of the waveguide Z_w can be obtained from $Z = Z_0 \frac{Z_w(l_w)+Z_0 tanh(\gamma_c l_c)}{Z_0+Z_w(l_w)tanh(\gamma_c l_c)}$, then $Z_w(l_w) = Z_0 \frac{Z_0 tanh(\gamma_c l_c)-Z}{Z tanh(\gamma_c l_c)-Z_0}$. Finally, we have $\gamma_w l_w = atanh(\frac{Z_w(l_w)}{z_0})$. The obtained values of magnetic field $B(T)$, current $i(A)$, and impedance are shown in Fig B.2.

Appendix C

Laser Doppler Vibrometer Characterization of YIG

We used a Laser Doppler Vibrometer (Polytec UHF 120) to measure the vibrations created on the YIG surface. This laser based interferometric technique, measures displacement in absolute units with picometer sensitivity. In Fig. C.1a we show the schematic set up of the LDV. A laser light (532 nm) is focused on the YIG like in Fig. C.1b with a 20x objective. A Signal Generator sends the excitation frequency at which we want to measure. In a standard measurement the output signal is connected to a vibrating plate that shakes the sample. In this case, the excitation is connected to the waveguide. The excitation signal is also sent to a photodetector placed in the same place as the laser. The rf signal sent to the photodetector is used to detect the reflected light at this frequency, in an heterodyne scheme. The light detected, is shifted in frequency which depends on the sample's velocity (due to Doppler effect), from which in turn the displacement is obtained.

In Fig. 5.16a from Chapter 4 we obtain a peak amplitude of 4.7 pm at 250 MHz with a RBW = 2.5 kHz, which corresponds to a displacement sensitivity of 94 fm $Hz^{-1/2}$. Assuming that the signal at the entrance of the waveguide was the one given by the source (3 V), the corresponding rf field is B = 80 μT and a senstivity of $\delta B_{min} = \frac{B}{\sqrt{RBW}}$ =1.6 μT $Hz^{-1/2}$.

From the linear fit reported on Fig. 5.16 on Chapter 4 we can estimate the amplitude that corresponds to the equivalent voltage applied to the waveguide for the minimum peak sensitivity on the microsphere experiment. A vibration amplitude of $\sim$ 90 fm measured by the vibrometer on the YIG surface would be induced by an applied rf magnetic magnetic field of 0.51 μT. This value is a rough approximation since the values of voltages smaller than 2 V in Fig. C.1b correspond to signals close the minimum amplitude that can be achieved with the instrument ($\sim$ 1pm).

We compare the square root of signal to noise ratio on the measurement with the vibrometer and the YIG-sphere magnetometer as a function of magnetic field intensity (see Fig. C.1b). Since both measurement were performed at

different bandwidths, the square root of the SNR was multiplied by the resolution bandwidths used on each experiment. We note that the YIG-Silica sphere hybrid system measures larger signals for the same magnetic fields and its response extends to smaller magnetic fields.

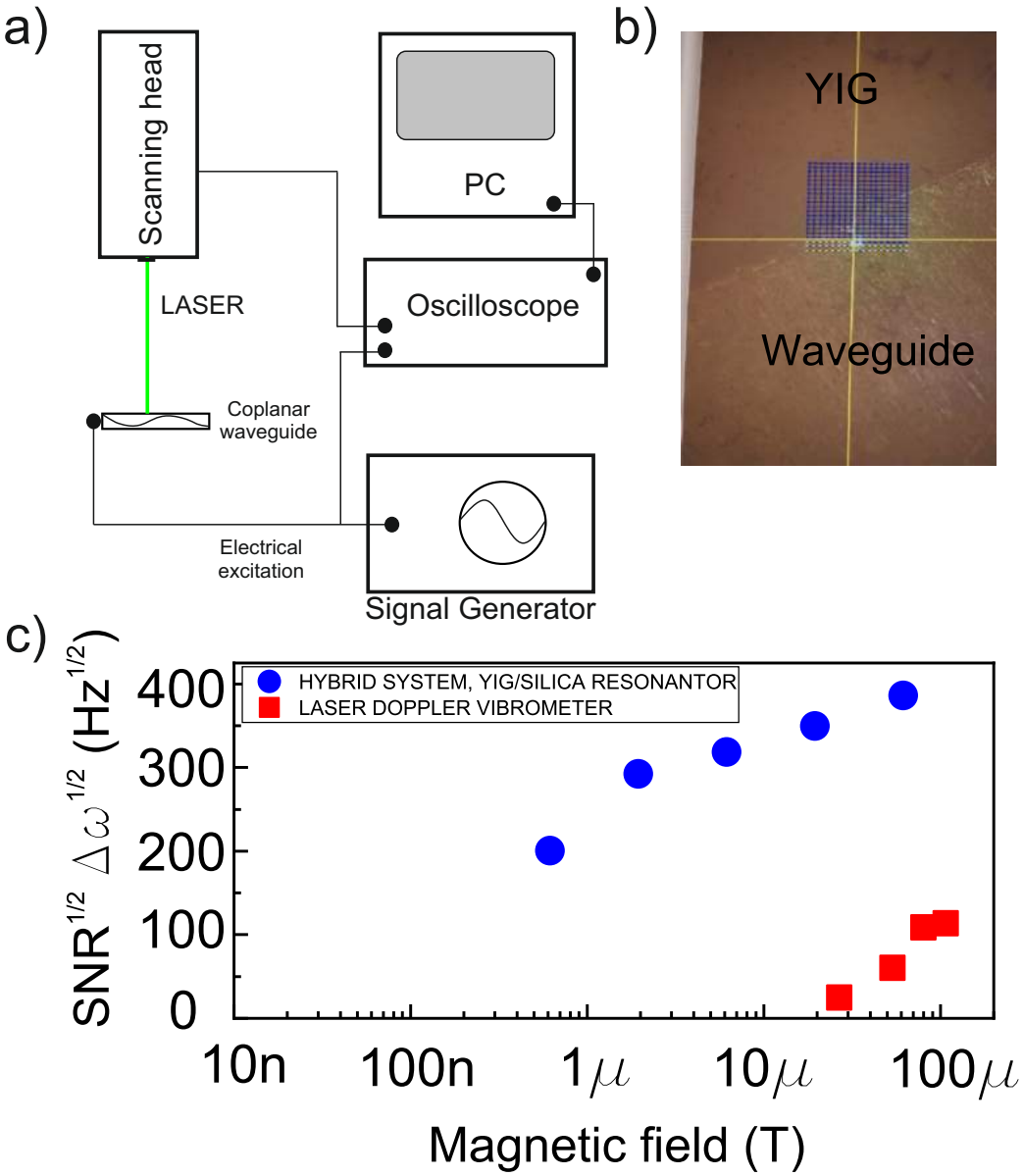

Figure C.1: (a) Schematic of the LDV set up. A Signal Generator sets the frequency of the coherent measurement. It is connected to the waveguide and the Laser. This allows to detect the reflected signal in an heterdyne scheme. (b) Optical image of the LDV measurement. A 20x objective focus the laser beam (532nm) on the sample. The YIG film is placed on top of the waveguide to create the rf field. (c) Response signal comparison between the vibrometer measurement and the magnetometer as a function of magnetic field. In order to compare the different measurment the response is represented as the square root of SNR multiplied by the bandwiidth used in each experiment.

List of Publications

1. "Self-sustained coherent phonon generation in optomechanical cavities", D. Navarro-Urrios, J. Gomis-Bresco, F. Alzina, N. E. Capuj, P. D. García, M. F. Colombano, E. Chavez-Angel & C. M. Sotomayor-Torres. **Journal of Optics** 18(9), 094006 (2016).
2. "Nonlinear dynamics and chaos in an optomechanical beam", Navarro-Urrios, D., Capuj, N. E., Colombano, M. F., García, P. D., Sledzinska, M., Alzina, F.& Sotomayor-Torres, C. M. **Nature Communications** 8 (2017).
3. "Optomechanical coupling in the Anderson-localization regime", García, P. D., Bericat-Vadell, R., Arregui, G., Navarro-Urrios, D., Colombano, M., Alzina, F., & Sotomayor-Torres, C. M. **Physical Review B** 95(11), 115129 (2017).
4. "Nanocrystalline silicon optomechanical cavities", Navarro-Urrios, D., Capuj, N. E., Maire, J., Colombano, M., Jaramillo-Fernandez, J., Chavez-Angel, E. & Sotomayor-Torres, C. M. **Optics express** 26(8) (2018).
5. "Optical modulation of coherent phonon emission in optomechanical cavities" Jeremie Maire, Guillermo Arregui, Nestor E Capuj, Martin F Colombano, Amadeu Griol, Alejandro Martinez, Clivia M Sotomayor-Torres, Daniel Navarro-Urrios. **APL Photonics** 3(12), 126102. (2018).
6. "Synchronization of Optomechanical Nanobeams by Mechanical Interaction", MF Colombano, G Arregui, NE Capuj, A Pitanti, Jeremie Maire, Amadeu Griol, B Garrido, Alejandro Martínez, Clivia M Sotomayor-Torres, Daniel Navarro-Urrios. **Physical Review Letters** 123(1), 017402. (2019).
7. "Ferromagnetic resonance assisted optomechanical magnetometer", MF Colombano, G Arregui, F Bonell, NE Capuj, E Chavez-Angel, A Pitanti, SO Valenzuela, CM Sotomayor-Torres, MV Costache, D Navarro-Urrios, Arxiv arXiv preprint arXiv:1909.03924. (2019). **Under review in Physical Review Letters**.
8. "Broadband dynamic polarization conversion in optomechanical metasurfaces", Zanotto, S., Colombano, M., Navarro-Urrios, D., Biasiol, G., Sotomayor-Torres, C. M., Tredicucci, A., & Pitanti, A. **Frontiers in Physics**, 7, 231. (2019).

9. "High frequency mechanical excitation of a silicon nanostring with piezoelectric aluminum nitride layers" Pitanti, A., Makkonen, T., Colombano, M. F., Zanotto, S., Vicarelli, L., Griol, A., ... & Ahopelto, J. . arXiv preprint arXiv:2003.11977.(2020). **Accepted in Physical Review Applied**.

Bibliography

[1] Johannes Kepler. "De cometis libelli tres" (1963).

[2] Arthur Ashkin. "History of optical trapping and manipulation of small-neutral particle, atoms, and molecules". *IEEE Journal of Selected Topics in Quantum Electronics* 6.6 (2000), pp. 841–856.

[3] Junaid Aasi, BP Abbott, Richard Abbott, Thomas Abbott, MR Abernathy, Kendall Ackley, Carl Adams, Thomas Adams, Paolo Addesso, RX Adhikari, et al. "Advanced ligo". *Classical and quantum gravity* 32.7 (2015), p. 074001.

[4] Yoichi Aso, Yuta Michimura, Kentaro Somiya, Masaki Ando, Osamu Miyakawa, Takanori Sekiguchi, Daisuke Tatsumi, Hiroaki Yamamoto, KAGRA Collaboration, et al. "Interferometer design of the KAGRA gravitational wave detector". *Physical Review D* 88.4 (2013), p. 043007.

[5] Harald Lück, Martin Hewitson, P Ajith, B Allen, Peter Aufmuth, Carsten Aulbert, Stanislav Babak, Ramachandran Balasubramanian, BW Barr, S Berukoff, et al. "Status of the GEO600 detector". *Classical and Quantum Gravity* 23.8 (2006), S71.

[6] Andrew N Cleland and Michael L Roukes. "A nanometre-scale mechanical electrometer". *Nature* 392.6672 (1998), pp. 160–162.

[7] K Jensen, Kwanpyo Kim, and A Zettl. "An atomic-resolution nanomechanical mass sensor". *Nature nanotechnology* 3.9 (2008), p. 533.

[8] Menghui Li, Alexei Matyushov, Cunzheng Dong, Huaihao Chen, Hwaider Lin, Tianxiang Nan, Zhenyun Qian, Matteo Rinaldi, Yuanhua Lin, and Nian X Sun. "Ultra-sensitive NEMS magnetoelectric sensor for picotesla DC magnetic field detection". *Applied Physics Letters* 110.14 (2017), p. 143510.

[9] Kerry J Vahala. "Optical microcavities". *nature* 424.6950 (2003), p. 839.

[10] JG Rarity and Claude Weisbuch. *Microcavities and photonic bandgaps: physics and applications*. Vol. 324. Springer Science & Business Media, 2012.

[11] Xuepeng Zhan, Huailiang Xu, and Hongbo Sun. "Femtosecond laser processing of microcavity lasers". *Frontiers of Optoelectronics* 9.3 (2016), pp. 420–427.

[12] Hongxing Dong, Beier Zhou, Jingzhou Li, Jingxin Zhan, and Long Zhang. "Ultraviolet lasing behavior in ZnO optical microcavities". *Journal of Materiomics* 3.4 (2017), pp. 255–266.

[13] Matjaž Humar. "Liquid-crystal-droplet optical microcavities". *Liquid Crystals* 43.13-15 (2016), pp. 1937–1950.

[14] H Rokhsari and KJ Vahala. "Ultralow loss, high Q, four port resonant couplers for quantum optics and photonics". *Physical review letters* 92.25 (2004), p. 253905.

[15] Vilson R Almeida, Carlos A Barrios, Roberto R Panepucci, and Michal Lipson. "All-optical control of light on a silicon chip". *Nature* 431.7012 (2004), pp. 1081–1084.

[16] Hansuek Lee, Tong Chen, Jiang Li, Oskar Painter, and Kerry J Vahala. "Ultra-low-loss optical delay line on a silicon chip". *Nature communications* 3.1 (2012), pp. 1–7.

[17] Rodrigo Gómez-Martínez, Alberto M Hernández-Pinto, Marta Duch, Patricia Vázquez, Kirill Zinoviev, J Enrique, Jaume Esteve, Teresa Suárez, and José A Plaza. "Silicon chips detect intracellular pressure changes in living cells". *Nature nanotechnology* 8.7 (2013), p. 517.

[18] Qianfan Xu, Bradley Schmidt, Sameer Pradhan, and Michal Lipson. "Micrometre-scale silicon electro-optic modulator". *Nature* 435.7040-(2005), pp. 325–327.

[19] Xu Yi, Yun-Feng Xiao, Yong-Chun Liu, Bei-Bei Li, You-Ling Chen, Yan Li, and Qihuang Gong. "Multiple-Rayleigh-scatterer-induced mode splitting in a high-Q whispering-gallery-mode microresonator". *Physical Review A* 83.2 (2011), p. 023803.

[20] Markus Aspelmeyer, Tobias J Kippenberg, and Florian Marquardt. *Cavity optomechanics: nano-and micromechanical resonators interacting with light*. Springer, 2014.

[21] Uroš Delić, Manuel Reisenbauer, Kahan Dare, David Grass, Vladan Vuletić, Nikolai Kiesel, and Markus Aspelmeyer. "Cooling of a levitated nanoparticle to the motional quantum ground state". *Science* (2020).

[22] Gregory M Harry, LIGO Scientific Collaboration, et al. "Advanced LIGO: the next generation of gravitational wave detectors". *Classical and Quantum Gravity* 27.8 (2010), p. 084006.

[23] Ming Cai, Oskar Painter, and Kerry J Vahala. "Observation of critical coupling in a fiber taper to a silica-microsphere whispering-gallery mode system". *Physical review letters* 85.1 (2000), p. 74.

[24] Pierre Etienne Allain, Lucien Schwab, Colin Mismer, Marc Gely, Estelle Mairiaux, Maxime Hermouet, Benjamin Walter, Giuseppe Leo, Sébastien Hentz, Marc Faucher, et al. "Optomechanical resonating probe for very high frequency sensing of atomic forces". *Nanoscale* 12.5 (2020), pp. 2939–2945.

[25] Rodrigo Benevides, Michaël Ménard, Gustavo S Wiederhecker, and Thiago P Mayer Alegre. "Ar/Cl 2 etching of GaAs optomechanical microdisks fabricated with positive electroresist". *Optical Materials Express* 10.1 (2020), pp. 57–67.

[26] Ewold Verhagen, Samuel Deléglise, Stefan Weis, Albert Schliesser, and Tobias J Kippenberg. "Quantum-coherent coupling of a mechanical oscillator to an optical cavity mode". *Nature* 482.7383 (2012), pp. 63–67.

[27] John D Teufel, Tobias Donner, MA Castellanos-Beltran, Jennifer W Harlow, and Konrad W Lehnert. "Nanomechanical motion measured with an imprecision below that at the standard quantum limit". *Nature nanotechnology* 4.12 (2009), pp. 820–823.

[28] Jasper Chan, TP Mayer Alegre, Amir H Safavi-Naeini, Jeff T Hill, Alex Krause, Simon Gröblacher, Markus Aspelmeyer, and Oskar Painter. "Laser cooling of a nanomechanical oscillator into its quantum ground state". *Nature* 478.7367 (2011), pp. 89–92.

[29] Amir H Safavi-Naeini, Jeff T Hill, Seán Meenehan, Jasper Chan, Simon Gröblacher, and Oskar Painter. "Two-dimensional phononic-photonic band gap optomechanical crystal cavity". *Physical Review Letters* 112.15 (2014), p. 153603.

[30] Jordi Gomis-Bresco, Daniel Navarro-Urrios, Mourad Oudich, Said El-Jallal, Amadeu Griol, Daniel Puerto, Emiglio Chavez, Yan Pennec, Bahram Djafari-Rouhani, Franscesca Alzina, et al. "A one-dimensional optomechanical crystal with a complete phononic band gap". *Nature communications* 5.1 (2014), pp. 1–6.

[31] Parag B Deotare, Irfan Bulu, Ian W Frank, Qimin Quan, Yinan Zhang, Rob Ilic, and Marko Loncar. "All optical reconfiguration of optomechanical filters". *Nature Communications* 3.1 (2012), pp. 1–8.

[32] Jing Ma and Michelle L Povinelli. "Applications of optomechanical effects for on-chip manipulation of light signals". *Current Opinion in Solid State and Materials Science* 16.2 (2012), pp. 82–90.

[33] Xiang Guo, Chang-Ling Zou, Xi-Feng Ren, Fang-Wen Sun, and Guang-Can Guo. "Broadband opto-mechanical phase shifter for photonic integrated circuits". *Applied Physics Letters* 101.7 (2012), p. 071114.

[34] Georg Anetsberger, Emanuel Gavartin, Olivier Arcizet, Quirin P Unterreithmeier, Eva Maria Weig, Michael L Gorodetsky, Jörg Peter Kotthaus, and Tobias J Kippenberg. "Measuring nanomechanical motion with an imprecision below the standard quantum limit". *Physical Review A* 82.6 (2010), p. 061804.

[35] Albert Schliesser, Olivier Arcizet, Rémi Rivière, Georg Anetsberger, and Tobias J Kippenberg. "Resolved-sideband cooling and position measurement of a micromechanical oscillator close to the Heisenberg uncertainty limit". *Nature Physics* 5.7 (2009), p. 509.

[36] V.B. Braginsky and Y.I. Vorontsov. "Quantum-mechanical limitations in macroscopic experiments and modern experimental technique". *Sov. Phys. Ups* 17.5 (1975), pp. 644–650.

[37] V.B. Braginsky and A. Manukin. *Measurement of Weak Forces in Physics Experiments*. University Press of Chicago, 1977.

[38] Michelle L Povinelli, Steven G Johnson, Marko Lončar, Mihai Ibanescu, Elizabeth J Smythe, Federico Capasso, and JD Joannopoulos. "High-Q enhancement of attractive and repulsive optical forces between coupled whispering-gallery-mode resonators". *Optics express* 13.20 (2005), pp. 8286–8295.

[39] Benjamin P Abbott, Richard Abbott, TD Abbott, MR Abernathy, Fausto Acernese, Kendall Ackley, Carl Adams, Thomas Adams, Paolo Addesso, RX Adhikari, et al. "Observation of gravitational waves from a binary black hole merger". *Physical review letters* 116.6 (2016), p. 061102.

[40] Jasper Chan, Matt Eichenfield, Ryan Camacho, and Oskar Painter. "Optical and mechanical design of a "zipper" photonic crystal optomechanical cavity". *Optics Express* 17.5 (2009), pp. 3802–3817.

[41] Matt Eichenfield, Ryan Camacho, Jasper Chan, Kerry J Vahala, and Oskar Painter. "A picogram-and nanometre-scale photonic-crystal optomechanical cavity". *nature* 459.7246 (2009), pp. 550–555.

[42] Alexander G Krause, Martin Winger, Tim D Blasius, Qiang Lin, and Oskar Painter. "A high-resolution microchip optomechanical accelerometer". *Nature Photonics* 6.11 (2012), p. 768.

[43] Alan Edelstein. "Advances in magnetometry". *Journal of Physics: Condensed Matter* 19.16 (2007), p. 165217.

[44] Michael I Faley. "Epitaxial oxide heterostructures for ultimate high-Tc quantum interferometers". *Applications of High-Tc Superconductivity, Rijeka: InTech* (2011), pp. 147–176.

[45] John Clarke and Alex I Braginski. *The SQUID handbook: Applications of SQUIDs and SQUID systems*. John Wiley & Sons, 2006.

[46] Michael V Romalis and Hoan B Dang. "Atomic magnetometers for materials characterization". *Materials today* 14.6 (2011), pp. 258–262.

[47] HB Dang, Adam C Maloof, and Michael V Romalis. "Ultrahigh sensitivity magnetic field and magnetization measurements with an atomic magnetometer". *Applied Physics Letters* 97.15 (2010), p. 151110.

[48] S Forstner, S Prams, J Knittel, ED Van Ooijen, JD Swaim, GI Harris, A Szorkovszky, WP Bowen, and H Rubinsztein-Dunlop. "Cavity optomechanical magnetometer". *Physical review letters* 108.12 (2012), p. 120801.

[49] Stefan Forstner, Eoin Sheridan, Joachim Knittel, Christopher L Humphreys, George A Brawley, Halina Rubinsztein-Dunlop, and Warwick P Bowen. "Ultrasensitive optomechanical magnetometry". *Advanced Materials* 26.36 (2014), pp. 6348–6353.

[50] Bei-Bei Li, Jan Bilek, Ulrich B Hoff, Lars S Madsen, Stefan Forstner, Varun Prakash, Clemens Schäfermeier, Tobias Gehring, Warwick P Bowen, and Ulrik L Andersen. "Quantum enhanced optomechanical magnetometry". *Optica* 5.7 (2018), pp. 850–856.

[51] MC Cross. "Improving the frequency precision of oscillators by synchronization". *Physical Review E* 85.4 (2012), p. 046214.

[52] Mian Zhang, Gustavo S Wiederhecker, Sasikanth Manipatruni, Arthur Barnard, Paul McEuen, and Michal Lipson. "Synchronization of micromechanical oscillators using light". *Physical review letters* 109.23-(2012), p. 233906.

[53] Mahmood Bagheri, Menno Poot, Linran Fan, Florian Marquardt, and Hong X Tang. "Photonic cavity synchronization of nanomechanical oscillators". *Physical review letters* 111.21 (2013), p. 213902.

[54] Eduardo Gil-Santos, Matthieu Labousse, Christophe Baker, Arthur Goetschy, William Hease, Carmen Gomez, Aristide Lemaître, Giuseppe Leo, Cristiano Ciuti, and Ivan Favero. "Light-mediated cascaded locking of multiple nano-optomechanical oscillators". *Physical review letters* 118.6 (2017), p. 063605.

[55] Shreyas Y Shah, Mian Zhang, Richard Rand, and Michal Lipson. "Master-slave locking of optomechanical oscillators over a long distance". *Physical review letters* 114.11 (2015), p. 113602.

[56] Jae K Jang, Alexander Klenner, Xingchen Ji, Yoshitomo Okawachi, Michal Lipson, and Alexander L Gaeta. "Synchronization of coupled optical microresonators". *Nature Photonics* 12.11 (2018), p. 688.

[57] Tobias J Kippenberg and Kerry J Vahala. "Cavity optomechanics: back-action at the mesoscale". *science* 321.5893 (2008), pp. 1172–1176.

[58] John D Joannopoulos, Robert David Meade, and Joshua N Winn. *Photonic crystals*. Princeton, 2008.

[59] Kartik Srinivasan. "Semiconductor optical microcavities for chip-based cavity QED". PhD thesis. California Institute of Technology, 2006.

[60] Chris Chatfield. *The analysis of time series: an introduction*. Chapman and Hall/CRC, 2003.

[61] Wolfram Hergert and Thomas Wriedt. *The Mie theory: basics and applications*. Vol. 169. Springer, 2012.

[62] Lord Rayleigh. "CXII. The problem of the whispering gallery". *The London, Edinburgh, and Dublin Philosophical Magazine and Journal of Science* 20.120 (1910), pp. 1001–1004.

[63] V. B. Braginsky, M. L. Gorodetsky, and V. S. Ilchenko. "Quality-factor and nonlinear properties of optical whispering-gallery modes". *Physics Letters A* 137.7-8 (1989), pp. 393–397. ISSN: 03759601. DOI: 10.1016/0375-9601(89)90912-2.

[64] Lefevreseguin Collot, V Lefevre-Seguin, M Brune, JM Raimond, and S Haroche. "Very high-Q whispering-gallery mode resonances observed on fused silica microspheres". *EPL (Europhysics Letters)* 23.5 (1993), p. 327.

[65] DW Vernooy, Vladimir S Ilchenko, H Mabuchi, EW Streed, and HJ Kimble. "High-Q measurements of fused-silica microspheres in the near infrared". *Optics letters* 23.4 (1998), pp. 247–249.

[66] H Jeff Kimble. "Strong interactions of single atoms and photons in cavity QED". *Physica Scripta* 1998.T76 (1998), p. 127.

[67] Serge Haroche and Daniel Kleppner. "Cavity quantum electrodynamics". *Phys. Today* 42.1 (1989), pp. 24–30.

[68] Lan Yang, DK Armani, and KJ Vahala. "Fiber-coupled erbium microlasers on a chip". *Applied physics letters* 83.5 (2003), pp. 825–826.

[69] Jonathan Ward and Oliver Benson. "WGM microresonators: sensing, lasing and fundamental optics with microspheres". *Laser & Photonics Reviews* 5.4 (2011), pp. 553–570.

[70] J Cheung Knight, G Cheung, F Jacques, and TA Birks. "Phase-matched excitation of whispering-gallery-mode resonances by a fiber taper". *Optics letters* 22.15 (1997), pp. 1129–1131.

[71] Kuang-Chao Fan, Hung-Yao Hsu, Po-Yuan Hung, and Weili Wang. "Experimental study of fabricating a microball tip on an optical fibre". *Journal of Optics A: Pure and Applied Optics* 8.9 (2006), p. 782.

[72] Pablo Bianucci, Chris R Fietz, John W Robertson, Gennady Shvets, and Chih-Kang Shih. "Whispering gallery mode microresonators as polarization converters". *Optics letters* 32.15 (2007), pp. 2224–2226.

[73] LL Martín, P Haro-González, IR Martín, D Navarro-Urrios, D Alonso, C Pérez-Rodríguez, D Jaque, and NE Capuj. "Whispering-gallery modes in glass microspheres: optimization of pumping in a modified confocal microscope". *Optics letters* 36.5 (2011), pp. 615–617.

[74] Valérie Lefèvre-Seguin. "Whispering-gallery mode lasers with doped silica microspheres". *Optical Materials* 11.2-3 (1999), pp. 153–165.

[75] Gregor R Elliott, Daniel W Hewak, G Senthil Murugan, and James S Wilkinson. "Chalcogenide glass microspheres; their production, characterization and potential". *Optics Express* 15.26 (2007), pp. 17542–17553.

[76] TJ Kippenberg, SM Spillane, and KJ Vahala. "Demonstration of ultra-high-Q small mode volume toroid microcavities on a chip". *Applied Physics Letters* 85.25 (2004), pp. 6113–6115.

[77] Albert Schliesser, Georg Anetsberger, Rémi Rivière, Olivier Arcizet, and Tobias J Kippenberg. "High-sensitivity monitoring of micromechanical vibration using optical whispering gallery mode resonators". *New Journal of Physics* 10.9 (2008), p. 095015.

[78] Silvia Soria, Simone Berneschi, Massimo Brenci, Franco Cosi, Gualtiero Nunzi Conti, Stefano Pelli, and Giancarlo C Righini. "Optical microspherical resonators for biomedical sensing". *Sensors* 11.1 (2011), bibrangedash 785–805.

[79] F Vollmer, S Arnold, and D Keng. "Single virus detection from the reactive shift of a whispering-gallery mode". *Proceedings of the National Academy of Sciences* 105.52 (2008), pp. 20701–20704.

[80] Frank Vollmer and Stephen Arnold. "Whispering-gallery-mode biosensing: label-free detection down to single molecules". *Nature methods* 5.7 (2008), p. 591.

[81] SM Spillane, TJ Kippenberg, and KJ Vahala. "Ultralow-threshold Raman laser using a spherical dielectric microcavity". *Nature* 415.6872 (2002), pp. 621–623.

[82] DW Vernooy, A Furusawa, N Ph Georgiades, VS Ilchenko, and HJ Kimble. "Cavity QED with high-Q whispering gallery modes". *Physical Review A* 57.4 (1998), R2293.

[83] Daniel Navarro-Urrios, Marta Baselga, Federico Ferrarese Lupi, Leopoldo L Martín, Carla Pérez-Rodríguez, Víctor Lavin, Inocencio R Martín, Blas Garrido, and Néstor E Capuj. "Local characterization of rare-earth-doped single microspheres by combined microtransmission and microphotoluminescence techniques". *JOSA B* 29.12 (2012), pp. 3293–3298.

[84] LL Martín, D Navarro-Urrios, F Ferrarese-Lupi, C Pérez-Rodríguez, IR Martín, J Montserrat, Carlos Domínguez, Blas Garrido, and N Capuj. "Laser emission in Nd3+ doped barium–titanium–silicate microspheres under continuous and chopped wave pumping in a non-coupled pumping scheme". *Laser Physics* 23.7 (2013), p. 075801.

[85] Lina He, Şahin Kaya Özdemir, and Lan Yang. "Whispering gallery microcavity lasers". *Laser & Photonics Reviews* 7.1 (2013), pp. 60–82.

[86] Frank Vollmer and Lan Yang. "Review Label-free detection with high-Q microcavities: a review of biosensing mechanisms for integrated devices". *Nanophotonics* 1.3-4 (2012), pp. 267–291.

[87] Anatolii N Oraevsky. "Whispering-gallery waves". *Quantum electronics* 32.5 (2002), p. 377.

[88] Tobias Jan August Kippenberg. "Nonlinear optics in ultra-high Q whispering-gallery optical microcavities". PhD thesis. California Institute of Technology, 2004.

[89] Albert Schließer. "Cavity optomechanics and optical frequency comb generation with silica whispering-gallery-mode microresonators". PhD thesis. lmu, 2009.

[90] Stéphane Balac. "WGMode: A Matlab toolbox for whispering gallery modes volume computation in spherical optical micro-resonators". *Computer Physics Communications* 243 (2019), pp. 121–134.

[91] JM Ramírez, D Navarro-Urrios, NE Capuj, Y Berencén, A Pitanti, B Garrido, and Alessandro Tredicucci. "Far-field characterization of the thermal dynamics in lasing microspheres". *Scientific reports* 5 (2015), p. 14452.

[92] Matt Eichenfield, Jasper Chan, Ryan M Camacho, Kerry J Vahala, and Oskar Painter. "Optomechanical crystals". *Nature* 462.7269 (2009), bibrangedash 78–82.

[93] Emanuel Gavartin, Remy Braive, Isabelle Sagnes, Olivier Arcizet, Alexios Beveratos, Tobias J Kippenberg, and Isabelle Robert-Philip. "Optomechanical coupling in a two-dimensional photonic crystal defect cavity". *Physical review letters* 106.20 (2011), p. 203902.

[94] Michael J Burek, Yiwen Chu, Madelaine SZ Liddy, Parth Patel, Jake Rochman, Srujan Meesala, Wooyoung Hong, Qimin Quan, Mikhail D Lukin, and Marko Lončar. "High quality-factor optical nanocavities in bulk single-crystal diamond". *Nature communications* 5.1 (2014), pp. 1–7.

[95] Daniel Navarro-Urrios, Néstor E Capuj, Martín F Colombano, P David García, Marianna Sledzinska, Francesc Alzina, Amadeu Griol, Alejandro Martínez, and Clivia M Sotomayor-Torres. "Nonlinear dynamics and chaos in an optomechanical beam". *Nature communications* 8 (2017), p. 14965.

[96] Emanuel Gavartin, Pierre Verlot, and Tobias J Kippenberg. "A hybrid on-chip optomechanical transducer for ultrasensitive force measurements". *Nature nanotechnology* 7.8 (2012), p. 509.

[97] MD LaHaye, Olivier Buu, Benedetta Camarota, and KC Schwab. "Approaching the quantum limit of a nanomechanical resonator". *Science* 304.5667 (2004), pp. 74–77.

[98] Amir H Safavi-Naeini, TP Mayer Alegre, Jasper Chan, Matt Eichenfield, Martin Winger, Qiang Lin, Jeff T Hill, Darrick E Chang, and Oskar Painter. "Electromagnetically induced transparency and slow light with optomechanics". *Nature* 472.7341 (2011), pp. 69–73.

[99] John D Teufel, Tobias Donner, Dale Li, Jennifer W Harlow, MS Allman, Katarina Cicak, Adam J Sirois, Jed D Whittaker, Konrad W Lehnert, and Raymond W Simmonds. "Sideband cooling of micromechanical motion to the quantum ground state". *Nature* 475.7356 (2011), p. 359.

[100] Amir H Safavi-Naeini, Simon Gröblacher, Jeff T Hill, Jasper Chan, Markus Aspelmeyer, and Oskar Painter. "Squeezed light from a silicon micromechanical resonator". *Nature* 500.7461 (2013), p. 185.

[101] Daniel Navarro-Urrios, Jordi Gomis-Bresco, Francesc Alzina, NE Capuj, PD García, MF Colombano, Emigdio Chávez-Angel, and Clivia M Sotomayor-Torres. "Self-sustained coherent phonon generation in optomechanical cavities". *Journal of optics* 18.9 (2016), p. 094006.

[102] Mourad Oudich, Said El-Jallal, Yan Pennec, Bahram Djafari-Rouhani, Jordi Gomis-Bresco, Daniel Navarro-Urrios, Clivia M Sotomayor Torres, Alejandro Martínez, and Abdelkader Makhoute. "Optomechanic interaction in a corrugated phoxonic nanobeam cavity". *Physical Review B* 89.24 (2014), p. 245122.

[103] Pedro David García, Robert Bericat-Vadell, Guillermo Arregui, Daniel Navarro-Urrios, Martín Colombano, Francesc Alzina, and Clivia Marfa Sotomayor-Torres. "Optomechanical coupling in the Anderson-localization regime". *Physical Review B* 95.11 (2017), p. 115129.

[104] Daniel Navarro-Urrios, Jordi Gomis-Bresco, Said El-Jallal, Mourad Oudich, A Pitanti, N Capuj, Alessandro Tredicucci, Francesc Alzina, Amadeu Griol, Yan Pennec, et al. "Dynamical back-action at 5.5 GHz in a corrugated optomechanical beam". *AIP Advances* 4.12 (2014), p. 124601.

[105] Daniel Navarro-Urrios, Alessandro Tredicucci, and Clivia M Sotomayor-Torres. "Coherent phonon generation in optomechanical crystals". *SPIE Newsroom, doi* 10.2.1201507 (2015), p. 006036.

[106] Jasper Chan, Amir H Safavi-Naeini, Jeff T Hill, Seán Meenehan, and Oskar Painter. "Optimized optomechanical crystal cavity with acoustic radiation shield". *Applied Physics Letters* 101.8 (2012), p. 081115.

[107] Thomas J Johnson, Matthew Borselli, and Oskar Painter. "Self-induced optical modulation of the transmission through a high-Q silicon microdisk resonator". *Optics express* 14.2 (2006), pp. 817–831.

[108] Qianfan Xu and Michal Lipson. "Carrier-induced optical bistability in silicon ring resonators". *Optics letters* 31.3 (2006), pp. 341–343.

[109] Paul E Barclay, Kartik Srinivasan, and Oskar Painter. "Nonlinear response of silicon photonic crystal microresonators excited via an integrated waveguide and fiber taper". *Optics express* 13.3 (2005), pp. 801–820.

[110] Christophe Baker, Sebastian Stapfner, David Parrain, Sara Ducci, Giuseppe Leo, Eva M Weig, and Ivan Favero. "Optical instability and self-pulsing in silicon nitride whispering gallery resonators". *Optics express* 20.27 (2012), pp. 29076–29089.

[111] Alexey E Fomin, Michael L Gorodetsky, Ivan S Grudinin, and Vladimir S Ilchenko. "Nonstationary nonlinear effects in optical microspheres". *JOSA B* 22.2 (2005), pp. 459–465.

[112] Wolfram HP Pernice, Mo Li, and Hong X Tang. "Time-domain measurement of optical transport in silicon micro-ring resonators". *Optics express* 18.17 (2010), pp. 18438–18452.

[113] Jinghui Yang, Tingyi Gu, Jiangjun Zheng, Mingbin Yu, Guo-Qiang Lo, Dim-Lee Kwong, and Chee Wei Wong. "Radio frequency regenerative oscillations in monolithic high-Q/V heterostructured photonic crystal cavities". *Applied Physics Letters* 104.6 (2014), p. 061104.

[114] Yang Deng, Fenfei Liu, Zayd C Leseman, and Mani Hossein-Zadeh. "Thermo-optomechanical oscillator for sensing applications". *Optics express* 21.4 (2013), pp. 4653–4664.

[115] Alessandro Volta. "XVII. On the electricity excited by the mere contact of conducting substances of different kinds. In a letter from Mr. Alexander Volta, FRS Professor of Natural Philosophy in the University of Pavia, to the Rt. Hon. Sir Joseph Banks, Bart. KBPR S". *Philosophical transactions of the Royal Society of London* 90 (1800), pp. 403–431.

[116] Hans Christian Oersted. *Experiments on the Effect of a Current of Electricityon the Magnetic Needle*. C. Baldwin, 1820.

[117] James Clerk Maxwell. "VIII. A dynamical theory of the electromagnetic field". *Philosophical transactions of the Royal Society of London* 155 (1865), pp. 459–512.

[118] W Shockley, J Bardeen, and W Brattain. "The first transistor". *Bell Laboratories (Dec. 16, 1947)* (1947), p. 27.

[119] Walther Gerlach and Otto Stern. "Das magnetische moment des silberatoms". *Zeitschrift für Physik A Hadrons and Nuclei* 9.1 (1922), pp. 353–355.

[120] EM Purcell, RV Pound, and N Bloembergen. "Nuclear magnetic resonance absorption in hydrogen gas". *Physical Review* 70.11-12 (1946), p. 986.

[121] Peter A Grünberg. "Nobel Lecture: From spin waves to giant magnetoresistance and beyond". *Reviews of Modern Physics* 80.4 (2008), p. 1531.

[122] Shuichi Murakami, Naoto Nagaosa, and Shou-Cheng Zhang. "Dissipationless quantum spin current at room temperature". *Science* 301.-5638 (2003), pp. 1348–1351.

[123] Jairo Sinova and Igor Žutić. "New moves of the spintronics tango". *Nature materials* 11.5 (2012), p. 368.

[124] Gerrit EW Bauer, Eiji Saitoh, and Bart J Van Wees. "Spin caloritronics". *Nature materials* 11.5 (2012), p. 391.

[125] Sebastian TB Goennenwein and Gerrit EW Bauer. "Spin caloritronics: Electron spins blow hot and cold". *Nature nanotechnology* 7.3 (2012), p. 145.

[126] M Pomerantz. "Excitation of spin-wave resonance by microwave phonons". *Physical Review Letters* 7.8 (1961), p. 312.

[127] Felix Bloch. "Zur theorie des ferromagnetismus". *Zeitschrift für Physik* 61.3-4 (1930), pp. 206–219.

[128] AV Chumak, VI Vasyuchka, AA Serga, and Burkard Hillebrands. "Magnon spintronics". *Nature Physics* 11.6 (2015), p. 453.

[129] Natalia Polzikova, Sergey Alekseev, Iosif Kotelyanskii, Alexander Raevskiy, and Yuri Fetisov. "Magnetic field tunable acoustic resonator with ferromagnetic-ferroelectric layered structure". *Journal of Applied Physics* 113.17 (2013), p. 17C704.

[130] VV Kruglyak, SO Demokritov, and D Grundler. "Magnonics". *Journal of Physics D: Applied Physics* 43.26 (2010), p. 264001.

[131] AA Serga, AV Chumak, and B Hillebrands. "YIG magnonics". *Journal of Physics D: Applied Physics* 43.26 (2010), p. 264002.

[132] Lei Bi, Juejun Hu, Peng Jiang, Dong Hun Kim, Gerald F Dionne, Lionel C Kimerling, and CA Ross. "On-chip optical isolation in monolithically integrated non-reciprocal optical resonators". *Nature Photonics* 5.12 (2011), p. 758.

[133] Chi Tang, Mohammed Aldosary, Zilong Jiang, Houchen Chang, Benjamin Madon, Kyle Chan, Mingzhong Wu, Javier E Garay, and Jing Shi. "Exquisite growth control and magnetic properties of yttrium iron garnet thin films". *Applied Physics Letters* 108.10 (2016), p. 102403.

[134] Xufeng Zhang, Na Zhu, Chang-Ling Zou, and Hong X Tang. "Optomagnonic whispering gallery microresonators". *Physical review letters* 117.12 (2016), p. 123605.

[135] Dany Lachance-Quirion, Yutaka Tabuchi, Seiichiro Ishino, Atsushi Noguchi, Toyofumi Ishikawa, Rekishu Yamazaki, and Yasunobu Nakamura. "Resolving quanta of collective spin excitations in a millimeter-sized ferromagnet". *Science advances* 3.7 (2017), e1603150.

[136] Yi-Heng Rao, Huai-Wu Zhang, Qing-Hui Yang, Dai-Nan Zhang, Li-Chuan Jin, Bo Ma, and Yu-Juan Wu. "Liquid phase epitaxy magnetic garnet films and their applications". *Chinese Physics B* 27.8 (2018), bibrangedash 086701.

[137] EA Giess, JD Kuptsis, and E Ao D White. "Liquid phase epitaxial growth of magnetic garnet films by isothermal dipping in a horizontal plane with axial rotation". *Journal of Crystal Growth* 16.1 (1972), pp. 36–42.

[138] TA Gilbert. "Equation of motion of magnetization". *Armour Research Foundation Rep.* 11 (1955).

[139] LALE Landau and Evgeny Lifshitz. "On the theory of the dispersion of magnetic permeability in ferromagnetic bodies". *Perspectives in Theoretical Physics*. Elsevier, 1992, pp. 51–65.

[140] Daniel D Stancil and Anil Prabhakar. *Spin waves*. Springer, 2009. Chap. 3, p. 95.

[141] Charles Kittel, Paul McEuen, and Paul McEuen. *Introduction to solid state physics*. Vol. 8. Wiley New York, 1996. Chap. 13, p. 381.

[142] CM Srivastava and R Aiyar. "Spin wave stiffness constants in some ferrimagnetics". *Journal of Physics C: Solid State Physics* 20.8 (1987), p. 1119.

[143] Ch Kittel. "Interaction of spin waves and ultrasonic waves in ferromagnetic crystals". *Physical Review* 110.4 (1958), p. 836.

[144] LeCraw R. C. and Comstock R. L. *Physical acoustics: principles and methods*. Vol. 3B. Academic press, 2013. Chap. 4.

[145] Asaf Grosz, Michael J Haji-Sheikh, and Subhas C Mukhopadhyay. *High sensitivity magnetometers*. Springer, 2017.

[146] AM Chang, HD Hallen, L Harriott, HF Hess, HL Kao, J Kwo, RE Miller, R Wolfe, J Van der Ziel, and TY Chang. "Scanning Hall probe microscopy". *Applied physics letters* 61.16 (1992), pp. 1974–1976.

[147] JM Taylor, P Cappellaro, L Childress, L Jiang, D Budker, PR Hemmer, A Yacoby, R Walsworth, and MD Lukin. "High-sensitivity diamond magnetometer with nanoscale resolution". *Nature Physics* 4.10 (2008), p. 810.

[148] F Bucholtz, DM Dagenais, and KP Koo. "High-frequency fibre-optic magnetometer with 70 fT/square root (Hz) resolution". *Electronics Letters* 25.25 (1989), pp. 1719–1721.

[149] M Vengalattore, JM Higbie, SR Leslie, J Guzman, LE Sadler, and DM Stamper-Kurn. "High-resolution magnetometry with a spinor Bose-Einstein condensate". *Physical review letters* 98.20 (2007), p. 200801.

[150] Pavel Ripka and Michal Janosek. "Advances in magnetic field sensors". *IEEE Sensors journal* 10.6 (2010), pp. 1108–1116.

[151] JR Kirtley, MB Ketchen, KG Stawiasz, JZ Sun, WJ Gallagher, SH Blanton, and SJ Wind. "High-resolution scanning SQUID microscope". *Applied Physics Letters* 66.9 (1995), pp. 1138–1140.

[152] Michael I Faley. "Epitaxial oxide heterostructures for ultimate high-Tc quantum interferometers". *Applications of High-Tc Superconductivity, Rijeka: InTech* (2011), pp. 147–176.

[153] Lisa Tauxe. *Paleomagnetic principles and practice*. Vol. 17. Springer Science & Business Media, 2006.

[154] Daniel Rugar, Raffi Budakian, HJ Mamin, and BW Chui. "Single spin detection by magnetic resonance force microscopy". *Nature* 430.6997 (2004), pp. 329–332.

[155] Matti Hämäläinen, Riitta Hari, Risto J Ilmoniemi, Jukka Knuutila, and Olli V Lounasmaa. "Magnetoencephalography—theory, instrumentation, and applications to noninvasive studies of the working human brain". *Reviews of modern Physics* 65.2 (1993), p. 413.

[156] Bei-Bei Li, Douglas Bulla, Varun Prakash, Stefan Forstner, Ali Dehghan-Manshadi, Halina Rubinsztein-Dunlop, Scott Foster, and Warwick P Bowen. "On-chip scalable optomechanical magnetometers". *arXiv preprint arXiv:1805.09660* (2018).

[157] Alessandra Toncelli, NE Capuj, B Garrido, Marianna Sledzinska, Clivia M Sotomayor-Torres, Alessandro Tredicucci, and Daniel Navarro-Urrios.

"Mechanical oscillations in lasing microspheres". *Journal of Applied Physics* 122.5 (2017), p. 053101.

[158] Tristan Briant, P-F Cohadon, Antoine Heidmann, and Michel Pinard. "Optomechanical characterization of acoustic modes in a mirror". *Physical Review A* 68.3 (2003), p. 033823.

[159] Isaak D Mayergoyz. *Handbook of giant magnetostrictive materials*. Elsevier, 1999.

[160] AE Clark, B DeSavage, W Coleman, ER Callen, and HB Callen. "Saturation Magnetostriction of Single-Crystal YIG". *Journal of Applied Physics* 34.4 (1963), pp. 1296–1297.

[161] Warwick P Bowen and Gerard J Milburn. *Quantum optomechanics*. CRC press, 2015.

[162] S Forstner, S Prams, J Knittel, ED Van Ooijen, JD Swaim, GI Harris, A Szorkovszky, WP Bowen, and H Rubinsztein-Dunlop. "Cavity optomechanical magnetometer". *Physical review letters* 108.12 (2012), p. 120801.

[163] Kwan H Lee, Terry G McRae, Glen I Harris, Joachim Knittel, and Warwick P Bowen. "Cooling and control of a cavity optoelectromechanical system". *Physical review letters* 104.12 (2010), p. 123604.

[164] F Baudenbacher, LE Fong, JR Holzer, and M Radparvar. "Monolithic low-transition-temperature superconducting magnetometers for high resolution imaging magnetic fields of room temperature samples". *Applied Physics Letters* 82.20 (2003), pp. 3487–3489.

[165] Vishal Shah, Svenja Knappe, Peter DD Schwindt, and John Kitching. "Subpicotesla atomic magnetometry with a microfabricated vapour cell". *Nature Photonics* 1.11 (2007), p. 649.

[166] A Sandhu, A Okamoto, I Shibasaki, and A Oral. "Nano and micro Hall-effect sensors for room-temperature scanning hall probe microscopy". *Microelectronic Engineering* 73 (2004), pp. 524–528.

[167] Thomas Wolf, Philipp Neumann, Kazuo Nakamura, Hitoshi Sumiya, Takeshi Ohshima, Junichi Isoya, and Jörg Wrachtrup. "Subpicotesla diamond magnetometry". *Physical Review X* 5.4 (2015), p. 041001.

[168] JR Maze, PL Stanwix, JS Hodges, Sungkun Hong, JM Taylor, P Cappellaro, L Jiang, MV Gurudev Dutt, E Togan, AS Zibrov, et al. "Nanoscale magnetic sensing with an individual electronic spin in diamond". *Nature* 455.7213 (2008), p. 644.

[169] Linh My Pham, David Le Sage, Paul L Stanwix, Tsun Kwan Yeung, D Glenn, Alexei Trifonov, Paola Cappellaro, Philip R Hemmer, Mikhail D Lukin, Hongkun Park, et al. "Magnetic field imaging with nitrogen-vacancy ensembles". *New Journal of Physics* 13.4 (2011), p. 045021.

[170] Kasper Jensen, Nathan Leefer, Andrey Jarmola, Yannick Dumeige, Victor M Acosta, Pauli Kehayias, Brian Patton, and Dmitry Budker. "Cavity-enhanced room-temperature magnetometry using absorption by nitrogen-vacancy centers in diamond". *Physical review letters* 112.16 (2014), p. 160802.

[171] G Srinivasan, CP De Vreugd, MI Bichurin, and VM Petrov. "Magnetoelectric interactions in bilayers of yttrium iron garnet and lead

magnesium niobate-lead titanate: Evidence for strong coupling in single crystals and epitaxial films". *Applied Physics Letters* 86.22 (2005), p. 222506.

[172] JM Taylor, P Cappellaro, L Childress, L Jiang, D Budker, PR Hemmer, A Yacoby, R Walsworth, and MD Lukin. "High-sensitivity diamond magnetometer with nanoscale resolution". *Nature Physics* 4.10 (2008), p. 810.

[173] Shaozhen Li, Wei Zhang, Junjia Ding, John E Pearson, Valentine Novosad, and Axel Hoffmann. "Epitaxial patterning of nanometer-thick Y 3 Fe 5 O 12 films with low magnetic damping". *Nanoscale* 8.1 (2016), pp. 388–394.

[174] Na Zhu, Houchen Chang, Andrew Franson, Tao Liu, Xufeng Zhang, E Johnston-Halperin, Mingzhong Wu, and Hong X Tang. "Patterned growth of crystalline Y3Fe5O12 nanostructures with engineered magnetic shape anisotropy". *Applied Physics Letters* 110.25 (2017), p. 252401.

[175] AV Chumak, AA Serga, B Hillebrands, and MP Kostylev. "Scattering of backward spin waves in a one-dimensional magnonic crystal". *Applied Physics Letters* 93.2 (2008), p. 022508.

[176] Yujiro Katoh, Naoto Sugimoto, and Atsushi Shibukawa. "Formation of Ridges on Gd3Ga5O12 by Ion-Beam Etching and Subsequent Phosphoric Acid Treatment Utilizing Tri-Layered Etching Mask". *Japanese journal of applied physics* 31.12R (1992), p. 3888.

[177] Kazuya Harii, Yong-Jun Seo, Yasumasa Tsutsumi, Hiroyuki Chudo, Koichi Oyanagi, Mamoru Matsuo, Yuki Shiomi, Takahito Ono, Sadamichi Maekawa, and Eiji Saitoh. "Spin Seebeck mechanical force". *Nature communications* 10.1 (2019), p. 2616.

[178] Christiaan Huygens. *Horologium Oscillatorium sive de motu pendulorum, F. Muguet, Paris, 1673. English translation by Richard J.* 1986.

[179] Arkady Pikovsky, Jurgen Kurths, Michael Rosenblum, and Jürgen Kurths. *Synchronization: a universal concept in nonlinear sciences*. Vol. 12. Cambridge university press, 2003.

[180] John William Strutt and Baron Rayleigh. *The theory of sound*. Dover, 1945.

[181] William Henry Eccles and JH Vincent. "On the variations of wavelength of the oscillations generated by three-electrode thermionic tubes due to changes in filament current, plate voltage, grid voltage, or coupling". *Proceedings of the Royal Society of London. Series A, Containing Papers of a Mathematical and Physical Character* 96.680 (1920), pp. 455–465.

[182] Edward Victor Appleton. "Automatic synchronization of triode oscillators". *Proc. Cambridge Phil. Soc*. Vol. 21. 231. 1922, p. 1923.

[183] Balth Van Der Pol. "Vii. forced oscillations in a circuit with non-linear resistance.(reception with reactive triode)". *The London, Edinburgh, and Dublin Philosophical Magazine and Journal of Science* 3.13 (1927), pp. 65–80.

[184] Alexander Balanov, Natalia Janson, Dmitry Postnov, and Olga Sosnovtseva. *Synchronization: from simple to complex*. Springer Science & Business Media, 2008.

[185] FK Lamb, J-J Aly, MC Cook, and DQ Lamb. "Synchronization of magnetic stars in binary systems". *The Astrophysical Journal* 274 (1983), pp. L71–L75.

[186] Renato E Mirollo and Steven H Strogatz. "Synchronization of pulse-coupled biological oscillators". *SIAM Journal on Applied Mathematics* 50.6 (1990), pp. 1645–1662.

[187] Rolf A Ims and Harry P Andreassen. "Spatial synchronization of vole population dynamics by predatory birds". *Nature* 408.6809 (2000), bibrangedash 194.

[188] Martin Fussenegger. "Synthetic biology: Synchronized bacterial clocks". *Nature* 463.7279 (2010), p. 301.

[189] Patrick M O'Connor and Joany Jackman. "Synchronization of mammalian cells". *Cell Cycle—Materials and Methods*. Springer, 1996, pp. 63–74.

[190] Rajarshi Roy and K Scott Thornburg Jr. "Experimental synchronization of chaotic lasers". *Physical Review Letters* 72.13 (1994), p. 2009.

[191] Kurt Wiesenfeld, Pere Colet, and Steven H Strogatz. "Synchronization transitions in a disordered Josephson series array". *Physical review letters* 76.3 (1996), p. 404.

[192] John Clarke. "SQUIDs". *Scientific American* 271.2 (1994), pp. 46–53.

[193] Seung-Bo Shim, Matthias Imboden, and Pritiraj Mohanty. "Synchronized oscillation in coupled nanomechanical oscillators". *science* 316.-5821 (2007), pp. 95–99.

[194] Deepak K Agrawal, Jim Woodhouse, and Ashwin A Seshia. "Observation of locked phase dynamics and enhanced frequency stability in synchronized micromechanical oscillators". *Physical review letters* 111.8 (2013), p. 084101.

[195] Matthew H Matheny, Matt Grau, Luis G Villanueva, Rassul B Karabalin, MC Cross, and Michael L Roukes. "Phase synchronization of two anharmonic nanomechanical oscillators". *Physical review letters* 112.1 (2014), p. 014101.

[196] Andrew S Tanenbaum and M Van Steen. "Distributed Systems: Principles and Paradigms, Prenctice Hall". *Computer Science* (2002).

[197] M S Hanay, S Kelber, AK Naik, D Chi, S Hentz, EC Bullard, E Colinet, L Duraffourg, and ML Roukes. "Single-protein nanomechanical mass spectrometry in real time". *Nature nanotechnology* 7.9 (2012), p. 602.

[198] I Bargatin, EB Myers, JS Aldridge, C Marcoux, P Brianceau, L Duraffourg, E Colinet, S Hentz, P Andreucci, and ML Roukes. "Large-scale integration of nanoelectromechanical systems for gas sensing applications". *Nano letters* 12.3 (2012), pp. 1269–1274.

[199] Mo Li, EB Myers, HX Tang, SJ Aldridge, HC McCaig, JJ Whiting, RJ Simonson, Nathan S Lewis, and ML Roukes. "Nanoelectromechanical resonator arrays for ultrafast, gas-phase chromatographic chemical analysis". *Nano letters* 10.10 (2010), pp. 3899–3903.

[200] Frank C Hoppensteadt and Eugene M Izhikevich. "Oscillatory neurocomputers with dynamic connectivity". *Physical Review Letters* 82.14 (1999), p. 2983.

[201] Steven H Strogatz. "Exploring complex networks". *nature* 410.6825 (2001), p. 268.

[202] Florian Dörfler and Francesco Bullo. "Synchronization in complex networks of phase oscillators: A survey". *Automatica* 50.6 (2014), pp. 1539–1564.

[203] Louis M Pecora, Francesco Sorrentino, Aaron M Hagerstrom, Thomas E Murphy, and Rajarshi Roy. "Cluster synchronization and isolated desynchronization in complex networks with symmetries". *Nature communications* 5 (2014), p. 4079.

[204] Ralf Riedinger, Sungkun Hong, Richard A Norte, Joshua A Slater, Juying Shang, Alexander G Krause, Vikas Anant, Markus Aspelmeyer, and Simon Gröblacher. "Non-classical correlations between single photons and phonons from a mechanical oscillator". *Nature* 530.7590 (2016), p. 313.

[205] Krishna C Balram, Marcelo I Davanço, Jin Dong Song, and Kartik Srinivasan. "Coherent coupling between radiofrequency, optical and acoustic waves in piezo-optomechanical circuits". *Nature photonics* 10.5 (2016), p. 346.

[206] Georg Heinrich, Max Ludwig, Jiang Qian, Björn Kubala, and Florian Marquardt. "Collective dynamics in optomechanical arrays". *Physical review letters* 107.4 (2011), p. 043603.

[207] V Peano, C Brendel, M Schmidt, and F Marquardt. "Topological phases of sound and light". *Physical Review X* 5.3 (2015), p. 031011.

[208] Mian Zhang, Shreyas Shah, Jaime Cardenas, and Michal Lipson. "Synchronization and phase noise reduction in micromechanical oscillator arrays coupled through light". *Physical review letters* 115.16 (2015), p. 163902.

[209] Shreyas Y Shah, Mian Zhang, Richard Rand, and Michal Lipson. "Long-range Synchronization of Nanomechanical Oscillators with Light". *arXiv preprint arXiv:1511.08536* (2015).

[210] Daniel Navarro-Urrios, Nestor E Capuj, Jordi Gomis-Bresco, Francesc Alzina, Alessandro Pitanti, Amadeu Griol, Alejandro Martínez, and CM Sotomayor Torres. "A self-stabilized coherent phonon source driven by optical forces". *Scientific reports* 5 (2015), p. 15733.

[211] Rick Leijssen, Giada R La Gala, Lars Freisem, Juha T Muhonen, and Ewold Verhagen. "Nonlinear cavity optomechanics with nanomechanical thermal fluctuations". *Nature communications* 8 (2017), p. 16024.

[212] MF Colombano, G Arregui, NE Capuj, A Pitanti, Jeremie Maire, Amadeu Griol, B Garrido, Alejandro Martínez, Clivia M Sotomayor-Torres, and Daniel Navarro-Urrios. "Synchronization of optomechanical nanobeams by mechanical interaction". *Physical review letters* 123.1 (2019), p. 017402.

[213] Jeremie Maire, Guillermo Arregui, Nestor E Capuj, Martin F Colombano, Amadeu Griol, Alejandro Martinez, Clivia M Sotomayor-Torres,

and Daniel Navarro-Urrios. "Optical modulation of coherent phonon emission in optomechanical cavities". *APL Photonics* 3.12 (2018), bibrangedash 126102.

[214] Kejie Fang, Matthew H Matheny, Xingsheng Luan, and Oskar Painter. "Optical transduction and routing of microwave phonons in cavity-optomechanical circuits". *Nature Photonics* 10.7 (2016), p. 489.

[215] Joerg Bochmann, Amit Vainsencher, David D Awschalom, and Andrew N Cleland. "Nanomechanical coupling between microwave and optical photons". *Nature Physics* 9.11 (2013), p. 712.

[216] Yichen Shen, Nicholas C Harris, Scott Skirlo, Mihika Prabhu, Tom Baehr-Jones, Michael Hochberg, Xin Sun, Shijie Zhao, Hugo Larochelle, Dirk Englund, et al. "Deep learning with coherent nanophotonic circuits". *Nature Photonics* 11.7 (2017), p. 441.

[217] Duncan J Watts and Steven H Strogatz. "Collective dynamics of 'small-world'networks". *nature* 393.6684 (1998), p. 440.

[218] Mark J Panaggio and Daniel M Abrams. "Chimera states: coexistence of coherence and incoherence in networks of coupled oscillators". *Nonlinearity* 28.3 (2015), R67.

[219] Daniel Navarro-Urrios, Nestor E Capuj, Jeremie Maire, M Colombano, Juliana Jaramillo-Fernandez, Emigdio Chavez-Angel, LL Martin, L Mercadé, Amadeu Griol, Alejandro Martínez, et al. "Nanocrystalline silicon optomechanical cavities". *Optics express* 26.8 (2018), pp. 9829–9839.

[220] Alan M Turing. "Computing machinery and intelligence". *Parsing the Turing Test*. Springer, 2009, pp. 23–65.

[221] Yann LeCun, Yoshua Bengio, and Geoffrey Hinton. "Deep learning". *nature* 521.7553 (2015), pp. 436–444.

[222] Jürgen Schmidhuber. "Deep learning in neural networks: An overview". *Neural networks* 61 (2015), pp. 85–117.